The radiative impact of clouds on the response of the midlatitude circulation to global warming

Zur Erlangung des akademischen Grades eines

DOKTORS DER NATURWISSENSCHAFTEN (Dr. rer. nat.)

von der KIT-Fakultät für Physik des

Karlsruher Instituts für Technologie (KIT)

genehmigte

DISSERTATION

von

M. Sc. Nicole Brigitte Silvia Albern

aus Hamburg

Tag der mündlichen Prüfung:	23.10.2020
Referent:	Prof. Dr. Joaquim Pinto
Korreferenten:	Prof. Dr. Corinna Hoose
	Dr. Aiko Voigt

Abstract

Clouds and the midlatitude circulation are strongly coupled via radiation. Previous work showed that about half of the annual-mean zonal-mean jet stream and storm track responses to global warming can be attributed to cloud-radiative changes. In this thesis, we investigate the impact of cloud-radiative changes on the global warming response of the midlatitude jet streams and storm tracks across seasons and regions with special focus on the North Atlantic, North Pacific and Southern Hemisphere. To this end, we perform global simulations with the atmospheric component of the ICOsahedral Nonhydrostatic (ICON) model in a present-day setup. We prescribe sea-surface temperatures (SST) to isolate the impact of changes in atmospheric cloud-radiative heating on the midlatitude circulation, and mimic global warming by a uniform 4 K or spatially-varying SST increase. We use the cloud-locking method to decompose the midlatitude circulation response into contributions from changes in cloud-radiative properties and from changes in SST.

In the first part of the thesis, we investigate the impact of global cloud-radiative changes on the response of the midlatitude jet streams and storm tracks to global warming. In the annual mean, cloud-radiative changes contribute one to two thirds to the poleward jet shift in all three ocean basins and support the jet strengthening in the North Atlantic and Southern Hemisphere. Cloud-radiative changes also impact the storm track, but the impact is more diverse across the three ocean basins. The cloud-radiative impact on the North Atlantic and North Pacific jet streams varies little from season to season in absolute terms, whereas its relative importance changes over the course of the year. In the Southern Hemisphere, cloud-radiative changes strengthen the jet stream in all seasons, whereas their impact on the jet shift is limited to austral summer and fall. The cloud-radiative impact is largely zonally symmetric and independent of whether global warming is mimicked by a uniform 4 K or spatially-varying SST increase.

In the second part of the thesis, we investigate the relative importance of tropical, midlatitude, and polar cloud-radiative changes for the annual-mean, wintertime, and summertime midlatitude circulation response across regions. Tropical cloud changes dominate the global cloud impact on the 850 hPa zonal wind, jet strength, and storm track responses across most seasons and regions. For the jet shift, a more diverse picture is found. In the annual mean and DJF, tropical and midlatitude cloud changes contribute substantially to the poleward jet shift in all regions. The poleward jet shift is further supported by polar cloud changes across the Northern Hemisphere but not in the Southern Hemisphere. In JJA, the impact of regional cloud changes on the jet position is small, consistent with an overall small jet shift during this season. The jet shift can be largely understood via the anomalous atmospheric cloud-radiative heating

in the tropical and midlatitude upper troposphere. The circulation changes are broadly consistent with the influence of cloud-radiative changes on upper-tropospheric baroclinicity and thus the mean potential energy available for conversion into eddy kinetic energy.

In the third part of the thesis, we focus on the North Atlantic jet stream response during boreal winter. The eastward extension of the North Atlantic jet stream towards Europe is robust across coupled climate models and atmosphere-only climate models that use prescribed SST. Global cloud-radiative changes contribute robustly to the eastward extension of the jet stream in the three atmosphere-only climate models ICON, MPI-ESM and IPSL-CM5A, but the magnitude of the contribution depends on the model. At the same time, the cloud-radiative changes contribute to model uncertainties in the jet stream response over the North Atlantic. Tropical cloud-radiative changes dominate the impact of global cloud-radiative changes on the eastward extension of the jet stream in ICON. Indian Ocean, western tropical Pacific and eastern tropical Pacific cloud-radiative changes all contribute about equally to the eastward jet extension while tropical Atlantic cloud-radiative changes have a minor impact. The jet response over the North Atlantic due to cloud changes over the tropical Pacific and tropical Atlantic are related to changes in the stationary eddy stream function and the development of Rossby wave trains. No Rossby wave evolves in response to cloud changes across the whole tropics and the Indian Ocean, which indicates that responses in transient eddies might be more important for these regional cloud changes.

Our results help to better understand the impacts of cloud-radiative changes. They emphasize the importance of cloud-radiative changes for the regional response of the midlatitude circulation to global warming, and highlight the contribution of tropical cloud-radiative changes for this response. Further, the results indicate that clouds can contribute to uncertainty in model projections of future circulations, in particular due to differences in upper-tropospheric cloud changes.

Zusammenfassung

Wolken und die atmosphärische Zirkulation der mittleren Breiten sind über Strahlungswechselwirkungen eng miteinander verbunden. Frühere Studien zeigten, dass etwa die Hälfte der jährlich und zonal gemittelten Klimawandelantworten der Jetstreams (Starkwindbänder) und Sturmzugbahnen auf Änderungen in den Strahlungseigenschaften von Wolken zurückgeführt werden können. In dieser Arbeit untersuchen wir den Einfluss von Änderungen in den Strahlungseigenschaften der Wolken auf die saisonalen und regionalen Klimawandelantworten der Jetstreams und Sturmzugbahnen in den mittleren Breiten. Hierbei liegt der Schwerpunkt auf dem Nordatlantik, Nordpazifik und der Südhemisphäre. Um den Einfluss der Wolkenänderungen zu untersuchen, werden globale Simulationen mit dem Atmosphärenmodell ICON durchgeführt. In ihnen werden Meeresoberflächentemperaturen vorgeschrieben, um den Einfluss von wolkenbedingten Temperaturänderungen in der Atmosphäre zu isolieren. Der Klimawandel wird mithilfe eines global einheitlichen oder örtlich variierenden Meeresoberflächentemperaturanstiegs simuliert. Ferner wird die cloud-locking Methode benutzt, um die Klimawandelantwort in Beiträge von Wolkenänderungen und Meeresoberflächentemperaturänderungen zu unterteilen.

Im ersten Teil der Arbeit wird der Einfluss von globalen Wolkenänderungen auf die Klimawandelantwort der Jetstreams und Sturmzugbahnen untersucht. Im Jahresmittel können ein bis zwei Drittel der polwärts gerichteten Verschiebung der Jetstreams in allen drei Ozeanbecken auf den Einfluss von Wolkenänderungen zurück geführt werden. Zudem tragen die Wolkenänderungen zu einer Verstärkung der Jetstreams im Nordatlantik und in der Südhemisphäre bei. Wolkenänderungen beeinflussen auch die Klimawandelantwort der Sturmzugbahnen, jedoch variiert ihr Einfluss je nach Ozeanbecken. Im Nordatlantik und Nordpazifik ist der absolute Einfluss der Wolkenänderungen auf den Jetstream im Laufe des Jahres nahezu konstant, wohingegen ihr relativer Einfluss im Laufe des Jahres variiert. In der Südhemisphäre tragen Wolkenänderungen in allen Jahreszeiten zu einer Verstärkung des Jetstreams bei und beeinflussen die Position des Jestreams im Sommer und im Herbst. Der Einfluss der Wolkenänderungen ist nahezu zonal symmetrisch und unabhängig davon, ob die Meeresoberflächentemperatur global einheitlich oder örtlich variierend angehoben wird.

Im zweiten Teil der Arbeit wird der relative Einfluss von Wolkenänderungen in den Tropen, mittleren Breiten und Polargebieten auf die regionale Klimawandelantwort der Zirkulation in den mittleren Breiten untersucht. Hierbei liegt der Fokus auf den Antworten im Jahresmittel, Winter und Sommer. Die regionale Klimawandelantwort des Zonalwindes auf dem 850 hPa Drucklevel, der Sturmzugbahnen und der Stärke der Jetstreams wird in den meisten Jahreszeiten durch Wolkenänderungen in den Tropen dominiert. Im Gegensatz hierzu variiert der Einfluss der regionalen Wolkenänderungen auf die Verschiebung

der Jetstreams je nach Jahreszeit und Region. Im Jahresmittel und Nordhemisphärenwinter tragen Wolkenänderungen in den Tropen und mittleren Breiten wesentlich zur polwärts gerichteten Verschiebung des Jetstreams bei. Diese Verschiebung wird in der Nordhemisphäre durch Wolkenänderungen in den Polargebieten unterstützt, in der Südhemisphäre jedoch nicht. Im Nordhemisphärensommer ist der Einfluss von regionalen Wolkenänderungen auf die Verschiebung des Jetstreams klein. Dies ist konsistent mit einer insgesamt kleinen Jetverschiebung in dieser Jahreszeit. Wolkenbedingte Temperaturänderungen in der oberen Troposphäre der Tropen und der mittleren Breiten führen zur Verschiebung des Jetstreams. Somit ist die Antwort der atmosphärischen Zirkulation in den mittleren Breiten konsistent mit dem Einfluss von Wolkenänderungen auf die Baroklinität in der oberen Troposphäre.

Im dritten Teil der Arbeit wird die Klimawandelantwort des Jetstreams im nordatlantischen Winter untersucht. Sowohl gekoppelte Klimamodelle als auch Atmosphärenmodelle mit vorgeschriebenen Meeresoberflächentemperaturen zeigen eine ostwärtige Ausdehnung des nordatlantischen Jetstreams Richtung Europa. Globale Wolkenänderungen tragen zur ostwärtigen Ausdehung in den drei Atmosphärenmodellen ICON, MPI-ESM und IPSL-CM5A bei. Allerdings ist die Stärke des Wolkeneinflusses ist modellabhängig. Gleichzeitig können Modellunsicherheiten in der Klimawandelantwort des Jetstreams über dem Nordatlantik auf den modellabhängigen Einfluss von Wolkenänderungen zurückgeführt werden. In ICON wird der Einfluss von globalen Wolkenänderungen auf die ostwärtige Ausdehnung des Jetstreams durch Wolkenänderungen in den Tropen dominiert. Wolkenänderungen über dem Indischen Ozean, dem westlichen tropischen Pazifik und dem östlichen tropischen Pazifik tragen etwa gleich stark zum Einfluss der tropischen Wolkenänderungen bei, wohingegen Wolkenänderungen über dem tropischen Atlantik einen geringen Beitrag haben. Die Jetstreamantwort über dem Nordatlantik infolge von Wolkenänderungen über dem tropischen Pazifik und tropischen Atlantik hängen mit der Antwort der stationären Eddystromfunktion und der Entstehung von Rossbywellen zusammen. Dies gilt jedoch nicht für die Jetstreamantwort auf Wolkenänderungen in den gesamten Tropen und im Indischen Ozean, was darauf hindeutet, dass hier der nicht stationäre Anteil der Klimawandelantwort wichtiger sein könnte.

Unsere Ergebnisse helfen dabei, die Einflüsse von Wolkenänderungen besser zu verstehen. Sie heben den Einfluss von Wolkenänderungen für die regionale Klimawandelantwort der atmosphärischen Zirkulation in den mittleren Breiten hervor und stellen den Einfluss von Wolkenänderungen in den Tropen heraus. Des Weiteren zeigen die Ergebnisse, dass insbesondere Unterschiede in den Wolkenänderungen in der oberen Troposphäre zu Unsicherheiten in den Klimawandelantworten verschiedener Modelle beitragen können.

Preface

The PhD candidate confirms that the research presented in this thesis contains significant scientific contributions by herself. This thesis reuses material from the following publications:

Albern, N., A. Voigt, and J. G. Pinto, 2019: Cloud-Radiative Impact on the Regional Responses of the Midlatitude Jet Streams and Storm Tracks to Global Warming. *J. Adv. Model. Earth Sy.*, **11 (7)**, 1940-1958, `https://doi.org/10.1029/2018MS001592`.

Albern, N., A. Voigt, D. W. J. Thompson, and J. G. Pinto, 2020: The Role of Tropical, Midlatitude, and Polar Cloud-Radiative Changes for the Midlatitude Circulation Response to Global Warming. *J. Climate*, **33 (18)**, 7927-7943, `https://doi.org/10.1175/JCLI-D-20-0073.1`, `https://journals.ametsoc.org/view/journals/clim/33/18/jcliD200073.xml`.

The abstract, chapters 1, 2, 3, 4, 5, 8 and appendix A reuse material from Albern et al. (2019). ©The Authors. The abstract, chapters 1, 2, 4, 6, 8 and appendix B reuse material from Albern et al. (2020). ©American Meteorological Society. Used with permission.

The candidate confirms that appropriate credit has been given within the thesis where reference has been made to the work of others. This copy has been supplied on the understanding that this is copyright material and that no quotation from the thesis may be published without proper acknowledgment.

Contents

1. Introduction

In this chapter, we give an overview over the midlatitude jet streams and storm tracks (section 1.1) and their responses to global warming (section 1.2). Clouds and their radiative interactions with the atmospheric circulation are an important factor that contributes to the midlatitude circulation response to global warming. Thus, we further introduce the radiative coupling between clouds and the midlatitude circulation (section 1.3) and highlight its role for the global warming response of the midlatitude circulation (section 1.4).

Parts of this chapter are based on the introductions in Albern et al. (2019) ©the Authors, and Albern et al. (2020) ©American Meteorological Society. Used with permission.

1.1. General Characteristics of the Midlatitude Jet Streams and Storm Tracks

The most dominant components of the midlatitude atmospheric circulation are the jet streams and storm tracks. The jet streams are bands of strong westerly winds that are located in the region where the vertically integrated thermal wind reaches its maximum (Holton, 2004). Conceptually, Earth's atmosphere has two jet streams in each hemisphere: the subtropical jet stream and the eddy-driven or subpolar jet stream (Vallis, 2017). The subtropical jet stream is a zonal wind maximum in the upper troposphere at around 200 hPa, and is located at the subtropical edge of the Hadley cells, where strong horizontal temperature gradients occur. It is characterized by a baroclinic vertical structure, i.e., strong vertical wind shear, with weak westerly winds or easterly winds at the surface and strong westerlies aloft. In contrast, the eddy-driven jet is driven by the midlatitude eddies, and is strongest in the storm track regions over the oceans. It exhibits an equivalent-barotropic vertical structure, i.e., weak vertical wind shear, with westerlies throughout the troposphere. The westerlies are strongest in the upper troposphere, where the eddy momentum fluxes converge, and weakest in the lower troposphere where surface friction acts to weaken the wind (e.g., Vallis, 2017).

Depending on the season and region, the two jet streams may occur as two distinct wind maxima in the upper troposphere or as one merged jet stream. The latter is found in particular in the zonal-mean perspective. Fig. 1.1 shows a cross section of the annual-mean zonal-mean zonal wind in the ERA-Interim reanalysis data set of the European Centre for Medium-Range Weather Forecast (Dee et al., 2011, cf. section 3.2 for a more detailed description of the data set). In the Southern Hemisphere, the two jet streams can be clearly distinguished as two wind maxima at around 200 hPa: the subtropical jet stream is located at around 30°S and the eddy-driven jet stream at around 50°S. In the Northern
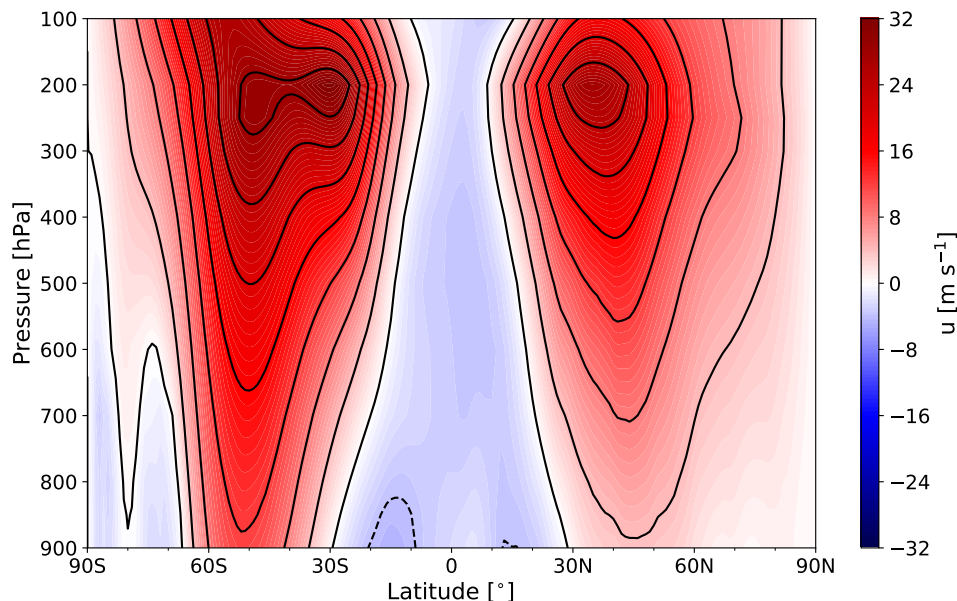
Figure 1.1.: Annual-mean zonal-mean zonal wind in the ERA-Interim reanalysis (mean over 1979-2008). Contour lines are in intervals of $4\,\mathrm{m\,s^{-1}}$ for better visualization of the upper-tropospheric zonal wind maxima.

Hemisphere, however, the two jet streams appear as a merged jet with one upper-tropospheric wind maximum at around 35°N.

The eddy-driven jet stream exhibits regional and seasonal variations. The regional variations mainly result from the presence of the continents which are important for shaping the midlatitude circulation (Brayshaw et al., 2009). The seasonal variations mainly arise from the seasonal cycle in insolation and the resulting variations in temperature gradients (e.g., Woollings, 2010). The regional and seasonal differences in the eddy-driven jet stream are illustrated in Fig. 1.2, which shows maps of the zonal wind at 850 hPa for boreal winter (December to February, DJF) and boreal summer (June to August, JJA). The jet streams are strongest over the ocean basins and exhibit different magnitudes in each ocean basin. Over the land, the jet streams are weaker due to increased surface friction compared to the ocean. Over the course of the year, the jet streams meander poleward and equatorward, which is accompanied by changes in their strengths. In the Northern Hemisphere, the strongest jet streams are found during winter when horizontal temperature gradients are largest.

The midlatitude storm tracks are strongly linked to the jet streams, and exist because extratropical low-pressure systems, or cyclones, travel along the jet streams. Cyclones are baroclinically unstable synoptic scale disturbances, whose growth rate is proportional to the strength of the basic state thermal wind (Holton, 2004). A quantitative estimate for the growth rate of baroclinic disturbances or eddies is the Eady growth rate λ, which is given by (e.g., Hoskins and Valdes, 1990; Yuval and Kaspi, 2016; Voigt and Shaw, 2016)

$$\lambda = -0.31g\frac{1}{N}\frac{1}{T}\frac{\partial T}{\partial y}. \tag{1.1}$$
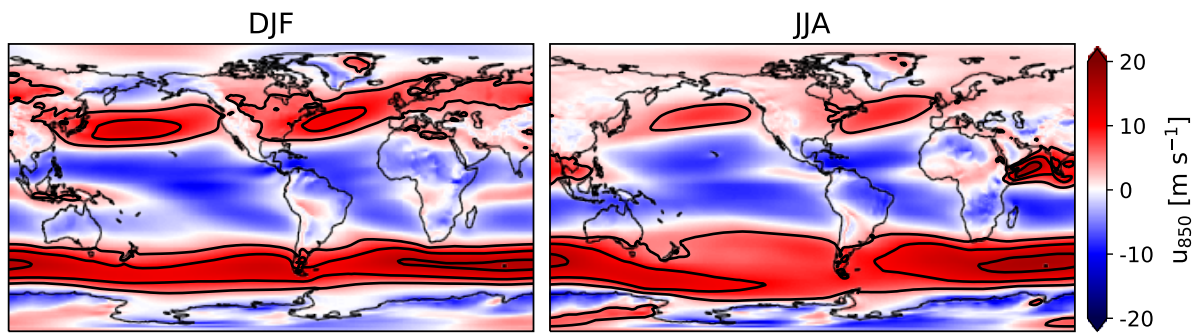
Figure 1.2.: Zonal wind at 850 hPa in the ERA-Interim reanalysis (mean over 1979-2008) during (left) boreal winter (DJF) and (right) boreal summer (JJA). The contours show the 5, 10 and 15 m s^{-1} isotachs.

Here, g is the gravitational acceleration, N is the Brunt-Väisälä frequency which is a function of static stability, T is atmospheric temperature, and $\partial T/\partial y$ is the meridional temperature gradient. The thermal wind, and thus the jet stream, is proportional to the meridional temperature gradient, which links the growth rate of the cyclones to the jet stream and vice versa.

The cyclones primarily develop at the east coasts of the continents where large horizontal temperature gradients occur, in particular due to land-sea thermal contrasts. The cyclones travel over the oceans along the jet streams, forming the storm track, and decay as soon as they reach land due to the increased surface friction. They strongly affect the weather in the midlatitudes and are a main reason for extreme wind and precipitation events at these latitudes (Pfahl et al., 2014; Roberts et al., 2014).

The midlatitude jet streams and storm tracks dominate the heat, momentum, and moisture transport outside of the tropics, making them important components of the large-scale atmospheric circulation (Hoskins and Valdes, 1990; Chang et al., 2002; Shaw et al., 2016). Understanding their responses to global warming is essential for reliable predictions of regional climate change (e.g., Ulbrich et al., 2009), and for the development of effective climate adaptation strategies. This is of special social and economic interest as large parts of the world's population live near or within the midlatitude jet stream and storm track regions.

1.2. Responses of the Midlatitude Jet Streams and Storm Tracks to Global Warming

General Circulation Models (GCMs) are to date the only tool to estimate the long-term response of the climate system to global warming on a global and regional scale. To enable comparison between different GCMs, the Coupled Model Intercomparison Project (CMIP) was initiated in the 1990s (Meehl et al., 2000). By performing coordinated simulations, CMIP aims to improve understanding of the climate system and climate variability, and to assess both robust responses to global warming and model uncertainties (Meehl et al., 2000; Taylor et al., 2012). An increasing number of modeling centers contributed with their climate models to the increasing number of experiments in each phase of CMIP. Analyzing the

response of the climate system in a large model ensemble allows one to establish understanding of the processes that determine the climate system and its response to global warming (Meehl et al., 2005).

Zonal-Mean Jet Stream and Storm Track Responses to Global Warming

Given their importance for the midlatitude circulation, the jet streams and storm tracks and their responses to global warming, were studied extensively during the last decades. Scientists used idealized simulations or output from CMIP coupled climate models in single-model or multi-model studies to assess and better understand the jet stream and storm track responses to global warming (e.g., Kushner et al., 2001; Yin, 2005; Chang et al., 2012; Barnes and Polvani, 2013; Simpson et al., 2014). The midlatitude jet streams and storm tracks are expected to change in response to global warming due to modifications in the thermal structure of the atmosphere. Global climate models project that in a zonal-mean perspective the midlatitude jet streams and storm tracks shift poleward in both hemispheres and that the Southern Hemisphere jet streams and storm tracks strengthen in response to global warming (e.g., Yin, 2005; Pinto et al., 2006; Chang et al., 2012; Simpson et al., 2014; Vallis et al., 2015). This general response was found for both idealized and more realistic coupled model studies (e.g., Kushner et al., 2001; Butler et al., 2010; Barnes and Polvani, 2013). While most climate models agree on the sign of this zonal-mean response, i.e., the poleward shift and/or strengthening, large uncertainties remain with respect to the magnitude of the response (e.g., Chang et al., 2012; Vallis et al., 2015).

Regional Jet Stream and Storm Track Responses to Global Warming

Many studies that investigated the jet stream and storm track responses to global warming, focused on the zonal-mean response in the annual mean or during one season (e.g., Yin, 2005; Vallis et al., 2015). However, the jet stream and storm track responses vary substantially over the course of the year and across regions (e.g., Chang et al., 2012; Barnes and Polvani, 2013; Simpson et al., 2014; Zappa et al., 2015). Barnes and Polvani (2013) investigated the zonal-mean jet shift in the North Atlantic, North Pacific and Southern Hemisphere ocean basins across seasons in CMIP5 coupled climate models. The authors showed that the jet shift exhibits a distinct seasonal cycle in each of the three ocean basins. In the model mean, the largest jet shifts are found during the fall season of each hemisphere, i.e., during September to November (SON) in the Northern Hemisphere and during March to May (MAM) in the Southern Hemisphere (Fig. 12 in Barnes and Polvani, 2013). In contrast, the smallest jet shifts occur during different seasons depending on the ocean basin. In the North Atlantic, the smallest and almost negligible jet shift is found during boreal winter (DJF), in the North Pacific during boreal summer (JJA), and in the Southern Hemisphere during austral spring (SON). Further, Barnes and Polvani (2013) highlighted the uncertainties in the magnitude of the poleward jet shift. In the Southern Hemisphere, several models project a poleward jet shift which is more than twice as large as the model mean jet shift. In the North Atlantic and North Pacific, in contrast, several models exhibit an equatorward jet shift which

is, for some models, even larger than the model mean poleward jet shift (Fig. 12 in Barnes and Polvani, 2013).

The study by Barnes and Polvani (2013) gave a first idea about the regional and seasonal differences in the jet response to global warming. Yet, it did not capture regional differences within the ocean basins because it focused on the zonal-mean response in the ocean basins. Simpson et al. (2014) showed maps of the seasonal-mean zonal wind response in coupled CMIP5 models. The authors found that the seasonal-mean jet stream shifts poleward and/or strengthens at most longitudes in the Southern Hemisphere, especially during DJF and MAM, and that most models agree on the sign of the zonal wind response (Fig. 6 in Simpson et al., 2014). Larger regional variations in the jet stream response are found in the North Atlantic and North Pacific (Figs. 7 and 8 in Simpson et al., 2014). During DJF, for example, the North Atlantic jet stream exhibits an eastward extension towards Europe rather than a poleward shift, consistent with the small ocean basin zonal-mean jet shift found in Barnes and Polvani (2013). During the same season, the North Pacific jet response exhibits a quadrupole structure with a poleward shift in the western part of the ocean basin and an equatorward shift in the eastern part (Fig. 7 in Simpson et al., 2014). In the North Pacific, the model consensus on the sign of the zonal wind response is small during most seasons, indicating that the jet response in the North Pacific is very uncertain across CMIP5 models. In the North Atlantic, the model consensus strongly depends on the season. High model consensus of a poleward jet shift is found during JJA and SON. Small model consensus is found during DJF and MAM, except for the eastward extension of the jet towards Europe during DJF which is robust across the investigated models.

Zappa et al. (2015) gave an even more detailed insight into the seasonal and regional variations in the jet stream response over the North Atlantic by showing maps of the zonal wind response over the North Atlantic and Europe in coupled CMIP5 models for each month. They found that in response to global warming, the model-mean North Atlantic jet stream extends eastward into Europe from November to April while the jet shifts poleward from May to October. This explains the smaller jet shifts during DJF and MAM and the larger jet shifts during JJA and SON that were found in studies that focused on the zonal-mean response (e.g., Fig. 12 in Barnes and Polvani, 2013).

The eastward extension of the North Atlantic jet stream and storm track towards Europe during DJF or an extended winter season is not only robust in coupled climate models of phase 5 of CMIP (e.g., Harvey et al., 2012, 2014; Simpson et al., 2014), but also in future climate projections of phases 3 and 6 of CMIP (e.g., Woollings and Blackburn, 2012; Harvey et al., 2012, 2020). As storms are strongest and most frequent during boreal winter, the eastward extension leads to an increased potential of extreme wind and precipitation over highly populated European regions (Schwierz et al., 2010; Pinto et al., 2012). Thus, several studies investigated the eastward extension of the North Atlantic jet stream and storm track towards Europe to better understand the physical mechanisms and processes (e.g., Woollings et al., 2012; Simpson et al., 2014; Harvey et al., 2015).

Simpson et al. (2014) found that the eastward extension of the North Atlantic jet stream towards Europe is associated with a barotropic anticyclonic circulation anomaly over the Mediterranean which is linked to a Rossby wave train over the Northern Hemisphere that emerges close to the Maritime Continent due to tropical heating (Fig. 13 in Simpson et al., 2014). This result is consistent with the impact of tropical heating associated with the Madden-Julian oscillation (Madden and Julian, 1971, 1972) or the El Niño Southern Oscillation on the North Atlantic circulation (e.g., Palmer and Mansfield, 1984; Cassou, 2008; Ciasto et al., 2016). Yet, the link between tropical heating and the North Atlantic jet stream and storm tracks is controversial and not fully understood (e.g., Wild et al., 2015; Goss and Feldstein, 2017).

Another factor that might affect the eastward jet stream extension towards Europe are changes in sea-surface temperatures (SST). The North Atlantic SST pattern was found to influence the North Atlantic jet streams and storm tracks in present-day climate (O'Reilly et al., 2017). However, the effects of changes in the Atlantic Meridional Overturning Circulation (AMOC) and in the North Atlantic SST pattern on the global warming responses of the North Atlantic jet stream and storm track are controversial. Woollings et al. (2012) argued that the storm track response is linked to the coupling between the atmosphere and the ocean. They found that CMIP3 models with a strong AMOC response show a pronounced strengthening and eastward extension of the North Atlantic storm track towards Europe. The authors showed that in the CMIP3 models differences in the response of the North Atlantic ocean circulation accounts for at least half of the inter-model differences in the storm track responses. In contrast to Woollings et al. (2012), Harvey et al. (2015) found little influence of the AMOC reduction on the North Atlantic storm track response to global warming. Instead, the circulation response to a globally-uniform SST increase captures the tri-polar response of the North Atlantic storm track in response to global warming, i.e., it shows a decrease in the subtropics and Arctic and an increase over north-western Europe. This result is consistent with the findings of Graff and LaCasce (2012) who found that storm tracks change due to changes in both mean SST and SST gradients. Harvey et al. (2015) concluded that changes in Arctic sea ice and/or the SST response around the Arctic sea ice edge are more important than changes in North Atlantic SST south of Greenland (subpolar gyre) in their simulations. Note that the uniform SST increase does not capture the poleward shift in the upstream end of the North Pacific storm track. These studies showed that the coupling between the atmosphere and ocean, and the role of SST pattern changes and resulting changes in sea-surface temperature gradients are not fully understood and further studies are needed to determine their impact on the jet stream and storm track responses to global warming.

Mechanisms for the Jet Stream and Storm Track Responses to Global Warming

Our discussion shows that even though the jet streams and storm tracks were studied extensively during the last decades, climate model projections of future changes in the jet streams and storm tracks exhibit large uncertainties (Shepherd, 2014). One main reason for the uncertainties is the fact that the dominant physical mechanisms contributing to a jet and storm track shift and/or strengthening are not fully understood (Bony et al., 2015; Vallis et al., 2015; Shaw et al., 2016). Several mechanisms that might

contribute to the jet response have been proposed in addition to the above discussed mechanisms for the eastward extension of the jet streams and storm tracks during DJF. These include changes in upper- and/or lower-tropospheric temperature gradients (Yin, 2005; Lu et al., 2008; Butler et al., 2010; Harvey et al., 2015), a rise of the tropopause (Yin, 2005; Lorenz and DeWeaver, 2007), an increase in the static stability of the subtropical and midlatitudinal troposphere (Lu et al., 2008), increases in the eddy length scale (Kidston et al., 2010), increased (Chen et al., 2008) or reduced (Kidston et al., 2011) eddy phase speeds, and changes in the index of refraction for wave propagation (Simpson et al., 2009). The recently published review by Shaw (2019) gave an overview of the possible mechanisms, including additionally the effects of increases in latent heat release in the upper-tropospheric tropics, radiative cooling in the stratosphere, increases in specific humidity and the impact of cloud-radiative changes. In this thesis, we focus on the cloud-induced changes in upper- and lower-tropospheric temperature gradients and their dynamical impact on the midlatitude circulation. Thus, we explain this mechanism in more detail.

It is generally accepted that the changes in upper-tropospheric temperature gradients and baroclinicity play an important role for the jet shifts. For example, the idealized study by Butler et al. (2010) provided evidence that upper-tropospheric tropical heating leads to a poleward jet shift. The authors also showed that a low-level polar warming leads to an equatorward shift of the jet stream. Harvey et al. (2014) studied the role of changes in upper- and lower-tropospheric equator-to-pole temperature differences across coupled CMIP5 climate models. The authors showed that the response in upper- and lower-tropospheric equator-to-pole temperature differences in the Southern Hemisphere are significantly correlated across models, and that they are strongly linked to the storm track responses. In the Northern Hemisphere, in contrast, the responses in upper- and lower-tropospheric temperature differences are not significantly correlated, and the relation with the storm tracks is more diverse. In boreal summer, the storm track response in the Northern Hemisphere is strongly linked to the response in lower-tropospheric temperature differences. In boreal winter, however, the responses in both upper- and lower-tropospheric temperature differences are linked to the storm track response. In general, the increase in temperature differences is found to yield increased storm activity in both hemispheres, with the storms reacting to the changes in baroclinicity due to changes in equator-to-pole temperature differences (Harvey et al., 2014). These results are supported by the study of Harvey et al. (2015) which showed that while the jet stream and storm track responses to global warming are primarily associated with the upper-tropospheric temperature gradient change, changes of the lower-tropospheric temperature gradients can also be determinant, notably for the North Atlantic ocean basin. The temperature changes in response to global warming can result from a multitude of factors, including moist convection (Vallis et al., 2015), ozone depletion (Polvani et al., 2011), and sea ice loss (Vavrus, 2018; Zappa et al., 2018). Clouds and their radiative interactions with the atmospheric circulation also strongly project on meridional temperature gradients (Voigt and Shaw, 2015; Ceppi and Hartmann, 2016). The radiative coupling of clouds with the atmospheric circulation and the role of cloud-radiative changes for the response of the atmospheric circulation to global warming are discussed in sections 1.3 and 1.4, respectively.

1.3. Cloud-Radiative Interactions with the Atmospheric Circulation

Clouds cover more than two-thirds of the Earth and significantly increase Earth's albedo, in particular compared to the low-albedo oceans (Ramanathan et al., 1989). Clouds reflect and scatter, but hardly absorb, shortwave radiation (spectral range from ultraviolet over visible to near-infrared) emitted from the sun. In the longwave (infrared spectral range), clouds mainly absorb radiation emitted by the Earth's surface and by the cloud-free atmosphere, and emit radiation themselves. This makes clouds one of the most important components of Earth's energy balance. In the global and annual mean, the net, i.e., longwave plus shortwave, effect of clouds at the top of the atmosphere is a cooling of the climate system by about $20\,\mathrm{W\,m^{-2}}$, with shortwave cooling due to enhanced scattering of sunlight dominating over longwave heating of clouds (Allan, 2011; Loeb et al., 2018).

Clouds are strongly linked to the atmospheric circulation, so that a zonal-mean latitude-height cross section of cloud incidence represents the main components of the zonal-mean atmospheric circulation. Deep convective clouds in the tropics are linked to the ascending branch of the Hadley circulation, while low cloud incidence in the subtropics (around 20-30°N/S) indicates the descending branches of the Hadley cells (Fig. 1.3a). Other regions of high cloud incidence are the midlatitudes of both hemispheres (around 50-70°N/S), which are associated with the storm track regions. Low-level clouds are mainly found in the subtropics and midlatitudes and are associated with subtropical stratocumulus clouds and the midlatitude storm track clouds, which mainly develop over the oceans.

To diagnose the heating and cooling effects of clouds, the cloud-radiative effect (CRE, formerly referred to as cloud-radiative forcing) is defined as the all-sky minus clear-sky radiative fluxes (e.g., Ramanathan et al., 1989). It can be derived for the longwave and shortwave domain, and at the top of the atmosphere (TOA) and the surface. The difference between the TOA and surface CRE yields the atmospheric cloud-radiative effect (ACRE), which is an estimate of the cloud-radiative heating and cooling in the whole atmospheric column without spatial information in which height the heating and/or cooling occurs.

Satellite observations provide an estimate of the regional pattern of cloud-radiative heating and cooling. In the shortwave domain, clouds have a strong radiative cooling effect at both the TOA and the surface (e.g., Allan, 2011, and our Fig. 1.3b, d). The TOA cooling mainly is a function of cloud cover and shows, for example, the location of the Intertropical Convergence Zone (ITCZ), the Maritime Continent, the storm track regions over the oceans, and the stratocumulus regions at the eastern boarders of the Pacific and Atlantic ocean basins (Fig. 1.3b). As clouds mainly scatter shortwave radiation but hardly absorb it, the surface CRE is very similar to the TOA CRE, and the atmospheric shortwave CRE is small (Allan, 2011, and our Fig. 1.3c, d).

In the longwave domain, clouds have a heating effect at both the TOA and the surface (Fig. 1.3e, g). In contrast to the shortwave CRE, the TOA longwave CRE is not only a function of cloud cover but also of cloud height. Thus, the TOA longwave CRE is largest in regions with high cloud cover and deep
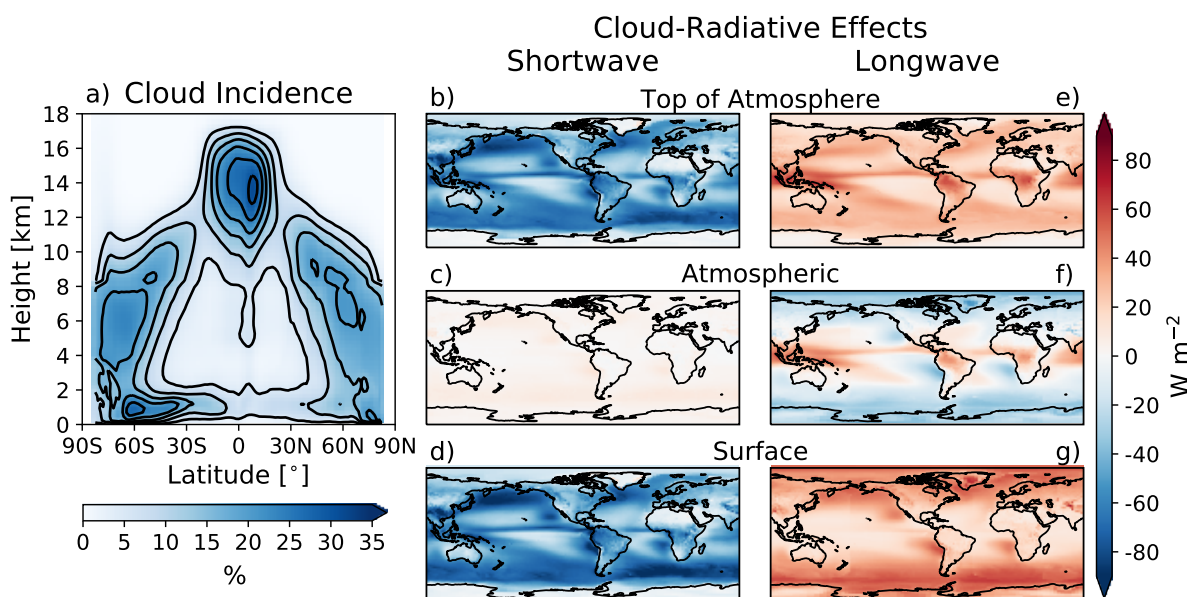
Figure 1.3.: Annual-mean zonal-mean cloud incidence from CloudSat/CALIPSO measurements (a) and maps of annual-mean cloud-radiative effects from CERES EBAF edition 4.1 (b-g). The contour lines in panel a are in intervals of 5%. The maps show and shortwave and longwave cloud-radiative effects at the top-of-atmosphere (b, e), inside the atmosphere (c, f) and at the surface (d, g), respectively. The data sets are described in more detail in section 3.2.

convective clouds which have low cloud-top temperatures, for example over the ITCZ and the storm track regions. At the same time, it is small over regions with low-level clouds that have a high cloud-top temperature, for example over the stratocumulus cloud decks off the west coasts of America and Africa (Fig. 1.3e). The low-level clouds have a longwave heating effect on the surface because they are warm and emit longwave radiation back to the surface (Fig. 1.3g). Inside the atmosphere, longwave CRE act to heat the tropics, especially in regions of deep convective clouds, and cool the subtropical stratocumulus regions as well as the extratropics and high latitudes for which the atmosphere is more transparent to longwave radiation (Allan, 2011, and our Fig. 1.3f).

The CRE maps and cloud incidence estimates show that the clouds and their radiative effects are strongly coupled to the atmospheric circulation. This coupling acts in two directions. On the one hand, the atmospheric circulation triggers or prevents the development of clouds, for example in regions with prevailing updrafts and downdrafts, respectively. On the other hand, clouds can alter the atmospheric circulation by their radiative heating and cooling effects. Given the importance of clouds for the Earth's energy balance and the strong radiative coupling between clouds and the atmospheric circulation, the dynamical impact of cloud-radiative heating and cooling on both the present-day atmospheric circulation and the circulation response to global warming were studied extensively in GCMs during the last decades (e.g., reviews by Ceppi and Hartmann, 2015; Voigt et al., 2020, and references therein).

1.4. Impact of Cloud-Radiative Changes on the Responses of the Jet Streams and Storm Tracks to Global Warming

As clouds are a major source of uncertainty in climate model projections, one focus of phase 5 of CMIP, CMIP5, is to improve understanding of clouds and cloud feedbacks in the climate system and their role for the global warming response of the atmospheric circulation (Taylor et al., 2012). The experiments that were designed for this purpose are part of the CMIP5 subproject Cloud Feedback Model Intercomparison Project (CFMIP, `https://www.earthsystemcog.org/projects/cfmip/cfmip2-cmip5`) and include simulations with atmosphere-only global climate models. These simulations use prescribed sea-surface temperatures (SST) and are based on the Atmospheric Model Intercomparison Project (AMIP) protocol (Gates, 1992).

While the CFMIP simulations are designed to study cloud feedbacks, they cannot be used to study the radiative interactions between clouds and the atmospheric circulation. There are two main approaches to study the radiative interactions between clouds and the atmospheric circulation in models: i) the Clouds On-Off Klimate Intercomparison Experiment (COOKIE; Stevens et al., 2012) method is used to study the impact of the presence of clouds and atmospheric cloud-radiative effects on the mean circulation in the present-day climate (e.g. Slingo and Slingo, 1988; Harrop and Hartmann, 2016; Popp and Silvers, 2017; Albern et al., 2018; Fläschner et al., 2018); and ii) the cloud-locking method (Wetherald and Manabe, 1988) is used to study the impact of ACRE on present-day internal variability (e.g., Rädel et al., 2016; Middlemas et al., 2019) and the impact of cloud-radiative changes on the circulation response to global warming (e.g., Voigt and Shaw, 2015; Ceppi and Hartmann, 2016). Voigt et al. (2020) present a comprehensive review on the cloud-circulation coupling for the present-day mean circulation, for internal variability, and for the circulation response to global warming. Here, we focus on the role of cloud-radiative changes for the circulation response to global warming.

The poleward shifts of the Southern Hemisphere storm track and jet stream in global warming simulations were found to depend on the radiative response of Southern Ocean clouds (Ceppi et al., 2014; Grise and Polvani, 2014a; Ceppi and Shepherd, 2017). Li et al. (2019) found that atmospheric cloud-radiative effects enhance the poleward jet shift in response to global warming in Amip-like simulations that apply the COOKIE framework. Caution is demanded, however, when COOKIE simulations are used to study the circulation response to global warming, because making clouds transparent to radiation modifies the basic state circulation in the control simulation (Voigt and Albern, 2019).

Most studies that investigated the impact of cloud-radiative changes on the circulation response to global warming used the cloud-locking method. By prescribing cloud- and other radiative properties to the radiation scheme of the investigated model, the method allows to decompose the circulation response into contributions from cloud-radiative changes, increases in atmospheric carbon dioxide or sea-surface temperatures (SST), and from, for example, changes in water vapor or surface albedo (e.g., Wetherald and Manabe, 1988; Voigt and Shaw, 2015; Ceppi and Hartmann, 2016; Ceppi and Shepherd, 2017; Voigt

et al., 2019). It is a common nomenclature to refer to the impact of cloud-radiative changes on the circulation response to global warming as "cloud-radiative impact" or "cloud impact". We will keep this nomenclature throughout the thesis (cf. section 4.3 for a more detailed description of the cloud-locking method and how it is used to decompose the circulation response).

The Atmospheric and Surface Pathways of the Cloud-Radiative Impact

Cloud-radiative changes can affect the response of the atmospheric circulation to global warming via two pathways which Voigt et al. (2019) called the atmospheric pathway and the surface pathway of the cloud-radiative impact. The two pathways depend on whether SST are interactive or prescribed. The surface pathway arises from changes in surface cloud-radiative heating and their impact on the surface energy balance. Surface temperatures react to changes in surface cloud-radiative heating to maintain the surface energy balance (Voigt et al., 2019). Their changes mainly manifest as changes in surface temperature gradients rather than changes in global-mean surface temperature (Ceppi and Hartmann, 2016; Ceppi and Shepherd, 2017). In contrast, the atmospheric pathway arises from changes in atmospheric cloud-radiative heating and their impact on the atmospheric energy balance (Voigt et al., 2019). It acts via changes in atmospheric temperatures that lead to responses in the atmospheric circulation in the absence of changes in surface temperatures. The atmospheric pathway of the cloud-radiative impact was found to yield half of the poleward jet shift in aquaplanet simulations (Voigt and Shaw, 2015) and simulations with present-day boundary conditions (Voigt et al., 2019).

Ceppi and Hartmann (2016) investigated the impact of cloud-radiative changes in aquaplanet simulations coupled to a slab ocean, and decomposed the cloud impact into contributions from cloud changes in the longwave and shortwave domains. As SST are interactive in their simulations, Ceppi and Hartmann (2016) study the total cloud-radiative impact, i.e., the sum of the atmospheric and surface pathways. They found that more than 50% of the poleward expansion of the Hadley circulation, jet streams and storm tracks in response to quadrupled atmospheric carbon dioxide can be attributed to cloud-radiative changes, even though they account for only about one fourth of the total global-mean surface warming. In their simulations, most of the cloud-induced circulation response can be attributed to shortwave cloud-radiative changes while the impact of longwave cloud-radiative changes on the circulation response is small. This indicates that the surface pathway of the cloud-radiative impact dominates their response as it is dominated by shortwave cloud changes while the atmospheric pathway is dominated by longwave cloud changes (Allan, 2011; Voigt et al., 2019).

Ceppi and Hartmann (2016) related the large impact of shortwave cloud-radiative changes on the circulation response to their impact on atmospheric temperatures. Shortwave cloud-radiative changes act to strongly enhance the meridional temperature gradient across the troposphere, which the authors argued to favor stronger and poleward-shifted eddies. In contrast, an increase in atmospheric carbon dioxide and the longwave cloud-radiative impact lead to polar amplification, i.e., warming in the high-

latitude lower troposphere. This reduces the lower-tropospheric meridional temperature gradient and midlatitude baroclinicity, resulting in a small circulation response.

Ceppi and Shepherd (2017) showed that the importance of cloud-radiative changes for the circulation response to global warming is reproduced in simulations that use present-day continents and sea ice, and are coupled to a slab ocean. The authors decomposed the circulation response to quadrupled atmospheric carbon dioxide into contributions from radiative changes of clouds, surface albedo and water vapor. Ceppi and Shepherd (2017) found that the impacts of cloud, water vapor and surface albedo changes are strongly linked to their impact on midlatitude baroclinicity. Similar to the aquaplanet simulations of Ceppi and Hartmann (2016), Ceppi and Shepherd (2017) showed that the cloud-radiative impact dominates the poleward jet shift and jet strengthening because they increase baroclinicity. The opposite, i.e., a reduced baroclinicity, was found for surface albedo changes. At the same time, water vapor changes were found to have opposing impacts on upper-tropospheric and lower-tropospheric baroclinicity, which results in small responses of the jet. Ceppi and Shepherd (2017) highlighted that remarkable differences in the cloud, surface albedo and water vapor impacts are present in their two models. Thus, they further argued that differences in shortwave cloud and albedo impacts contribute substantially to the model uncertainty across CMIP5 models.

The Atmospheric Pathway of the Cloud-Radiative Impact

In contrast to Ceppi and Hartmann (2016) and Ceppi and Shepherd (2017), Voigt and Shaw (2015) focused on the atmospheric pathway of the cloud-radiative impact. They investigated the cloud impact in idealized aquaplanet simulations with prescribed SST, which mimicked global warming by a uniform 4 K SST increase. The authors found that about half of the annual-mean zonal-mean poleward jet shift in their two models can be attributed to cloud-radiative changes. At the same time, water vapor-radiative changes were found to yield an equatorward jet shift (Fig. 3 in Voigt and Shaw, 2015). Similar to Ceppi and Hartmann (2016), Voigt and Shaw (2015) related the impact of cloud-radiative changes on the poleward jet shift to increases in meridional temperature gradients throughout the troposphere. In contrast, water vapor-radiative changes were found to reduce the meridional temperature gradients, which is in line with the results of Ceppi and Shepherd (2017).

Voigt and Shaw (2016) extended the work of Voigt and Shaw (2015) and used aquaplanet simulations from the same two models to decompose the cloud-radiative impact into contributions from tropical, midlatitude and polar cloud-radiative changes. The authors found that tropical and midlatitude cloud changes dominate the radiative impact from global cloud changes. Cloud changes in both regions lead to about one third to half of the poleward jet shift from global cloud changes. In one of their models, polar cloud changes also contribute to the poleward jet shift, but the polar cloud impact is negligible in the other model (Fig. 2 in Voigt and Shaw, 2016). Voigt and Shaw (2016) found that their results are qualitatively robust in moist and dry versions of one of their models, highlighting the impact of cloud-radiative changes on large-scale dynamics.

Voigt and Shaw (2016) chose to investigate the individual impacts of tropical, midlatitude and polar cloud-radiative changes because the change in atmospheric cloud-radiative heating (referred to as cloud-radiative forcing in Voigt and Shaw, 2016) has three main regional components. These are i) a maximum in the tropical upper troposphere due to upward shifted tropical clouds; ii) a maximum in the midlatitude upper troposphere due to upward shifted storm track clouds; and iii) a minimum in the high-latitude lower troposphere due to increased polar clouds. The latter is found to be strongly model dependent, and in one model showed a tripole rather than a minimum (Fig. 2 in Voigt and Shaw, 2016).

Thus, the aquaplanet work of Voigt and Shaw (2015, 2016) identified that cloud-radiative changes are important even when SST are prescribed, showing that a large part of the cloud-radiative impact results from direct atmospheric cloud-radiative heating and not from changes in surface temperatures. This result is further supported by the study of Voigt et al. (2019). Using simulations with present-day continents and sea ice, the authors quantified the magnitude of the atmospheric pathway and the surface pathway and related it to the total cloud-radiative impact. Voigt et al. (2019) found that in their model the atmospheric pathway leads to about half of the total cloud-radiative impact and half of the total annual-mean zonal-mean circulation response to global warming, highlighting the importance of the atmospheric pathway of the cloud-radiative impact.

Voigt et al. (2019) showed that the atmospheric pathway results from changes in atmospheric cloud-radiative heating which are substantial across the troposphere. The largest contribution is found in the tropical and midlatitude upper troposphere due to upward shifts in upper-tropospheric ice clouds. The contribution in the lower troposphere is smaller and partly limited because SST were prescribed. Further, Voigt et al. (2019) showed that the change in atmospheric cloud-radiative heating and the cloud-induced poleward jet shift are qualitatively robust across three atmosphere-only climate models. However, there is substantial spread in the circulation response as the change in atmospheric cloud-radiative heating and its impact on the circulation response to global warming varies across models. A similar conclusion was drawn by Ceppi and Shepherd (2017) (see above).

To conclude, the discussed studies found evidence that changes in cloud-radiative properties have a substantial impact on the annual-mean zonal-mean midlatitude circulation response to global warming. Cloud-radiative changes were found to yield half or more of the poleward jet shift in all models. This general result is independent of whether i) the simulations are performed in aquaplanet or present-day setup, and ii) the sum of the atmospheric and surface pathways or the atmospheric pathway alone are investigated. Most of the studies related the impact of cloud-radiative changes on the midlatitude circulation response to global warming to changes in meridional temperature gradients and baroclinicity. Even though the qualitative circulation response is similar across models, large differences in the magnitude of the cloud impact occur, which is related to differences in the change in atmospheric and surface cloud-radiative heating across models.

Previous studies were limited to the cloud-radiative impact on the annual-mean zonal-mean circulation response to global warming. However, in section 1.2, we discussed that the jet stream and storm

track responses to global warming depend on the season and region. This indicates that the cloud-radiative impact might also depend on the season and region. Thus, in this thesis, we will investigate the cloud-radiative impact on the jet stream and storm track responses to global warming across seasons and regions. The research questions of this thesis are introduced in the next chapter.

2. Research Questions and Outline

In this chapter, we introduce the three research questions that we will address in this thesis. Each of the questions is divided into more detailed sub-questions to make it more explicit. The sub-questions of research questions 1 and 2 are the same as in Albern et al. (2019) ©the Authors, and Albern et al. (2020) ©American Meteorological Society, respectively. Used with permission.

In chapter 5, we investigate the impact of global cloud-radiative changes on the jet stream and storm track responses to global warming, and address the following research questions:

1. How large is the impact of global cloud-radiative changes on the midlatitude circulation response to global warming in a present-day simulation setup?

   1.1. How important is the cloud-radiative impact for the midlatitude jet stream and storm track responses to global warming in the North Atlantic, North Pacific, and Southern Hemisphere ocean?

   1.2. To what extent does the cloud-radiative impact vary across seasons and ocean basins?

   1.3. Does the cloud-radiative impact depend on the pattern of the SST increase?

These questions are motivated by i) the fact that jet stream and storm track responses to global warming exhibit regional and seasonal variations, especially in the Northern Hemisphere; and ii) previous studies found that cloud-radiative changes have a substantial impact on the jet stream and storm track responses to global warming but were limited to the annual-mean zonal-mean perspective and were largely based on aquaplanet simulations. Thus, we extend the previous work with research question 1 and use simulations that include, for example, a seasonal cycle, continents and sea ice to study the regional and seasonal differences in the cloud-radiative impact on the jet stream and storm track responses to global warming. We compare two sets of global warming simulations that use different SST changes to mimic global warming. This allows us to study to what extent the cloud-radiative impact depends on the pattern of the surface warming, which Woollings et al. (2012) identified to shape the storm track response in the North Atlantic and over Europe. At the same time, Harvey et al. (2015) found little dependence of the storm track response to global warming to SST gradient changes in the North Atlantic.

In chapter 6, we investigate the impact of regional cloud-radiative changes on the jet stream and storm track responses to global warming, and address the following research questions:

2. Which regional cloud-radiative changes dominate the global cloud-radiative impact on the response of the midlatitude circulation to global warming?

2.1. Are tropical, midlatitude or polar cloud-radiative changes more important for the global cloud impact on the zonal wind, jet stream and storm track responses to global warming? Do the results depend on the season and the ocean basin?

2.2. Can we understand the circulation impact of regional cloud-radiative changes on the zonal wind and jet responses based on (established) dynamical arguments?

These questions are motivated by the study of Voigt and Shaw (2016) that investigated the impact of tropical, midlatitude and polar cloud-radiative changes on the annual-mean zonal-mean jet stream response to global warming in an aquaplanet setup. The authors used two models and found that tropical and midlatitude cloud-radiative changes contribute about equally to the poleward jet shift in the two models, whereas the impact of polar cloud-radiative changes was smaller and not robust in the two models that they used. With research question 2, we aim to better understand which regional cloud-radiative changes dominate the global cloud-radiative impact on the jet stream and storm track responses in simulations that include continents, and whether the result depends on the region and season. Further, we want to better understand the cloud-radiative impact on the jet stream response from the perspective of large-scale dynamics.

In chapter 7, we investigate the cloud-radiative impact on the zonal wind and jet stream responses to global warming over the North Atlantic-European region during boreal winter. We address the following research questions:

3. Do cloud-radiative changes contribute robustly to the wintertime response of the North Atlantic jet stream to global warming, and which clouds are most important?

3.1. What aspects of the global warming response over the North Atlantic-European region during boreal winter are robust across coupled and atmosphere-only climate models?

3.2. How much of the robust circulation response can be attributed to cloud-radiative changes, and is the cloud impact robust across models?

3.3. Which regional cloud-radiative changes are most important for the circulation response over Europe, and how can we understand their impact?

These questions are motivated by the fact that, during boreal winter, the North Atlantic jet stream rather exhibits an eastward extension over Europe than a poleward shift in response to global warming. This response is robust across coupled climate models of phases 3, 5 and 6 of CMIP but the dominating mechanisms for this response are still uncertain. With research question 3, we investigate how much of the response over the North Atlantic and Europe can be attributed to cloud-radiative changes and whether the cloud-radiative impact is robust across models. This is of interest as clouds are a major source of uncertainty in climate models. Further, we investigate which regional cloud changes are most important, and study tropical-extratropical teleconnections to better understand the role of tropical cloud-radiative changes on the North Atlantic jet stream response to global warming.

To address the three research questions, we perform simulations with the atmospheric component of the ICOsahedral Non-hydrostatic (ICON) model (Zängl et al., 2015), and prescribed sea surface temperatures. The simulations use a present-day setup that includes continents, sea ice and a seasonal cycle, and mimic global warming by a uniform or spatially varying SST increase. We apply the cloud-locking method to decompose the jet stream and storm track responses to global warming into contributions from global and regional cloud-radiative changes and from the SST increase.

The thesis is structured as follows: We introduce the global weather and climate model ICON and additional data sets, and show that ICON can be used to perform present-day simulations in chapter 3. In chapter 4, we discuss the investigated regions, the circulation metrics and the diagnostic tools, which are the cloud-locking method and the Partial-Radiative Perturbation calculation. These are applied to diagnose the role of cloud-radiative changes and the change in atmospheric cloud-radiative heating under global warming. In chapters 5-7, we address the three research questions and their sub-questions. Thus, in chapter 5, we investigate the impact of global cloud-radiative changes on the circulation response to global warming. In chapter 6, we investigate the impacts of tropical, midlatitude and polar cloud-radiative changes and determine which regional cloud changes are most important for the global cloud-radiative impact. In chapter 7, we focus on the eastward extension of the North Atlantic jet stream towards Europe during boreal winter and investigate the role of regional cloud-radiative changes for this response. We conclude in chapter 8 by summarizing the main results and by providing suggestions for future work that could extend the results of this thesis.

3. The ICON Model and Additional Data Sets

In this chapter, the ICOsahedral Non-hydrostatic (ICON) model is described. The model will be used in chapters 5-7 to investigate the impact of global and regional cloud-radiative changes on the response of the midlatitude circulation to global warming. We begin this chapter with a general description of the model and the used model setup in section 3.1, followed by a summary of additionally used data sets which include CMIP5 simulations, reanalysis data and satellite observations (section 3.2). Finally, we compare the representation of the large-scale atmospheric circulation and the circulation response to global warming in ICON to the other data sets (section 3.3). Sections 3.1.2 and 3.3.2 are adapted from Albern et al. (2019). ©The Authors.

3.1. The ICON Model

In this section, we provide a general introduction of the ICON model and the physics parameterizations (section 3.1.1). In section 3.1.2, we describe the model setup that we use for our simulations.

3.1.1. General Introduction

ICON is a unified modeling system for numerical weather prediction (NWP) and climate modeling, and is developed by the German Weather Service and the Max Planck Institute for Meteorology (Zängl et al., 2015). The model consists of a non-hydrostatic dynamical core and packages of physical parameterizations for climate modeling, numerical weather prediction and large-eddy simulations (Zängl et al., 2015; Dipankar et al., 2015; Heinze et al., 2017; Giorgetta et al., 2018). ICON simulations can be performed on a global scale and in limited-area mode with resolutions ranging from the meso scale (order of hundreds of kilometers) to the micro scale (order of hundreds of meters). The large range of horizontal resolutions is possible because the model uses an unstructured triangular Arakawa C grid that can be refined easily (Zängl et al., 2015). In the vertical dimension, ICON uses a terrain following geometric altitude grid (Rast, 2017). For the time integration, a two-time-level predictor-corrector scheme is applied which is explicit except for the terms that describe vertical sound-wave propagation (Zängl et al., 2015).

The horizontal grid is based on an icosaeder with 20 equilateral triangles of equal size that is projected on a sphere (Rast, 2017). Successive refinements of the icosaeder's triangles in two steps yield the desired grid resolution "RnBk". The first step is referred to as root division step. For this step, the edges of the triangles are divided into n equal pieces, and lines are drawn to connect the new edge points in parallel lines to the triangles' vertices. This division results in n^2 new equilateral triangles. The second step is

the bisection step. For this step, each triangle is recursively divided into 4 smaller triangles, resulting in 4^k new triangles per triangle. The root division and bisection steps result in $n_c = 20 \cdot n^2 \cdot 4^k$ triangles on the sphere. The effective grid resolution is then calculated as

$$\Delta x = \sqrt{\frac{4\pi r_e^2}{n_c}} = \sqrt{\frac{\pi}{5}} \frac{r_e}{n 2^k}, \tag{3.1}$$

where r_e is the Earth's radius. In this study, we run ICON in R2B4 horizontal resolution, corresponding to a grid resolution of approximately 160 km. A more detailed description of the horizontal and vertical grids is provided, for example, by Zängl et al. (2015) and Rast (2017).

As recommended by Gassmann and Herzog (2008), the equation system of ICON, which represents the dynamical core of the model, uses the horizontal velocity component normal to the triangle edges, the vertical wind component, air density and virtual potential temperature as prognostic variables (Zängl et al., 2015). The equation system of the dynamical core does not include the representation of sub-grid scale physical processes. These are included as additional packages in the model, and differ between the numerical weather prediction and climate simulation modes of the model.

In this thesis, we use ICON with the physical parameterization package developed for numerical weather prediction. We will briefly introduce the NWP physics parameterizations and focus in more detail on the cloud and radiation parameterizations as these are most important for studying the impact of cloud-radiative changes on the midlatitude circulation response to global warming. The information is based on the ICON model tutorial from the German weather service (Prill et al., 2019), which gives a summary of the NWP physics parameterizations.

The physical parameterizations are divided into fast and slow physics. The fast-physics parameterizations are usually called every fourth or fifth dynamical core-time step (Zängl et al., 2015). They include the saturation adjustment, cloud microphysics, turbulent diffusion and land/surface calculations. They are, except for the saturation adjustment, based on the operational regional Consortium for Small-scale Modeling (COSMO; Doms and Baldauf, 2018) model (Zängl et al., 2015).

- For the **cloud microphysics**, we apply a single-moment scheme which calculates the specific mass content of different hydrometeor classes like cloud water, rain water, cloud ice and snow (Seifert, 2008; Doms et al., 2011). It distinguishes two ice classes, namely cloud ice and snow (but no graupel).

- For the **turbulent diffusion**, we apply a prognostic turbulent kinetic energy scheme that consists of two components which describe the free troposphere and the surface layer, respectively (Raschendorfer, 2001).

- The soil-vegetation-atmosphere transfer component TERRA (Schrodin and Heise, 2001; Heise et al., 2006) is the lower boundary condition for the atmospheric component of ICON for land-covered grid points. It computes the exchange of heat, moisture and momentum fluxes between

the **land surface** and the atmosphere, as well as the energy and water budget at the land surface. It uses a tile approach to account for small-scale inhomogeneities in surface characteristics. Additional important parameterizations for land and surface processes are the lake parameterization scheme FLake (Mironov, 2008; Mironov et al., 2010, 2012) and the sea-ice parameterization scheme (Mironov et al., 2012).

The slow-physics parameterizations are called less frequently in the model than the fast-physics parameterizations, and the frequency can be specified by the user. The slow-physics parameterizations include convection, cloud cover, radiation, non-orographic gravity wave drag and sub-grid scale orographic drag. The slow-physics parameterizations are based on the Integrated Forecast System (IFS) model from the European Centre for Medium-Range Weather Forecast (Zängl et al., 2015).

- For atmospheric moist **convection**, we apply the Tiedtke-Bechtold scheme which is a bulk mass flux convection scheme (Tiedtke, 1989; Bechtold et al., 2008). It includes three convective cloud types, which are shallow, mid-level and deep convection. Each column comprises one convective cloud type at each time step. The convection scheme runs through three steps to decide if a grid cell contains convection and if so, which convective cloud type is present. In the first step, the grid-scale conditions are investigated to determine if convection can be triggered in the column. In the second step, the tendencies of heat, moisture and momentum changes are calculated for air parcels in the column. In the third step, the strength of the convection is identified by a cloud base mass flux closure. Different approaches are used for the closure depending on the convection type. For deep, mid-level and shallow convection, the closure depends on convective available potential energy, large-scale vertical velocity, and the boundary layer, respectively.

- For the **radiation** scheme, we apply the Rapid Radiative Transfer Model (Mlawer et al., 1997). It uses the output from the diagnostic **cloud cover** scheme, which combines information from the microphysics, convection and turbulence schemes to prepare the variables cloud cover, cloud water and cloud ice for the radiation scheme. In ICON, these three cloud variables determine the optical properties of clouds. The RRTM is based on the correlated k approach with k being the mass absorption coefficient. This approach allows to strongly reduce the computational costs while keeping an accuracy of the results which is comparable to that from line-by-line calculations. The radiative calculations are performed separately for different wavelength bands. 30 spectral bands are used with 16 bands in the longwave domain and 14 bands in the shortwave domain. These spectral bands cover the absorption bands of important atmospheric (greenhouse) gases such as water vapor, carbon dioxide, ozone and different chlorofluorocarbons (CFCs). The RRTM provides shortwave and longwave radiative fluxes and heating rates.

- For the **non-orographic gravity wave drag**, we apply the Orr-Ern-Bechtold scheme (Orr et al., 2010), which accounts for the interaction of non-orographically forced gravity waves with the atmospheric background flow, in particular in the middle and upper atmosphere.

- For the **sub-grid scale orographic drag**, we apply the Lott and Miller scheme (Lott and Miller, 1997), which incorporates a low-level flow that is blocked when the sub-grid scale orography reaches a certain height. The blocked flow circulates around the mountain, introducing a form drag, or flows over the mountain, introducing gravity waves.

3.1.2. Model Setup

We perform numerical simulations with the atmospheric component of ICON (Zängl et al., 2015). The model is run with the physics package used for numerical weather prediction (ICON-NWP; version 2.1.00). The simulations are performed in R2B04 horizontal resolution (approximately 160 km) with 47 levels extending up to 75 km. A time step of 720 s is used.

We use a model setup with present-day continents, sea ice and a seasonal cycle, and with prescribed sea-surface temperatures (SST). Throughout this thesis, we refer to this simulation setup as present-day setup. SST are prescribed to isolate atmospheric cloud-radiative interactions, which primarily arise from longwave radiation (Allan, 2011). We use climatological SST and sea-ice fields, which are obtained by calculating multiyear monthly means of the SST and sea-ice fields over the Atmospheric Model Intercomparison Project (AMIP) period (1979-2008; Gates, 1992). In the control simulation ("CTL"), the multiyear monthly mean SST and sea-ice fields are prescribed to the model. The annual-mean SST pattern of the control simulation is shown in Fig. 3.1 (left panel). In addition, we perform two sets of global warming simulations. In the first set, global warming is mimicked by a uniform 4 K SST increase ("UNI"), similar to the Amip4K simulations that are part of CMIP5 (Taylor et al., 2012) (cf. section 3.2 for the Amip4K setup). In the second set, global warming is mimicked by increasing the SST by a pattern ("PAT"), similar to the AmipFuture simulations in CMIP5 (cf. section 3.2 for the AmipFuture setup). We use the same SST pattern that is used for the AmipFuture simulations and which is provided by CFMIP (`https://www.earthsystemcog.org/projects/cfmip/cfmip2-cmip5`). The SST pattern is derived from the multimodel mean SST response simulated by CMIP3 global atmosphere-ocean models at the time of quadrupling of atmospheric carbon dioxide (CO_2) in the 1% CO_2 increase per year experiment (Taylor et al., 2009, 2012). The SST pattern is scaled to a global mean of 4 K so that both UNI and PAT experience the same global-mean SST increase. In contrast to UNI, however, PAT includes changes in the SST gradients as represented in the CMIP3 multimodel mean. Thus, the SST impact derived from the PAT simulations implicitly includes the surface pathway of the cloud-radiative impact. Fig. 3.1 (right panel) shows the anomalous annual-mean SST pattern used in PAT. Compared to the uniform 4 K SST increase, the SST increase in PAT is about 1-2 K larger in the Tropics, the northern North Pacific, and the Barents Sea. At the same time, SST is hardly increased south of Greenland (subpolar gyre), in the Southern Ocean, and in the eastern South Pacific.

To isolate the effect of increased SST, sea ice is set to control values in all simulations, and atmospheric greenhouse gas concentrations are kept constant (CO_2 = 390 ppmv, CH_4 = 1,800 ppbv, N_2O = 322 ppbv, CFC_{11} = 240 pptv, CFC_{12} = 532 pptv). We use the GEMS (Global and Regional Earth-System
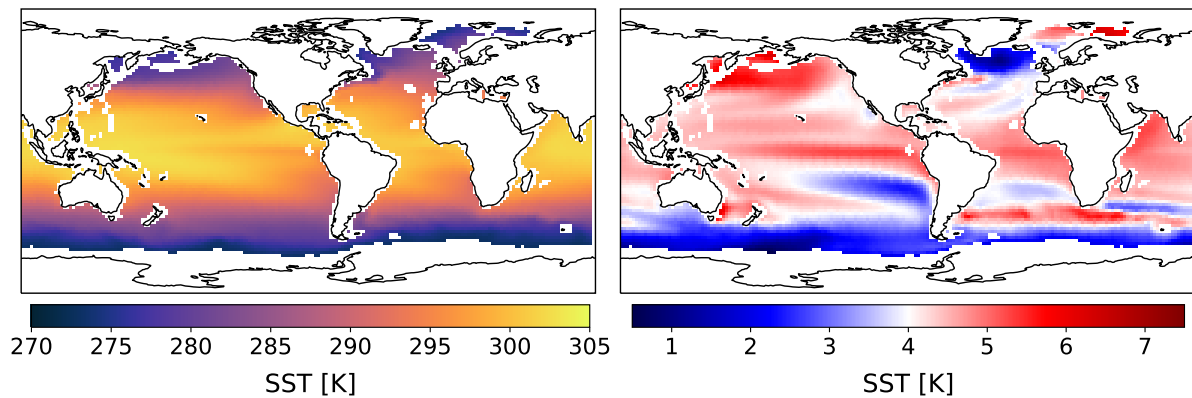
Figure 3.1.: Annual-mean sea surface temperature (SST) pattern of the CTL simulation (left) and anomalous SST pattern used for the PAT simulation (right). Regions covered by land or more than 15% of sea ice are masked. Reprinted from Albern et al. (2019). ©The Authors.

Monitoring using Satellite and In-Situ Data; Hollingsworth et al., 2008) ozone climatology from the European Centre for Medium-Range Weather Forecast Integrated Forecast System model. Aerosols are specified according to Tegen et al. (1997). For every simulation, we run the model for 31 years, with the first year being excluded from the analysis to avoid model initialization effects.

3.2. Additional Data Sets

We compare the ICON simulations to several other data sets. These data sets are introduced in this section and include climate model simulations of CMIP5, the ERA-Interim reanalysis and satellite observations.

Climate Models: CMIP5

The setup of our ICON simulations is based on the Amip, Amip4K and AmipFuture simulations of CMIP5. Thus, in this study, we compare the ICON simulations to the CMIP5 Amip, Amip4K and AmipFuture simulations. The Amip simulations are part of the CMIP5 Core experiments, which needed to be performed by all models participating in CMIP5 (Taylor et al., 2012). They are performed with atmosphere-only General Circulation Models (AGCMs) and have a length of 30 years. The simulations are run with observed time-evolving SST and sea ice from 1979 to 2008. Other conditions, such as atmospheric composition (including atmospheric concentration of carbon dioxide), solar forcing, emissions and concentrations of short-lived species and natural and anthropogenic aerosols, as well as land use, are also based on observations and vary over time (Taylor et al., 2009). The major purposes of the Amip simulations are to i) evaluate the model performance in AGCMs, for example, by comparison with observations; ii) investigate whether the AGCMs with prescribed SST and sea ice show the same errors

as coupled models; and iii) build a reference simulation for the perturbed SST simulations Amip4K and AmipFuture (Taylor et al., 2009).

The AmipFuture and Amip4K simulations are part of the CMIP5 Tier 1 and Tier 2 experiments, respectively (Taylor et al., 2012). They were designed by CFMIP to study cloud feedbacks and responses to an imposed SST change in AGCMs (Taylor et al., 2009, cf. CFMIP website at `https://www.earthsystemcog.org/projects/cfmip/`). A main aim of the AmipFuture simulations is to study atmospheric processes that are important for the global warming response of clouds and precipitation (Taylor et al., 2009). The SST change in Amip4K is a globally uniform 4 K increase. The SST change in AmipFuture is a pattern derived from ocean-atmosphere General Circulation Models of phase 3 of CMIP in response to a transient quadrupling of atmospheric CO_2 (Taylor et al., 2009, cf. section 3.1.2).

Since the Amip4K and AmipFuture simulations are part of the CMIP5 Tier experiments, they were not performed by all modeling centers that contributed to CMIP5. Data for all three, the Amip, Amip4K and AmipFuture simulations, is available for 11 climate models (marked by an x in the second column of Tabs. 3.1 and 3.2).

In addition to the response in the Amip simulations, we compare the global warming response in ICON to the global warming response in coupled CMIP5 models. To this end, we investigate the historical simulation (1975-2004) and the RCP8.5 simulation (2070-2099) of 37 CMIP5 coupled climate models (marked by an x in the first column of Tabs. 3.1 and 3.2). The historical simulation is part of the CMIP5 core experiments and is run with observed changes in atmospheric composition due to anthropogenic and natural sources, and time-evolving land cover (Taylor et al., 2012). This makes the historical simulation the counterpart to the Amip simulation, but with coupled models instead of AGCMs. The historical simulation covers the years 1850-2005. Its main purposes include i) the evaluation of model performance for the present-day climate and for observed climate change; and ii) the generation of initial conditions for future climate scenarios (Taylor et al., 2009).

To investigate the circulation response to global warming, we compare the historical simulation to the representative concentration pathway 8.5 (RCP8.5) simulation. The RCP8.5 simulation is a scenario that expects approximately $8.5\,\mathrm{W\,m^{-2}}$ radiative forcing in year 2100 relative to pre-industrial conditions, making it the high-emission scenario of the CMIP5 core experiments (Taylor et al., 2012). As part of the CMIP5 core experiments, it is run with prescribed CO_2 conditions for the years 2006-2100, and extended up to year 2300 as part of the CMIP5 Tier 2 experiments. The main purposes of the RCP scenarios include i) the estimation of future anthropogenic climate change based on different scenarios; and ii) the direct comparison between models with and without a representation of the carbon cycle (Taylor et al., 2009).

Reanalysis: ERA-Interim

In addition to the CMIP5 Amip simulations, we compare the present-day ICON simulations to the global atmospheric reanalysis ERA-Interim (Dee et al., 2011). ERA-Interim was produced by the European

Table 3.1.: CMIP5 models used in this study. For models 6 and 23, the model name differs between the coupled model version (historical and RCP8.5 simulations) and the atmosphere-only model version (Amip, Amip4K and AmipFuture simulations), so that both names are provided. For all simulations, we use monthly-mean data of the r1i1p1 ensemble member. The letters in the last column are the same as in the Figures in Appendix A.

	Model		historical, RCP8.5	Amip, Amip4K, AmipFuture
1	ACCESS1-0	Australian Community Climate and Earth-System Simulator, version 1.0	x	-
2	ACCESS1-3	Australian Community Climate and Earth-System Simulator, version 1.3	x	-
3	bcc-csm1-1-m	Beijing Climate Center, Climate System Model, version 1.1, moderate resolution	x	-
4	bcc-csm1-1	Beijing Climate Center, Climate System Model, version 1.1	x	x (A)
5	BNU-ESM	Beijing Normal University – Earth System Model	x	-
6	CanESM2; CanAM4	Second Generation Canadian Earth System Model; Fourth Generation Canadian Atmospheric General Circulation Model	x	x (B)
7	CCSM4	Community Climate System Model, version 4	x	x (C)
8	CESM1-BGC	Community Earth System Model, version 1 (biogeochemistry, or carbon cycle)	x	-
9	CESM1-CAM5	Community Earth System Model, version 1 (Community Atmosphere Model, version 5)	x	-
10	CMCC-CESM	Centro Euro-Mediterraneo sui Cambiamenti Climatici Carbon Cycle Earth System Model	x	-
11	CMCC-CM	Centro Euro-Mediterraneo sui Cambiamenti Climatici Climate Model	x	-
12	CMCC-CMS	Centro Euro-Mediterraneo sui Cambiamenti Climatici Stratosphere-resolving Climate Model	x	-
13	CNRM-CM5	Centre National de Recherches Météorologiques Coupled Global Climate Model, version 5	x	x (D)
14	CSIRO-Mk3-6-0	Commonwealth Scientific and Industrial Research Organisation Mark 3.6.0	x	-
15	EC-EARTH	European Consortium Earth System Model	x	-
16	FGOALS-g2	Flexible Global Ocean–Atmosphere–Land System Model, gridpoint version 2.0	x	-
17	FIO-ESM	First Institute of Oceanography (FIO) Earth System Model (ESM)	x	-
18	GFDL-CM3	Geophysical Fluid Dynamics Laboratory Climate Model, version 3	x	-
19	GFDL-ESM2G	Geophysical Fluid Dynamics Laboratory Earth System Model with GOLD component	x	-

Table 3.2.: Table 3.1 continued.

	Model		historical, RCP8.5	Amip, Amip4K, AmipFuture
20	GFDL-ESM2M	Geophysical Fluid Dynamics Laboratory Earth System Model with MOM, version 4 component	x	-
21	GISS-E2-H	Goddard Institute for Space Studies Model E2, coupled with HYCOM	x	-
22	GISS-E2-R	Goddard Institute for Space Studies Model E2, coupled with the Russell ocean model	x	-
23	HadGEM2-AO;	Hadley Centre Global Environment Model, version 2, Atmosphere and Ocean;	x	
	HadGEM2-A	Hadley Centre Global Environment Model, version 2, Atmosphere		x (E)
24	HadGEM2-CC	Hadley Centre Global Environment Model, version 2, Carbon Cycle (AO configuration with biogeochemistry)	x	-
25	HadGEM2-ES	Hadley Centre Global Environment Model, version 2, Earth System (CC configuration with chemistry)	x	-
26	inmcm4	Institute of Numerical Mathematics Coupled Model, version 4.0	x	-
27	IPSL-CM5A-LR	L'Institut Pierre-Simon Laplace Coupled Model, version 5A, low resolution	x	x (F)
28	IPSL-CM5A-MR	L'Institut Pierre-Simon Laplace Coupled Model, version 5A, mid resolution	x	-
29	IPSL-CM5B-LR	L'Institut Pierre-Simon Laplace Coupled Model, version 5B, low resolution	x	x (G)
30	MIROC5	Model for Interdisciplinary Research on Climate, version 5	x	x (H)
31	MIROC-ESM-CHEM	Model for Interdisciplinary Research on Climate, Earth System Model, Chemistry Coupled	x	-
32	MIROC-ESM	Model for Interdisciplinary Research on Climate, Earth System Model	x	-
33	MPI-ESM-LR	Max Planck Institute Earth System Model, low resolution	x	x (I)
34	MPI-ESM-MR	Max Planck Institute Earth System Model, medium resolution	x	x (J)
35	MRI-CGCM3	Meteorological Research Institute Coupled Atmosphere-Ocean General Circulation Model, version 3	x	x (K)
36	NorESM1-ME	Norwegian Earth System Model, version 1, intermediate resolution, with prognostic biogeochemical cycling	x	-
37	NorESM1-M	Norwegian Earth System Model, version 1, intermediate resolution	x	-

Centre for Medium-Range Weather Forecasts (ECMWF) from 2006 to 2019, and covers the period January 1979 to August 2019. Its main purposes include the improvement of the representation of the hydrological cycle, the quality of the stratospheric circulation and the handling of biases compared to ERA-Interim's predecessor ERA-40 (Berrisford et al., 2011). To achieve these aims, a 4-dimensional variational analysis (4D-Var) with a 12-hour analysis window was used together with other model improvements such as modified humidity analysis, variational bias correction and revised data handling (Berrisford et al., 2011). In this study, we use 6-hourly output for the 30-year period 1979-2008 to cover the same time frame as the CMIP5 Amip simulations that are run with observed sea-surface temperatures.

Observations: CloudSat/CALIPSO and CERES/MODIS

Many general circulation models have biases in the representation of clouds and their radiative effects (e.g., Ceppi et al., 2012; Grise and Medeiros, 2016). Since the impact of changes in cloud-radiative properties on the global warming response of the atmospheric circulation is the main focus of this thesis, we compare cloud cover and cloud-radiative effects in the control simulation of ICON to satellite observations to verify that ICON reasonably simulates clouds and cloud-radiative effects, which are comparable to those from other atmosphere-only General Circulation Models.

For cloud incidence, we investigate the 2B-GEOPROF-LIDAR product (version P2R04; Mace et al., 2009), which combines observations from the CloudSat Cloud Profiling Radar (CPR) and from the Cloud-Aerosol Lidar and Infrared Pathfinder Satellite Observation (CALIPSO) Cloud-Aerosol Lidar with Orthogonal Polarization (CALIOP). CloudSat and CALIPSO are part of the NASA Afternoon Train (A-Train), a convoy of polar orbiting satellites that travel along the same track to provide nearly-simultaneous observations of cloud properties and other atmospheric variables (Stephens et al., 2002). Details about the instruments aboard CloudSat and CALIPSO as well as available data products can be found at `https://cloudsat.atmos.colostate.edu/` and `https://www-calipso.larc.nasa.gov/`.

The 2B-GEOPROF-LIDAR product is available for roughly 5 years from June 2006 to April 2011. As described for example in Li et al. (2014), the CPR and lidar measurements are complementary to each other because the CPR is able to detect optically thick hydrometeor layers while the lidar measures optically thin hydrometeor layers. Thus, combining the two data sets allows to estimate the vertical and horizontal distribution of hydrometeors, and thus clouds, in the atmosphere, ranging from the surface to the stratosphere (e.g., Li et al., 2014; Verlinden et al., 2011, and references therein). We show zonal-mean cloud incidence as derived by Li et al. (2014) (also see Verlinden et al., 2011) which indicates for each atmospheric volume the likelihood that the instruments observed a cloud that covers more than 50% of that volume. The data was provided by Ying Li (cf. Li et al., 2014).

For cloud-radiative effects, we investigate the Clouds and Earth's Radiant Energy Systems (CERES) Energy Balanced and Filled (EBAF) product, edition 4.1 (Loeb et al., 2018; Kato et al., 2018). It combines measurements from CERES and MODIS (Moderate Resolution Imaging Spectrometer) aboard

the polar orbiting Terra and Aqua satellites, and measurements from geostationary imagers (CERES, 2020). CERES EBAF 4.1 is available for March 2000 to November 2019. It contains monthly means of observed top-of-atmosphere (TOA) and calculated surface radiative fluxes for all-sky (cloudy) and clear-sky (cloud free) conditions, the resulting cloud-radiative effects, as well as different cloud properties. The TOA net (longwave plus shortwave) radiative flux is adjusted to remove inconsistencies between the global net TOA flux and the heat storage in the climate system (CERES, 2020). The surface radiative fluxes are computed in a way to be consistent with the observed TOA radiative fluxes. More information about the data set is available and in the data quality summary (CERES, 2020) and at `https://ceres.larc.nasa.gov/data/#energy-balanced-and-filled-ebaf`. The data was obtained from `https://ceres.larc.nasa.gov/data/`.

3.3. The Large-Scale Atmospheric Circulation in ICON

ICON-NWP is a global numerical weather prediction model designed to perform simulations with a length of several hours or days. However, we use ICON-NWP to perform simulations with a length of 30 years. Even though the CMIP5 protocol envisages that the Amip atmosphere-only simulations may be performed by different types of models, including numerical weather prediction models (Taylor et al., 2009), we have to verify that ICON-NWP reasonably simulates the large-scale structure of the present-day atmospheric circulation. To this end, we compare ICON to the model mean of the CMIP5 Amip simulations, to the ECMWF ERA-Interim reanalysis (years 1979-2008) and to satellite observations (section 3.3.1). Further, we compare the circulation response in ICON to the robust circulation response in the CMIP5 Amip4K and AmipFuture simulations (section 3.3.2).

3.3.1. Present-Day Climatological Circulation

In this section, we compare the control simulation of ICON to the model-mean of the CMIP5 Amip simulations, to the ERA-Interim reanalysis, and to cloud cover and cloud-radiative effect observations from CloudSat/CALIPSO and CERES/MODIS, respectively. Fig. 3.2 shows the annual-mean zonal-mean atmospheric temperature, zonal wind and mass stream function for the ICON, CMIP5 and ERA-Interim data. Note that ICON and the CMIP5 data cover vertical levels between 1000-10 hPa, whereas ERA-Interim covers 900-100 hPa.

Overall, the three data sets agree well for the three variables. The isotherms are located at approximately the same height, with slightly warmer poles and an upper troposphere / lower stratosphere in ICON than in the other two data sets (Fig. 3.2, top). Similar to the reanalysis and the CMIP5 models, ICON exhibits a merged jet stream in the Northern Hemisphere and a split jet stream in the Southern Hemisphere (Fig. 3.2, middle row). The jet streams are of similar magnitude but shifted polewards in ICON compared to the jet streams in CMIP5 and ERA-Interim. Note that previous studies found an equatorward bias in the jet latitude in coupled climate models of phases 3 and 5 of CMIP (e.g., Kidston and
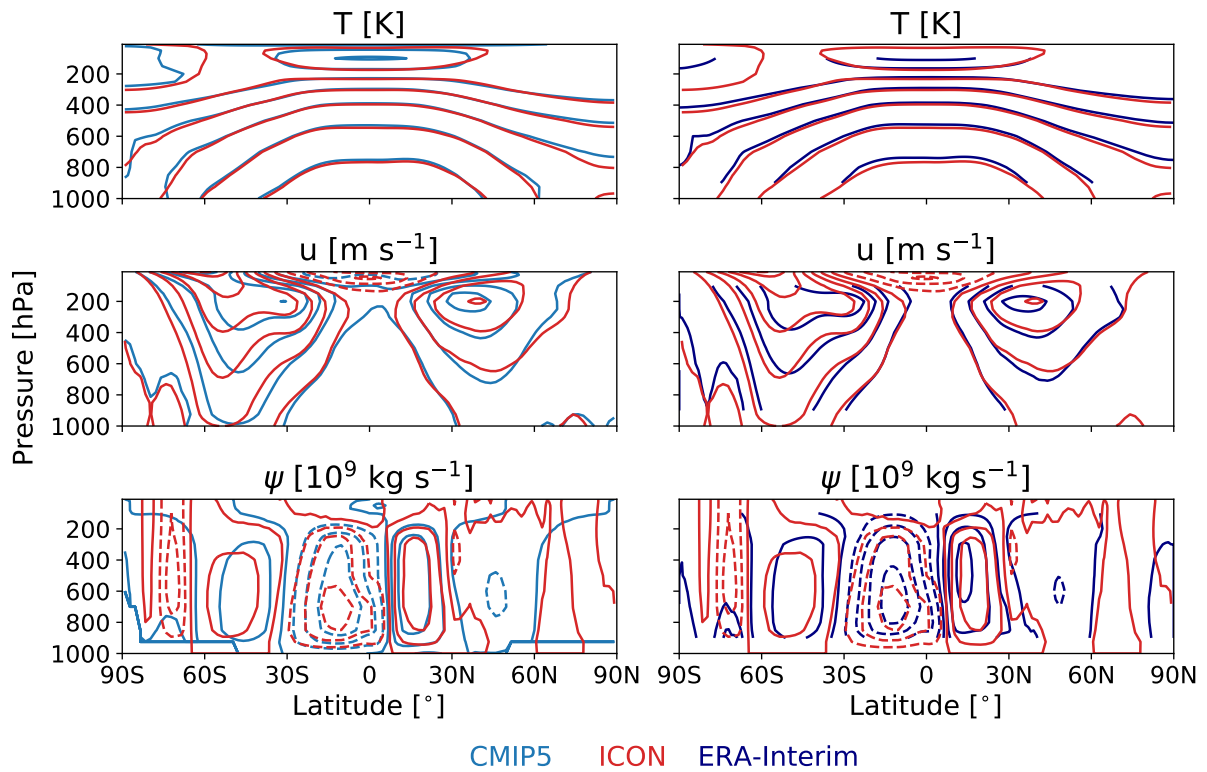
Figure 3.2.: Annual-mean zonal-mean atmospheric temperature (top, contour intervals of 15 K starting from 180 K), zonal wind (middle, contour intervals of $8\,\mathrm{m\,s^{-1}}$) and mass stream function (bottom, contour intervals of $25{\cdot}10^9\,\mathrm{kg\,s^{-1}}$) in ICON (red), the model mean of the CMIP5 Amip simulations (light blue), and the ERA-Interim reanalysis (dark blue). The isolines for ICON are identical in the left and right columns.

Gerber, 2010; Bracegirdle et al., 2013), and related it, for example, to biases in shortwave cloud-radiative effects (Ceppi et al., 2012).

The location, extent and strength of the Hadley cells agree well between ICON, CMIP5 and ERA-Interim (Fig. 3.2, bottom). In ICON, the Ferrel cells are slightly shifted polewards and the cell in the Northern Hemisphere is weaker than in CMIP5 and ERA-Interim, consistent with the more poleward located jet streams in ICON. Deviations between the data sets are found for the location and strength of the polar cells for which ICON simulates a much stronger cell in the Southern Hemisphere than the other two data sets.

ICON does not only agree with the CMIP5 and ERA-Interim data sets in the zonal-mean perspective, but also regionally. The annual-mean zonal wind maxima, i.e., the jet streams, in the North Atlantic, North Pacific and Southern Hemisphere as well as the tropical easterlies are located in the same regions in all three data sets (Fig. 3.3). ICON captures well the jet tilt in the North Atlantic, which is also present in ERA-Interim but too weak in CMIP5 (Zappa et al., 2013). In the North Pacific, the pattern of the zonal wind maximum is similar in all data sets, but the western North Pacific jet is weaker in ICON than in

CMIP5   ICON   ERA-Interim
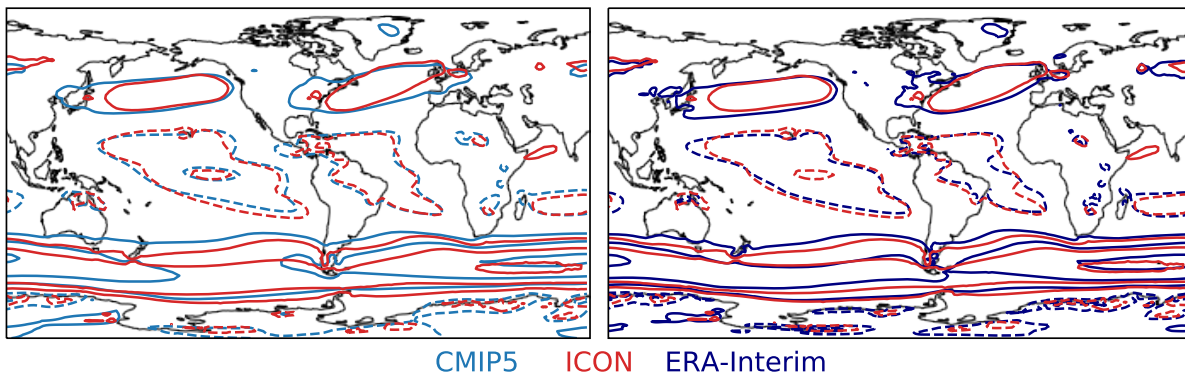
Figure 3.3.: Annual-mean zonal wind at 850 hPa in ICON (red), the model mean of CMIP5 Amip simulations (light blue), and the ERA-Interim reanalysis (dark blue). The contour interval is $5 \, \mathrm{m \, s^{-1}}$; the $0 \, \mathrm{m \, s^{-1}}$ isotach is not shown. The isolines for ICON are identical in the left and right columns.

CMIP5 and ERA-Interim. In the Southern Hemisphere, the zonal wind maximum agrees well, especially between ICON and ERA-Interim.

Fig. 3.4 shows the annual-mean zonal-mean cloud cover as well as maps of cloud-radiative effects at the top of atmosphere, inside the atmosphere, and at the surface based on the control simulation of ICON. Overall, the cloud cover and cloud-radiative effects in ICON agree well with the estimates from satellite observations (cf. Fig. 1.3). The zonal-mean cloud cover in ICON is similar to the cloud incidence derived from CloudSat/CALIPSO observations. Yet, cloud incidence and cloud cover cannot be compared quantitatively as cloud incidence shows how often a certain grid box exhibited more than 50% cloud cover (Li et al., 2014).

Across large parts of the Earth, the cloud-radiative effects in ICON are smaller than the CRE estimates form satellite observations (cf. Fig. 3.4 b-g to Fig. 1.3 b-g). The largest differences between ICON and the observations are found over the polar regions and Greenland, in particular in the Southern Hemisphere. Note that these differences occur for both the all-sky and the clear-sky situations (not shown). Thus, assuming that the satellite observations show the "truth", the differences are possibly related to shortcomings in the representation of clouds in ICON (e.g., Grise and Medeiros, 2016), i.e., differences in the all-sky situation, and in the prescribed ice cover, i.e., differences in the clear-sky situation.

3.3.2. Circulation Response to Global Warming

In section 3.3.1, we showed that the large-scale atmospheric circulation in the control simulation of ICON agrees well with the ERA-Interim reanalysis and the CMIP5 model mean of the Amip simulation. Here, we investigate the circulation response to a uniform and spatially varying SST increase (cf. sections 3.1.2 and 3.2), and compare the circulation response in ICON to the robust CMIP5 Amip4K and AmipFuture responses.
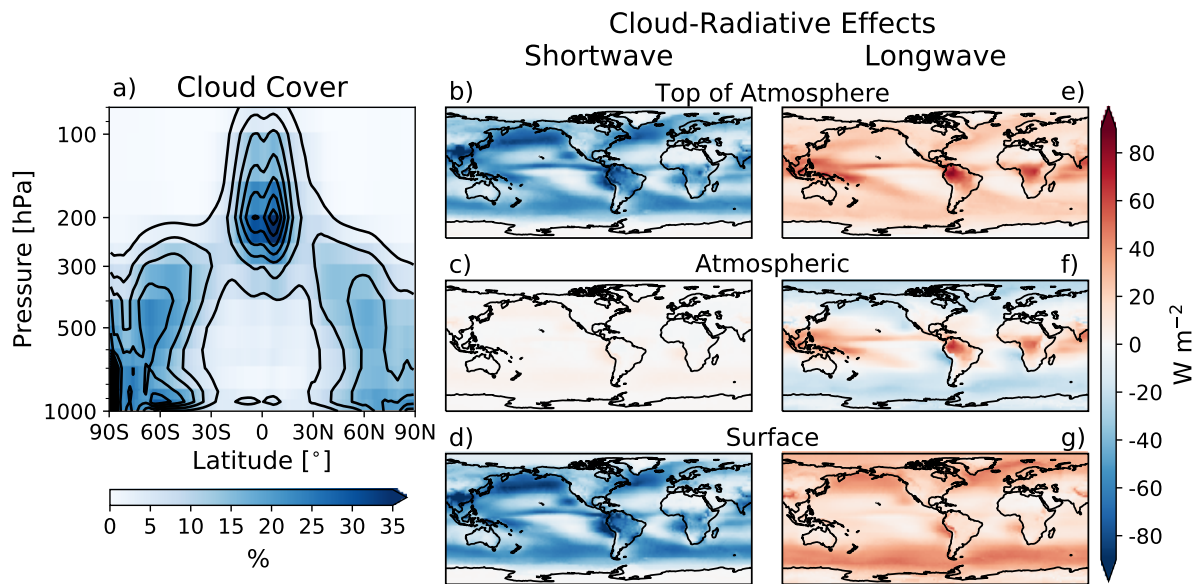
Figure 3.4.: Annual-mean zonal-mean cloud cover (a) and maps of annual-mean cloud-radiative effects (b-g) in ICON. The contour lines in the left panel are in intervals of 5%. The maps show shortwave and longwave cloud-radiative effects at the top-of-atmosphere (b, e), inside the atmosphere (c, f) and at the surface (d, g), respectively.

The left column of Fig. 3.5 shows the global warming response of the annual-mean zonal-mean circulation to a uniform 4 K SST increase in the UNI simulation of ICON. The model simulates the changes expected from global coupled atmosphere-ocean models (e.g., Lu et al., 2008; Ma and Xie, 2013; Grise and Polvani, 2014b; Harvey et al., 2015). This includes amplified upper-tropospheric warming in the tropics (Fig. 3.5a) and a vertical expansion of the troposphere, which manifests in upward shifts of the upper-level jet streams (Fig. 3.5b) and the upper boundary of the Hadley cells (Fig. 3.5c). ICON also simulates a weakening and horizontal expansion of the tropics, which are indicated by a poleward shift of the midlatitude jet streams in the lower and middle troposphere (Fig. 3.5b) and a weakening and poleward expansion of the Hadley cells (Fig. 3.5c). These responses agree well with the robust Amip4K responses of the CMIP5 model mean (Fig. 3.5d-f). Very similar results are found for the spatially-varying SST increase in the PAT (ICON) and AmipFuture (CMIP5) simulations (Fig. 3.6). Note, however, that the Southern Hemisphere Hadley cell strengthens close to the equator in the PAT simulation, whereas it weakens in the CMIP5 model mean for the AmipFuture simulation.

The regional annual-mean u_{850} response to a uniform and spatially-varying SST increase is shown in Fig. 3.7. In the ICON simulations, the North Atlantic, North Pacific and Southern Hemisphere jet streams shift poleward and strengthen in response to global warming (Fig. 3.7, left). This response agrees well with the robust Amip4K and AmipFuture responses of the CMIP5 models (Fig. 3.7, right).

In conclusion, our results show that the ICON simulations agree well with the ERA-Interim reanalysis data, with the CMIP5 model mean for the Amip simulation, and with satellite observations from
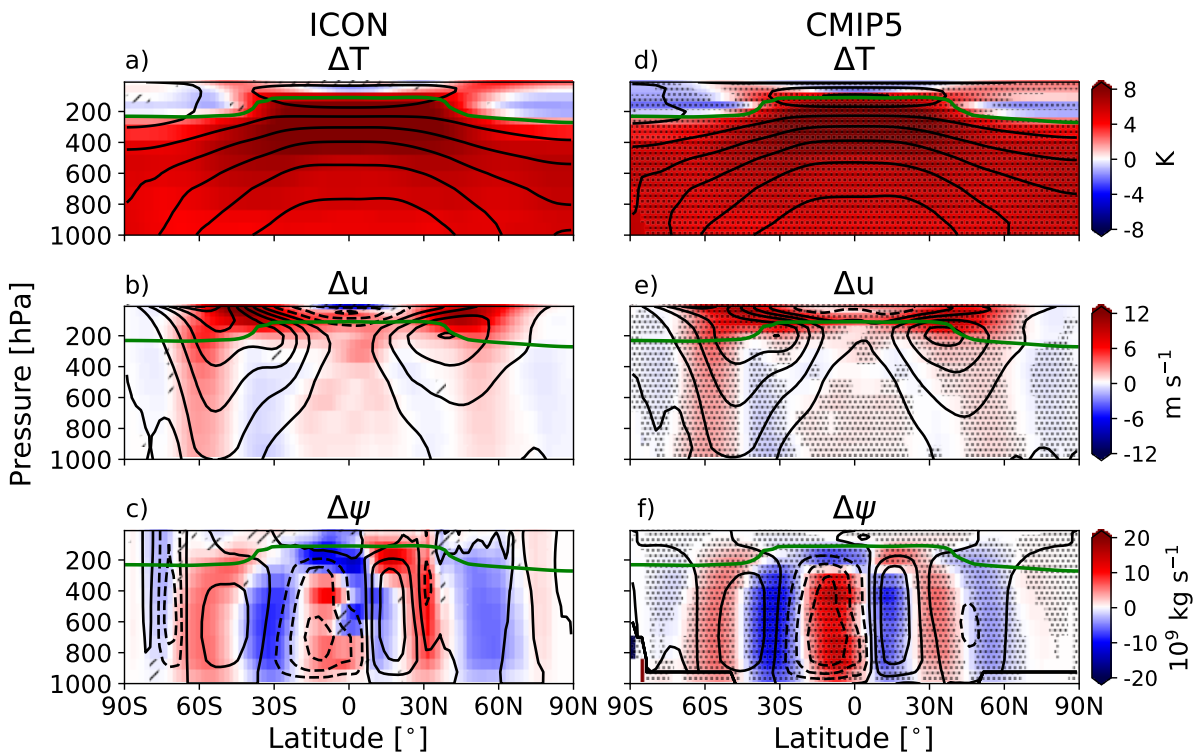
Figure 3.5.: Response of the annual-mean zonal-mean atmospheric temperature (a, d), zonal wind (b, e), and mass stream function (c, f) to a uniform SST increase in ICON (UNI, left) and the CMIP5 model mean (Amip4K, right). Stippling in the right column shows where 9 or more out of 11 CMIP5 models agree on the sign of the response. Hatching in the left column indicates where the response in ICON deviates from the robust CMIP5 response. The contours are the same as in the left panel of Fig. 3.2. The green line in each panel shows the tropopause height in the control simulation of ICON. Left column adapted from Albern et al. (2019). ©The Authors.

CloudSat/CALIPSO and CERES/MODIS for the present-day control simulation and with the CMIP5 model mean for the global warming responses. This gives us confidence to use ICON-NWP to perform long-term Amip-like climate simulations.
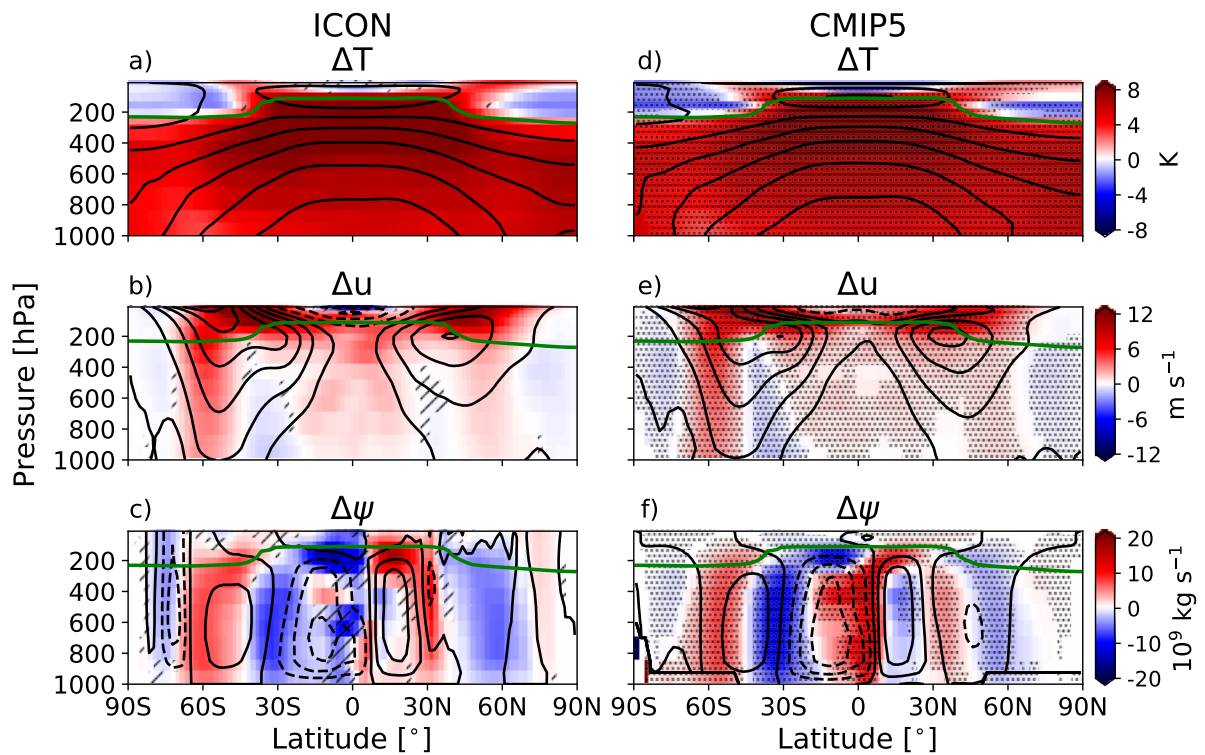
Figure 3.6.: Same as Fig. 3.5, but for the spatially varying SST increase of the PAT and AmipFuture simulations. Left column adapted from Albern et al. (2019). ©The Authors.
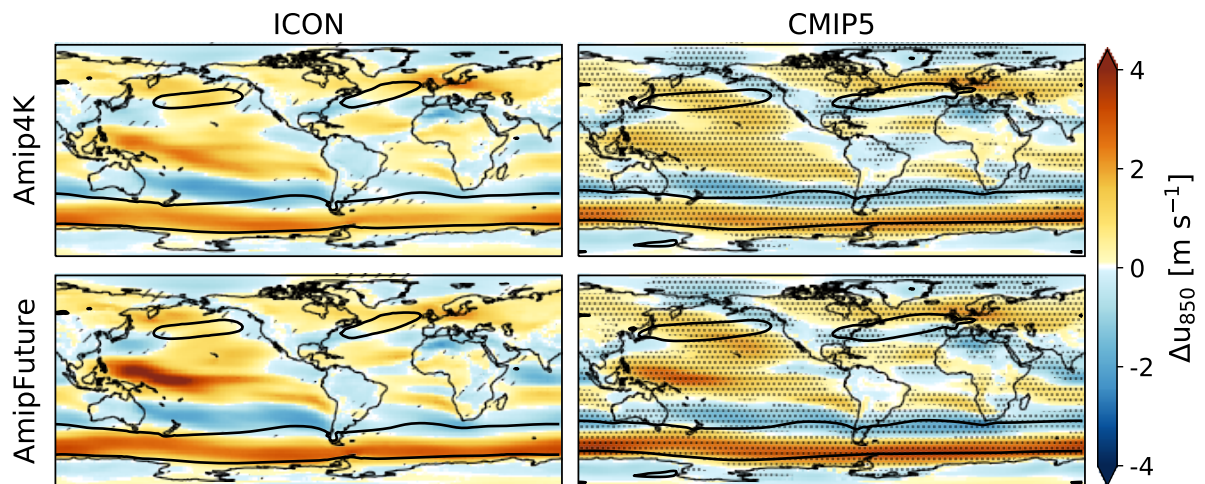
Figure 3.7.: Response of the annual-mean zonal wind at 850 hPa to a uniform (top) and spatially varying (bottom) SST increase in ICON (left) and the CMIP5 model mean (right). Stippling in the right column shows where 9 or more out of 11 CMIP5 models agree on the sign of the response. Hatching in the left column indicates where the response in ICON deviates from the robust CMIP5 response. The contours show the 6 m s^{-1} isolines of u_{850} in the control simulations of ICON and the CMIP5 model mean.

4. Methods

We quantify the midlatitude circulation and its response to global warming based on the midlatitude jet streams and storm tracks across different seasons and regions. In this chapter, we introduce the regions of interest (section 4.1) and the jet stream and storm track metrics (section 4.2). In section 4.3, we introduce the cloud-locking method, which is applied to decompose the circulation response to global warming into contributions from cloud-radiative changes and from the SST increase, and show that its application does not affect the circulation response to global warming. Finally, we discuss the Partial-Radiative Perturbation Calculation that allows us to determine the change in cloud-radiative heating under global warming (section 4.4).

Sections 4.2, 4.3.1, and 4.4 are adapted from Albern et al. (2019). ©The Authors. Sections 4.1 and 4.3.2 are adapted from Albern et al. (2020). ©American Meteorological Society. Used with permission.

4.1. Regions of Interest

We investigate the jet stream response to global warming at each longitude and in a zonal-mean perspective. For the zonal-mean perspective, we analyze both the zonal mean over all longitudes in the Northern and Southern Hemispheres as well as the zonal mean over the North Atlantic (60°W-0°) and North Pacific (135°E-125°W) ocean basins. The longitudinal boundaries of the ocean basins are taken from Barnes and Polvani (2013). Thus, our four regions of interest are i) the North Atlantic (NA), ii) the North Pacific (NP), iii) the Northern Hemisphere (NH), and iv) the Southern Hemisphere (SH). We focus on the North Atlantic, North Pacific and Southern Hemisphere in chapter 5, and include the zonal mean for the Northern Hemisphere in chapter 6. In chapter 7, we investigate the circulation response over the North Atlantic-European sector, and show, among others, zonal-mean jet responses over the North Atlantic (same boundaries as above) and over Europe (0°-25°E).

4.2. Circulation Metrics

Jet Stream

Following Barnes and Polvani (2013), we define the latitude and strength of the midlatitude jet streams based on the maximum zonal wind at 850 hPa, u_{850}. In the Northern (Southern) Hemisphere, we search for the maximum u_{850} between 25°N and 70°N (25°S and 70°S) and perform a quadratic fit around the maximum and its two neighboring grid points on an interpolated 0.01° latitude grid. The maximum of

the quadratic fit yields the jet strength, u_{jet}, and the jet latitude, φ_{jet}. For zonal-mean values of the jet and its response to global warming, the calculations of the jet latitude and jet strength are based on the zonal-mean u_{850} field over the longitudinal boundaries of the respective region (cf. section 4.1). For maps, the jet latitude and jet strength are calculated at each longitude based on u_{850} at the respective longitude. To make the comparison between the two hemispheres easier, all latitudes for the Northern Hemisphere are shown in "degrees North" and all latitudes for the Southern Hemisphere in "degrees South". Thus, for both hemispheres, a positive change in φ_{jet} indicates a poleward jet shift. We will focus on the eddy-driven jet stream throughout the thesis and always refer to the eddy-driven jet stream when we mention "jet streams" or the "jet".

In addition to the method by Barnes and Polvani (2013) (referred to as $\varphi_{jet,1}$ in the following), we tested two other methods for the jet latitude to account for the tilt of the jet stream. The jet tilt is particularly pronounced in the North Atlantic, where the annual-mean jet stream is located at around 42°N in the western part of the ocean basin and at around 55°N close to the British Isles (Fig. 4.1, black crosses). The jet tilt is largest during boreal summer (Fig. 4.1, green crosses) and smallest during boreal winter (Fig. 4.1, blue crosses). In the North Pacific, the jet tilt is much smaller than in the North Atlantic during most seasons, and the annual-mean North Pacific jet stream is located at around 42°N. The Southern Hemisphere jet stream meanders between around 50-60°S.

The jet tilt can strongly modify the zonal-mean u_{850} profile and, thus, the detection of the jet latitude and jet strength. In the case of a small jet tilt, the maximum in the u_{850} profile is located at about the same latitude for each longitude, so that the zonal-mean u_{850} profile exhibits a distinct peak which marks
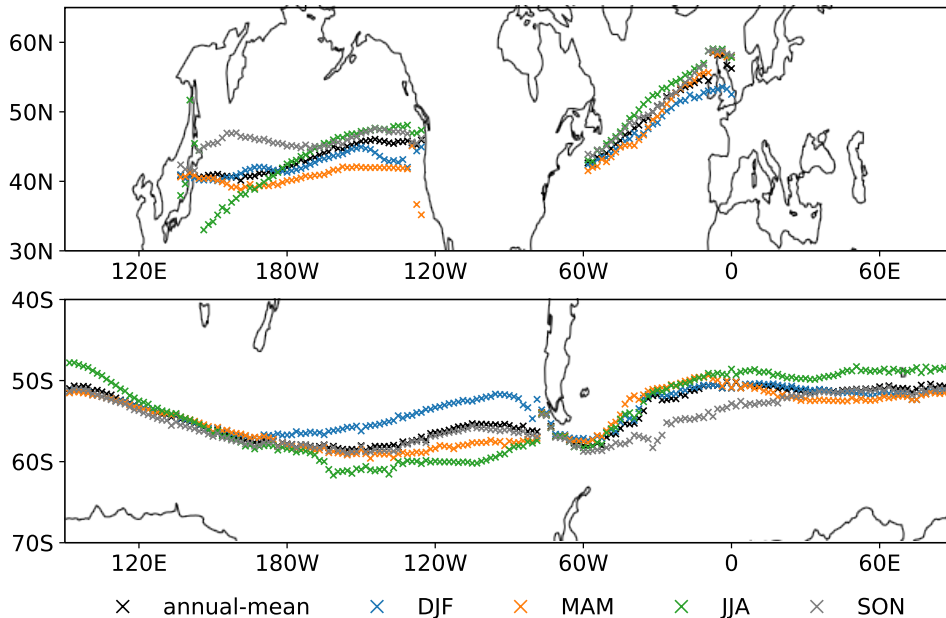
Figure 4.1.: Annual-mean and seasonal-mean jet latitude based on the jet metric by Barnes and Polvani (2013).

the jet latitude. In the case of a large jet tilt, however, the maximum in the u_{850} profile is located at varying latitudes depending on the longitude, so that the zonal-mean u_{850} profile is flatter and wider than the profile for the small jet tilt (assuming similar values for u_{850} for both cases). The detection of the jet latitude based on the flat u_{850} profile is more sensitive to small changes in the profile's shape, which might result in overestimated jet shifts.

This consideration shows that it can be of great importance to account for the jet tilt, depending on the North-South extent of the jet tilt and the strength of the zonal wind. Thus, we test two jet metrics that account for the jet tilt to check if the jet latitude and jet shift in our ICON simulations depend on the method. We investigate the jet in the North Atlantic, North Pacific and Southern Hemisphere.

The calculation of the jet latitude described above is based on the zonal-mean zonal wind. In contrast, the two additionally tested methods are based on the jet latitude at each longitude. First, we derive the jet latitude at each longitude following Barnes and Polvani (2013). In the next step, we determine the zonal-mean jet latitude as i) the zonal mean over the longitude-dependent jet latitude

$$\varphi_{jet,2} = \frac{1}{N_\lambda} \sum_{i=\lambda_1}^{\lambda_2} \varphi_{jet}(i),$$

(4.1)

and ii) the zonal mean jet latitude weighted by the square of the jet strength

$$\varphi_{jet,3} = \frac{\int \varphi_{jet}(\lambda) \cdot u_{jet}^2(\lambda) d\lambda}{\int u_{jet}^2(\lambda) d\lambda},$$

(4.2)

where $\varphi_{jet,2}$ and $\varphi_{jet,3}$ are the unweighted and weighted zonal-mean jet latitudes, λ is the longitude, λ_1 and λ_2 are the western and eastern boundaries of the region of interest, N_λ is the number of longitude grid points in the sum, and $\varphi_{jet}(\lambda)$ and $u_{jet}(\lambda)$ are the jet latitude and jet strength at each longitude, respectively. The boundaries of the integrals are the boundaries of the region of interest given in section 4.1. For each of the three methods, the zonal-mean jet latitude is calculated for the control simulation CTL and for the global warming simulations UNI and PAT. The jet response is derived based on the zonal-mean jet latitudes in CTL and UNI/PAT.

Fig. 4.2 shows the zonal-mean jet latitude (top) and jet latitude response (bottom) for all three methods. The method based on the zonal-mean u_{850} profile ($\varphi_{jet,1}$) is shown on the horizontal axis and the methods based on the longitude-dependent jet latitude ($\varphi_{jet,2}$ and $\varphi_{jet,3}$) are shown on the vertical axis. Overall, the three methods agree well in the North Pacific and Southern Hemisphere where the jet tilts are small (Fig. 4.2, second and third columns). Exceptions are found in the North Pacific during JJA, where the jet is located further South in the western part of the ocean basin than in the eastern part of the ocean basin (Fig. 4.1). During this season, $\varphi_{jet,2}$ and $\varphi_{jet,3}$ are located further equatorward than $\varphi_{jet,1}$ with a minor impact of the weighting, and the jet tends to shift equatorward rather than keeping its position (Fig. 4.2, second column). A similar result is found for the jet shift in the North Atlantic throughout the year: the shifts of $\varphi_{jet,2}$ and $\varphi_{jet,3}$ are smaller than the shift of $\varphi_{jet,1}$ and tend to be equatorward rather than poleward (Fig. 4.2, first column). As described above, the larger shift of $\varphi_{jet,1}$ results from the fact
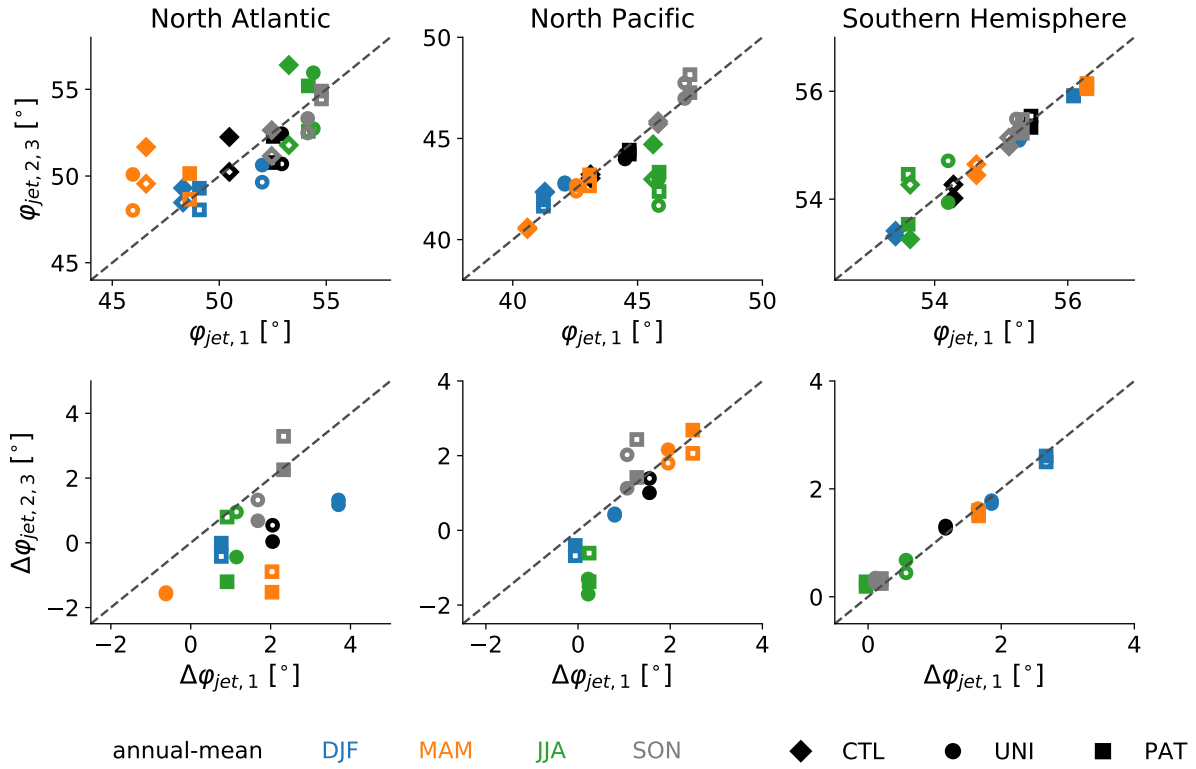
Figure 4.2.: Zonal-mean jet latitude (top) and jet latitude response (bottom) for the North Atlantic, North Pacific and Southern Hemisphere (left to right). The jet latitude defined by Barnes and Polvani (2013) is shown on the horizontal axis ($\varphi_{jet,1}$). The jet latitudes that account for the jet tilt are shown on the vertical axis with open markers for $\varphi_{jet,2}$ and filled markers for $\varphi_{jet,3}$. The dashed lines mark the "1:1" lines for which the metrics agree on the jet latitude and jet latitude response, respectively.

that taking the zonal mean without accounting for the jet tilt results in a flat u_{850} profile that is sensitive to small changes and, thus, yields to large jet shifts.

Our results indicate that it is important to account for the jet tilt rather than deriving the jet latitude from the zonal-mean u_{850} profile. However, for reasons of comparability, we will use the method defined by Barnes and Polvani (2013) in this study. Future studies should investigate the role of the jet tilt for the North Atlantic jet stream response to global warming.

Storm Track

We further characterize the storm tracks, which measure the synoptic activity of the midlatitude atmosphere (e.g., Hoskins and Valdes, 1990; Christoph et al., 1995; Chang et al., 2002; Yin, 2005; Pinto et al., 2007; Ulbrich et al., 2008; Shaw et al., 2016). While their magnitude and variability are dominated by transient low pressure systems, they also contain some variability associated with high pressure systems (which typically have longer time scales). We calculate the storm tracks from the standard deviation of

the 2.5- to 6-day band-pass filtered 500-hPa geopotential field (e.g., Blackmon, 1976), using the band-pass filter of the Climate Data Operators (version 1.9.4., available at `https://www.mpimet.mpg.de/cdo`).

4.3. Cloud-Locking Method

We apply the cloud-locking method to determine how much of the circulation response to global warming can be attributed to global and regional changes in cloud-radiative properties. The method allows us to break the radiative interactions and feedbacks between clouds and the atmospheric circulation by prescribing the radiative properties of clouds to the model's radiative transfer scheme (e.g., Wetherald and Manabe, 1988; Colman and McAvaney, 1997; Voigt and Shaw, 2015). While originally devised to study the impact of radiative feedbacks on global-mean and regional surface warming (e.g., Wetherald and Manabe, 1988; Schneider et al., 1999; Langen et al., 2012; Mauritsen et al., 2013), the locking method has become the most appropriate tool (Voigt and Albern, 2019) to investigate the contribution of cloud-radiative changes to circulation changes in response to global warming (e.g., Ceppi and Hartmann, 2016; Voigt and Shaw, 2016). The locking method has also been used to further decompose the circulation response to study the radiative impacts of water vapor (Voigt and Shaw, 2015; Voigt et al., 2019) and surface albedo changes (Ceppi and Shepherd, 2017).

In this section, we define how the impacts of global (section 4.3.1) and regional (section 4.3.2) cloud-radiative changes on the circulation response to global warming are determined. Other radiative properties such as water vapor and surface albedo are interactive. Further, we introduce the cloud- and water-vapor locking method (section 4.3.3) which is used to decompose the circulation response to global warming into contributions from cloud changes, water vapor changes and SST changes.

4.3.1. Global Cloud-Radiative Impact

We begin with determining the impact of global cloud-radiative changes. In a first step, we diagnose the instantaneous cloud-radiative properties (i.e., cloud water, cloud ice, and cloud fraction) in the CTL, UNI, and PAT simulations. Because cloud-radiative effects are nonlinear functions of cloud-radiative properties, we store the latter at every call of the radiative transfer scheme (every 36 min), as was done in previous studies (e.g., Voigt and Shaw, 2015; Ceppi and Hartmann, 2016). We store 10 years of cloud data to adequately sample cloud variability.

In a next step, we simulate 30 years with cloud-radiative properties prescribed to values from CTL, UNI, or PAT. We cycle three times through the 10 years of stored cloud fields. We have checked that this does not introduce any spurious periodicity to the midlatitude circulation in the prescribed-clouds simulations. The "cloud locking" only affects the radiative transfer scheme. All other components of ICON use the internally simulated clouds. The prescribed cloud-radiative properties are offset by at least 1 year relative to the simulated climate of the model to achieve a spatiotemporal decorrelation of the

cloud-radiative properties and the atmospheric circulation, temperature, and moisture. This decorrelation might result in situations in which a cloud-free subsidence region is simulated by the model, but the radiation scheme is run with cloud-radiative properties of a deep convective cloud at the same time. The impact of this decorrelation on the climatological circulation is found to be mainly small in our simulations. This is in line with other studies that used the cloud-locking method to investigate the circulation response to global warming (Voigt and Shaw, 2015, 2016; Ceppi and Hartmann, 2016; Ceppi and Shepherd, 2017; Voigt et al., 2019).

To quantify the cloud-radiative contribution to the circulation change in the UNI simulation, we perform the four additional simulations: T1C1, T1C2, T2C1, and T2C2. The numbers indicate whether SST (T) and cloud-radiative properties (C) are prescribed to values from CTL (simulation 1) or UNI (simulation 2). With this, we decompose the circulation response into a contribution from the SST increase, assuming no changes in the cloud-radiative properties, and a contribution from changes in the cloud-radiative properties assuming no SST increase. The total response of any given variable X to the combined effect of a uniform SST increase and cloud-radiative changes is given by

$$\Delta X = X_{\text{UNI}} - X_{\text{CTL}} = X_{\text{T2C2}} - X_{\text{T1C1}} + Res, \qquad (4.3)$$

where X_{UNI} and X_{CTL} denote the simulations with free clouds and *Res* is the residual due to the application of the cloud-locking method (see below for more explanations).

The contribution of the SST increase is given by

$$\Delta X_{\text{SST}} = \frac{1}{2} \left[(X_{\text{T2C1}} - X_{\text{T1C1}}) + (X_{\text{T2C2}} - X_{\text{T1C2}}) \right], \qquad (4.4)$$

and is referred to as "SST impact" hereafter. Analogously, the contribution of global cloud-radiative changes, hereafter referred to as "cloud-radiative impact" or "cloud impact", is given by

$$\Delta X_{\text{clouds}} = \frac{1}{2} \left[(X_{\text{T1C2}} - X_{\text{T1C1}}) + (X_{\text{T2C2}} - X_{\text{T2C1}}) \right]. \qquad (4.5)$$

In the following, we always refer to the impact of cloud-radiative changes if we talk about "cloud changes" and "cloud impacts".

By construction, the SST and cloud-radiative impacts sum up to the total locked response $X_{\text{T2C2}} - X_{\text{T1C1}}$, so that $\Delta X = \Delta X_{\text{SST}} + \Delta X_{\text{clouds}} + Res$. The cloud-radiative impact and the SST impact in the PAT simulation are quantified in an analogous manner.

Importantly, the residual *Res* in general is found to be much smaller than ΔX for both the uniform and the spatially-varying SST increase. This can be verified by comparing the responses in the simulations with "free" clouds to their "locked" counterparts, for which the prescribed cloud-radiative properties are decorrelated from the circulation (Fig. 4.3; cf. left panels of Figs. 3.5 and 3.6 for the response with free clouds). The fact that the residual *Res* of the locking method is small implies that the locking method can be used to meaningfully separate SST and cloud-radiative impacts.
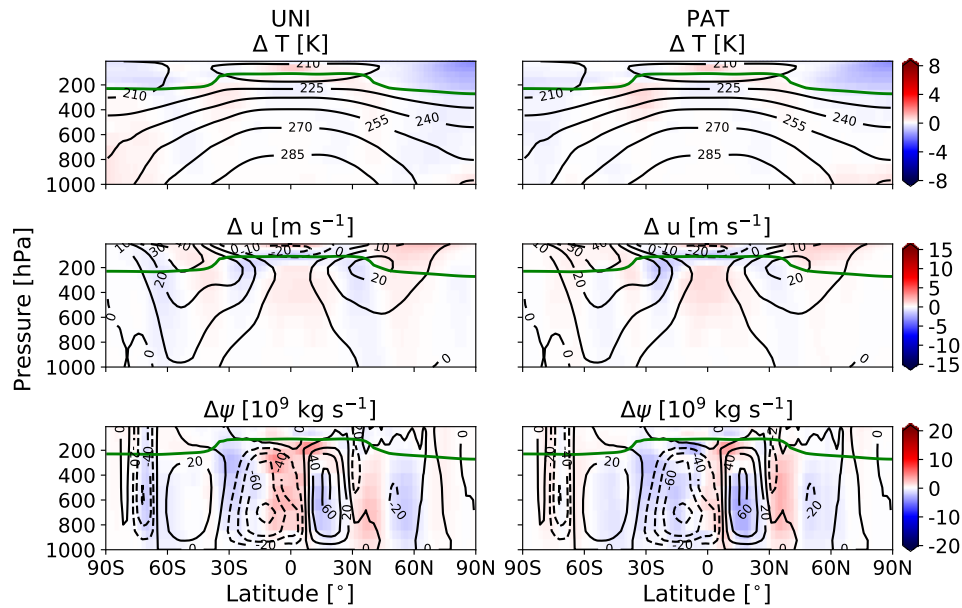
Figure 4.3.: Difference between the annual-mean zonal-mean global warming response in the simulations with locked clouds and the simulations with free clouds. Shown are the differences in the response for atmospheric temperature (top), zonal wind (center), and mass stream function (bottom) to a uniform (UNI, left) and spatially varying (PAT, right) SST increase. The colorbar limits are the same as in Figs. 3.5 and 3.6 for easier assessment of the small residual. The green line in each panel shows the tropopause height in the control simulation CTL. Figure adapted from Albern et al. (2019). ©The Authors.

While the zonal-mean circulation and jet stream responses to global warming in the North Pacific and Southern Hemisphere are similar in the simulations with free and locked clouds, larger differences occur for the jet response over the North Atlantic in the annual mean and during boreal winter (DJF) and spring (MAM) (Fig. 4.4). During these seasons, the North Atlantic jet stream of the control simulation is located more equatorward for locked clouds than for free clouds. This is possibly related to decreased convective activity over the Maritime Continent and western tropical Pacific when clouds are locked, as indicated by increased outgoing longwave radiation and decreased high-level cloud cover (not shown; e.g., Cassou, 2008; Henderson et al., 2016). At the same time, the North Atlantic jet stream of the UNI and PAT simulations is located more poleward when clouds are locked. This is possibly related to enhanced warming of North America in the simulations with locked clouds (not shown; Ceppi et al., 2018). As a result, in these seasons, the North Atlantic jet shift in the locked simulations is larger than in the free simulations and larger than what is commonly simulated by coupled climate models. However, we are mainly interested in quantifying the impact of cloud-radiative changes in relation to the total (locked) response. Also, the magnitude of the cloud-radiative impact appears to be less sensitive to the jet position in the control simulation. This can be seen by comparing the cloud-radiative impact for each ocean basin across seasons (cf. section 5.2). Although the seasons differ with respect to the control
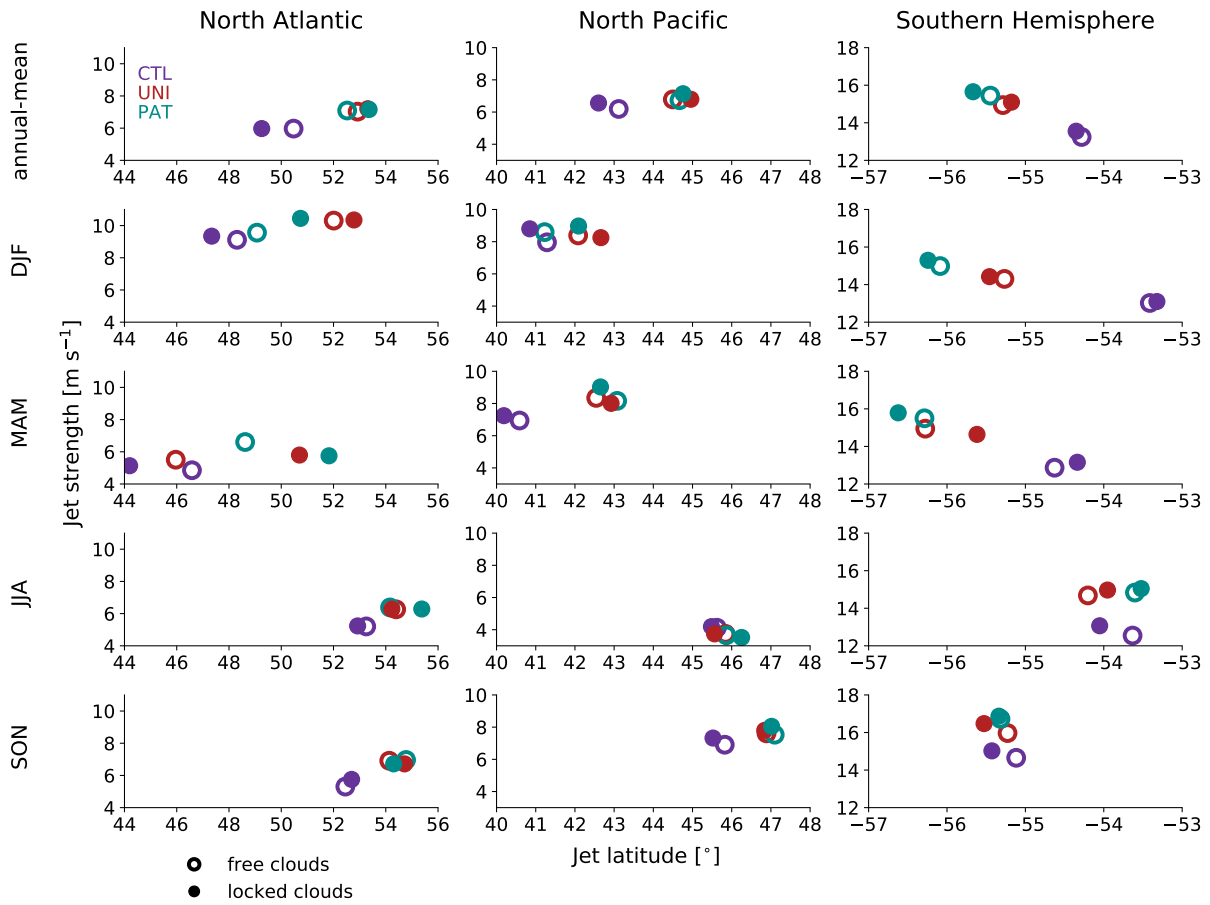
Figure 4.4.: Ocean basin zonal-mean jet latitude versus jet strength for simulations with free clouds and simulations with locked clouds for the North Atlantic (left), North Pacific (middle) and Southern Hemisphere (right). Results are shown for the annual-mean (first row), and the four seasons (second to fifth rows). Reprinted from Albern et al. (2019). ©The Authors.

jet position (Fig. 4.4), the cloud-radiative impact is similar across seasons, especially in the Northern Hemisphere (cf. section 5.2 for a more detailed discussion of the results).

The residual between the jet responses in the simulations with free and locked clouds can either be caused by internal variability or by the decorrelation due to the application of the cloud-locking method. To check that the difference between the simulations is a result of the large internal variability and to verify that the zonal-mean jet stream responses with free and locked clouds are statistically similar, we analyze their difference for the annual mean and each season. To this end, we calculate the bootstrap distributions for the difference between the jet responses in the simulations with free and locked clouds.

For each region, the bootstrap distributions are obtained as follows: In the first step, we perform a sampling with replacement based on the time series of the annual-mean or seasonal-mean zonal-mean u_{850} profile. The resample has the same size as the original time series (i.e., 29 years for simulations with locked clouds, 30 years for simulations with free clouds). In the next step, we calculate the mean

over the resample time series to obtain a new time-mean u_{850} profile from which the jet latitude and jet strength are derived. We perform these two steps for the simulations with free and locked clouds and for both the control and global warming simulations. In the last step, we calculate the jet stream responses in the simulations with free and locked clouds, respectively, and subtract the two responses from each other. This whole procedure is done 1000 times to get a bootstrap distribution of the jet response differences in the free and locked simulations. We consider the jet stream response in the locked simulation to be statistically the same as in the free simulation on a 95% significance level, if the 2.5th-to-97.5th percentile range, referred to as 95% percentile, includes a difference of $0°$ and $0\,\mathrm{m\,s^{-1}}$, respectively.

Fig. 4.5 shows the North Atlantic jet latitude response during MAM and SON for the response to a uniform SST increase. For MAM, the mean difference between the responses based on the bootstrap distribution is about -7.5° and the 95% percentile ranges from about -13.5° to -2.5°. Thus, the 95% percentile does not include the difference of $0°$ and the responses in the free and locked simulations are not statistically similar. In SON, however, the mean difference between the two responses is about -0.1° and the 95% percentile ranges from about -3.5° to 4°. Thus, the responses are statistically similar on a 95% significance level. The width of the distribution points to the large internal variability in our simulations.

Fig. 4.6 shows the mean difference between the jet responses in the free and locked simulations for both global warming setups in each season for the North Atlantic, North Pacific and Southern Hemisphere. In the North Pacific and Southern Hemisphere, the jet latitude and jet strength responses are statistically similar on a 95% significance level and close to zero during most seasons. In the North Atlantic, however, large differences between the jet latitude response in the free and locked simulations occur in the annual mean, DJF, and MAM. The largest differences are present in MAM, pointing to a
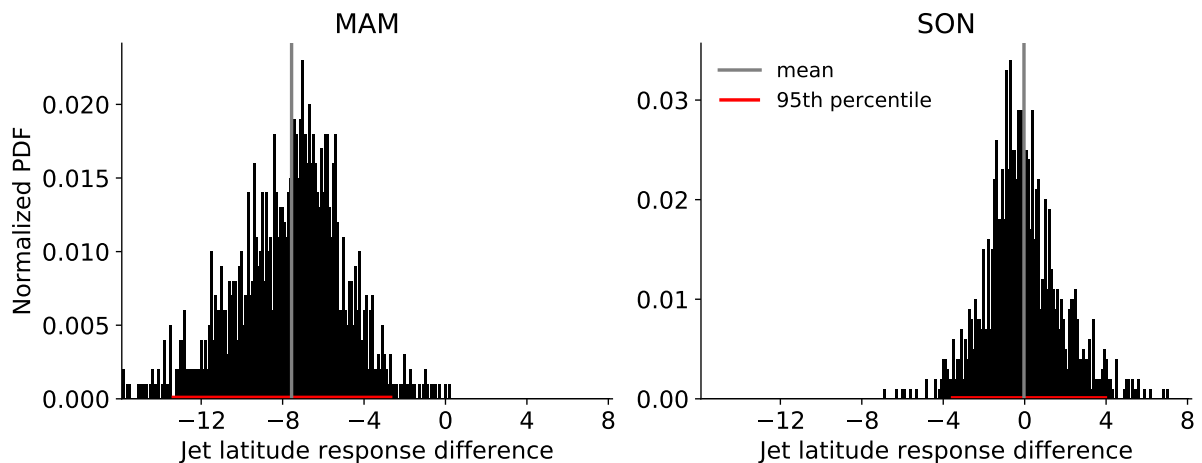
Figure 4.5.: Normalized Probability Density Function of the difference in the jet latitude response between simulations with free and locked clouds based on bootstrapping in the North Atlantic in response to UNI. Results are shown for MAM (left) and SON (right). Reprinted from Albern et al. (2019). ©The Authors.
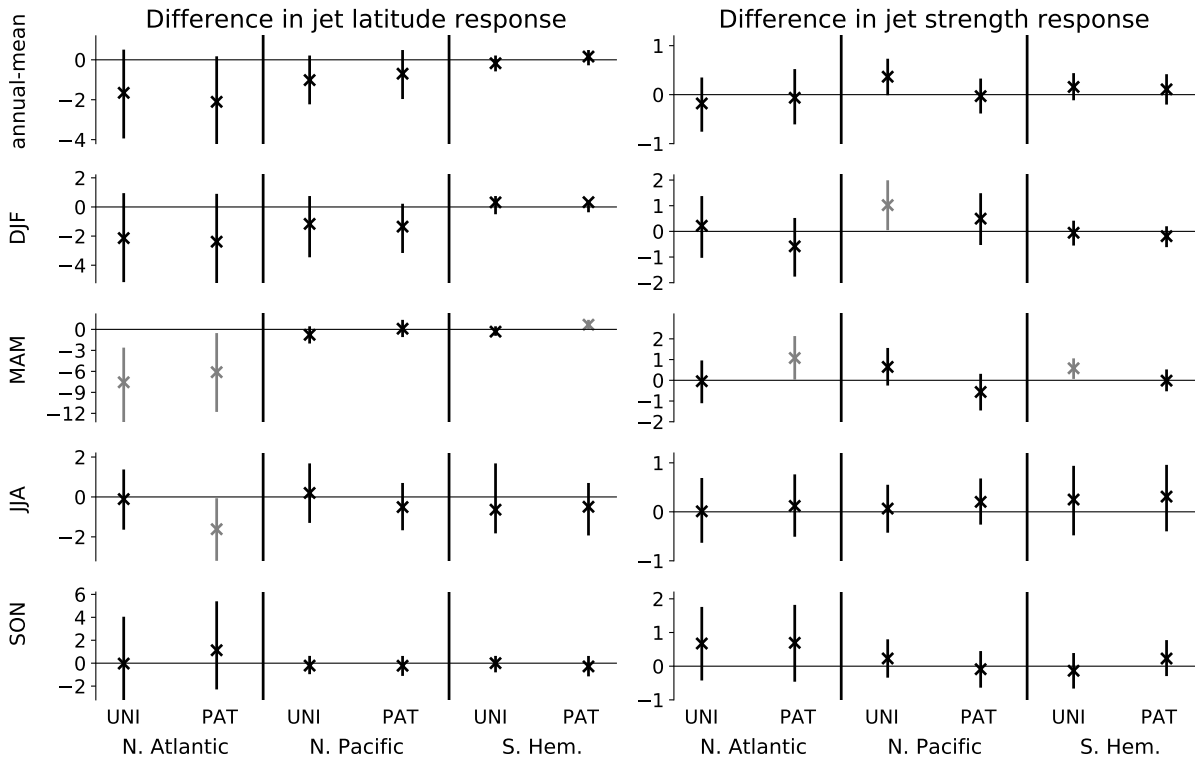
Figure 4.6.: Mean (crosses) and 95% significance level (vertical lines) for the difference in the jet latitude (left) and jet strength (right) responses between simulations with free clouds and simulations with locked clouds. Results are shown for each season, ocean basin, and global warming setup. Black symbols indicate that the responses in simulations with locked and free clouds are statistically similar; gray symbols indicate that they are not statistically similar on a 95% level. Note the different ranges for the vertical axes of the panels. Reprinted from Albern et al. (2019). ©The Authors.

decorrelation effect due to the application of the cloud-locking method in this season. Thus, the results for the jet latitude response in MAM should be interpreted with caution.

We have shown that the residual between the jet responses in the simulations with free and locked clouds is small and that the jet response in the simulations with free and locked clouds are statistically similar during most seasons and ocean basins. In chapters 5-7, we will show the results for the simulations with locked clouds, so that the SST impact and global cloud-radiative impact sum up to the total response.

4.3.2. Regional Cloud-Radiative Impact

In addition to the impact of global cloud-radiative changes, we study the impact of regional cloud-radiative changes. To this end, we perform additional simulations based on the cloud-radiative properties from the control simulation and from the global warming simulation with a uniform SST increase. We begin with the impact of tropical (30°S-30°N, all longitudes), midlatitude (30°N-60°N and 30°S-60°S, all

longitudes) and polar (poleward of 60°N/S, all longitudes) cloud-radiative changes in chapter 6 (Fig. 4.7, top row). In chapter 7, we further study the impacts of cloud-radiative changes in smaller tropical regions and over a North Atlantic-European region (30°N-60°N, 90°W-30°E). For the smaller tropical regions, we study the impact of cloud-radiative changes over the Indian Ocean and tropical Pacific (30°S-30°N, 40°E-70°W) as well as of cloud-radiative changes over the tropical Atlantic (30°S-30°N, 70°W-40°E), Indian Ocean (30°S-30°N, 40°E-120°E), western tropical Pacific (30°S-30°N, 120°E-150°W), and eastern tropical Pacific (30°S-30°N, 150°W-70°W) (Fig. 4.7, second and third rows).

To determine the impact of tropical cloud-radiative changes, we perform four additional simulations to the ones described in section 4.3.1. In the first simulation, we prescribe the cloud-radiative properties in the tropics to the values from the global warming simulation and in the midlatitudes and polar regions to the values from the control simulation. In the second simulation, we prescribe cloud-radiative properties from the control simulation in the tropics, and from the global warming simulation in the midlatitudes and polar regions. These two simulations are once performed with SST from the control simulation and once with +4 K SST. We run each simulation for 30 years and exclude the first year to avoid possible effects from model initialization. To determine the impact of cloud-radiative changes in the midlatitudes and polar regions, we perform two analogous sets of simulations. To limit the number
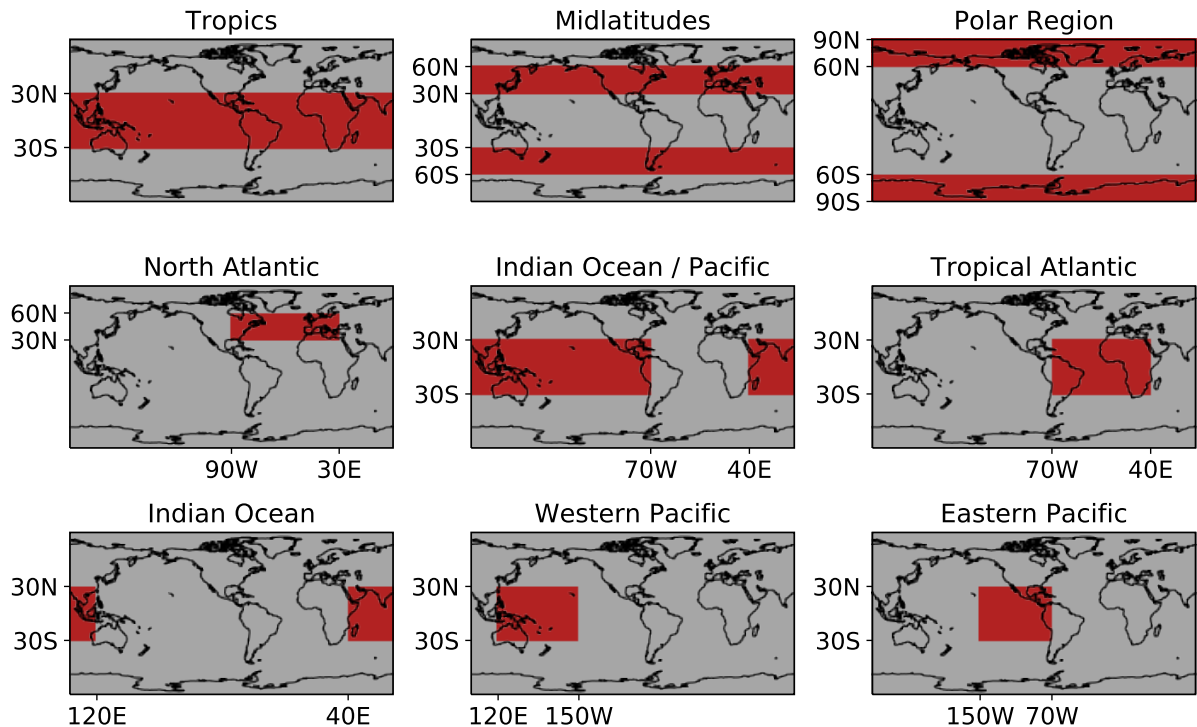
Figure 4.7.: Regions for which the regional cloud-radiative impact is determined in chapters 6 and 7. The lateral and longitudinal boundaries of each region are given by the labels of the respective map. Top row adapted from Albern et al. (2020). ©American Meteorological Society. Used with permission.

of required simulations, we change the cloud-radiative properties simultaneously in the Northern and Southern Hemisphere. For both the midlatitude and the polar cloud-radiative changes, we have tested that the circulation response in the Northern (Southern) Hemisphere is largely due to cloud-radiative changes in the Northern (Southern) Hemisphere. Interhemispheric teleconnections occur (Ceppi et al., 2013), but they are small in our simulations (not shown). Analogously, 4 simulations are performed for each of the smaller tropical regions and for the North Atlantic-European region.

Based on the above simulations, the impact of regional cloud-radiative changes is given by

$$
\begin{aligned}
\Delta X_{\text{clouds, reg}} = \frac{1}{4}[&(X_{\text{T1C}_a\text{2C}_b\text{1}} - X_{\text{T1C}_a\text{1C}_b\text{1}}) + (X_{\text{T1C}_a\text{2C}_b\text{2}} - X_{\text{T1C}_a\text{1C}_b\text{2}}) \\
&+ (X_{\text{T2C}_a\text{2C}_b\text{1}} - X_{\text{T2C}_a\text{1C}_b\text{1}}) + (X_{\text{T2C}_a\text{2C}_b\text{2}} - X_{\text{T2C}_a\text{1C}_b\text{2}})].
\end{aligned}
\tag{4.6}
$$

The subscript *a* denotes the region for which the regional cloud-radiative impact is calculated (e.g., the tropics). The subscript *b* refers to the other regions (e.g., midlatitudes and polar region). The cloud-radiative properties in the regions of *b* are prescribed to the same climate state. We refer to the regional cloud impacts as the tropical cloud impact (cloud TR), the midlatitude cloud impact (cloud ML), the polar cloud impact (cloud PO), the Indian Ocean and Pacific cloud impact (cloud IOWPEP), the Indian Ocean cloud impact (cloud IO), the western tropical Pacific cloud impact (cloud WP), the eastern tropical Pacific cloud impact (cloud EP), the tropical Atlantic cloud impact (cloud TA), and the North Atlantic cloud impact (cloud NA).

By construction, the SST impact and the global cloud-radiative impact sum up to the total locked response (cf. section 4.3.1). In contrast, the impacts from the regional cloud changes do not sum up to the global cloud-radiative impact, because Eq. 4.6 does not sample all possible combinations of cloud-radiative properties in the different regions. For example, the cloud-radiative properties in the regions of *b* are prescribed to the same climate state. Nevertheless, the sum of the tropical, midlatitude and polar cloud-radiative impacts on any variable exhibits a similar structure as the global cloud-radiative impact, and the magnitude of the difference is typically below 10%. This is shown for the cloud impact on the global warming response of the zonal wind at 850 hPa, u_{850}, in Fig. 4.8. Similarly, the cloud impact for the sum of the smaller tropical regions is similar to the tropical cloud-radiative impact (cf. chapter 7). This result is consistent with the finding of Butler et al. (2010) that the response to the sum of multiple thermal forcings is larger than the response to the simultaneously applied thermal forcings. In our simulations, the non-linearity is additionally increased by possible gradients in the cloud-radiative property fields at the borders of the cloud regions.

4.3.3. Cloud-Radiative Impact from Cloud- and Water Vapor-Locking

In Chapter 7, we compare the cloud-locking simulations of ICON with a uniform SST increase to cloud- and water vapor-locking simulations from ICON and from the atmospheric components of the CMIP5 models MPI-ESM-LR (Giorgetta et al., 2013; Stevens et al., 2013) and IPSL-CM5A-LR (Dufresne et al.,
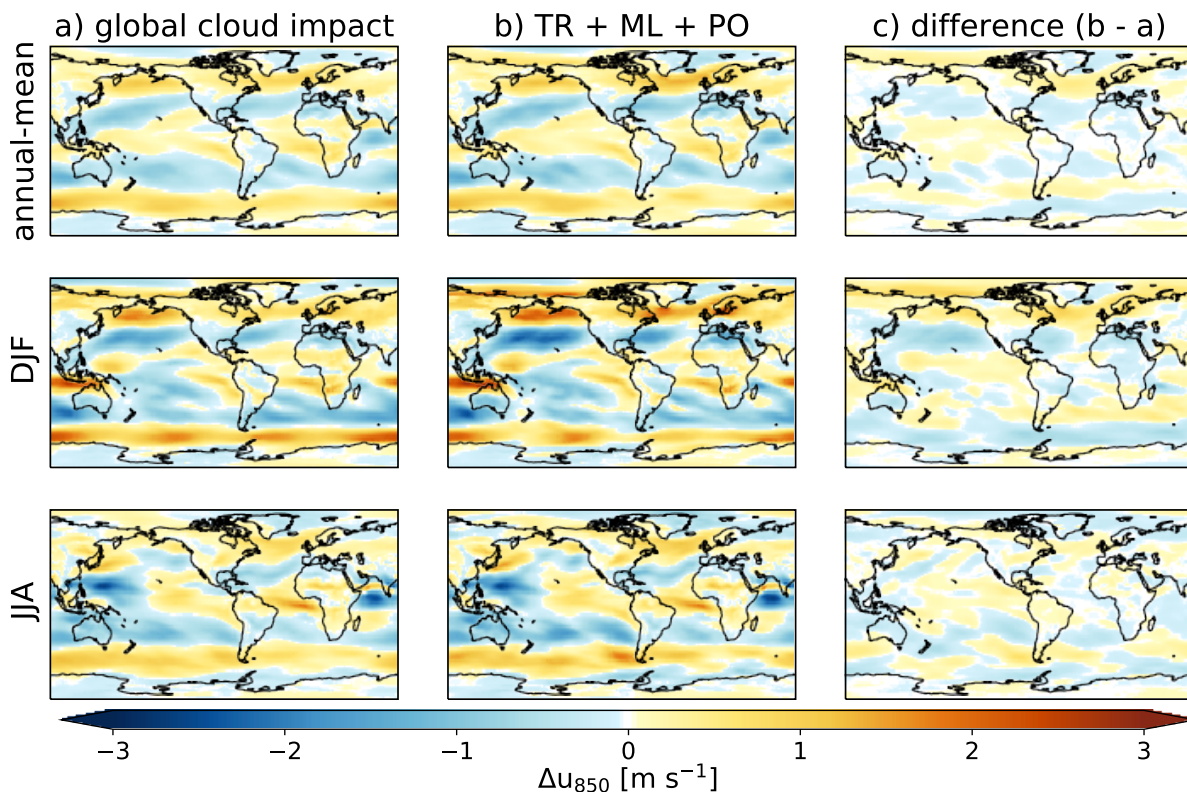
Figure 4.8.: Annual-mean, DJF and JJA response of zonal wind at 850 hPa to global cloud-radiative changes (left) and to the sum of tropical, midlatitude and polar cloud-radiative changes (center). The right column shows the difference. Reprinted from Albern et al. (2020). ©American Meteorological Society. Used with permission.

2013). Hereafter, we omit the "LR" in both model names. The cloud- and water vapor-locking simulations are taken from Voigt et al. (2019), where the details of the model setups are given. Similar to our ICON simulations, the simulations from Voigt et al. (2019) are performed with continents, prescribed present-day sea ice cover and prescribed climatological SST. Global warming is mimicked by a uniform 4 K SST increase.

By prescribing cloud-radiative properties and water vapor-radiative properties in the simulations, the cloud- and water vapor-locking method allows to decompose the total circulation response into contributions from cloud-radiative changes, from water vapor-radiative changes, and from the SST increase (e.g., Voigt and Shaw, 2015). The cloud- and water vapor-locking is performed similarly to the cloud-locking. First, control and global warming simulations with interactive clouds and water vapor are performed, and the cloud- and water vapor-radiative properties are stored at every call of the radiation scheme. In the next step, eight simulations with all possible combinations of SST and prescribed cloud- and water

vapor-radiative properties are performed. The cloud-radiative impact is diagnosed as (e.g., Voigt and Shaw, 2015; Voigt et al., 2019)

$$\Delta X_{\text{clouds}} = \frac{1}{4}[(X_{\text{T1C2W1}} - X_{\text{T1C1W1}}) + (X_{\text{T1C2W2}} - X_{\text{T1C1W2}})$$
$$+ (X_{\text{T2C2W1}} - X_{\text{T2C1W1}}) + (X_{\text{T2C2W2}} - X_{\text{T2C1W2}})], \tag{4.7}$$

where T, C and W denote the SST, the cloud-radiative properties and the water vapor-radiative properties, respectively. The numbers indicate whether T, C and W are prescribed to values from the control simulation (simulation 1) or from the global warming simulation (simulation 2). The water vapor-radiative impact ΔX_{vap} is diagnosed analogously to the cloud-radiative impact.

The SST impact is given by

$$\Delta X_{\text{SST}} = \frac{1}{2}[(X_{\text{T2C1W1}} - X_{\text{T1C1W1}}) + (X_{\text{T2C2W2}} - X_{\text{T1C2W2}})]. \tag{4.8}$$

By construction, the cloud-radiative impact, the water vapor-radiative impact and the SST impact sum up to the total locked response

$$\Delta X_{\text{lock,cloud,vap}} = X_{\text{T2C2W2}} - X_{\text{T1C1W1}} = \Delta X_{\text{cloud}} + \Delta X_{\text{vap}} + \Delta X_{\text{SST}}. \tag{4.9}$$

Fig. 4.9 contrasts the DJF 850 hPa zonal wind response in ICON with locked clouds to the response with locked clouds and locked water vapor. We show the DJF response because we focus on this season in chapter 7. Overall, the total response, the SST impact and the cloud-radiative impact agree well for the two setups. In particular, the differences between the cloud-radiative impacts from both setups are small. This result agrees well with the finding of Voigt and Albern (2019) that the cloud-radiative impact is largely independent of how water vapor is treated. Note that for the cloud-radiative impact, differences of more than $1\,\text{m\,s}^{-1}$ occur over the Maritime Continent. The cloud-radiative impact on the u_{850} response over this region is larger when water vapor is interactive than when it is locked. When water vapor is locked, most of the u_{850} response over the Maritime Continent can be attributed to the water vapor-radiative impact. The differences in the cloud-radiative impact over this highly convective region are probably related to the spatiotemporal decoupling of clouds and water vapor when both fields are locked, so that clouds are not necessarily located in the moist regions anymore.

4.4. Partial-Radiative Perturbation Calculation

We implemented a module for an online forward Partial-Radiative Perturbation (PRP) calculation in ICON. The PRP calculation was originally used to diagnose individual radiative feedbacks of, for example, temperature, clouds, water vapor and surface albedo (e.g., Wetherald and Manabe, 1988; Colman and McAvaney, 1997; Colman, 2003; Soden and Held, 2006; Klocke et al., 2013; Mauritsen et al., 2013; Geoffroy et al., 2014). More recently, it has become a tool to study the change in cloud-radiative heating
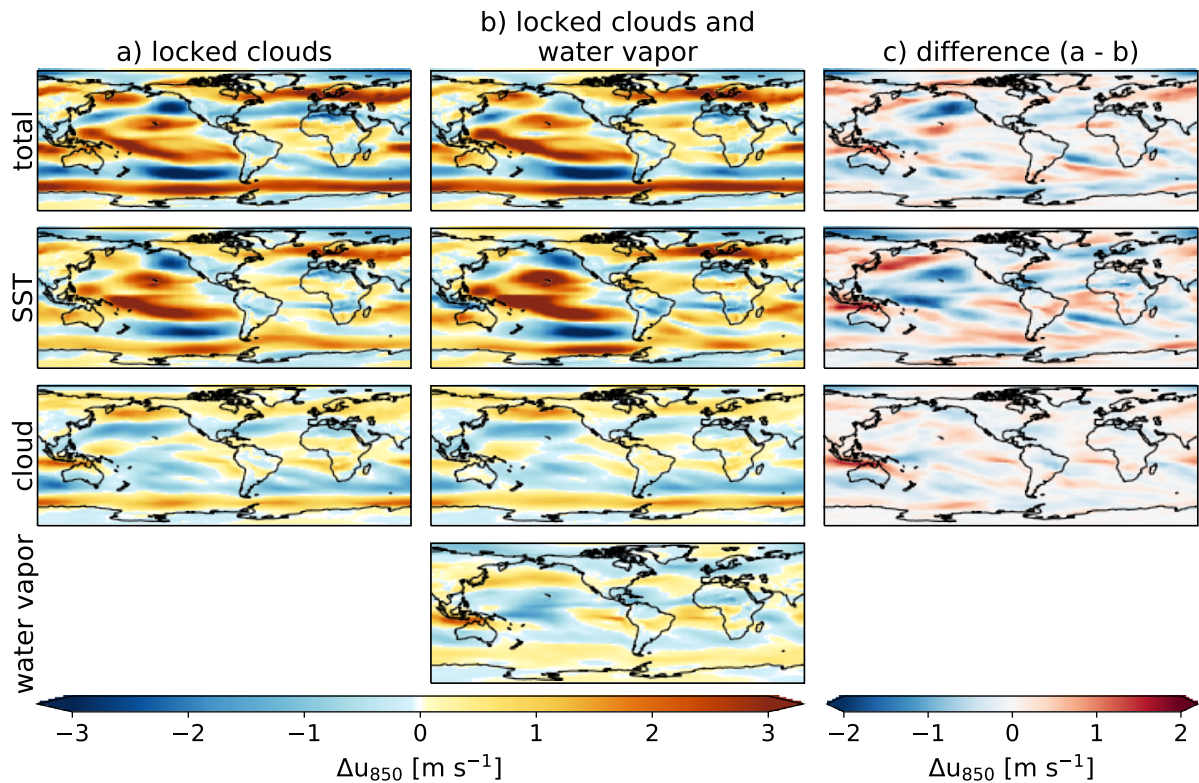
Figure 4.9.: Zonal wind response at $850\,hPa$ to a uniform $4\,K$ SST increase in ICON during DJF. (a) The total response is decomposed into SST impact and cloud impact using the cloud-locking method. (b) The total response is decomposed into SST impact, cloud impact and water vapor impact using the cloud- and water vapor-locking method. (c) Difference between (a) and (b).

in response to global warming to better understand the impact of cloud-radiative changes on the global warming response of the midlatitude circulation (Voigt and Shaw, 2016; Voigt et al., 2019).

The implemented module in ICON allows to diagnose the change in atmospheric temperature tendencies between the control and global warming simulations due to changes in i) cloud-radiative properties (cloud cover, cloud water and cloud ice); ii) water vapor-radiative properties (specific humidity); and iii) both cloud-radiative properties and water vapor-radiative properties. In this thesis, we focus on the atmospheric temperature tendencies which are due to changes in cloud-radiative properties, i.e., we study the change in atmospheric cloud-radiative heating and its impact on the midlatitude circulation response to global warming.

The change in atmospheric cloud-radiative heating is diagnosed by contrasting the temperature tendencies from the control simulation to those from a simulation in which $4\,K$ clouds are inserted into the control climate, i.e., by contrasting temperature tendencies from the T1C1 simulation to the T1C2 or T1C3 simulation described in section 4.3. Thus, a double call of the radiation scheme is required.

The atmospheric cloud-radiative heating $\partial T/\partial t$ is given by

$$\left.\frac{\partial T(\varphi, \vartheta, p)}{\partial t}\right|_{\text{PRP}} = R(T_{\text{CTL}}, q_{\text{CTL}}, c_{4\text{K}}) - R(T_{\text{CTL}}, q_{\text{CTL}}, c_{\text{CTL}}), \tag{4.10}$$

where R is the atmospheric temperature tendency calculated by the model's radiation scheme and T, q, and c are atmospheric temperature, specific humidity, and cloud-radiative properties at latitude φ, longitude ϑ, and pressure p. The subscripts CTL and 4K indicate whether the variables are taken from the control and global-warming simulations, respectively. This PRP calculation is referred to as forward PRP calculation (Wetherald and Manabe, 1988; Voigt and Shaw, 2016). In contrast, a backward PRP calculation compares the temperature tendencies from the global warming simulation and those from a simulation in which control-climate clouds are inserted into the global-warming climate, i.e., by contrasting temperature tendencies from the T2C2 and T2C1 simulations.

Note that in hydrostatic models the vertical change of the radiative flux is converted into a temperature tendency based on the specific heat capacity at constant pressure c_p (Peixoto and Oort, 1992):

$$\left.\frac{\partial T(\varphi, \vartheta, p)}{\partial t}\right|_{\text{rad}} = \frac{1}{c_p \rho}\frac{\partial F}{\partial z} = -\frac{g}{c_p}\frac{\partial F}{\partial p}, \tag{4.11}$$

where T is atmospheric temperature, t is time, φ is latitude, ϑ is longitude, p is atmospheric pressure, ρ is air density, F is the net radiative flux, z is the altitude above ground, and g the gravitational acceleration. The hydrostatic approximation $\partial p/\partial z = -\rho g$ was used to get from height coordinates to pressure coordinates.

In ICON, however, the vertical change of the radiative flux is converted into temperature tendencies using the specific heat capacity at constant volume c_v:

$$\left.\frac{\partial T(\varphi, \vartheta, p)}{\partial t}\right|_{\text{rad}} = \frac{1}{m_{air} \cdot (c_{v,d} + (c_{v,v} - c_{v,d}) \cdot pqv)}\frac{\partial F}{\partial z}. \tag{4.12}$$

Here, m_{air} is the mass of the air in the column, $c_{v,d}$ and $c_{v,v}$ are the specific heat capacities at constant volume for dry and moist air, respectively, and pqv is the specific humidity at the last time step. The specific heat capacity at constant volume is used in ICON because the total air density ρ is one of the model's prognostic variables. Thus, the physics-dynamics coupling is performed at constant density/volume and not at constant pressure to keep ρ constant in the physics-dynamics interface (Zängl et al., 2015).

We perform forward PRP calculations for both the UNI and PAT simulations with locked clouds, and determine the change in cloud-radiative heating (Eq. 4.10) for every grid point at every call of the radiation scheme (every 36 minutes) for a 5-year period. The changes in cloud-radiative heating will be discussed in chapters 5-7 to improve understanding of the impact of cloud-radiative changes on the midlatitude circulation response to global warming.

5. The Impact of Global Cloud-Radiative Changes on the Midlatitude Circulation Response to Global Warming

In this chapter, we address research question 1 "How large is the impact of global cloud-radiative changes on the midlatitude circulation response to global warming in a present-day simulation setup?". To this end, we answer the following more detailed sub-questions:

1. How important is the cloud-radiative impact for the midlatitude jet stream and storm track responses to global warming in the North Atlantic, North Pacific, and Southern Hemisphere ocean?

2. To what extent does the cloud-radiative impact vary across seasons and ocean basins?

3. Does the cloud-radiative impact depend on the pattern of the SST increase?

The structure of this chapter is as follows: We begin this chapter with the annual-mean jet stream and storm track responses to global warming in section 5.1. The seasonal-mean responses are discussed in section 5.2. In section 5.3, we show correlations between the jet stream and atmospheric temperature gradients. The main results are summarized and discussed in section 5.4.

With some minor adjustments in the text, this chapter is based on Albern et al. (2019). ©The Authors.

5.1. Annual-Mean Circulation Response

In this section, we study the annual-mean response of the midlatitude circulation in the UNI and PAT simulations based on the total response in the prescribed-clouds setup and the decomposition of the response into a cloud-radiative impact and an SST impact. The zonal wind at 850 hPa and the storm tracks undergo significant changes in response to both a uniform (Figs. 5.1a and 5.1d) and a patterned SST increase (Figs. 5.2a and 5.2d). For the zonal wind shown in the left panels of Figs. 5.1 and 5.2, the black lines indicate the control jet latitude. In the right panels, the gray contours show the storm track in the control simulation. Statistical significance of the responses is indicated by dots and is calculated with a two-sided t test for two samples and using a p value of 0.05 (95% confidence interval).

We have verified that the annual-mean total responses in UNI and PAT are in line with the robust responses in the CMIP5 Amip4K and AmipFuture simulations (Figs. A.1 and A.2, top rows; Grise and Polvani, 2014b). Differences to the robust annual-mean responses in the CMIP5 models occur mainly in the eastern North Pacific where ICON shows a poleward jet shift, whereas the CMIP5 models show a weakening of the jet, and in the Southern Hemisphere east of South America (in UNI) where ICON shows a jet strengthening and the CMIP5 models show a poleward shift. These differences result in a
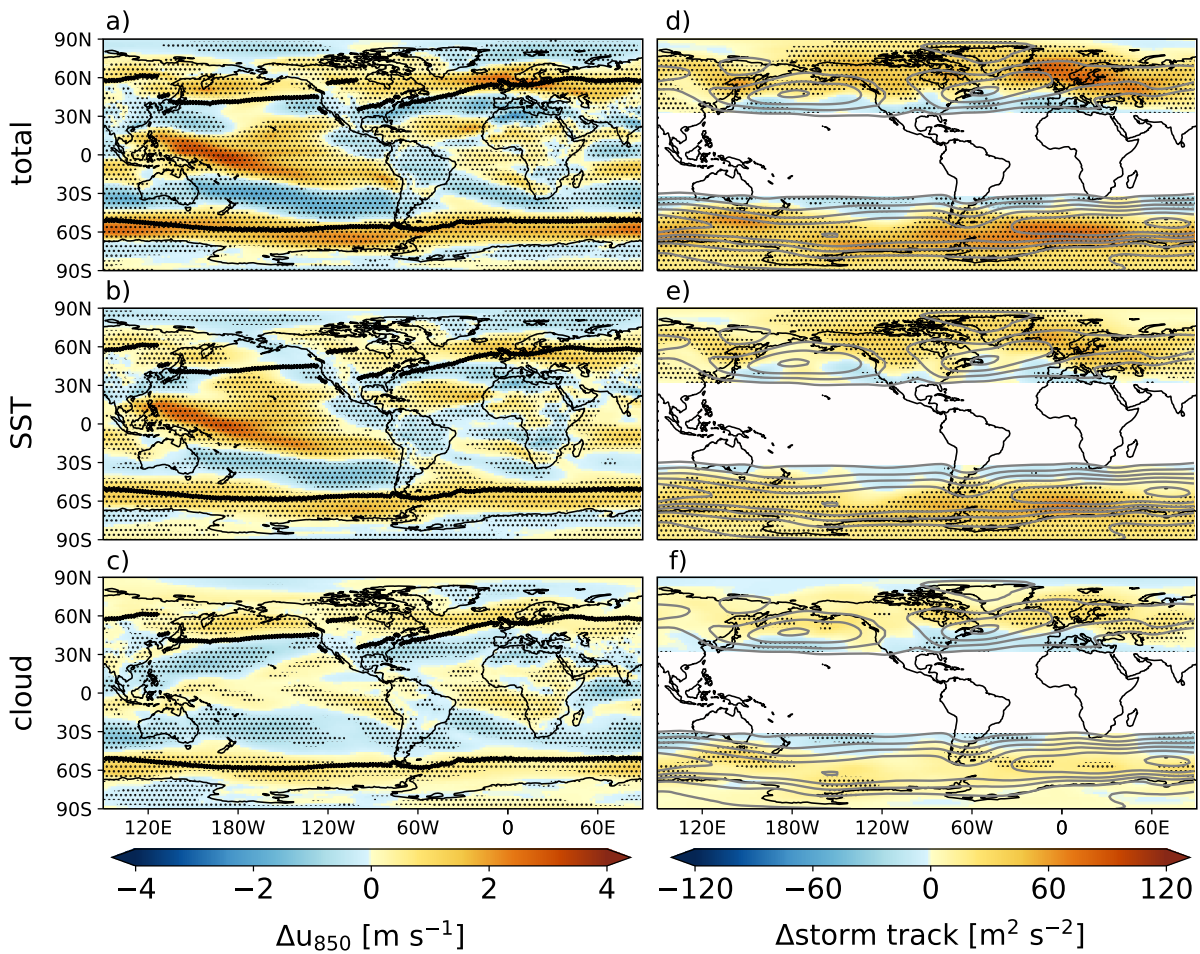
Figure 5.1.: Annual-mean response of the 850-hPa zonal wind, u_{850}, (left) and storm track (right) in the UNI simulations. The total response (a, d) is decomposed into the SST impact (b, e) and the cloud-radiative impact (c, f). The black line in the left column indicates the jet latitude in the control simulation; the gray contours in the right column show the storm track in the control simulation (contour interval of $100\,\mathrm{m^2\,s^{-2}}$). For the storm track, the Tropics are not shown. The dots indicate where the response is significant at 95% level. Reprinted from Albern et al. (2019). ©The Authors.

slightly overestimated annual-mean poleward jet shift in the North Pacific and reduced poleward jet shift in the Southern Hemisphere in both global warming setups (Figs. A.3 and A.4; top rows).

Fig. 5.1a shows the total response in the UNI simulations. In the North Pacific, changes in u_{850} indicate a poleward jet shift in the western and eastern parts of the ocean basin and a strengthening in the central part. In the North Atlantic, the wind response is more zonal, with a poleward jet shift across the ocean basin and a strengthening in the jet exit region over Europe. In the Southern Hemisphere, the jet exhibits a poleward shift at most longitudes and a strengthening south of Australia and southeast of South America.
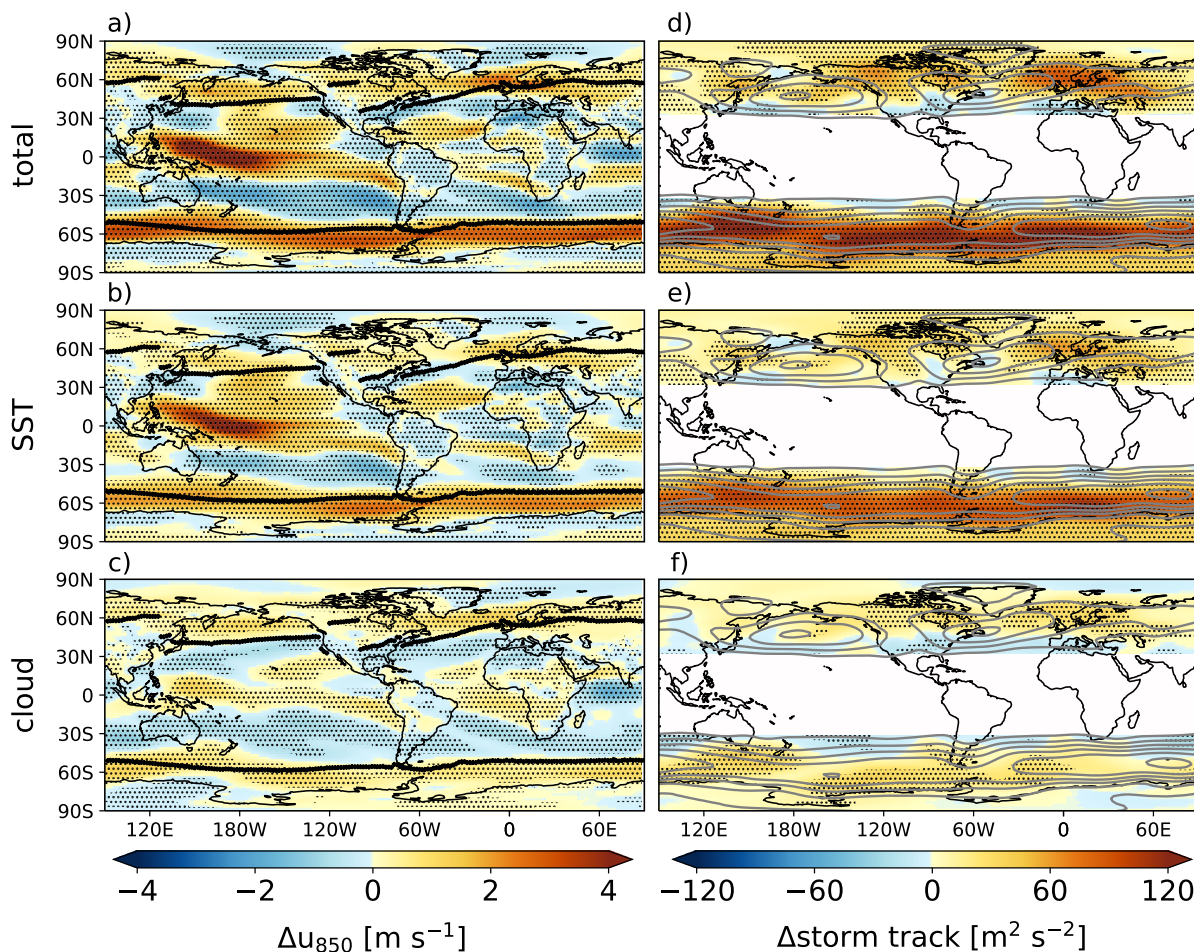
Figure 5.2.: Same as Figure 5.1 but for the PAT simulations. Reprinted from Albern et al. (2019). ©The Authors.

Decomposing the total response into SST and cloud-radiative impacts reveals that in all three ocean basins, a substantial part of the midlatitude zonal wind response, and hence jet shift, is attributed to the cloud-radiative impact (Fig. 5.1c). Remarkably, the cloud-radiative impact is almost zonally symmetric in all three ocean basins. In contrast, the SST impact is much more zonally asymmetric (Fig. 5.1b). For example, the jet strengthening over Europe results from the SST impact.

The total storm track response is in line with the total u_{850} response (Fig. 5.1d). The storm track exhibits a poleward shift in the North Pacific and a poleward shift in the North Atlantic with a strengthening in the exit region over Europe. In the Southern Hemisphere, the storm track strengthens at most longitudes, with decreased storm activity on its equatorward flank. This total storm track response is consistent with Ulbrich et al. (2009). As for u_{850}, the cloud-radiative impact is nearly zonally symmetric in all three ocean basins (Fig. 5.1f). The cloud-radiative impact dominates the poleward storm track shift in the North Pacific and is strong in the North Atlantic and over Europe. As for u_{850}, the SST impact on the storm track response shows a more complicated spatial structure (Fig. 5.1e).

53

Fig. 5.2 shows the analogous responses in the PAT simulations. Using a patterned instead of a uniform SST increase leads to a somewhat larger total response and SST impact in the North Pacific and Southern Hemisphere for both the u_{850} and storm track responses (also see Fig. A.5). In the North Atlantic, the total response and SST impact are slightly reduced for u_{850} and increased in the exit region of the storm track. The cloud-radiative impact on the zonal wind and storm track responses, in contrast, is very similar between the PAT and UNI simulations in all ocean basins.

To allow for a more quantitative analysis, we quantify the response of the jet latitude and jet strength by calculating the zonal-mean u_{850} response over the three ocean basins, using the longitudinal sectors given in section 4.1. Fig. 5.3 shows the ocean-basin zonal-mean u_{850} response and the associated poleward jet shift and jet strengthening. u_{850} of CTL is shown in small insets for reference. The u_{850} response shows a dipole pattern around the control jet latitude (gray bars in Fig. 5.3, left), with a less pronounced dipole in the North Pacific than in the other two ocean basins. The dipole pattern is found for the total response, the SST impact, and the cloud-radiative impact and is consistent with a poleward jet shift in all three ocean basins and a jet strengthening in the North Atlantic and Southern Hemisphere (Fig. 5.3, right). In the North Atlantic and Southern Hemisphere, an almost linear relationship between the poleward jet shift and the jet strengthening is found.

The cloud-radiative impact on the jet response, measured in absolute values, is very similar in UNI and PAT. This shows that in all three ocean basins, the cloud-radiative impact is largely independent of the spatial pattern of SST increase. At the same time, the relative importance of the cloud-radiative impact is modulated by the pattern of SST increase in the Southern Hemisphere. In the Southern Hemisphere, the cloud-radiative impact contributes more than one third to the jet response in UNI but less than one third in PAT. This results from a stronger total response and stronger SST impact in PAT compared to UNI, consistent with increased SST gradients (cf. Fig. 3.1). In the North Pacific, the jet strengthening is slightly enhanced in PAT compared to UNI. At the same time, the pattern of SST increase has little or no impact on the jet strength response in the North Atlantic and on the jet latitude response in both ocean basins. In both ocean basins, about half to two thirds of the poleward jet shift can be attributed to the cloud-radiative impact for UNI and PAT. In addition, the cloud-radiative impact contributes half to the jet strengthening in the North Atlantic for both UNI and PAT.

The above analysis shows that cloud-radiative changes contribute substantially to the circulation response independent of the pattern of surface warming and that the cloud-radiative impact is nearly zonally symmetric. To understand this, Fig. 5.4 shows cloud cover changes and changes in cloud-radiative heating in the UNI and PAT simulations. The cloud cover changes and cloud-radiative heating changes are consistent with the vertical expansion of the troposphere and poleward expansion of the Tropics shown in Figs. 3.5 and 3.6 and with the fixed anvil temperature hypothesis, which states that high-level clouds rise in response to increased tropospheric temperatures to maintain their cloud-top temperature (Hartmann and Larson, 2002; Thompson et al., 2017). With high-level clouds warming at their base and cooling at their top (see also Slingo and Slingo, 1988; Li and Thompson, 2016), the cloud rise leads to posi-
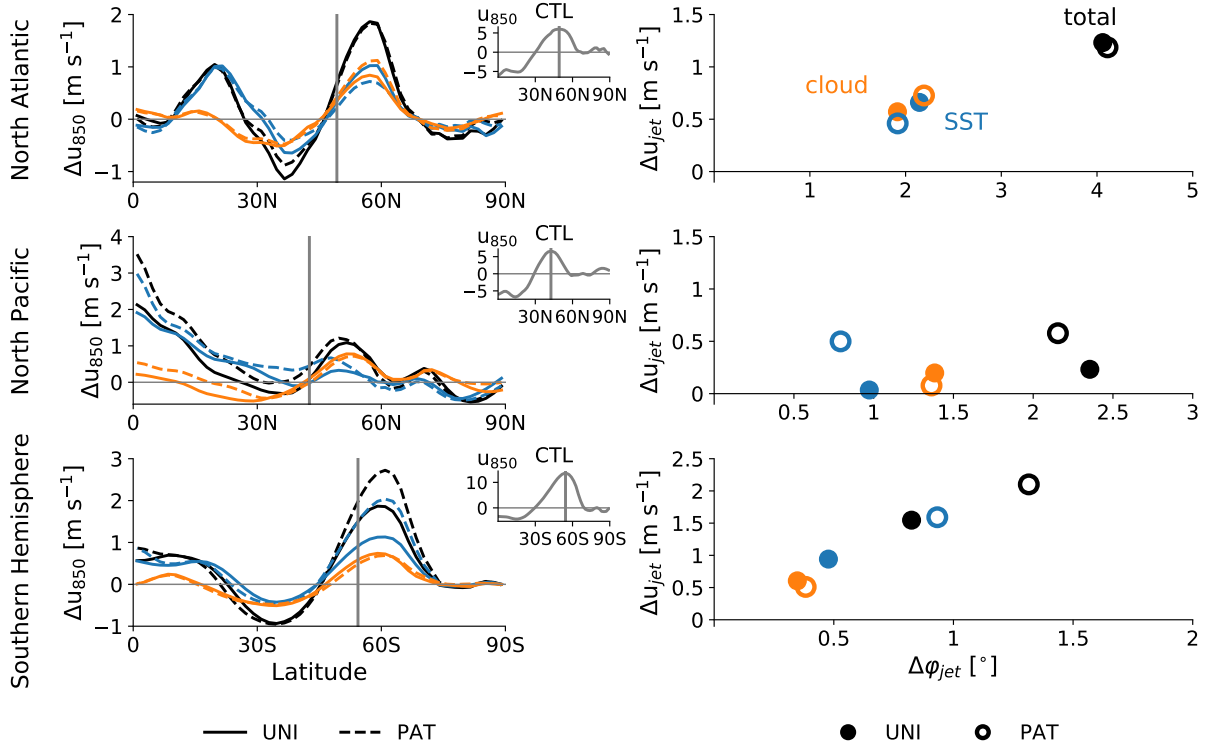
Figure 5.3.: The left panels show the annual-mean response of ocean basin zonal-mean u_{850} in UNI (straight lines) and PAT (dashed lines). The gray bars indicate the jet latitude in CTL derived from the maximum in u_{850} (small inserted figures). The right panels show the poleward jet shift $\Delta\varphi_{jet}$ versus jet strengthening Δu_{jet}. Results are shown for the North Atlantic (top), North Pacific (middle), and Southern Hemisphere (bottom). The total locked response (black) is decomposed into cloud-radiative impact (orange) and SST impact (blue). Reprinted from Albern et al. (2019). ©The Authors.

tive changes in cloud-radiative heating in the tropical and midlatitude upper troposphere. The stronger tropical SST increase in PAT compared to UNI leads to a slightly larger change in cloud-radiative heating in the tropical upper troposphere (Fig. A.6), but overall, the cloud-radiative heating change is very similar between UNI and PAT. A very similar pattern of cloud-radiative heating changes was previously found in aquaplanet simulations in which global warming was mimicked by a uniform 4 K SST increase (Figs. 2c and 2d in Voigt and Shaw, 2016) and in present-day simulations in a slab ocean setup under quadrupling of atmospheric CO_2 (Fig. 2b of Voigt et al., 2019). Additionally, the pattern is consistent with the atmospheric cloud-radiative heating changes derived from present-day COOKIE simulations (Fig. 4b in Li et al., 2019). This supports the idea that the changes in cloud-radiative heating and, thus, the cloud-radiative impact do not strongly depend on the details of surface warming.

Because our simulations include zonal asymmetries from continents, we further investigate the zonal structure of the changes in cloud-radiative heating. The largest changes in cloud-radiative heating are located in the upper troposphere. We therefore analyze the vertical-mean changes in cloud-radiative
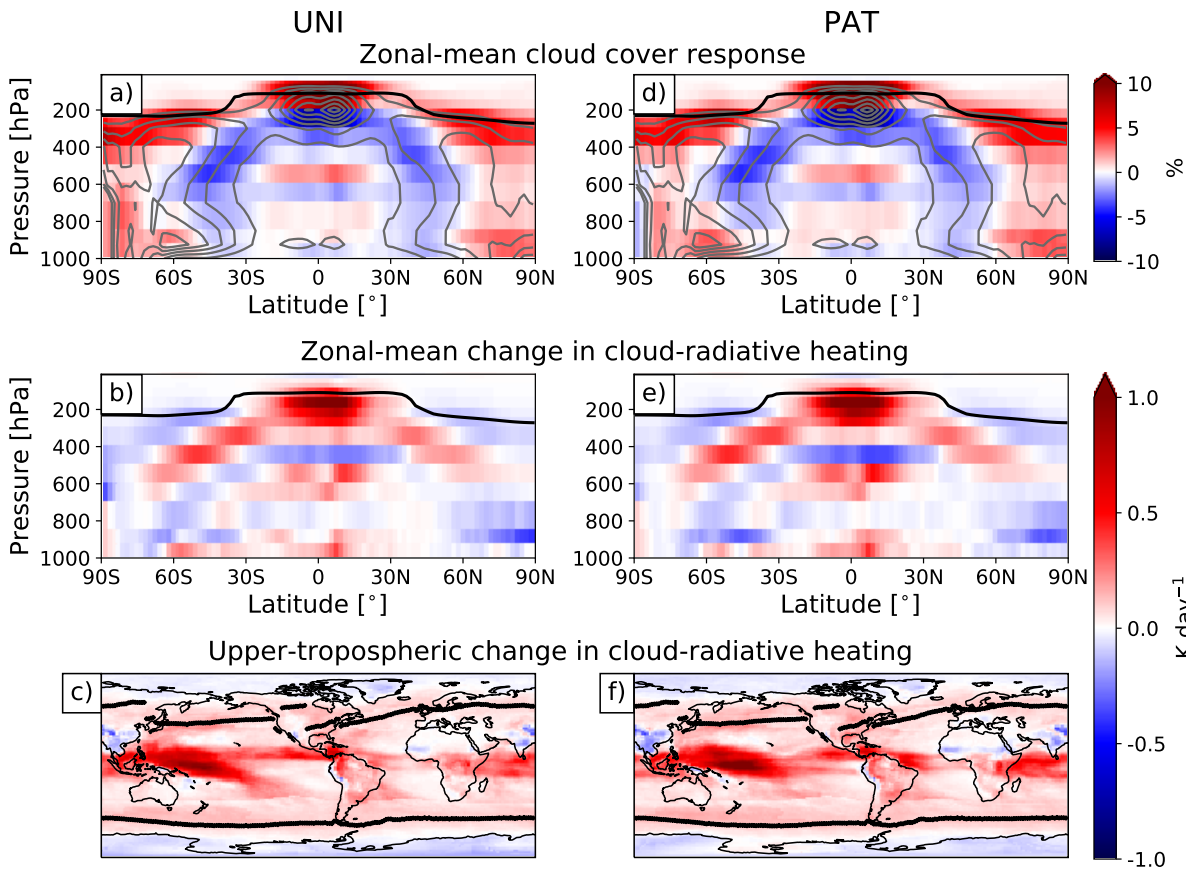
Figure 5.4.: Annual-mean zonal-mean response of cloud cover in the simulations with free clouds (a, d) and annual-mean zonal-mean change in cloud-radiative heating (b, e). The bottom panels (c, f) depict the vertical-mean changes in cloud-radiative heating for a 300-hPa-thick layer below the tropopause. Results are shown for the UNI (left) and PAT (right) simulations. The black lines in the zonal-mean responses indicate the tropopause height in the control simulation; the black line in the maps shows the jet latitude in the control simulation. Reprinted from Albern et al. (2019). ©The Authors.

heating for a 300-hPa-thick layer below the tropopause (Fig. 5.4c, f). In the midlatitudes of both hemispheres, the changes in cloud-radiative heating are zonally symmetric and exhibit a similar magnitude in both global warming setups (Fig. A.6). This is consistent with the zonally symmetric cloud-radiative impact in Figs. 5.1 and 5.2, which also exhibits similar magnitudes in both global warming setups. Zonal asymmetries in the cloud-radiative heating changes are found in the Tropics, especially in the regions of deep convection over the western Pacific and the Indian Ocean (Fig. 5.4c, f). This region also shows the largest change in cloud-radiative heating. Because increased convection over this region can affect the jet latitude in the North Atlantic (e.g., Cassou, 2008; Henderson et al., 2016), we expect that the large change in cloud-radiative heating modifies the jet response in the North Atlantic. However, even though UNI and PAT exhibit different patterns of the upper-tropospheric change in cloud-radiative heating, the cloud-radiative impact on the North Atlantic jet stream response is similar in both global warming se-

tups. This indicates that the small-scale structure of the change in cloud-radiative heating might be less important than its location in the western tropical Pacific.

5.2. Seasonal-Mean Circulation Response

In this section, we investigate the cloud-radiative impact on the seasonal-mean jet stream response and compare it to the annual-mean response. As in section 5.1, we base our analysis on the total response in the prescribed-clouds setup and its decomposition into a cloud-radiative impact and an SST impact. To this end, Figs. 5.5-5.7 show the seasonal-mean wind and jet responses separately for each ocean basin. As for the annual mean, an almost linear relationship between the poleward jet shift and jet strengthening is found in all three ocean basins during seasons which exhibit both the jet shift and jet strengthening. The linear behavior is most strongly pronounced in the Southern Hemisphere during DJF and MAM.

As for the annual mean, the seasonal-mean total zonal wind responses in UNI and PAT reproduce most of the robust zonal wind responses of the CMIP5 Amip4K and AmipFuture simulations (Figs. A.1 and A.2, second to fifth rows). The largest differences compared to the robust response in the CMIP5 models occur in the North Pacific during DJF and MAM. In DJF, ICON does not reproduce the equatorward jet shift in the eastern part of the North Pacific. In MAM, ICON simulates a poleward shift in the North Pacific, whereas the CMIP5 models show a jet strengthening. In the Southern Hemisphere, ICON shows a jet strengthening east of South America in JJA and SON, whereas most of the CMIP5 models show a poleward shift in this region. The ocean basin mean jet responses in ICON are within the range of the CMIP5 models during most of the seasons and for all three ocean basins (Figs. A.3 and A.4; second to fifth rows), although ICON shows a comparably small poleward shift of the Southern Hemisphere jet in DJF and MAM and little jet responses in JJA and SON, as well as a comparably large jet shift in the North Pacific during MAM.

In the North Atlantic, the cloud-radiative impact supports the poleward jet shift in UNI and PAT during all seasons (Fig. 5.5). It contributes to the jet strengthening in JJA and SON for the UNI simulations and during all seasons for the PAT simulations. With respect to the jet shift, the cloud-radiative impact exhibits only a small seasonal cycle and is of similar magnitude as in the annual mean (cf. Fig. 5.5 to top row of Fig. 5.3), except for MAM in the PAT simulations for reasons that are unknown to us. As in the annual mean and with the exception of MAM, the seasonal-mean cloud-radiative impact is largely independent of the SST pattern. In contrast, the total jet shift and the SST impact exhibit distinct seasonal cycles. This leads to strong seasonal variations of the relative importance of the cloud-radiative impact. The relative importance of the cloud-radiative impact can range from about a quarter (during DJF in PAT) to almost all of the poleward jet shift (during SON in PAT). With respect to the jet strength, the seasonal cycles of the total response, the cloud-radiative impact, and the SST impact are of similar magnitude. In the UNI simulations, the relative importance of the cloud-radiative impact on the jet strength varies
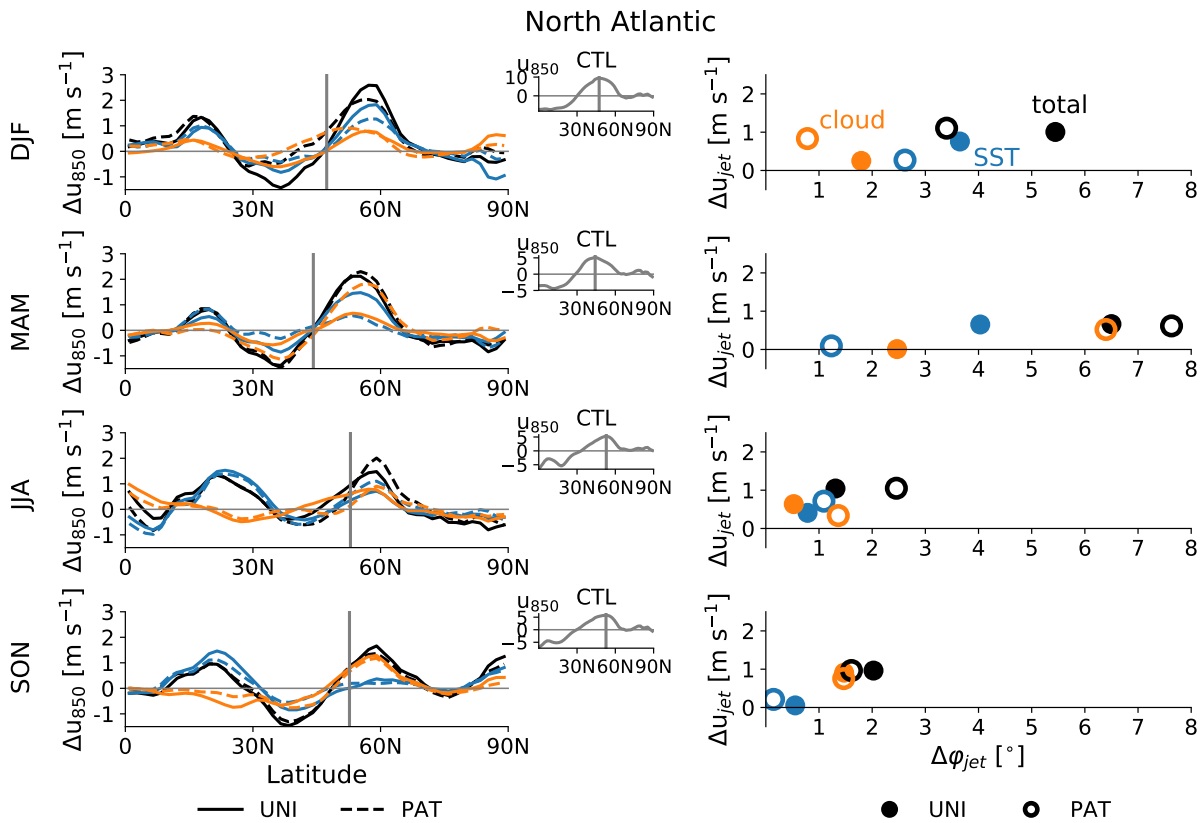
Figure 5.5.: Seasonal-mean response of the ocean basin zonal-mean u_{850} response to a uniform (straight line) and patterned (dashed line) SST increase (left) in the North Atlantic. The gray bar indicates the jet latitude in the control simulation derived from the maximum in u_{850} (small inserted figures). The right panel shows the poleward jet shift $\Delta\varphi_{jet}$ versus the jet strengthening Δu_{jet}. The total locked response (black) is decomposed into cloud-radiative impact (orange) and SST impact (blue). Reprinted from Albern et al. (2019). ©The Authors.

between seasons. In the PAT simulations, more than three quarters of the total jet strength response can be attributed to the cloud-radiative impact (except JJA).

In the North Pacific, the cloud-radiative impact leads to a poleward jet shift in all seasons while having essentially no impact on the seasonal jet strength response (Fig. 5.6). Apart from JJA, the cloud-radiative impact on the jet latitude response is mostly independent of the SST pattern, consistent with the annual-mean response (Fig. 5.3, middle row). In terms of relative importance, the cloud-radiative impact contributes between about one third to the jet shift during MAM and is in fact larger than the total response during JJA. The strong seasonal cycle in the relative importance reflects the strong seasonal cycle of the SST impact, which contributes to a poleward jet shift in MAM but tends to lead to an equatorward shift in JJA. We note that the equatorward shift and weakening of the jet during JJA likely arises from negative land-sea equivalent potential temperature contrasts when SST are warmed, but atmospheric CO_2 is kept at the present-day level (Shaw and Voigt, 2015).
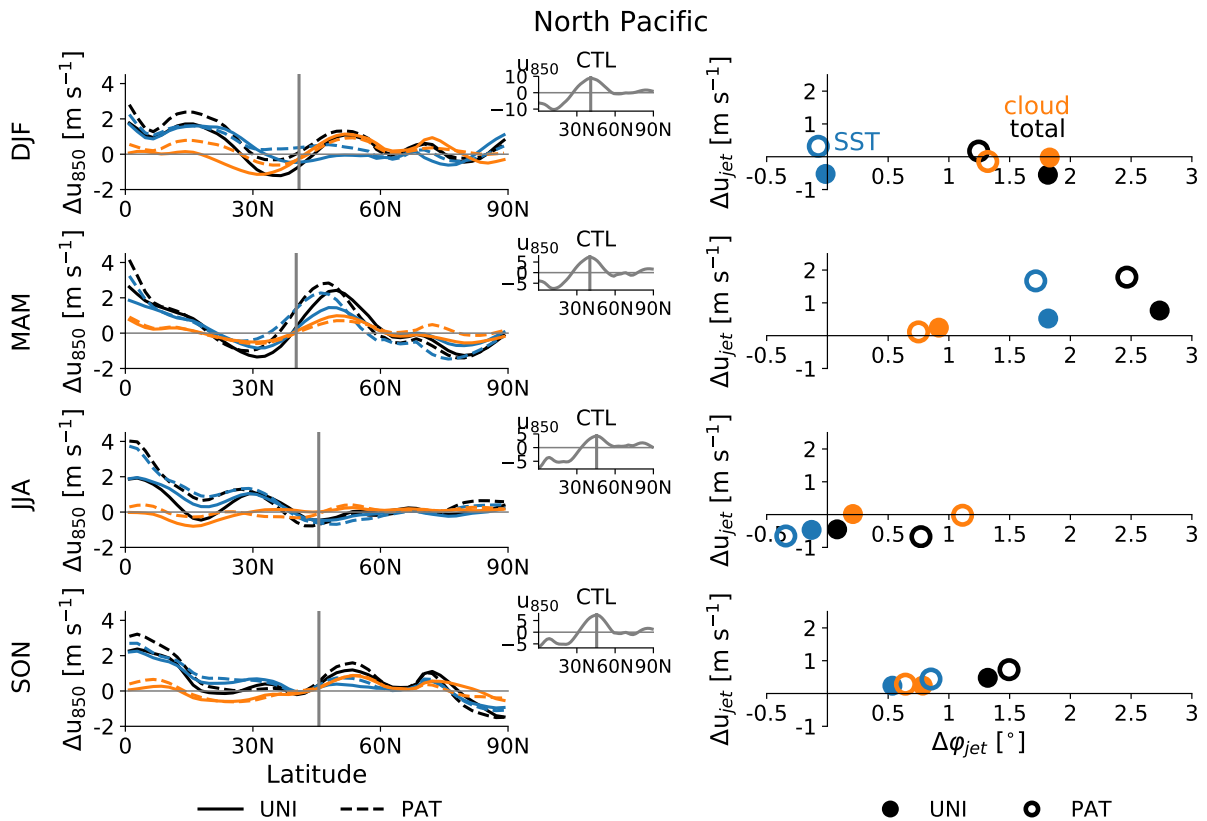
Figure 5.6.: Same as Fig. 5.5 but for the North Pacific. Reprinted from Albern et al. (2019). ©The Authors.

In the Southern Hemisphere, the four seasons can be arranged into two groups according to the simulated jet shifts (Fig. 5.7). The first group consists of DJF and MAM, for which the jet shifts poleward, similar to the annual mean (cf. Fig. 5.7 to lower row of Fig. 5.3). The cloud-radiative impact is of similar magnitude during both seasons and for both global warming setups. At the same time, the increased SST gradients in PAT lead to a much stronger SST impact compared to UNI, so that the relative importance of the cloud-radiative impact ranges between about one third (during DJF in PAT) and more than half (during DJF in UNI) of the total jet shift. The second group consists of SON and JJA, for which the total jet shift is small or even slightly equatorward, independent of the pattern of SST increase. The slight equatorward shift during JJA is supported by the cloud-radiative impact, while in SON, the jet latitude hardly responds to global warming, and the cloud-radiative impact is negligible. In contrast to seasonally dependent changes in its position, the jet becomes stronger in all four seasons. The cloud-radiative impact on the jet strengthening is of similar magnitude during all seasons and its relative importance ranges between about one fifth (during DJF and JJA in PAT) and half (during SON in UNI) of the total response.

Figs. A.7-A.9 show maps of the seasonal-mean u_{850} responses in UNI and PAT, as well as the differences between the two global warming setups. As for the annual mean, the seasonal-mean cloud-radiative
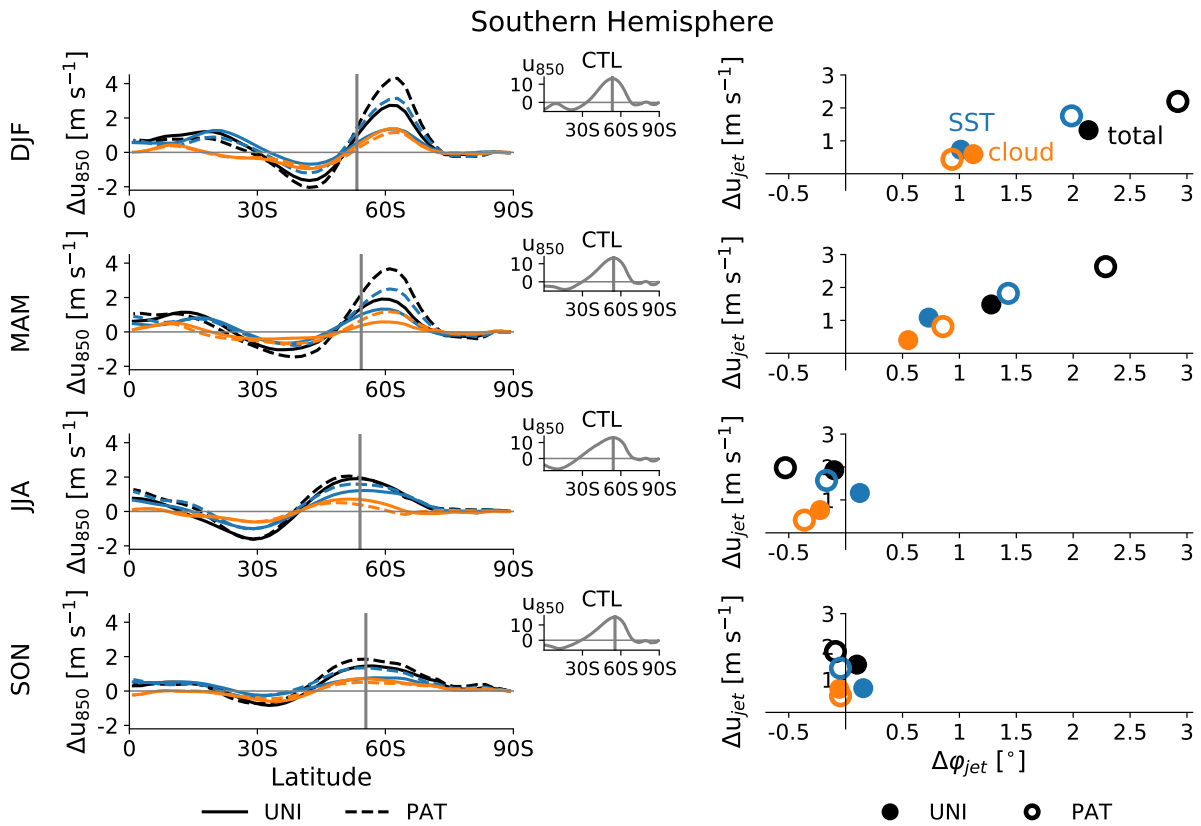
Figure 5.7.: Same as Fig. 5.5 but for the Southern Hemisphere. Reprinted from Albern et al. (2019). ©The Authors.

impact is largely zonally symmetric in all ocean basins and during most seasons, except for JJA. During this season, exceptions of the zonal cloud-radiative impact are found in the North Pacific (in UNI), in the North Atlantic (in PAT), and in the Southern Hemisphere (in PAT). Note that during JJA, the cloud-radiative impact is larger than the total jet shift in the North Pacific and counteracted by an almost ocean basin wide equatorward shift due to the SST impact.

To sum up, we have shown that the seasonal-mean cloud-radiative impact is largely zonally symmetric and shows little dependence on the pattern of SST increase during most seasons in all three ocean basins. In the North Atlantic and North Pacific, the cloud-radiative impact varies little over the course of the year and supports the poleward jet shift during all seasons. The relative importance of the cloud-radiative impact depends on the season, because the total response and SST impact exhibit seasonal cycles. A similar result is found for the Southern Hemisphere during DJF and MAM. The cloud-radiative impact supports the jet strengthening in the North Atlantic during JJA and SON for UNI and during all seasons for PAT and contributes to the jet strengthening in the Southern Hemisphere during all seasons.

5.3. Relations Between the Jet Stream and the Atmospheric Equator-to-Pole Temperature Gradient

In this section, we investigate to what extent the jet stream and its response to global warming are correlated with the upper-tropospheric meridional temperature gradients in all three ocean basins and all seasons. Following Harvey et al. (2014), we calculate the upper-tropospheric (250 hPa) equator-to-pole temperature gradient as the difference between ocean basin zonal mean tropical (30°S-30°N) and polar (poleward of 60°N/S) atmospheric temperatures. We chose this pressure level because in our simulations, the jet stream and the temperature gradient and their responses show higher correlations in the upper troposphere than in the lower troposphere.

In a first step, we investigate to what extent the annual-mean and seasonal-mean jet streams and upper-tropospheric temperature gradients are correlated for different states of the climate system. For this, we use the ocean basin mean jet latitude, jet strength, and equator-to-pole temperature gradient of the seven simulations with locked clouds. These simulations are T1C1, T1C2, T2C1, T2C2, T1C3, T3C1, and T3C3. As described in section 4.3.1, the numbers indicate whether SST (T) and cloud-radiative properties (C) are prescribed to values from CTL (simulation 1), UNI (simulation 2), or PAT (simulation 3). Fig. A.10 shows the scatter plots from which the correlation coefficients of Tab. 5.1 were derived. The seven simulations are not strongly clustered according to the underlying SST pattern during most seasons and for most of the ocean basins. Thus, the significant correlations between the temperature gradient and jet stream are not driven by the SST increase. In the Southern Hemisphere, the jet latitude and jet strength are significantly correlated with the upper-tropospheric temperature gradient both in the annual-mean and in most seasons (except for JJA and SON for the jet latitude; Tab. 5.1). In the North Pacific, the jet stream is significantly correlated with the temperature gradient during MAM and SON. Note that in both ocean basins, negative correlations between the temperature gradient and jet latitude or jet strength are found and are significant in the North Pacific during JJA. The negative correlation during JJA is consistent with the findings of Shaw and Voigt (2015), who showed that ocean warming can result in an equatorward shift of the North Pacific jet in summer. The North Atlantic jet stream is not significantly correlated with the temperature gradient during most seasons. In summary, our results indicate that the upper-tropospheric temperature gradient bears some information for the position and strength of the Southern Hemisphere jet stream but little information for the North Pacific and North Atlantic jet streams.

Previous studies related the global warming response of the midlatitude circulation to changes in upper- and/or lower-tropospheric meridional temperature gradients (e.g., Lorenz and DeWeaver, 2007; Yin, 2005; Harvey et al., 2014, 2015). Thus, in a second step, we investigate whether the cloud-radiative impact on the temperature gradient response in the three ocean basins can be used to infer the cloud-radiative impact on the jet stream response in the respective ocean basin. The idea for this originated from the work of Gerber and Son (2014) who related, and thereby attributed, the jet shift to changes in

Table 5.1.: Correlation coefficients for linear correlation between ocean basin mean jet latitude and upper-tropospheric temperature gradient (a). Panel b shows the same for the jet strength. Correlation coefficients which are significant at a 95% level are shown in bold letters for better visualization of large linear correlations. Positive correlations indicate that increased (decreased) temperature gradients correspond to (a) a more poleward (equatorward) located and (b) a stronger (weaker) jet stream. Reprinted from Albern et al. (2019). ©The Authors.

a)

	Jet latitude		
	North Atlantic	North Pacific	Southern Hemisphere
Annual-mean	**0.87**	0.74	**0.95**
DJF	0.71	0.19	**0.96**
MAM	0.66	**0.97**	**0.87**
JJA	0.75	-0.09	-0.37
SON	0.58	**0.92**	0.18

b)

	Jet strength		
	North Atlantic	North Pacific	Southern Hemisphere
Annual-mean	0.76	0.76	**0.96**
DJF	0.63	-0.04	**0.90**
MAM	0.45	**0.81**	**0.93**
JJA	**0.89**	**-0.89**	**0.96**
SON	0.58	**0.90**	**0.97**

polar stratospheric temperatures (due to ozone) and changes in tropical upper-tropospheric temperatures (due to greenhouse gases). A similar approach was taken by Ceppi and Shepherd (2017). Here we investigate the relation between the jet response and the temperature gradient response for the SST impact and the cloud-radiative impact. The correlation between the jet stream response and the equator-to-pole temperature gradient response at 250 hPa is shown in Fig. 5.8. In all three ocean basins, the temperature gradient increases in response to global warming in all seasons (Fig. 5.8). At the same time, the jet strengthens and shifts poleward in the North Atlantic and strengthens in the Southern Hemisphere during all seasons. However, as discussed in section 5.2, during some seasons, the North Pacific jet stream weakens and shifts equatorward, and the Southern Hemisphere jet stream shifts equatorward.

To assess to what extent the temperature gradient response and the jet stream response are correlated, we calculate correlation coefficients individually for the total response, SST impact, and cloud-radiative impact based on the annual-mean and seasonal-mean responses in both UNI and PAT. The cloud-radiative impact shows rather small correlations, except for the jet shift in the Southern Hemisphere (Fig. 5.8). This is due to the fact that the cloud-radiative impact is of similar magnitude over the course of the
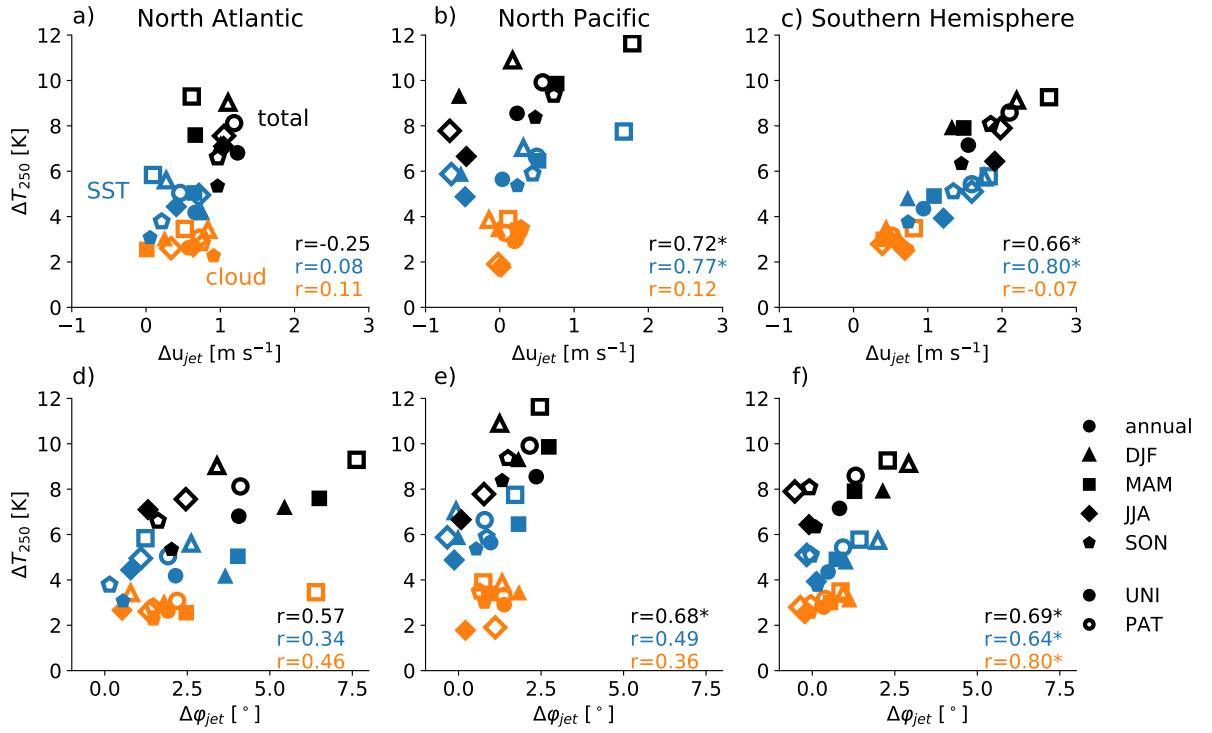
Figure 5.8.: Correlation between temperature gradient response at 250 hPa, ΔT_{250}, and jet strength response, Δu_{jet}, (a-c) and jet latitude response, $\Delta \varphi_{jet}$, (d-f) for the North Atlantic, North Pacific, and Southern Hemisphere. Filled markers are for the response in UNI; open markers for the response in PAT. The total response (black markers) is decomposed into the cloud-radiative impact (orange markers) and the SST impact (blue markers). Correlation coefficients r are marked with a star if they are significant on a 95% level. Reprinted from Albern et al. (2019). ©The Authors.

year and for both global warming simulations. In contrast, the total response and SST impact exhibit distinct seasonal cycles, resulting in significant correlations between the jet response and the temperature gradient response, especially in the Southern Hemisphere and North Pacific. This suggests that in a large model ensemble for which only the total response is available, such as CMIP5/6, the SST impact could be inferred indirectly from the upper-tropospheric temperature response, but the cloud-radiative impact could not. Thus, a proper diagnostic of the cloud-radiative impact requires dedicated cloud-locking simulations.

The fact that we generally could not find a linear correlation for the cloud-radiative impact is in agreement with McGraw and Barnes (2016), who used a dry dynamical model to investigate the jet stream response to a time-constant tropical upper-tropospheric thermal forcing. They found that the temperature response to the thermal forcing does not exhibit a seasonal cycle, whereas the jet latitude and jet strength responses do exhibit distinct seasonal cycles. As a result, McGraw and Barnes (2016) found no correlation between the jet stream response and the temperature gradient response. This is in line with our results.

5.4. Discussion and Conclusions

We study the impact of cloud-radiative changes on the global warming responses of the midlatitude jet streams and storm tracks in the North Atlantic, North Pacific, and Southern Hemisphere and determine whether the cloud-radiative impact depends on the ocean basin, season, and pattern of SST increase. For this purpose, we use the atmospheric component of the ICON model and prescribe SST to isolate the impact of cloud-radiative changes via the atmospheric pathway, that is, the impact of changes in atmospheric cloud-radiative heating in the absence of a cloud-radiative impact on ocean surface temperatures (Voigt et al., 2019).

Changes in atmospheric cloud-radiative heating have a substantial impact on the annual-mean jet stream and storm track responses to global warming, with little dependence on the pattern of SST increase. Note that the impact of surface cloud-radiative heating, which is disabled in our simulations, may depend on the pattern of SST increase, because they lead to changes in surface temperatures (Ceppi and Hartmann, 2016; Voigt et al., 2019). The cloud-radiative impact is largely zonally symmetric, consistent with a zonally symmetric change in cloud-radiative heating in the midlatitude upper troposphere. The magnitude of the cloud-radiative impact depends on the ocean basin. In a relative sense, cloud-radiative changes contribute one to two thirds to the annual-mean poleward jet shift in all three ocean basins and support the jet strengthening in the North Atlantic and Southern Hemisphere. Regarding the seasonal jet response, the cloud-radiative impact varies little with seasons in the North Atlantic and North Pacific. Yet, because the total jet stream response and the SST impact exhibit distinct seasonal cycles, the relative importance of the cloud-radiative impact changes over the course of the year. In the Southern Hemisphere, the cloud-radiative impact supports the jet strengthening in all seasons and contributes to the poleward jet shift in austral summer and fall. As for the annual mean, the cloud-radiative impact on the seasonal jet stream response is largely zonally symmetric and depends little on the pattern of SST increase.

Similar to the zonal cloud-radiative impact, the direct radiative impact of CO_2 on the zonal wind response is also largely zonally uniform in present-day simulations of atmospheric general circulation models (Grise and Polvani, 2014b). Grise and Polvani (2014b) also attributed the asymmetries in the total response to changes in the SST, as in our study with the cloud-locking method.

Previous studies investigated the zonal-mean jet stream and storm track responses to global warming in idealized aquaplanet simulations without a seasonal cycle. They found that cloud-radiative changes cause more than half of the zonal-mean near-surface zonal wind (Voigt and Shaw, 2015) and jet latitude responses (Ceppi and Hartmann, 2016) and dominate the storm track response (Ceppi and Hartmann, 2016). Voigt et al. (2019) showed that more than half of the annual-mean zonal-mean jet shift in a present-day setup can be attributed to the atmospheric pathway of the cloud-radiative impact. We extend this prior work and show that the absolute value of the cloud-radiative impact strongly depends on the ocean basin and has only a small seasonal cycle in the Northern Hemisphere. In addition, we show

that the relative role of the cloud-radiative impact on the jet stream response varies across ocean basins and seasons. This highlights the importance of the present-day setup, and the investigation of individual ocean basins, for understanding the role of cloud-radiative changes on the midlatitude circulation response to global warming.

While continents are important for the jet stream response in the three ocean basins, the pattern of SST increase plays a minor role for the cloud-radiative impact on the jet stream and storm track responses. In our simulations, the pattern of the SST increase has only a small impact on the absolute value of the cloud-radiative impact in all three ocean basins and across seasons. Thus, the uniform 4 K SST increase provides meaningful estimates of the absolute value of the cloud-radiative impact, although is not able to reproduce the total jet stream response of coupled climate models, especially in the Southern Hemisphere, where the jet strongly responds to changes in SST gradients.

Even though the cloud-radiative impact does not strongly depend on the pattern of SST increase and season in the model used here, previous work indicates that the cloud-radiative impact strongly differs between models. Voigt et al. (2019) showed that the annual-mean zonal-mean change in atmospheric cloud-radiative heating and, thus, the magnitude of the cloud-radiative impact strongly depend on the model. These model differences arise both from differences in the cloud response as well as differences in the radiation schemes and assumptions regarding the radiative characteristics of ice clouds. Additionally, in coupled climate models, the cloud-radiative impact is a sum of the atmospheric and surface pathways of the change in cloud-radiative heating. The latter might depend on the pattern of SST increase and season.

Finally, we investigated the correlation between the upper-tropospheric temperature gradient response and the jet stream response. For the cloud-radiative impact, increased temperature gradients coincide with a strengthening of the Southern Hemisphere jet stream, while correlations between cloud-induced changes in the temperature gradient and the jet are weak in the Northern Hemisphere. This lack of correlation is a result of the fact that the cloud-radiative impact does not strongly depend on season in the Northern Hemisphere. In contrast, the total response and SST impact exhibit distinct seasonal cycles, resulting in significant linear correlations between the jet stream response and upper-tropospheric temperature gradient response, with statistically significant correlations in the Southern Hemisphere and North Pacific. This also indicates that the cloud-radiative impact on the jet cannot be inferred indirectly from the temperature response but requires cloud-locking simulations.

6. The Role of Tropical, Midlatitude and Polar Cloud-Radiative Changes for the Midlatitude Circulation Response to Global Warming

In this chapter, we address research question 2 "Which regional cloud-radiative changes dominate the global cloud-radiative impact on the response of the midlatitude circulation to global warming?". To this end, we answer the following more detailed sub-questions:

1. Are tropical, midlatitude or polar cloud-radiative changes more important for the global cloud impact on the zonal wind, jet stream and storm track responses to global warming? Do the results depend on the season and the ocean basin?

2. Can we understand the circulation impact of regional cloud-radiative changes on the zonal wind and jet responses based on (established) dynamical arguments?

The structure of this chapter is as follows: In section 6.1, we will introduce our measure for significance. We show the response of the midlatitude jet streams and storm tracks to regional cloud-radiative changes in section 6.2, and link the jet response to changes in upper-tropospheric baroclinicity in section 6.3. We conclude with the main results in section 6.4.

This chapter is based on Albern et al. (2020). ©American Meteorological Society. Used with permission.

6.1. Statistical Significance

In chapter 5, we used a two-sided t test for two samples to determine statistical significance of the zonal wind and storm track responses to global warming. We decided to switch from the t test to bootstrapping as a measure for significance in this chapter because bootstrapping does not make any assumptions about the distribution of the data while the t test assumes that the data is normally distributed. However, the zonal wind data are not normally distributed.

Fig. 6.1 shows that bootstrapping in general yields to larger regions with significant 850 hPa zonal wind responses to a uniform SST increase compared to the t test. This is especially pronounced for the cloud-radiative impact which shows the smallest zonal wind responses to global warming (Fig. 6.1, right). These results indicate that the use of bootstrapping does not affect our conclusions from chapter 5 that cloud-radiative changes have a significant impact on the u_{850} and storm track response in the midlatitude ocean basins, but yield to larger regions with significant responses, especially if the responses are small.
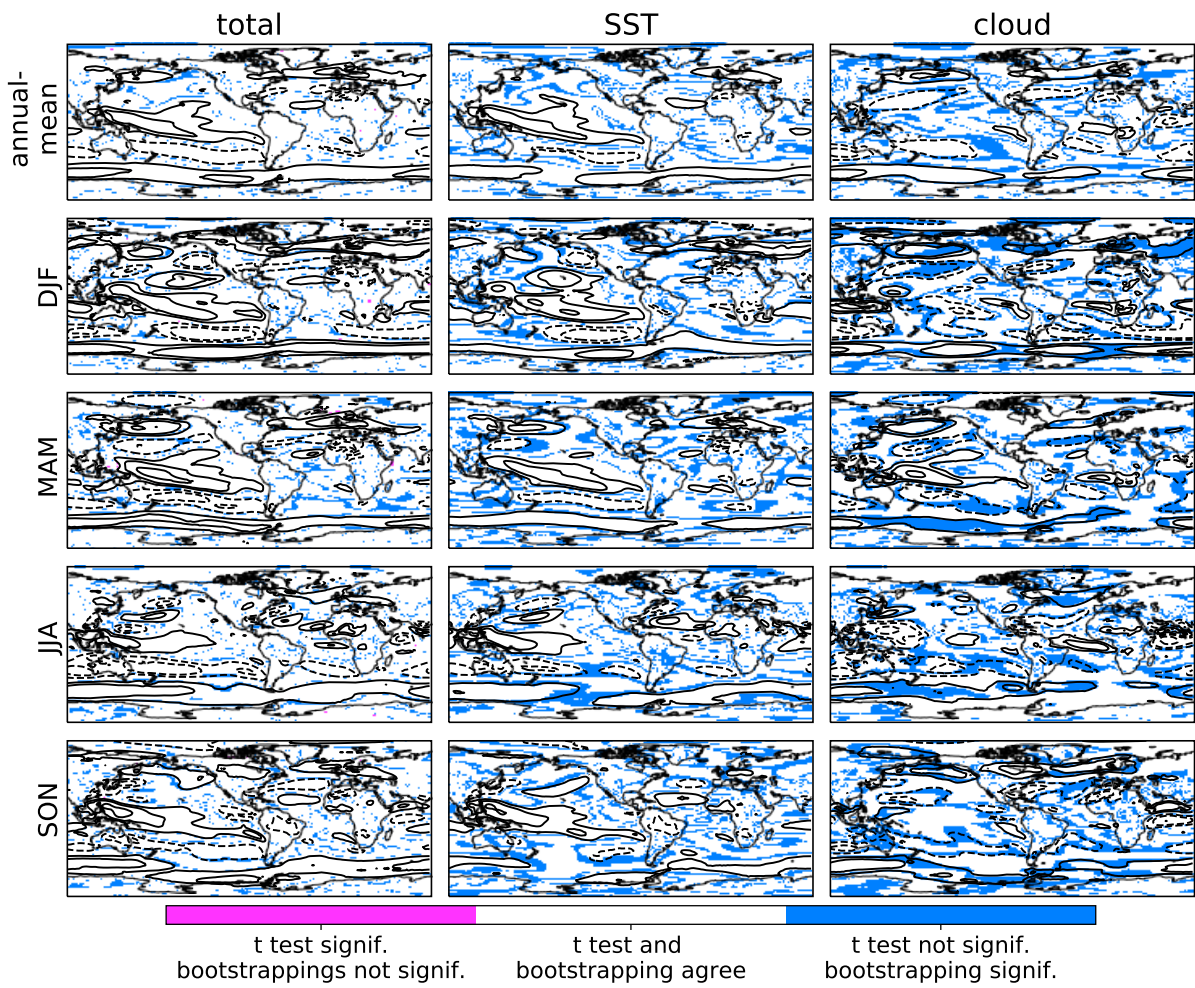
Figure 6.1.: Comparison of t test and bootstrapping as a measure for significance for the annual-mean (first row) and seasonal-mean (second to fifth rows) u_{850} response to global warming. The total response (left) is decomposed into SST impact (center) and cloud impact (right). White areas indicate that the t test and bootstrapping agree, i.e. both show significant or not significant responses in the same region. Blue areas indicate that bootstrapping shows more significant regions than the t test and pink areas show the opposite. The contours depict the u_{850} response. Contour levels are -4, -2, -1, 1, 2, 4 m s^{-1} in all panels with additional contours for -0.5 and 0.5 m s^{-1} for the cloud impact.

Statistical significance of the zonal wind and jet responses are calculated based on the 5th-95th-percentile range of the bootstrap distributions of the zonal wind and jet responses to global warming. The bootstrap distributions are determined in four steps: 1) for each simulation, we calculate the annual-mean or seasonal-mean time series of the zonal wind field at 850 hPa for each of the 29 simulated years; 2) based on this time series, we perform a sampling with replacement (the resample has the same size as the original time series), and calculate the time mean over the resample; 3) the zonal-mean jet latitude and jet strength are determined from the zonal-mean of this time-mean u_{850} field; and 4) the total zonal wind

and jet responses and the global and regional cloud impacts are calculated as described in section 4.3. These four steps are performed 1000 times to obtain bootstrap distributions of the zonal wind and jet responses. We consider the zonal wind response to be significant if the 5th-95th-percentile range of the bootstrap distribution does not include $0\,\mathrm{m\,s^{-1}}$. The jet latitude and jet strength responses are significant if the 5th-95th-percentile ranges of the bootstrap distributions do not include $0°$ latitude and $0\,\mathrm{m\,s^{-1}}$, respectively. For the jet response, we also investigate the 1st-99th-percentile range of the bootstrap distributions to determine the spread in the response.

6.2. Jet Stream Response to Regional Cloud-Radiative Changes

In this section, we investigate the impact of tropical, midlatitude, and polar cloud changes on the zonal wind, jet stream, and storm track responses to global warming and determine which regional cloud impacts are most important for the global cloud impact. Albern et al. (2019) found that the global cloud impact is very similar across seasons. Here, we investigate whether this is also the case for the regional cloud impacts. Therefore, we focus our analysis on the annual-mean, DJF and JJA responses as these seasons span the range of large (DJF) and small (JJA) total jet responses. Note that in some regions, the JJA jet shift in ICON tends to be smaller than in other models (cf. Fig. S6 in Albern et al., 2019). We also investigated MAM and SON and found similar results for the cloud impacts. Note that in all figures, the shown total response is always the total response for the simulations with locked clouds.

We begin with a brief summary of the main results of Albern et al. (2019), who studied the total response, the SST impact, and the global cloud impact. We include the results for the zonal mean over the Northern Hemisphere, which was not studied in Albern et al. (2019), and highlight the annual-mean, DJF, and JJA responses. Albern et al. (2019) found that for most seasons and regions, the total u_{850} response, the SST impact, and the global cloud impact exhibit dipole patterns around the jet latitude of the control simulation (cf. Fig. 6.2). The dipole patterns indicate poleward jet shifts in the annual-mean and DJF in all regions, whereas the jets hardly shift in JJA, with the exception of modest poleward shifts of the North Atlantic and Northern Hemisphere jets. Further, the dipoles indicate a jet strengthening in the North Atlantic, Northern Hemisphere, and Southern Hemisphere during all seasons, while the North Pacific jet weakens in DJF and JJA. The global cloud impact supports the jet shift and jet strengthening in all regions that show a substantial total response.

The tropical, midlatitude, and polar cloud impacts also exhibit dipole patterns around the control jet latitude, especially in the annual mean and during DJF. This indicates that in principle all regional cloud changes can contribute to the u_{850} and jet responses (Fig. 6.3). Yet, the tropical cloud impact clearly dominates the global cloud impact in the North Atlantic and Southern Hemisphere during all seasons (except for NA during DJF), and in the Northern Hemisphere and North Pacific during DJF. In the latter two regions, all regional cloud impacts are important in the annual mean and negligible in JJA, which reflects the small total response during this season.
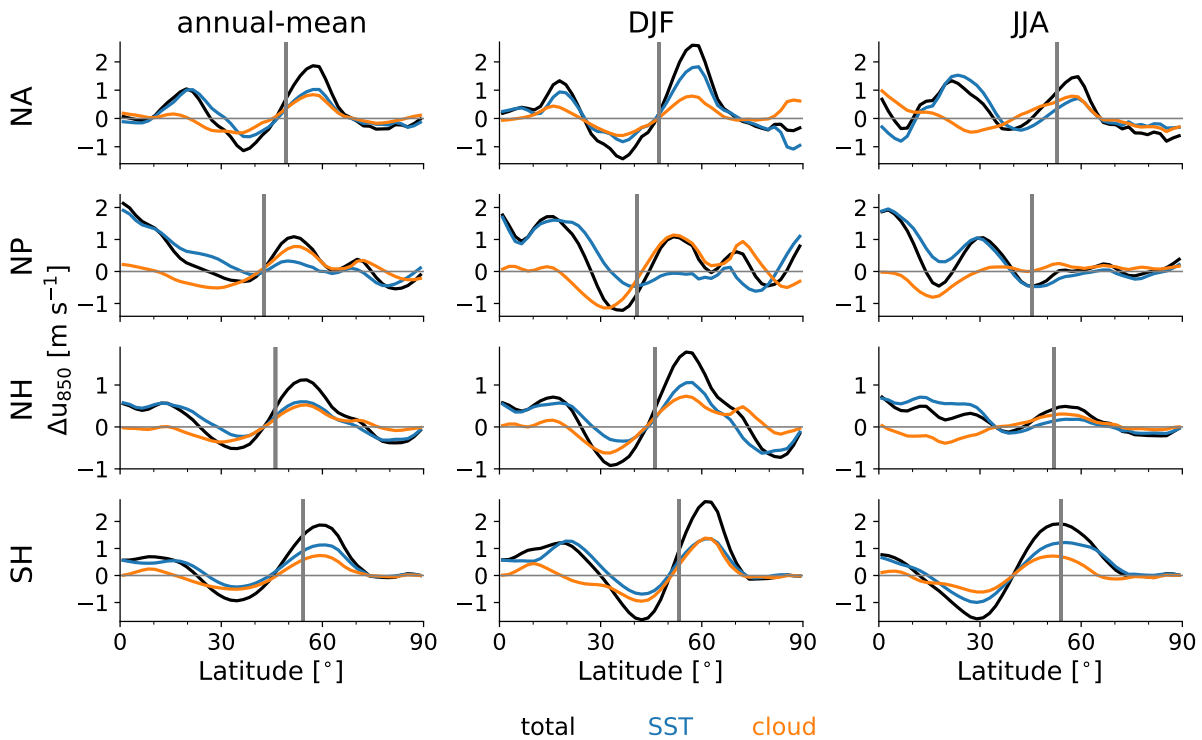
Figure 6.2.: Zonal-mean response of the 850 hPa zonal wind (u_{850}) (left) in the annual mean and during (center) DJF and (right) JJA in the (top to bottom) North Atlantic (NA), North Pacific (NP), Northern Hemisphere (NH), and Southern Hemisphere (SH). The total response (black) is decomposed into the SST impact (blue) and the global cloud impact (orange). The gray bars show the jet latitude in the control simulation with locked clouds. Reprinted from Albern et al. (2020). ©American Meteorological Society. Used with permission.

Moving from the zonal-mean perspective to the response at each longitude, we find that the global cloud impact is dominated by the tropical cloud impact (Fig. 6.4). The tropical cloud impact is significant in most regions in which the global cloud impact is significant. The midlatitude and polar cloud impacts are in general smaller and less significant. To first order, the impacts of regional cloud changes on the u_{850} response are zonally symmetric in the midlatitude ocean basins, with the exception of the North Pacific during JJA. These results are in line with the finding of Albern et al. (2019) that the global cloud impact is largely zonally symmetric across the midlatitude ocean basins, whereas the SST increase causes a more zonally asymmetric u_{850} response.

As an overview, Fig. 6.5 presents the relation between the zonal-mean poleward jet shift and jet strengthening in a scatterplot. This allows for immediate comparison with Albern et al. (2019). The statistical significance of the jet responses is shown in Figs. 6.6 and 6.7. Similar to the zonal wind response, the global cloud impact on the jet strength response is dominated by a significant tropical cloud impact (Figs. 6.5 and 6.6). The midlatitude and polar cloud changes hardly affect the jet strength response in any region and during any time of the year, and their small impacts are mostly not statistically significant. Note that in DJF, the total response of the North Pacific jet strength is not significant even
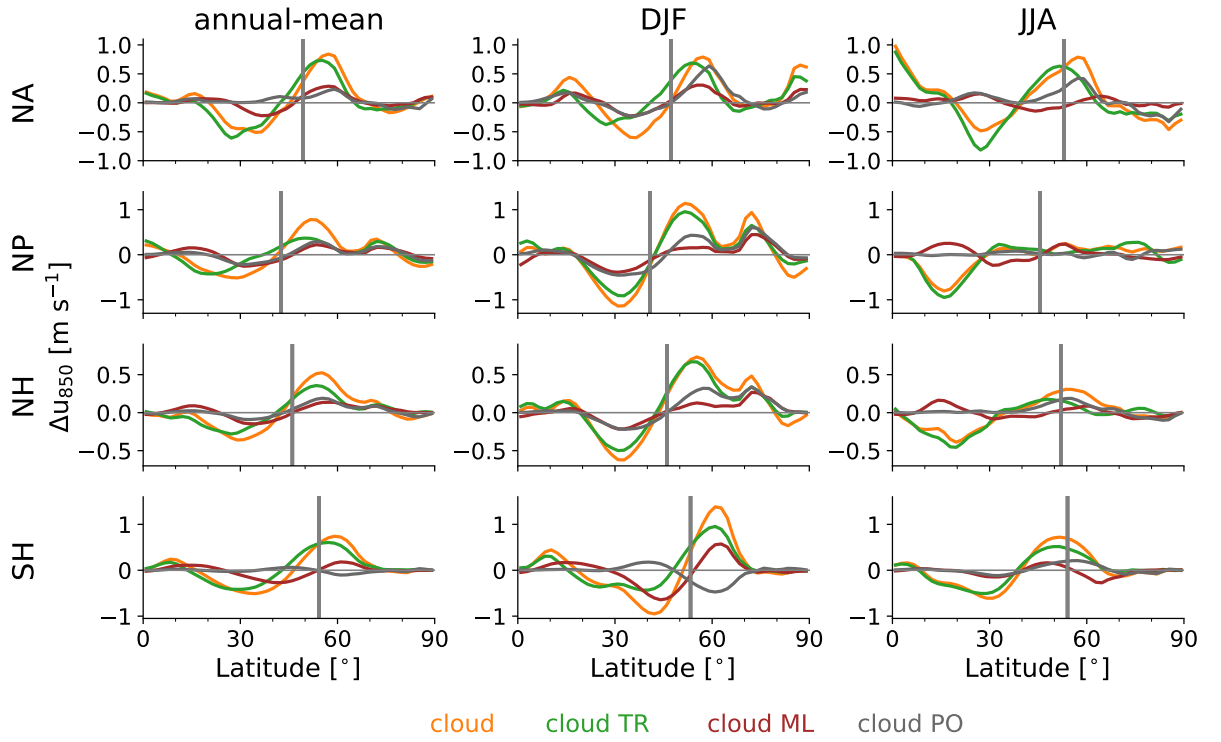
Figure 6.3.: Zonal-mean response of the 850 hPa zonal wind (u_{850}) (left) in the annual mean and during (center) DJF and (right) JJA in the (top to bottom) North Atlantic (NA), North Pacific (NP), Northern Hemisphere (NH), and Southern Hemisphere (SH). Shown are the global (orange), tropical (cloud TR; green), midlatitude (cloud ML; brown), and polar (cloud PO; gray) cloud impacts. The gray bars show the jet latitude in the control simulation with locked clouds. Reprinted from Albern et al. (2020). ©American Meteorological Society. Used with permission.

though it is similar to the SST impact. This is because the variability in the total response is larger than for the SST impact. In general, the variabilities of the total u_{jet} and φ_{jet} responses and SST impacts are larger than the variabilities of the regional cloud impacts. This means that even though the regional cloud impacts are smaller in most cases, they are, at the same time, more robust than the total response and the SST impact (Figs. 6.6 and 6.7).

In contrast to the u_{850} and u_{jet} responses, all regional cloud changes contribute about equally to the annual-mean and DJF φ_{jet} response in the three Northern Hemisphere regions, except for the North Pacific in DJF, which is dominated by tropical cloud changes (Fig. 6.5). In the Southern Hemisphere, tropical and midlatitude cloud changes contribute to the annual-mean and DJF poleward jet shift, whereas polar cloud changes tend to shift the jet equatorward. Most of the regional cloud impacts on $\Delta\varphi_{jet}$ are significant for the 1st-99th-percentile range (mainly cloud TR) or for the 5th-95th-percentile range (mainly cloud ML and cloud PO) (Fig. 6.7). In JJA, the total jet shift, the SST impact and all cloud impacts are small and mostly not significant (Figs. 6.5 and 6.7, bottom rows).
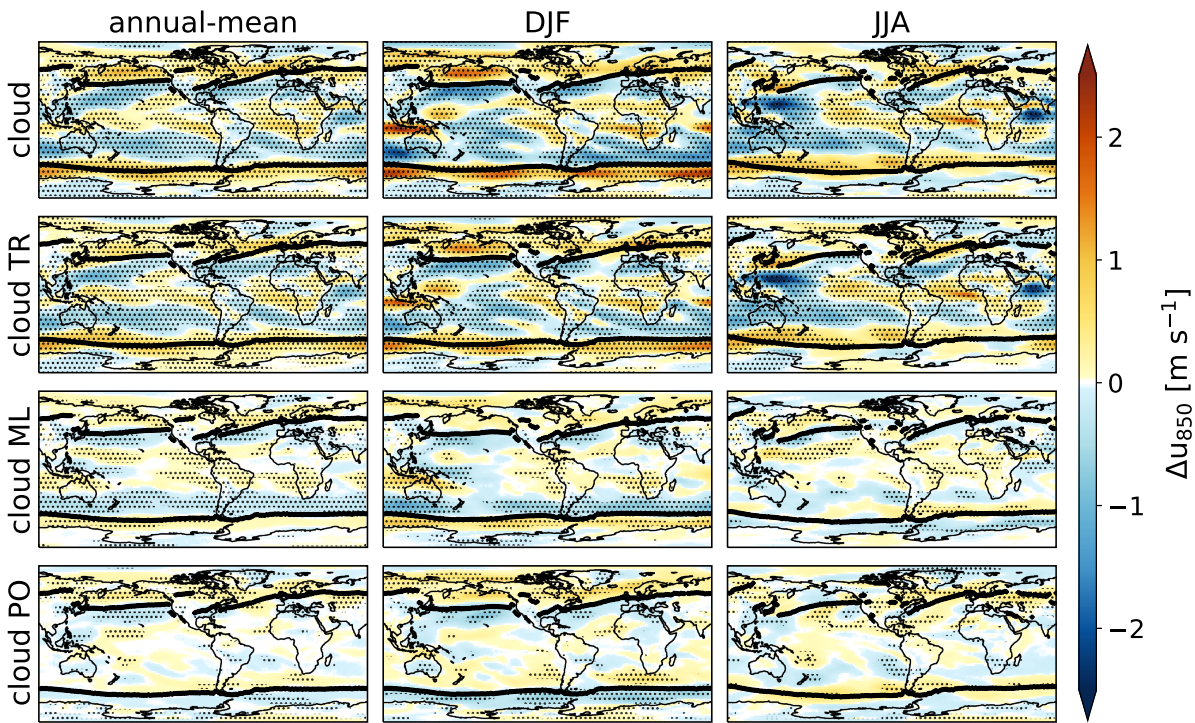
Figure 6.4.: (left) Annual-mean, (center) DJF, and (right) JJA response of the zonal wind at 850 hPa (u_{850}) to global warming. Depicted are the (top to bottom) global (cloud), tropical (cloud TR), midlatitude (cloud ML), and polar (cloud PO) cloud impacts. The dots indicate where the response is statistically significant based on the 5th-95th-percentile range of the bootstrap distribution for each grid point. The black line indicates the jet latitude in the control simulation with locked clouds. Reprinted from Albern et al. (2020). ©American Meteorological Society. Used with permission.

The jet shift in response to regional cloud changes in our simulations is in agreement with the jet response to regional cloud changes in aquaplanet simulations (Voigt and Shaw, 2016). In both the aquaplanet setup and the present-day setup, tropical and midlatitude cloud changes contribute about equally to the poleward jet shift. This highlights the importance of tropical and midlatitude cloud-radiative heating for the poleward jet shift (cf. section 6.3). At the same time, the role of polar cloud changes is more uncertain and seems to be model dependent. In one of the aquaplanet models of Voigt and Shaw (2016) the polar cloud impact was about half of the tropical and midlatitude cloud impacts whereas it was negligible in the other model. In our simulations, the polar cloud impact on the jet shift is more important and contributes in some circumstances as much to the poleward jet shift as the tropical and midlatitude cloud impacts (cf. Fig. 6.5; e.g., the DJF jet shift in the North Atlantic).

Considering the differences in the model setups of the aquaplanet and the present-day simulations, it is surprising how well the results agree. As the cloud impacts are similar across seasons, the aquaplanet (without a seasonal cycle) is a useful tool to study the role of (regional) cloud changes. Differences between the simulations might be related to the inclusion of sea ice and continents in our simulations,
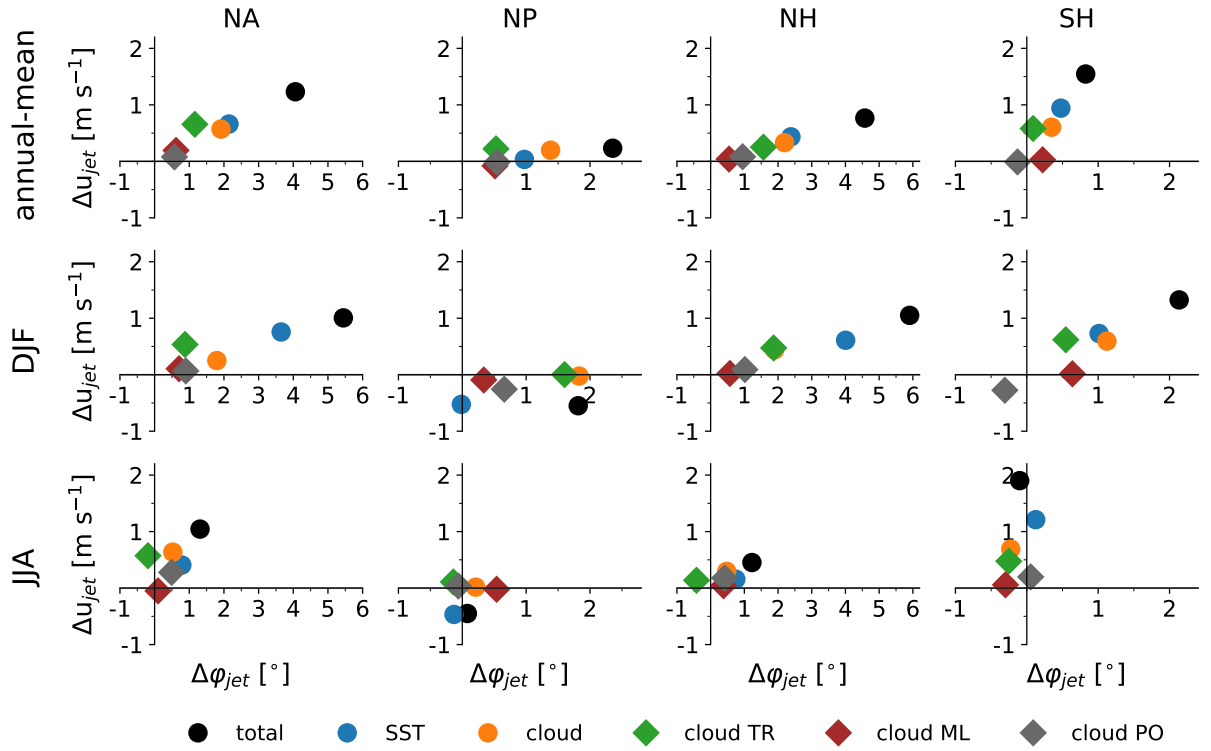
Figure 6.5.: Zonal-mean jet shift $\Delta\varphi_{jet}$ versus jet strengthening Δu_{jet} (top) in the annual mean and during (middle) DJF and (bottom) JJA. Shown are the total response (black), the SST impact (blue), and the global (orange), tropical (cloud TR; green), midlatitude (cloud ML; brown), and polar (cloud PO; gray) cloud impacts for the (left to right) North Atlantic (NA), North Pacific (NP), Northern Hemisphere (NH), and Southern Hemisphere (SH). Reprinted from Albern et al. (2020). ©American Meteorological Society. Used with permission.

which was found to be important for the jet (Brayshaw et al., 2009) and the cloud impact in different ocean basins (Albern et al., 2019). Additionally, Voigt and Shaw (2016) prescribe water vapor to values from the control simulation in the global warming simulation, whereas water vapor is free in our simulations. Finally, Voigt and Shaw (2016) do not calculate the mean over four simulations to derive the cloud impact (cf. Eq. 4.6), but determine it as $\Delta X_{cloud,VS16} = X_{T1C_a2C_b1} - X_{T1C_a1C_b1}$. In our simulations, this calculation results in a highly overestimated global cloud impact on the jet response, whereas the three regional cloud impacts in the aquaplanet simulations almost sum up to the global cloud impact.

The jet streams are tightly coupled to the storm tracks, which are a measure of synoptic activity in the midlatitudes (e.g., Hoskins and Valdes, 1990; Pinto et al., 2007). Depending on the ocean basin and season, the storm tracks shift poleward and strengthen in response to global warming (Fig. 6.8, first row). The global cloud impact contributes significantly to the total response in all ocean basins in the annual mean and to the North Atlantic response in JJA (Fig. 6.8, second row) (statistical significance of the storm track response is determined analogously to the u_{850} response). Similar to the u_{850} response, the global cloud impact on the storm track response is dominated by tropical cloud changes, whose impact is significant in large parts of the ocean basins and across seasons, even in regions where the
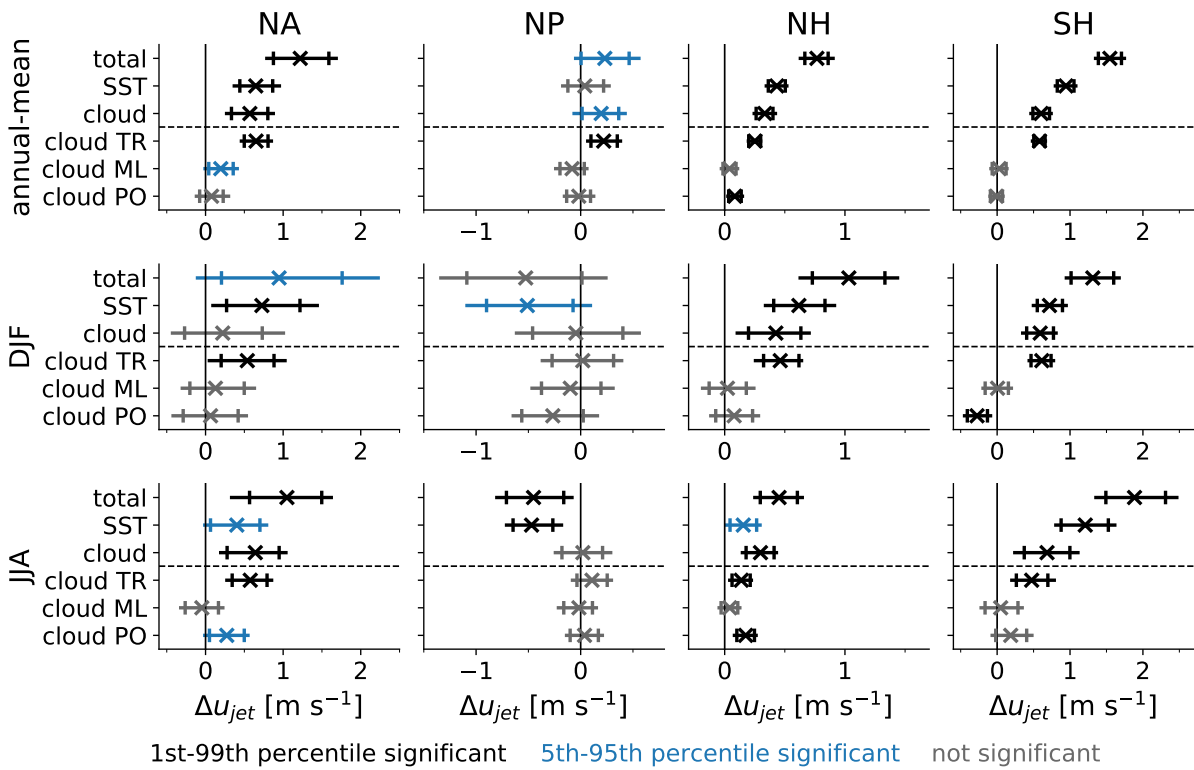
Figure 6.6.: The 1st-99th-percentile range (horizontal lines), median (crosses), and 5th and 95th percentiles (vertical lines) of bootstrap distributions of the zonal-mean jet strength response (Δu_{jet}). Results are shown for (top) the annual mean, (middle) DJF, and (bottom) JJA, and for the (left to right) North Atlantic (NA), North Pacific (NP), Northern Hemisphere (NH), and Southern Hemisphere (SH). Shown are the total response, the SST impact, and the global and regional cloud impacts. The colors indicate whether the response is significant based on the 1st-99th-percentile range or the 5th-95th-percentile range or whether the response is not significant. Reprinted from Albern et al. (2020). ©American Meteorological Society. Used with permission.

global cloud impact is not significant (Fig. 6.8, third row). The midlatitude and polar cloud impacts also contribute to the global cloud impact but are weaker and less significant (Fig. 6.8, fourth and fifth rows). Significant impacts of midlatitude and polar cloud changes are mainly found in the North Atlantic and at the equatorward flank of the North Pacific and Southern Hemisphere storm tracks.

6.3. Dynamical Processes - Changes in Baroclinicity and Eddies

In this section, we explore the dynamics behind the zonal wind and jet stream responses to cloud-radiative changes. As summarized in the previous section, there are two primary and robust linkages between regional changes in cloud-radiative heating and responses in the extratropical circulation: 1) changes in tropical cloud-radiative heating dominate changes in the strength of the jets, and 2) changes in both tropical and midlatitude cloud-radiative heating contribute to the poleward jet shifts. There are interesting and important seasonal differences in the jet responses, but these are due as much to the SST increase
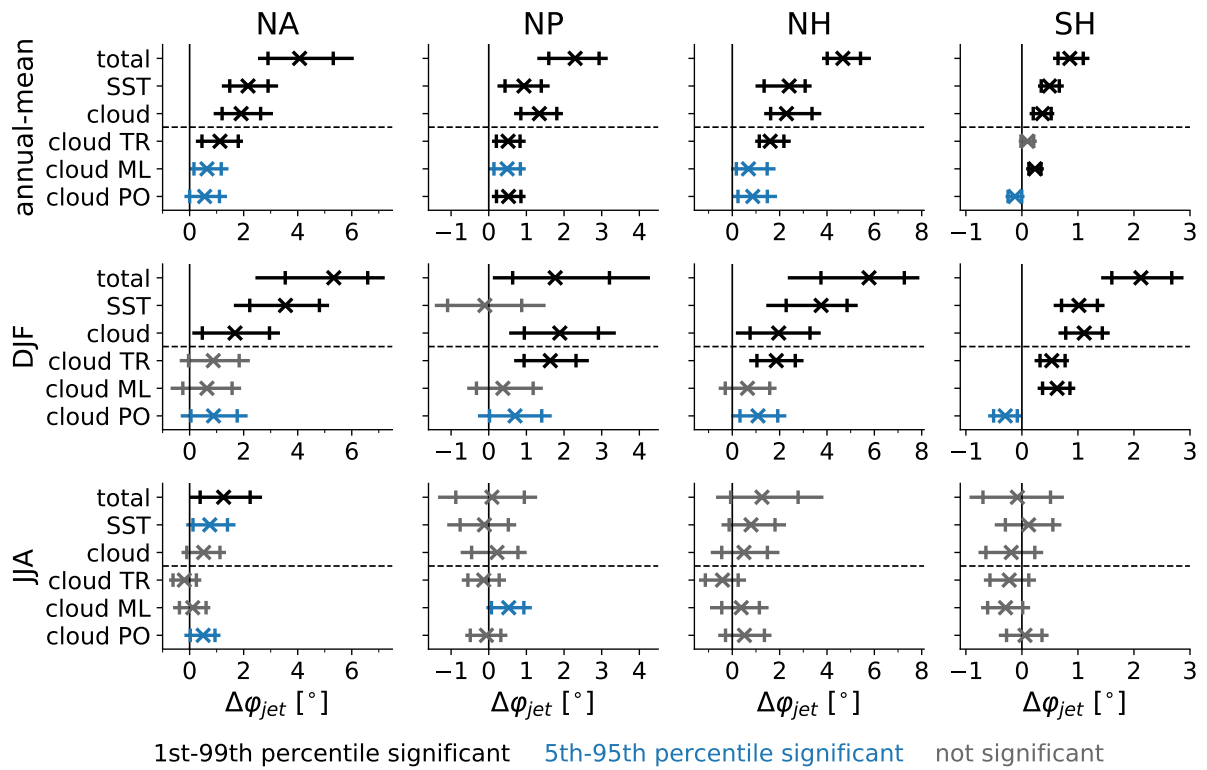
Figure 6.7.: As in Fig. 6.6, but for jet latitude response ($\Delta\varphi_{jet}$). Reprinted from Albern et al. (2020). ©American Meteorological Society. Used with permission.

as to changes in cloud-radiative properties (Figs. 6.6 and 6.7). The fact that the jets hardly shift in JJA indicates that the background climate state on which the cloud-radiative heating and SST increase are imposed is important for the jet shift. The dominating processes, however, are still unclear and an area of active research. For this reason, here we focus on the annual-mean jet shift and investigate the qualitative relationships between changes in cloud-radiative heating and various dynamical properties of the extratropical atmosphere. We begin with the changes in atmospheric cloud-radiative heating since they are the forcing whereby changes in clouds influence the circulation.

The contours in Fig. 6.9 show the changes in zonal-mean atmospheric cloud-radiative heating for the global and regional cloud impacts. The changes in cloud-radiative heating are all dominated by their longwave components (not shown). The shading in Fig. 6.9 shows the corresponding responses in zonal-mean atmospheric temperature. Note that the responses in temperature are due not only to the imposed cloud-radiative heating, but also to the resulting changes in atmospheric dynamical and diabatic processes.

The qualitative structure of changes in upper-level cloud-radiative heating (Fig. 6.9, top) is consistent with the response of high-level clouds to global warming (e.g., Manabe and Wetherald, 1987) and can be understood primarily from 1) the lifting of the tropopause across all latitudes in response to global warming (Hartmann and Larson, 2002; Singh and O'Gorman, 2012; Thompson et al., 2017); 2) the
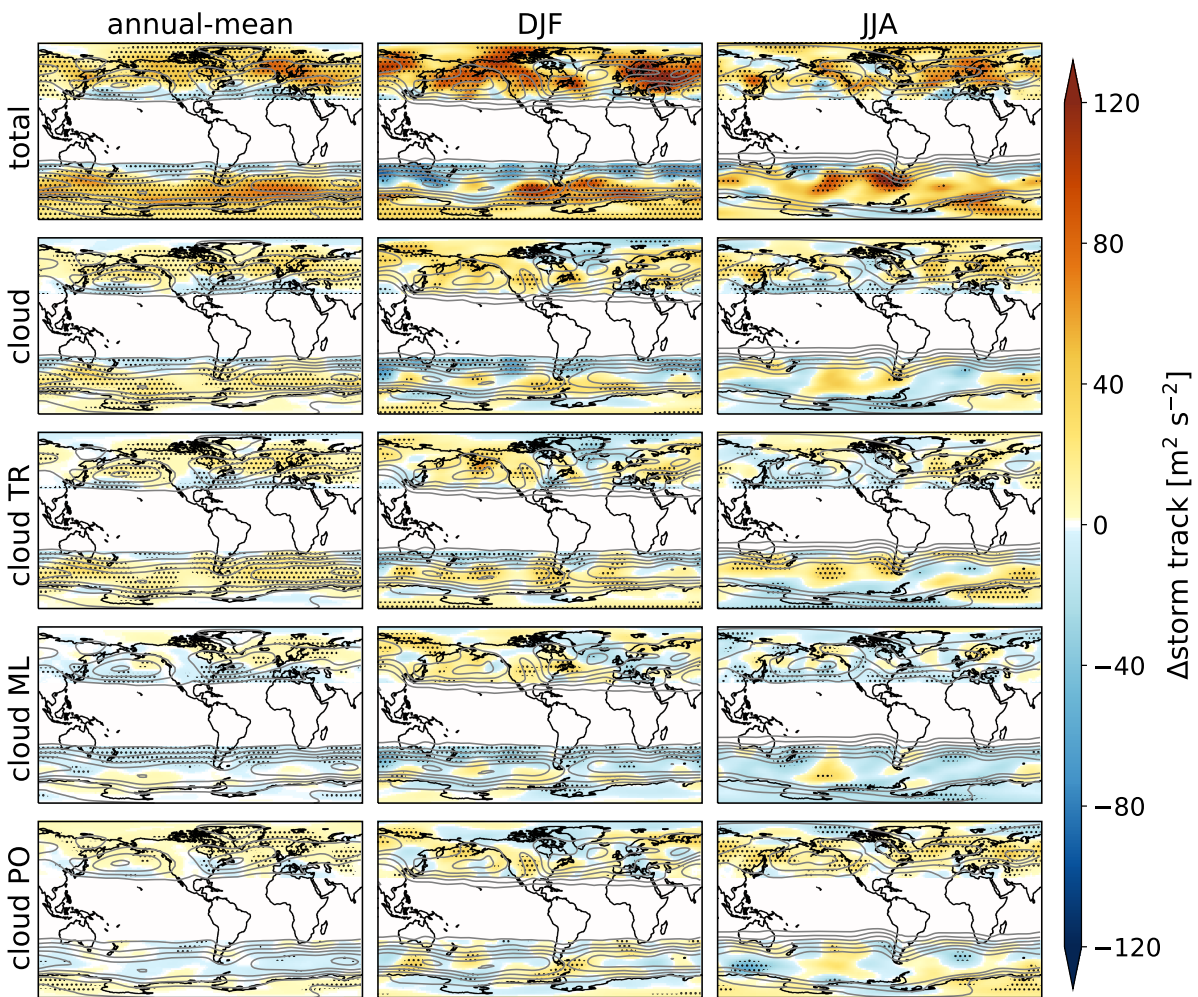
Figure 6.8.: (left) Annual-mean, (center) DJF, and (right) JJA storm track response to global warming. Depicted are the (top to bottom) total response and the global (cloud), tropical (cloud TR), midlatitude (cloud ML), and polar (cloud PO) cloud impacts. The dots indicate regions with a statistically significant response based on the 5th-95th-percentile range of the bootstrap distribution. The gray contours show the storm track in the control simulation (contour interval: $100\,\mathrm{m}^2\,\mathrm{s}^{-2}$). The tropics are not shown because the storm track is weak in this region. Reprinted from Albern et al. (2020). ©American Meteorological Society. Used with permission.

poleward shift of the extratropical storm tracks and their associated cloud fields (e.g., Kushner et al., 2001); and 3) the fact that high-level clouds warm at their base and cool at their top (Slingo and Slingo, 1988). The changes in lower-level cloud-radiative heating reflect a reduction in subtropical low-level clouds and an upward extension of extratropical low-level clouds, whose radiative effect in the present-day climate is dominated by cooling (Li et al., 2015).

The bowed structure of the cloud-radiative heating change in the upper troposphere reflects the meridional structure of the tropopause and is robust in climate change simulations in aquaplanet setups (Voigt and Shaw, 2016), and in Amip-like simulations with prescribed SST (Li et al., 2019; Albern et al., 2019) and with interactive SST (Ceppi and Shepherd, 2017; Voigt et al., 2019). Yet, the magnitude of the
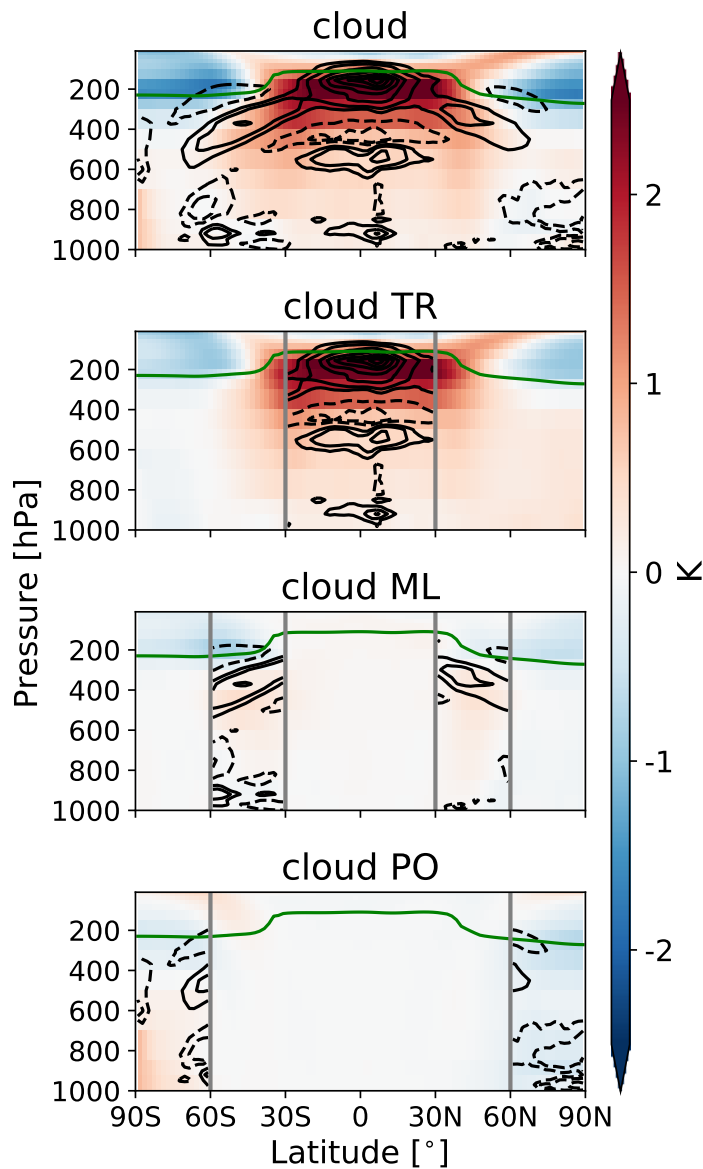
Figure 6.9.: Annual-mean global and regional cloud impacts on the temperature response (shading) vs change in atmospheric cloud-radiative heating (contours). The gray bars indicate the latitudinal boundaries of the tropical, midlatitude, and polar regions. The contour interval is $0.2 \, \text{K} \, \text{day}^{-1}$ for absolute values larger than $0.2 \, \text{K} \, \text{day}^{-1}$ and $0.1 \, \text{K} \, \text{day}^{-1}$ for absolute values smaller than $0.2 \, \text{K} \, \text{day}^{-1}$. The $0 \, \text{K} \, \text{day}^{-1}$ contour is not shown. The green lines show the tropopause height in the control simulation. Reprinted from Albern et al. (2020). ©American Meteorological Society. Used with permission.

change in cloud-radiative heating differs across models, which to a large extent is due to model shortcomings regarding the cloud-radiative heating in the present-day climate (Voigt et al., 2019). At the same time, the response in the lower-tropospheric polar region is uncertain across models, even when the lower-tropospheric response is limited due to prescribed sea surface temperatures and sea ice. For the

most part, the changes in cloud-radiative heating and the resulting temperature response are much larger for the tropical cloud impact than they are for the extratropical cloud impacts (e.g., compare the lower three panels in Fig. 6.9). Nevertheless, as indicated in the previous section, the changes in extratropical clouds appear to play an important role for the jet response. For the midlatitude cloud changes, this is likely because the cloud-radiative heating occurs right at the jet latitude and its poleward flank and modifies the baroclinicity in this region (see discussion below).

How do the changes in cloud-radiative heating influence the midlatitude circulation from a dynamical perspective? It is helpful to split the task of understanding how changes in cloud-radiative heating lead to the jet shifts into three parts. The first part corresponds to the direct, linear (dry) atmospheric response that follows from the imposed change in external heating. The second part includes understanding the resulting response in the (dry) eddy transports of heat and momentum that result from the linear response. The third part includes moist processes such as convection. The first part is relatively straightforward, but the second part is nonlinear and more difficult to quantify. In fact, understanding the eddy response to external heating lies at the root of understanding the circulation response to climate change, to the ozone hole, to stratospheric dynamical processes, and to sea surface temperature anomalies. It is a key and topical problem in climate dynamics. Regarding the third part, Voigt and Shaw (2016) found a 3-times-larger jet shift in the dry version of one of their aquaplanet models than they did in the moist full-physics version of the model. This indicated an important role of small-scale processes in compensating for some of the cloud-radiative heating, in particular due to convection and boundary layer mixing. In this section, we will focus on the second part, because the first part is relatively straightforward and the third part requires running a model, since there is no theoretical framework that predicts the response of small-scale processes to cloud-radiative heating changes.

The eddy response to external heating arises through a combination of two processes. These are 1) barotropic processes, in which changes in the configuration of the free-tropospheric flow influence the meridional propagation of waves (Hoskins and Karoly, 1981; Chen and Held, 2007; Simpson et al., 2009; Barnes et al., 2010; Barnes and Thompson, 2014); and 2) baroclinic processes, in which changes in the baroclinicity lead to changes in the eddy fluxes of heat (Lindzen and Farrell, 1980; Kushner and Held, 1998; O'Gorman, 2010; Butler et al., 2011) and – through the resulting changes in the "stirring" of the flow – changes in the meridional flux of wave activity and thus momentum fluxes aloft (e.g., Dickinson, 1969; Held, 1975).

For the specific case of the midlatitude response to cloud-radiative heating changes: Previous work has argued that the pattern of cloud-radiative heating in the upper troposphere that results from global warming (e.g., similar to that shown in Fig. 6.9, top) leads to a poleward shift of the midlatitude jet (e.g., Voigt and Shaw, 2016; Albern et al., 2019; Li et al., 2019; Voigt et al., 2019). In fact, a pattern of cloud-radiative heating very similar to that found in Fig. 6.9 leads to a poleward shift in the midlatitude jets when applied to the dynamical core of a global climate model (Li et al., 2019). In that case, the influence of the heating on upper-tropospheric baroclinicity appears to play a key role in driving responses in

the amplitudes of baroclinic eddies and thus the extratropical wave fluxes of heat. Figs. 6.10 and 6.11 suggest that a similar process is important for understanding at least a component of the results shown here. Note that in contrast to earlier figures, the results are shown as a function of logarithmic pressure to emphasize relationships in the upper troposphere. The eddy fluxes of heat and momentum are calculated based on 6-hourly data following Peixoto and Oort (1992). The meridional temperature gradient and eddy momentum flux convergence are calculated as

$$
\frac{1}{a}\frac{\partial \overline{T}}{\partial \varphi} \quad \text{and} \quad -\frac{1}{a \cdot \cos^2 \varphi}\frac{\partial (\overline{u'v'} \cdot \cos^2 \varphi)}{\partial \varphi}, \tag{6.1}
$$

respectively. Here, the overbar $\overline{(\cdot)}$ denotes the time mean and zonal mean, the prime $(\cdot)'$ is the eddy component (i.e., the deviation from the time mean or zonal mean), $a = 6371\,\mathrm{km}$ is the Earth's radius, T is the atmospheric temperature, $u'v'$ is the eddy momentum flux, and φ is the latitude.

The left column in Fig. 6.10 shows the response in the zonal-mean temperature (shading; reproduced from Fig. 6.9) along with the attendant response in the meridional temperature gradients (contours) for all cloud impacts. Note that the response in the meridional temperature gradients dominate the total changes in the baroclinicity and thus the Eady growth rate (Fig. B.1). As expected, the largest response in the meridional temperature gradient are found on the poleward flanks of the tropical upper-tropospheric temperature increases (about 40-50°N/S) (Fig. 6.10, left column) and are dominated by tropical cloud changes, which yield the largest temperature response of all three regions due to enhanced tropical heating (Fig. 6.10, left column, shading). The response in the meridional temperature gradients associated with midlatitude and polar cloud changes are relatively modest. Note that the largest meridional temperature gradient and eddy heat flux responses are found in the upper troposphere, even though the largest values in the control simulation are found in the lower troposphere around 800-900 hPa.

If the changes in cloud-radiative heating directly influence the eddy fluxes of heat, then we would expect to see three relationships hold in the results: 1) the response in the eddy fluxes of heat should be downgradient (i.e., diffusive) with respect to the response in atmospheric temperatures; 2) the response in the eddy fluxes should be dominated by their transient rather than stationary components, since the transient component is most closely associated with baroclinic eddies; and 3) the response in the eddy fluxes should be most clearly diffusive at upper tropospheric levels, where the temperature response is forced directly by the changes in the cloud-radiative heating and not solely by the resulting changes in atmospheric dynamics. Though not perfect, all three relationships are evident in the model responses (Fig. 6.10, second and third columns): The changes in the transient eddy fluxes of heat are largely downgradient in the upper troposphere. The diffusive nature of the heat fluxes is most clear in association with the tropical cloud impact, but is also apparent for the midlatitude and polar cloud impacts.

To the extent that most baroclinic eddies do not extend into the lower stratosphere, increases in the transient eddy fluxes of heat in the upper troposphere should lead to increases in the so-called stirring of the upper-tropospheric flow. Increases in the amplitude of the stirring should, in turn, lead to increases in the meridional propagation of Rossby waves and thus the convergence of the eddy momentum flux.
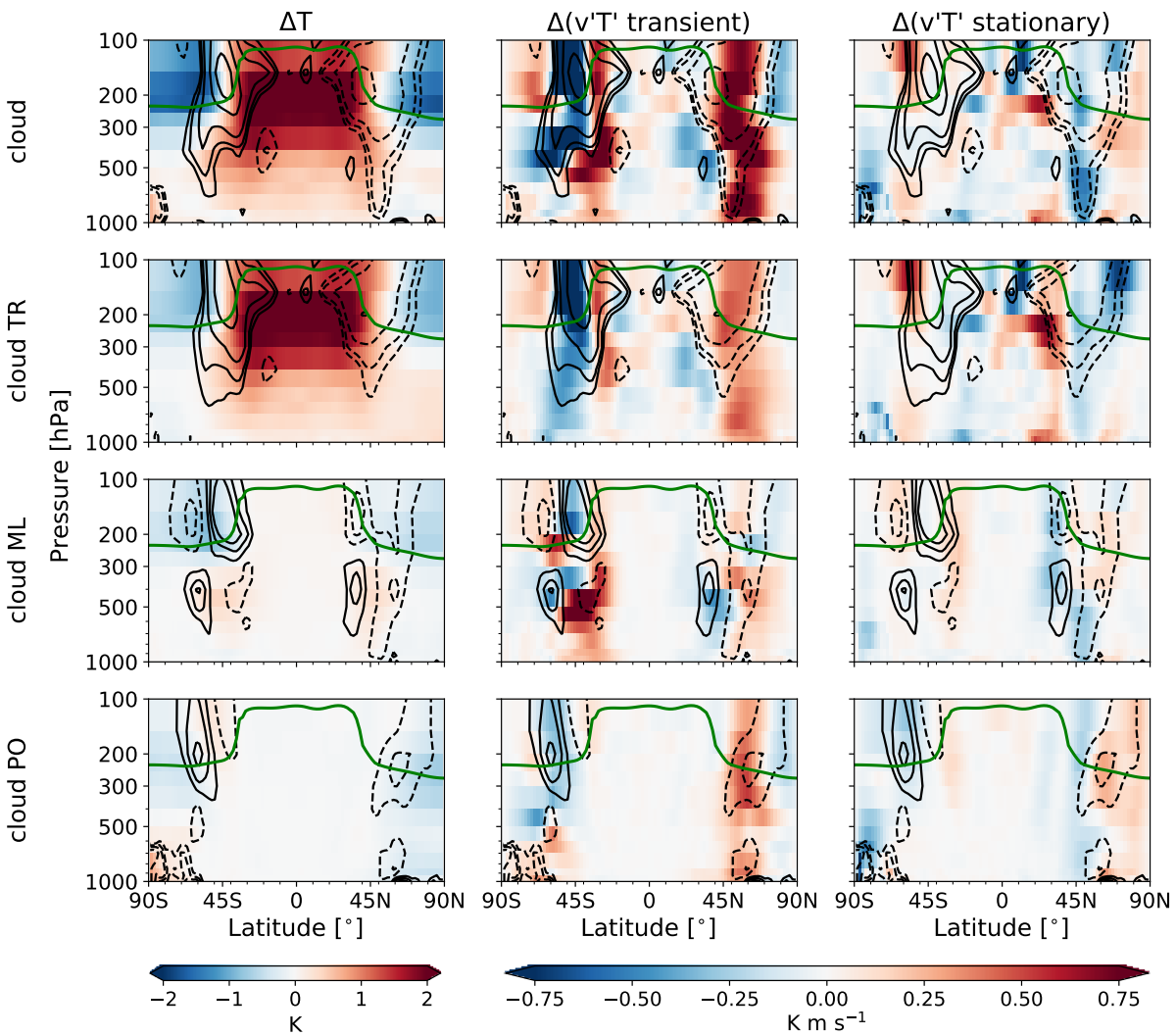
Figure 6.10.: Cloud impacts on the response of the annual-mean zonal-mean (left) atmospheric temperature, (middle) transient eddy heat flux, and (right) stationary eddy heat flux (shading), overlaid by responses in the meridional temperature gradient (contours). The contours are in intervals of $0.5\,\mathrm{K}\,(10^3\mathrm{km})^{-1}$ between -4 and $-0.5\,\mathrm{K}\,(10^3\mathrm{km})^{-1}$ and between 0.5 and $4\,\mathrm{K}\,(10^3\mathrm{km})^{-1}$, with additional contours for ± 0.3 and $\pm 0.2\,\mathrm{K}\,(10^3\mathrm{km})^{-1}$ for the global and tropical cloud impacts, and ± 0.3, ± 0.2, and $\pm 0.1\,\mathrm{K}\,(10^3\mathrm{km})^{-1}$ for the midlatitude and polar cloud impacts. The green lines show the tropopause height in the control simulation. Reprinted from Albern et al. (2020). ©American Meteorological Society. Used with permission.

The first two columns of Fig. 6.11 show the responses in the transient eddy momentum flux convergence (shading; first column) and stationary eddy momentum flux convergence (shading; second column) overlaid with the responses in the meridional temperature gradients (contours). The third column shows the total responses in the eddy momentum flux convergence (stationary plus transient component; shading) overlaid with the responses in the zonal-mean zonal wind. Consistent with our hypothesis, the largest responses in the transient eddy momentum flux convergence lie within – albeit on the poleward side of – the largest responses in the meridional temperature gradient (Fig. 6.11, left column). The re-
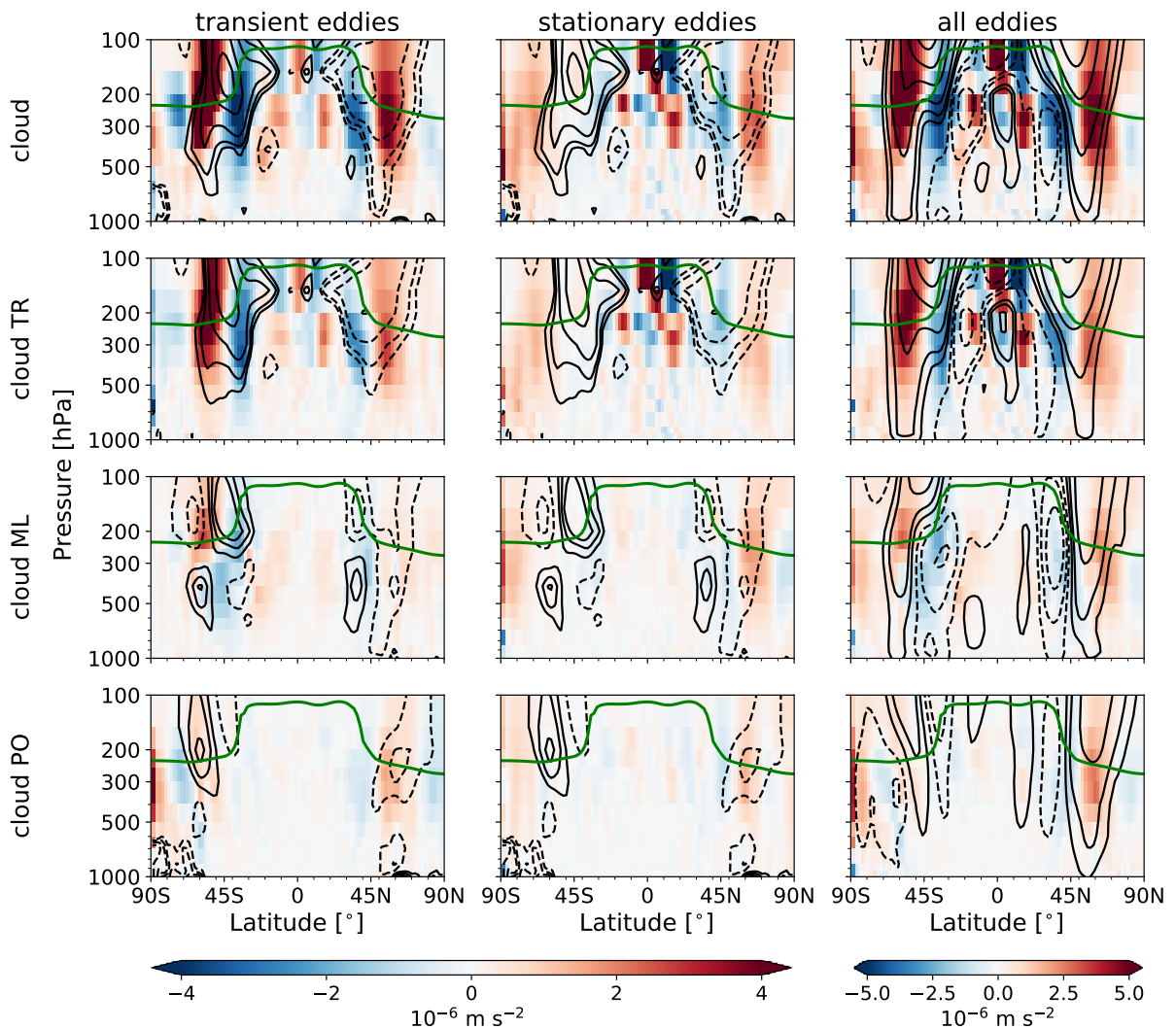
Figure 6.11.: Cloud impacts on the response of the (left) transient, (center) stationary, and (right) total eddy momentum flux convergence (shading), overlaid by responses in the meridional temperature gradient (contours in the first and second columns; contour intervals are as in Fig. 6.10) or responses in the zonal wind (contours in the third column). The contours for the zonal wind are in intervals of $1\,\mathrm{m\,s^{-1}}$ between -4 and -1 $\mathrm{m\,s^{-1}}$ and between 1 and 4 $\mathrm{m\,s^{-1}}$, with additional contours for ± 0.5 and $\pm 0.25\,\mathrm{m\,s^{-1}}$ for the global and tropical cloud impacts, and ± 0.5, ± 0.25, and $\pm 0.1\,\mathrm{m\,s^{-1}}$ for the midlatitude and polar cloud impacts. The green lines show the tropopause height in the control simulation. Reprinted from Albern et al. (2020). ©American Meteorological Society. Used with permission.

lationships are most clear for the global and tropical cloud impacts. Interestingly, the midlatitude and polar cloud impacts are marked by more substantial responses in the stationary eddy momentum fluxes in the Northern Hemisphere, which is consistent with the results of Simpson et al. (2014), who found that the stationary component of the eddy momentum flux is apparently important in simulations with continents, especially in the Northern Hemisphere during DJF. The responses in the stationary eddy fluxes are important, but they are not clearly linked to changes in tropospheric baroclinicity and the responses

are more difficult to interpret physically. The zonal wind response is – as expected – consistent with the response of the eddy momentum fluxes (Fig. 6.11, right column), and the responses in the surface flow follow from the attendant responses in the vertically integrated momentum transport (Vallis, 2017). Yet, the results indicate that the linkages between baroclinicity and transient eddies are not the complete story in the Northern Hemisphere, and that the stationary component of the eddy momentum flux cannot be neglected in simulations with continents and a seasonal cycle. The stationary component of the eddy momentum flux is important for regional cloud impacts outside of the tropics.

Together the results in Figs. 6.9-6.11 suggest that the jet responses to cloud-radiative changes are at least qualitatively consistent with the following reasoning: 1) cloud-radiative changes influence upper-tropospheric baroclinicity and thus the available potential energy for wave motions; 2) the changes in baroclinicity lead to anomalous downgradient wave fluxes of heat associated with transient waves; 3) the changes in the transient wave fluxes of heat and thus the vertical propagation of wave activity lead to changes in the so-called stirring of the upper-tropospheric flow; and 4) the changes in stirring lead to changes in the meridional flux of wave activity and thus eddy momentum fluxes aloft. Whether the cloud-radiative heating change leads to a shift or strengthening of the jet presumably depends on whether the changes in upper-tropospheric baroclinicity project onto the climatological-mean jet or its poleward flank.

6.4. Conclusions

We investigate the impact of regional cloud-radiative changes on the annual-mean, DJF, and JJA jet stream responses to a uniform 4 K SST increase across regions, using the atmospheric component of the ICON model. We apply the cloud-locking method, and isolate the atmospheric pathway of the cloud impact by prescribing SST (Voigt et al., 2019). We summarize the main findings of this study by answering the research questions that we posed in the introduction:

1. Are tropical, midlatitude or polar cloud-radiative changes more important for the global cloud impact on the zonal wind, jet stream, and storm track responses to global warming? Do the results depend on the season and the region?

   The global cloud impacts on the 850 hPa zonal wind, jet strength, and storm track responses are dominated by significant tropical cloud impacts across seasons, especially in the North Atlantic and Southern Hemisphere. The regional cloud impacts on the zonal wind response are largely zonally symmetric. The tropical and midlatitude cloud impacts contribute substantially to the annual-mean and DJF poleward jet shifts in most regions. The polar cloud impact contributes to the poleward jet shifts in the three northern hemispheric regions, but shifts the Southern Hemisphere jet equatorward. Thus, while in principle all clouds can contribute to the zonal wind, jet stream, and storm track responses, our study highlights the importance of tropical cloud changes.

2. Can we understand the impact of regional cloud-radiative changes on the zonal wind and jet responses based on (established) dynamical arguments?

   While the temperature response to cloud-radiative heating is difficult to understand, the zonal wind response to cloud-induced temperature changes can be understood from dry dynamics and previous work with idealized dry models. The circulation changes are broadly consistent with the influence of cloud-radiative changes on upper-tropospheric baroclinicity. For example, increases in the upper-tropospheric meridional temperature gradients due to cloud-radiative changes are associated with 1) anomalously poleward eddy fluxes of heat and thus vertical wave propagation and 2) anomalous eddy momentum flux convergence aloft consistent with enhanced stirring of the upper-tropospheric flow. These relationships are most prevalent for the tropical cloud changes and weaker for the midlatitude and polar cloud impacts. The transient component of the eddy momentum fluxes dominates the annual-mean global and tropical cloud impacts, whereas the stationary component is also important for the midlatitude and polar cloud impacts in the Northern Hemisphere.

7. The Impact of Cloud-Radiative Changes on the North Atlantic Jet Response During Winter

In this chapter, we address research question 3 "Do cloud-radiative changes contribute robustly to the wintertime response of the North Atlantic jet stream to global warming, and which clouds are most important?". To this end, we answer the following more detailed sub-questions:

1. What aspects of the global warming response over the North Atlantic-European region during boreal winter are robust across coupled and atmosphere-only climate models?

2. How much of the robust circulation response can be attributed to cloud-radiative changes, and is the cloud impact robust across models?

3. Which regional cloud-radiative changes are most important for the circulation response over Europe, and how can we understand their impact?

The structure of this chapter is as follows: In section 7.1, we identify which regional responses of the zonal wind and jet stream to global warming over the North Atlantic-European region are robust across simulations with coupled climate models and simulations with atmosphere-only models with prescribed sea-surface temperatures. In section, 7.2, we investigate the global cloud-radiative impact in ICON, MPI-ESM and IPSL-CM5A to study whether it contributes to the robust circulation response, and whether it is robust across the three models. The global cloud impact in ICON is decomposed into regional cloud impacts in section 7.3 to investigate which regional cloud impact dominates the global cloud impact. We conclude with the main results in section 7.4.

7.1. Robust Wintertime Circulation Response over the North Atlantic-European Region

In this section, we investigate the global warming response of the wintertime circulation over the North Atlantic-European region. We determine which regional responses in the zonal wind and jet stream to global warming are robust across simulations with coupled climate models and simulations with atmosphere-only General Circulation Models (GCMs) with prescribed SST and sea ice concentrations. For the simulations with coupled climate models, we investigate the historical simulation (years 1975-2004) and the RCP8.5 simulation (years 2070-2099) from 37 models that participated in CMIP5 (Taylor et al., 2012). For the simulations with atmosphere-only GCMs, we investigate output from 11 models that performed the Amip, Amip4K and AmipFuture simulations (years 1979-2008) of CMIP5 (Taylor et al., 2012). The models are listed in Tabs. 3.1 and 3.2.

Fig. 7.1 shows the model-mean zonal wind response at 850 hPa, Δu_{850}, in the RCP8.5, AmipFuture and Amip4K simulations (panels a-c). In the model mean, all three scenarios show a poleward shift and strengthening of the jet stream over the North Atlantic ocean basin, an eastward extension of the North Atlantic jet stream towards Europe, and a strengthening of the wind maximum over Europe (Fig. 7.1a-c). The responses over Europe are robust across models in all three scenarios whereas the models do not agree on the u_{850} strengthening on the poleward flank of the North Atlantic jet stream in the coupled models, and on the weakening on the equatorward flank of the North Atlantic jet stream in the atmosphere-only models.

In addition to the CMIP5 simulations, we performed Amip-like simulations with ICON that apply the cloud-locking method and with ICON, and the atmospheric components of MPI-ESM and IPSL-CM5A that apply the cloud- and water vapor-locking method (cf. section 4.3.3). The ICON simulations with locked clouds are the same as in chapters 5 and 6. The ICON simulations with locked clouds and locked water vapor, and the MPI-ESM and IPSL-CM5A simulations are taken from Voigt et al. (2019). All three models show the eastward extension of the North Atlantic jet stream and the u_{850} strengthening
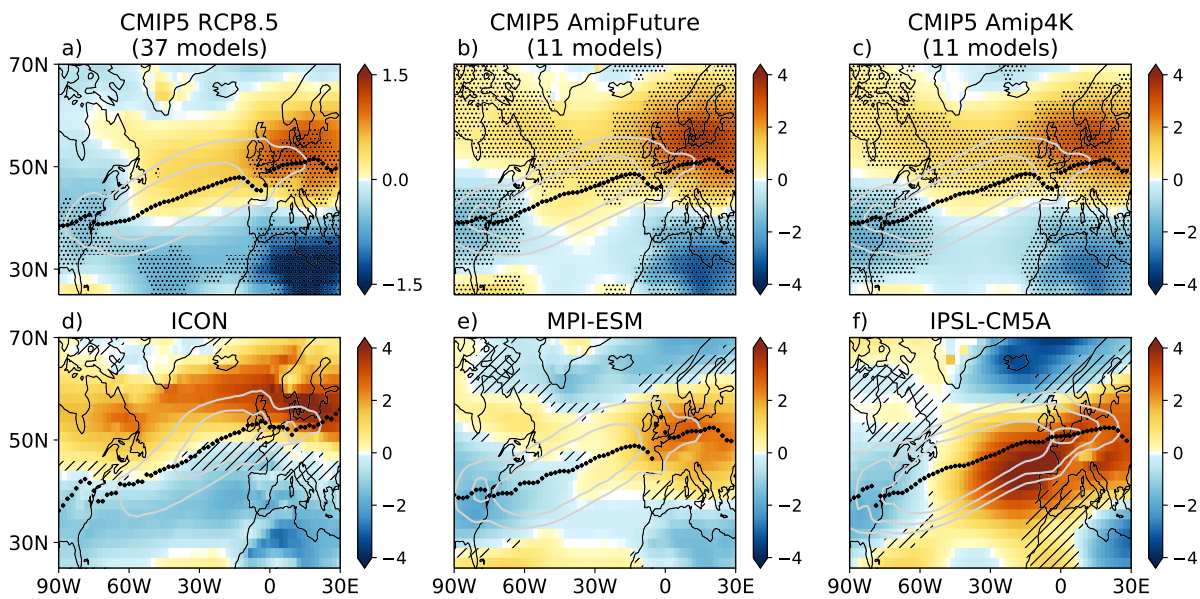
Figure 7.1.: Response of the 850 hPa zonal wind u_{850} to global warming. Shown are the model-mean responses for the RCP8.5 (a), AmipFuture (b) and Amip4K (c) scenarios. The bottom row shows the total locked response to the uniform 4 K SST increase in ICON (d), MPI-ESM (e), and IPSL-CM5A (f) that apply the cloud- (ICON) and cloud- and water vapor-locking (MPI-ESM and IPSL-CM5A) methods. The black dots show the model-mean jet latitude in the historical (a) and Amip (b, c) simulations, as well as in the control simulations of ICON (d), MPI-ESM (e) and IPSL-CM5A (f). The contours show the 8, 10 and 12 m s^{-1} u_{850} isolines from the control simulations. Stippling in the first row indicates where more than 80% of the models agree on the sign of the response. Hatching in the bottom panels indicates where the sign of the responses in ICON, MPI-ESM and IPSL-CM5A does not agree with the sign of the robust Amip4K response.

over Europe (Fig. 7.1d-f). The latter is limited to central to northern Europe in ICON and extends to southern Europe in MPI-ESM, IPSL-CM5A and the CMIP5 model mean. At the same time, the three models reflect the CMIP5 model uncertainties over the North Atlantic: ICON shows a poleward jet shift across the North Atlantic while MPI-ESM and IPSL-CM5A exhibit a jet strengthening over the eastern part of the North Atlantic, and in IPSL-CM5A, the jet even shifts equatorward over the eastern North Atlantic close to France and the Iberian Peninsula. Note that for ICON, we only show the total response for the simulations with interactive water vapor, because the pattern of the response is very similar for the simulations with free and locked water vapor (cf. section 4.3.3 and section 7.2).

Fig. 7.2 contrasts the jet response over Europe (0°-25°E) with the jet response over the North Atlantic (60°W-0°) in all CMIP5 models, ICON, MPI-ESM, and IPSL-CM5A. In both regions, most models exhibit poleward jet shifts of up to 2.5°. At the same time, several models exhibit an equatorward jet shift over the North Atlantic which is less pronounced over Europe. Note that some models (CMCC-CMS and CSIRO-Mk3-6-0 for RCP8.5; bcc-csm1-1, IPSL-CM5B and MIROC5 for AmipFuture and Amip4K) exhibit very large jet shifts of more than 10° and are not shown in Fig. 7.2. These large jet shifts are due to the fact that the models exhibit very weak jet streams over Europe, resulting in a weak and flat u_{850} profile that does not exhibit a clear peak and is very sensitive to small changes in its shape.
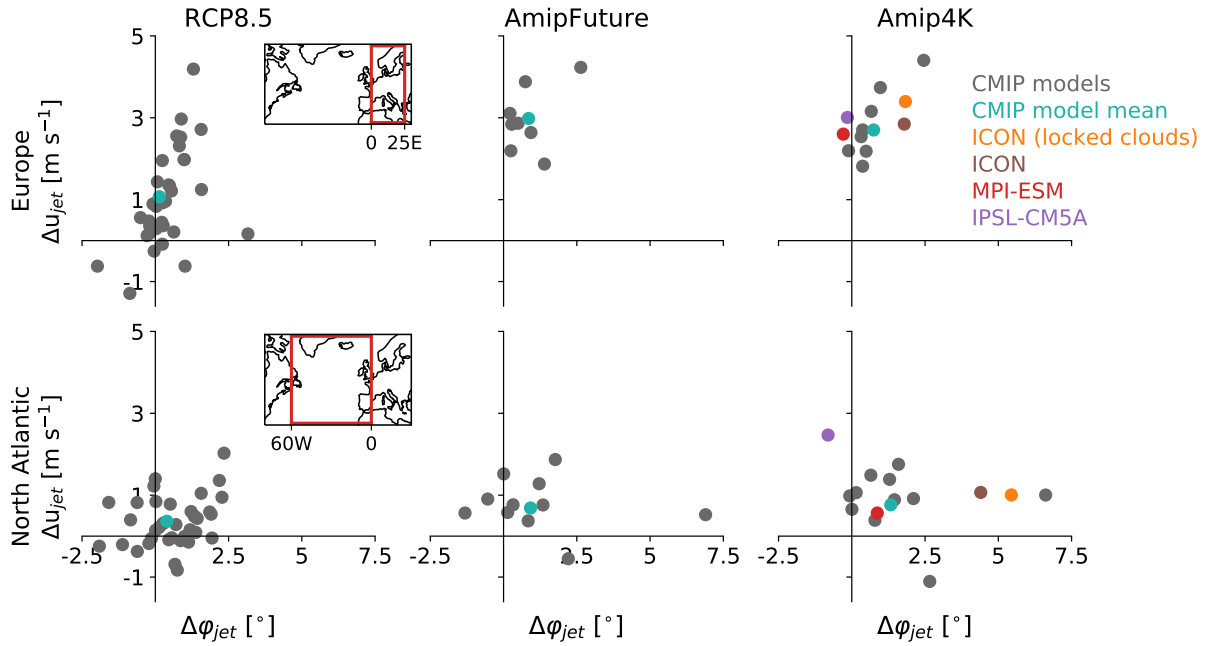
Figure 7.2.: Zonal-mean jet shift $\Delta\varphi_{jet}$ versus jet strengthening Δu_{jet} over Europe (0°-25°E, top row) and over the North Atlantic (60°W-0°, bottom row). The regions are highlighted in the small inserted maps. Depicted are the responses in the individual CMIP5 models and the CMIP5 model mean for the RCP8.5 (left), AmipFuture (center) and Amip4K (right) scenarios. The Amip4K panels also show the total locked responses in ICON (for locked clouds in orange and for locked clouds and locked water vapor in brown), MPI-ESM and IPSL-CM5A.

Larger differences between the North Atlantic and Europe are found in the jet strength response. In the atmosphere-only models, the jet strengthening over Europe is up to twice as large as over the North Atlantic. The same general behavior is found for the coupled climate models. Yet, several coupled models show only small responses in the jet strength over Europe, reflecting the larger inter-model variability in the RCP8.5 response compared to the Amip4K and AmipFuture responses (which is also due to the larger ensemble). For the Amip4K response, ICON, MPI-ESM and IPSL-CM5A lie well within the jet responses of the atmosphere-only CMIP5 models both over Europe and over the North Atlantic and for the jet strengthening and the jet shift (Fig. 7.2, right).

In conclusion, our results show that the coupled models and the atmosphere-only models exhibit an eastward extension of the jet streams towards Europe combined with an u_{850} strengthening over Europe during boreal winter. The jet strengthening over Europe is enhanced compared to the jet strengthening over the North Atlantic and robust across models and simulation setups. In the following sections, we focus our analysis on the eastward jet extension and the u_{850} increase over (northern) Europe and refer to it as "jet exit strengthening".

7.2. Global Cloud-Radiative Impact on the Circulation Response in ICON, MPI-ESM and IPSL-CM5A

In this section, we investigate how much global cloud-radiative changes contribute to the jet exit strengthening during boreal winter, and if the cloud-radiative impact is robust across ICON, MPI-ESM and IPSL-CM5A. As mentioned in section 7.1, we apply the cloud-locking and the cloud- and water vapor-locking methods for ICON, and the cloud- and water vapor-locking method for MPI-ESM and IPSL-CM5A. Fig. 7.3 shows the zonal wind response at 850 hPa in ICON, MPI-ESM and IPSL-CM5A. In ICON, the different treatment of water vapor, i.e., free water vapor versus locked water vapor, hardly affects the pattern and magnitude of the total locked response and the cloud-radiative impact over the North Atlantic-European region (Fig. 7.3). Thus, we can directly compare the cloud-radiative impact in the ICON simulations with free water vapor with the cloud-radiative impacts in the ICON, MPI-ESM and IPSL-CM5A simulations with locked water vapor.

The cloud-radiative impact and the SST impact contribute significantly to the jet exit strengthening in all three models (Fig. 7.3). Over the North Atlantic, however, the impact of cloud-radiative changes differs between the three models so that the cloud impact can be considered as one source of model uncertainty in the circulation response over this region, which is consistent with the non-robust circulation response over the North Atlantic (cf. section 7.1). The water vapor-radiative impact counteracts the jet exit strengthening, and has a robust dipole-shaped impact on the zonal wind response over the North Atlantic and over Europe.

The opposing impacts of cloud and water vapor changes on the jet response were also found for the annual-mean zonal-mean jet shift in aquaplanet (Voigt and Shaw, 2015) and present-day simulations
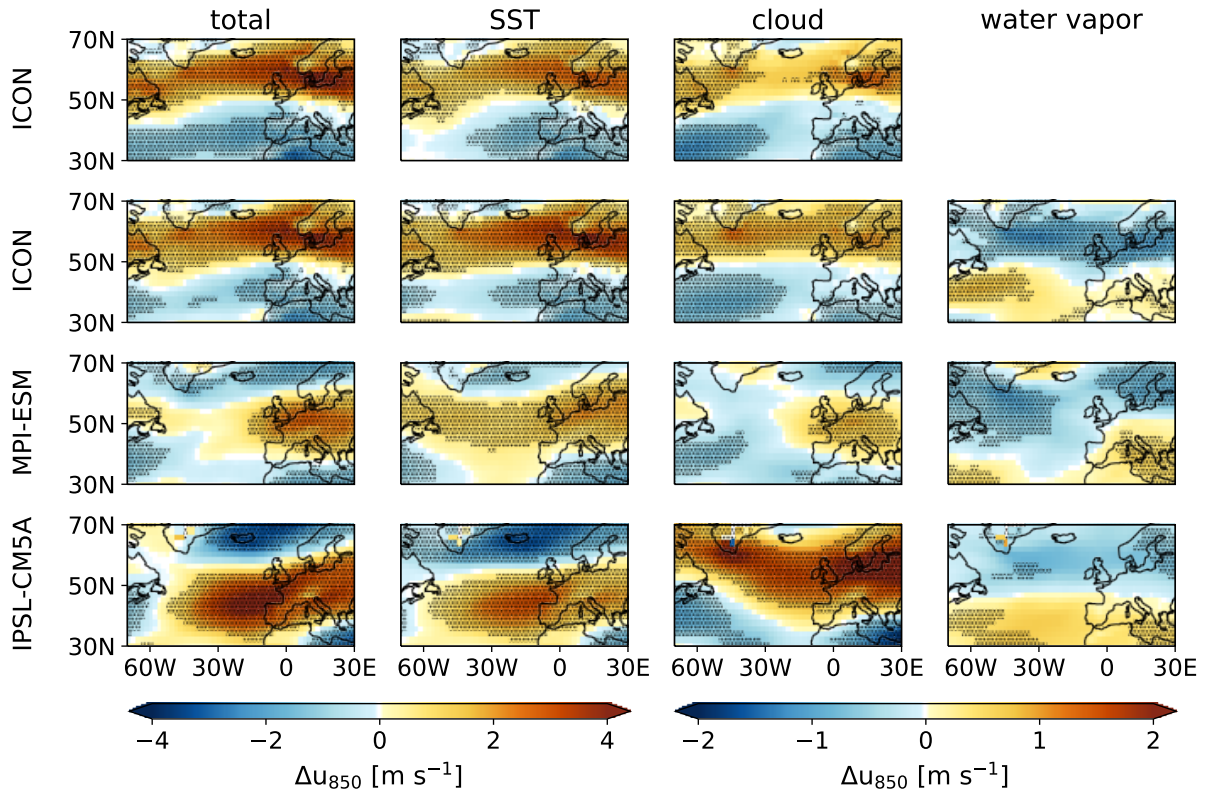
Figure 7.3.: Response of the zonal wind at 850 hPa, Δu_{850}, in ICON with locked clouds (first row), and in ICON (second row), MPI-ESM (third row), and IPSL-CM5A (fourth row) with locked clouds and locked water vapor. The total response (first column) is decomposed into the SST impact (second column), cloud-radiative impact (third column) and water vapor-radiative impact (fourth column). Stippling indicates where the response is statistically significant based on the 5th-95th-percentile range of the bootstrap distribution for each grid point.

(Voigt et al., 2019). They were related to the differing impacts of cloud and water vapor changes on the atmospheric temperature response to global warming. In the aquaplanet simulations of Voigt and Shaw (2015), cloud changes acted to enhance meridional temperature gradients throughout the troposphere via warming in the tropical middle and upper troposphere and cooling in the high-latitude lower troposphere. At the same time, water vapor changes led to a reduction in meridional temperature gradients by upper-tropospheric cooling at most latitudes and high-latitude warming throughout large parts of the troposphere. A qualitatively similar temperature response is also found in our simulations, though cloud-radiative changes warm the high-latitude lower troposphere in ICON and MPI-ESM, in particular in the Northern Hemisphere (Fig. C.1; cf. Voigt et al., 2019). This reduces the lower-tropospheric meridional temperature gradient in these two models, which might explain that the cloud-induced circulation response is smaller in ICON and MPI-ESM than in IPSL-CM5A (Shaw et al., 2016; Voigt et al., 2019). Note that the changes in high-latitude lower-tropospheric atmospheric cloud-radiative heating were found to be strongly model dependent in both aquaplanet (Voigt and Shaw, 2016) and present-day

(Voigt et al., 2019) simulations, which can yield different temperature responses in the different models and simulation setups.

Even though cloud changes contribute robustly to the jet exit strengthening, the magnitude of the cloud impact varies strongly between ICON, MPI-ESM and IPSL-CM5A, as does the total response (Fig. 7.3). Thus, we investigate the relative contribution of the cloud impact to the total u_{850} response to determine if the relative cloud contribution is similar in the three models even though the absolute responses differ. We focus on the European region with a robust u_{850} response (cf. Fig. 7.1), and investigate the area-mean response. To define the area, we determine where the u_{850} responses in the coupled and atmosphere-only CMIP5 models, and in ICON, MPI-ESM and IPSL-CM5A exceed a certain percentage of the Δu_{850} maximum over Europe. Additionally, we restrict the area to lie within the region in which the total locked responses in ICON, MPI-ESM and IPSL-CM5A agree with the robust Amip4K response. The European area which fulfills the above conditions covers the region 50°N-60°N and 5°W-25°E, which corresponds to a threshold of 80-85% of the Δu_{850} maximum over Europe (Fig. C.2). The lateral boundaries of the area are largely independent of the threshold for the exceeded percentage of the Δu_{850} maximum over Europe. The longitudinal boundaries differ depending on the threshold, but the area-mean u_{850} response is largely independent of the exact location of the longitudinal boundaries (not shown).

Tab. 7.1 summarizes the area-mean u_{850} response over Europe in ICON, MPI-ESM and IPSL-CM5A by showing absolute changes and relative contributions to the total response. In ICON and MPI-ESM, cloud changes contribute to about 25% of the total u_{850} response over Europe, while most of the total response is due to the SST increase (Tab. 7.1). In IPSL-CM5A, however, the roles of the SST increase and the cloud-radiative changes are switched and the total response can be largely attributed to cloud-radiative changes. In all three models, water vapor changes weaken u_{850} over Europe by about 30%. Thus, the cloud impact and the water vapor impact almost cancel each other out in ICON and MPI-ESM, while the cloud impact dominates in IPSL-CM5A.

The differing relations between the cloud and water vapor impacts in MPI-ESM and IPSL-CM5A were also found for the annual-mean zonal-mean circulation response to a uniform 4 K SST increase in aquaplanet simulations of the two models (Voigt and Shaw, 2015). Voigt and Shaw (2015) related this result to the model-dependent contributions of cloud and water vapor changes on the temperature response in the tropical upper troposphere and lower stratosphere (UTLS). The warming of the tropical UTLS due to cloud changes was found to be similar in both models. The cooling due to water vapor changes was similar to the cloud-induced warming in MPI-ESM but reduced by a factor of 3 in IPSL-CM5A. In our simulations, the magnitude of the cloud-induced warming of the tropical UTLS is similar in ICON and IPSL-CM5A but reduced in MPI-ESM (Fig. C.1, third column). For the water vapor-induced cooling of the tropical UTLS, we find a slightly reduced cooling in IPSL-CM5A compared to ICON and MPI-ESM (Fig. C.1, fourth column), which might explain the importance of cloud changes in IPSL-CM5A. At the same time, it does not explain why the cloud impacts on the jet exit strengthening are

Table 7.1.: Area-mean zonal wind response at 850 hPa over Europe (50°N-60°N, 5°W-25°E) in m s^{-1} in ICON, MPI-ESM and IPSL-CM5A. The numbers in the brackets give the relative contributions of the SST impact, cloud-radiative impact and water vapor-radiative impact to the total response in percent.

Model	total response	SST impact	cloud impact	water vapor impact
ICON (locked clouds)	2.84	2.05 [72.10]	0.79 [27.90]	–
ICON	2.59	2.71 [104.77]	0.71 [27.42]	-0.83 [-32.19]
MPI-ESM	1.61	1.63 [101.43]	0.36 [22.33]	-0.38 [-23.76]
IPSL-CM5A	2.08	0.58 [28.00]	2.00 [96.28]	-0.50 [-24.28]

similar in ICON and MPI-ESM. This indicates that processes other than changes in UTLS temperatures and meridional temperature gradients dominate and should be investigated further.

To better understand the different magnitudes of the cloud-radiative impacts on the u_{850} response in ICON, MPI-ESM and IPSL-CM5A, we investigate the changes in cloud-radiative heating derived from Partial-Radiative Perturbation (PRP) calculations (cf. section 4.4). For ICON and MPI-ESM, the PRP calculations are based on the locked simulations and show the changes in temperature tendencies due to changes in cloud-radiative properties under global warming (forward PRP). For IPSL-CM5A, we show the mean over forward and backward PRP calculations that are based on the locked simulations (cf. section 4.4). Differences between the forward and backward PRP calculations are small (not shown; cf. Voigt and Shaw (2016) for aquaplanet simulations and Voigt et al. (2019) for present-day MPI-ESM simulations with a slab ocean).

In the zonal mean, the largest changes in atmospheric cloud-radiative heating in ICON, MPI-ESM and IPSL-CM5A are found in the tropical and midlatitude upper troposphere (cf. Voigt et al. (2019) for the annual-mean; during DJF, the heating and cooling patterns are slightly shifted to the South, following the ascending branch of the Hadley circulation). Previous studies proposed that changes in high-level ice clouds under global warming play an important role for the response of the midlatitude circulation to global warming (Voigt and Shaw, 2015, 2016; Voigt et al., 2019). We therefore focus our analysis on the upper troposphere and investigate the regional vertical-mean changes in atmospheric cloud-radiative heating for a 200-hPa-thick layer below the wintertime tropopause.

In all three models, the changes in upper-tropospheric cloud-radiative heating peak over the western tropical Pacific and Maritime Continent with secondary peaks over the Indian Ocean and eastern tropical Pacific in ICON and MPI-ESM, and over the Southern Hemisphere central subtropical Pacific in IPSL-CM5A (Fig. 7.4). Albern et al. (2020) showed that tropical cloud-radiative changes dominate the u_{850} response to global warming in ICON. The changes in atmospheric cloud-radiative heating in MPI-ESM are similar to those in ICON in a sense that the largest changes in atmospheric cloud-radiative heating, which are of similar magnitude in both models, are found in the tropics while the changes over the
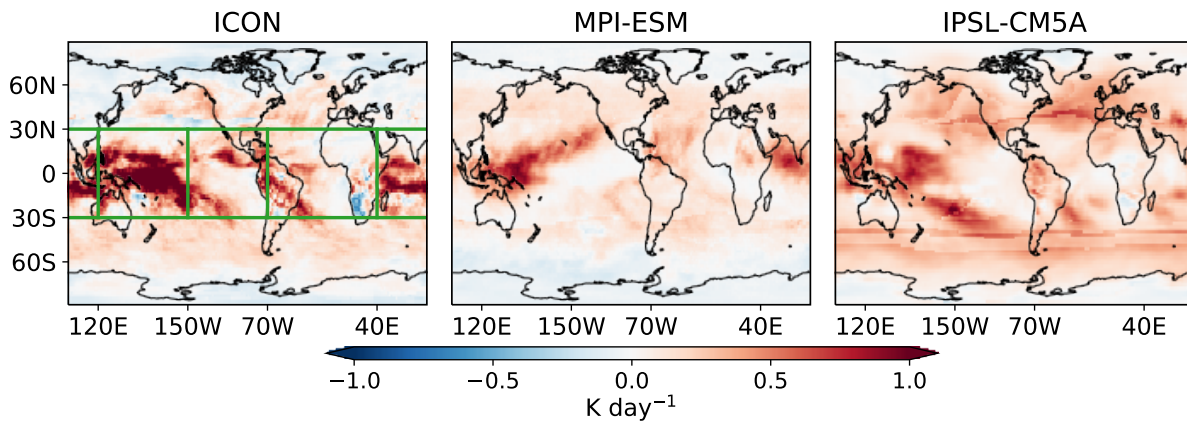
Figure 7.4.: Vertical-mean changes in atmospheric cloud-radiative heating for a 200-hPa-thick layer below the tropopause in ICON (left), MPI-ESM (center) and IPSL-CM5A (right). The green boxes in the left panel show the regions which are investigated in section 7.3.

midlatitudes and polar regions are smaller or even negative. This indicates that in MPI-ESM the tropical cloud-radiative changes also dominate the u_{850} response to global warming and that midlatitude and polar cloud changes play a minor role. A different response is found in IPSL-CM5A. In this model, the tropical peak in atmospheric cloud-radiative heating changes is smaller than in ICON and MPI-ESM, and the changes in upper-tropospheric atmospheric cloud-radiative heating in the midlatitudes are larger and of similar magnitude as across large parts of the tropics, except for the regions with peaks in atmospheric cloud-radiative heating changes. This indicates that midlatitude cloud-radiative changes might be more important for the midlatitude circulation response to global warming in IPSL-CM5A than in ICON and MPI-ESM because larger cloud-radiative heating changes occur around the jet. Yet, further investigations about the impact of tropical, midlatitude and polar cloud-radiative changes in MPI-ESM and IPSL-CM5A are needed to test these hypotheses about the contributions of tropical and midlatitude cloud changes to the midlatitude circulation responses in the two models (cf. Albern et al., 2020, for regional cloud impacts in ICON). Note that the qualitative differences in the magnitude and pattern of the change in atmospheric cloud-radiative heating between the models is independent of whether the the vertical mean is calculated over a 200 or 300 hPa thick layer below the tropopause.

To conclude, our results show that cloud-radiative changes contribute robustly to the jet exit strengthening over Europe, and can be considered as one source of model uncertainty in the circulation response over the North Atlantic. The absolute and relative contributions of the cloud impacts vary across ICON, MPI-ESM and IPSL-CM5A. At the same time, the relative contribution of water vapor changes is more robust in the three models. The differing magnitudes of the cloud-radiative impacts in the models can be related to differing magnitudes and patterns in the changes in atmospheric cloud-radiative heating between ICON, MPI-ESM and IPSL-CM5A.

7.3. Regional Cloud-Radiative Impact on the Circulation Response in ICON

In the last section, we showed that global cloud-radiative changes contribute robustly to the jet exit strengthening in ICON, MPI-ESM and IPSL-CM5A but that the magnitude of the cloud impact depends on the model. In this section, we focus on the ICON simulations with locked clouds and interactive water vapor to investigate which regional cloud-radiative changes are most important for the global cloud-radiative impact on the circulation response over the North Atlantic-European region, in particular on the jet exit strengthening.

Based on global maps, Albern et al. (2020) showed that tropical cloud-radiative changes dominate the annual-mean, wintertime and summertime global cloud-radiative impact on the midlatitude u_{850} response to global warming (cf. their Fig. 3). Here, we investigate the wintertime u_{850} response over the North Atlantic-European region in more detail. We find that tropical cloud-radiative changes dominate the global cloud-radiative impact over Europe, and thus the jet exit strengthening (Fig. 7.5a-b), while midlatitude and polar cloud-radiative changes have minor contributions over Europe (Fig. 7.5c-d). Over the North Atlantic, however, tropical, midlatitude and polar cloud changes all contribute to the poleward jet shift, and tropical cloud changes lead to a significant strengthening of the North Atlantic jet (cf. Albern et al., 2020). In contrast to the tropical, midlatitude and polar cloud changes, local cloud-radiative changes from a midlatitude region which covers eastern North America, the North Atlantic and Europe, lead to a slight weakening of the zonal wind and midlatitude jet stream over the North Atlantic-European region (Fig. 7.5e) (cf. Fig. 4.7 for the regions). Thus, our results show that tropical cloud-radiative changes dominate the jet exit strengthening while midlatitude and polar cloud changes play a minor role and local cloud changes over the North Atlantic-European region weaken the zonal wind and jet stream in this region.

In the next step, we investigate which tropical region is most important for the tropical cloud-radiative impact on the jet exit strengthening. Based on the regional changes in upper-tropospheric atmospheric cloud-radiative heating (Fig. 7.4), and under the assumption that the largest changes in tropical cloud-radiative heating have the largest impact on the midlatitude circulation response to global warming via tropical-extratropical teleconnections, we hypothesize that cloud-radiative changes over the tropical Pacific and Indian Ocean dominate the tropical cloud-radiative impact on the jet exit strengthening while cloud-radiative changes over the tropical Atlantic have a minor impact (cf. boxes in Fig. 7.4, left panel).

To test our hypothesis, Fig. 7.6 contrasts the impact of cloud-radiative changes over the Indian Ocean and tropical (western and eastern) Pacific, referred to as IOWPEP, to the impact of cloud-radiative changes over the tropical Atlantic, referred to as TA, on the u_{850} response over the North Atlantic-European region (cf. Fig. 4.7 for the regions). The Figure shows that most of the jet exit strengthening due to tropical cloud changes can indeed be attributed to cloud-radiative changes over the Indian Ocean and tropical Pacific (Fig. 7.6, left panel). Cloud changes over the tropical Atlantic also contribute to the jet exit strengthening but play a minor role (Fig. 7.6, right panel). Over the North Atlantic, IOWPEP
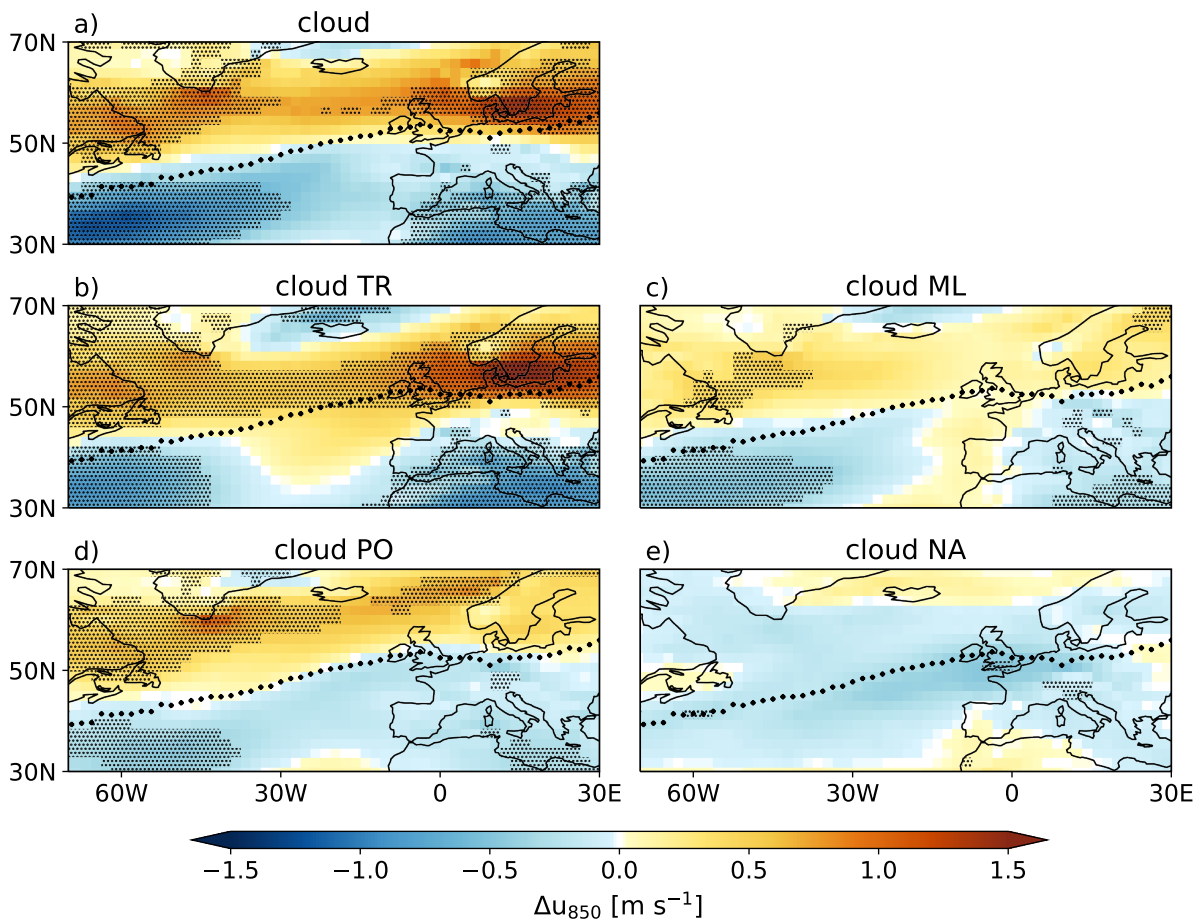
Figure 7.5.: Impact of global (a) and regional cloud-radiative changes over the tropics (b; cloud TR), midlatitudes (c; cloud ML), polar regions (d; cloud PO), and over a midlatitude region which covers parts of eastern North America, the North Atlantic and Europe (e; cloud NA) on the zonal wind response at 850 hPa, Δu_{850}, over the North Atlantic-European region (cf. Fig. 4.7 for the regions). Stippling indicates where the response is statistically significant based on the 5th-95th-percentile range of the bootstrap distribution for each grid point. The thick black dots indicate the jet latitude in the control simulation with locked clouds.

cloud changes dominate the poleward jet shift while TA cloud changes lead to an equatorward shift and strengthening of the jet over the eastern North Atlantic (cf. Fig. 7.6 to Fig. 7.5a). Note that due to non-linearities the sum of the IOWPEP and TA cloud impacts underestimates the tropical cloud-induced jet exit strengthening by up to $0.7 \, \text{m s}^{-1}$ (Fig. C.3a-c).

In ICON, the change in upper-tropospheric atmospheric cloud-radiative heating has three maxima. The largest response is found over the western tropical Pacific, followed by maxima over the Indian Ocean and over the eastern tropical Pacific (Fig. 7.4, left). Thus, in the next step, we investigate the individual cloud-radiative impacts from these three regions to determine if one of them dominates the tropical cloud-radiative impact on the jet exit strengthening (cf. Fig. 4.7 third row for the regions).
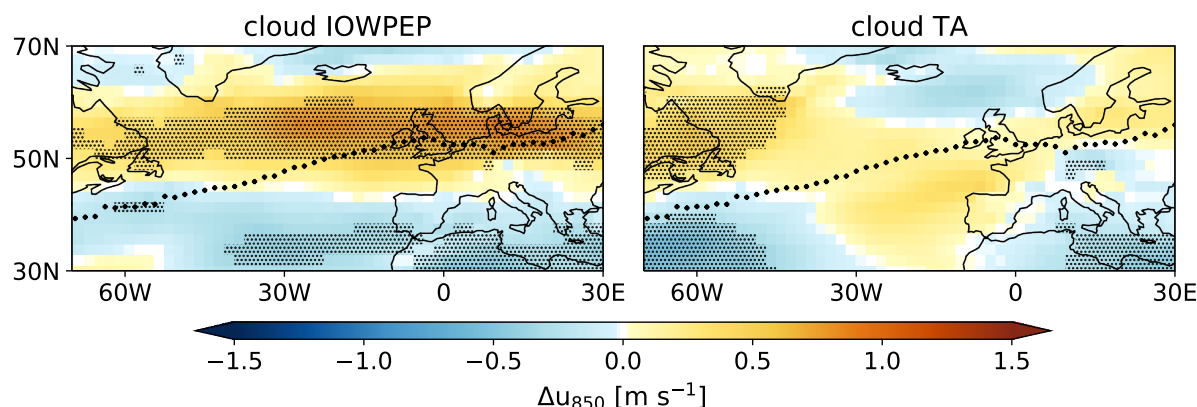
Figure 7.6.: Impact of cloud-radiative changes over the Indian Ocean and tropical Pacific (cloud IOWPEP, left) and over the tropical Atlantic (cloud TA, right) on the zonal wind response at 850 hPa, Δu_{850} (cf. Fig. 4.7 for the regions). Stippling and thick black dots as in Fig. 7.5.

Based on the changes in upper-tropospheric cloud-radiative heating, one would assume that the impact from cloud-radiative changes over the western tropical Pacific dominates the response over Europe as this region exhibits the largest changes in upper-tropospheric cloud-radiative heating changes (Fig. 7.4, left). Yet, this is not the case. The impacts from cloud changes over the Indian Ocean (cloud IO), western tropical Pacific (cloud WP) and eastern tropical Pacific (cloud EP) all contribute about equally to the jet exit strengthening. At the same time, the cloud impacts on the u_{850} response differ over the North Atlantic, where western tropical Pacific clouds shift the jet poleward, eastern tropical Pacific cloud strengthen the jet and shift it equatorward, and Indian Ocean clouds shift the jet poleward and weaken it (Fig. 7.7). For the Indian Ocean cloud impact, the u_{850} weakening even extends eastward over central to southern Europe while the Pacific cloud changes rather strengthen the zonal wind over this part of Europe.

The pattern of the zonal wind response over the North Atlantic-European region due to eastern tropical Pacific cloud changes is similar to that from tropical Atlantic cloud changes but the response is larger (Figs. 7.6 and 7.7). Thus, cloud changes over the eastern tropical Pacific and tropical Atlantic dominate the jet strengthening over the eastern North Atlantic. Note that the sum of the Indian Ocean, western tropical Pacific, eastern tropical Pacific, and tropical Atlantic cloud impacts is similar to the tropical cloud impact over Europe and large parts of the North Atlantic (Fig. C.3a, d, e). Some non-linearities are expected because we divide the tropics into smaller regions which might introduce large gradients at, in particular, the longitudinal boundaries of the regions because we do not smooth the cloud-radiative property fields.

In addition to the impacts from cloud changes over the Indian Ocean, western tropical Pacific and eastern tropical Pacific shown in Fig. 7.6 and Fig. 7.7, we investigated the impacts from simultaneous cloud changes over the Indian Ocean and western tropical Pacific (cloud IOWP) and over the western

95
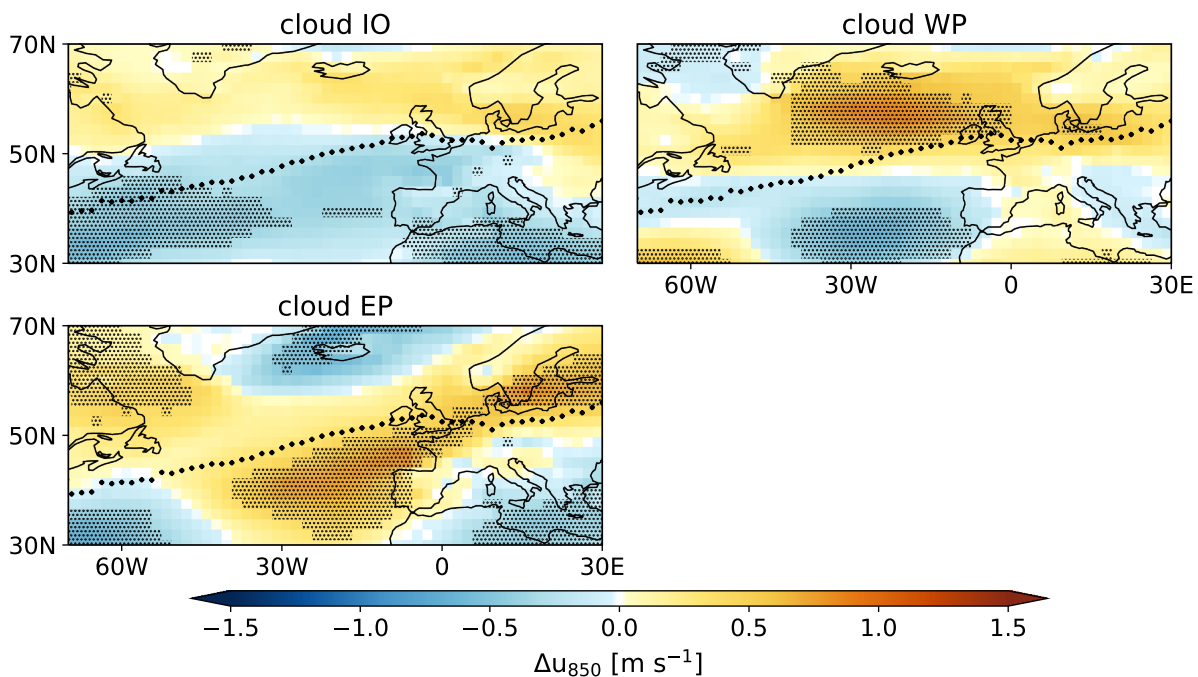
Figure 7.7.: Same as in Fig. 7.6, but for the impact of cloud-radiative changes over the Indian Ocean (cloud IO, top left), the western tropical Pacific (cloud WP, top right) and the eastern tropical Pacific (cloud EP, bottom) (cf. Fig. 4.7 for the regions).

and eastern tropical Pacific (cloud WPEP), respectively. However, the cloud impacts from these two additional regions also do not exhibit the jet exit strengthening that is found for the tropical cloud impact (Fig. C.4). Thus, we conclude that no smaller tropical region can be identified that dominates the tropical cloud-radiative impact on the jet exit strengthening. This indicates that large-scale processes and interactions, such as the Walker circulation over the tropical Pacific, are important for the circulation response over Europe. Further, the change in atmospheric cloud-radiative heating has a rather complex spatial structure, making it almost impossible to cut it into smaller regions without introducing artificial heating gradients.

How do tropical cloud changes impact the jet response over the North Atlantic-European region? To answer this question, we begin by arranging the tropical regions into groups depending on their cloud impact on the u_{850} response over the North Atlantic-European region. The tropical cloud impact seems to result from two superimposed responses. The first response is an equatorward jet shift over the eastern North Atlantic and a jet strengthening across large parts of the North Atlantic. This response is found for cloud EP and cloud TA, which form the first group (Figs. 7.6 and 7.7). The second response is a poleward jet shift with a dipole in the u_{850} response over the North Atlantic around the jet latitude from the control simulation. This response is found for cloud IOWPEP, cloud WP and cloud IO, which form

the second group (Figs. 7.6 and 7.7). The third group consists of cloud TR which, to first order, is the sum of the described responses (Fig. 7.5).

A key mechanism for tropical-extratropical teleconnections are Rossby waves, which develop due to anomalous tropical heating (e.g., review by Yuan et al., 2018, for tropical-polar teleconnections). On intraseasonal and interannual time scales, this heating can be caused by increased convection and latent heating related to the Madden Julian Oscillation (MJO Madden and Julian, 1971, 1972) or by SST anomalies related to the El Niño Southern Oscillation (ENSO), respectively. These two phenomena are the leading modes of tropical variability on these time scales. The tropical heating causes anomalous ascending motions and upper-tropospheric divergences. Rossby waves are then triggered, and, in the Northern Hemisphere, propagate over the North Pacific to North America and the North Atlantic (e.g., Jiménez-Esteve and Domeisen, 2020). In our case, the anomalous heating is mainly caused by upper-tropospheric changes in tropical atmospheric cloud-radiative heating.

To visualize possible Rossby waves, Fig. 7.8 shows the response of the stationary eddy stream function at 300 hPa to tropical cloud-radiative changes. Rossby waves of different signs are triggered in response to cloud changes in the smaller tropical regions. These Rossby waves propagate from the region of cloud heating over the North Pacific and North American continent and finally reach the North Atlantic (Fig. 7.8a-e). The eddy stream function responses can be arranged into the same groups as the u_{850} responses over the North Atlantic. In the first group, tropical Atlantic and eastern tropical Pacific cloud changes trigger Rossby waves that yield to an equivalent barotropic cyclonic eddy stream function anomaly over the eastern North Atlantic and an equivalent barotropic anticyclonic anomaly to the South (Fig. 7.8a, b and Fig. C.5a, b). This response is consistent with the equatorward jet shift in the eastern North Atlantic in response to tropical Atlantic and eastern tropical Pacific cloud changes. Note that the eddy stream function response to cloud EP is stronger than the response to cloud TA, as is the u_{850} response over the eastern North Atlantic.

In the second group, Indian Ocean and tropical Pacific (IOWPEP) and western tropical Pacific cloud changes trigger Rossby waves of the opposite sign from the first group, resulting in an equivalent barotropic anticyclonic eddy stream function anomaly over the southern North Atlantic and an equivalent barotropic cyclonic anomaly to the North (Fig. 7.8c, d and Fig. C.5c, d). The response in the eddy stream function is consistent with the poleward shift of the North Atlantic jet stream in response to these cloud changes. Indian Ocean cloud changes, the third member of the second group, trigger a weaker eddy stream function response over the North Atlantic which is not barotropic, so that the jet response cannot be related to a Rossby wave (Fig. 7.8e and Fig. C.5e). This might indicate that transient rather than stationary responses in the eddy momentum fluxes are more important for the impact of Indian Ocean cloud changes.

For the third group, the tropical cloud changes, an equivalent barotropic anticyclonic eddy stream function anomaly is located central Europe with an equivalent barotropic cyclonic anomaly to the North. This response can be related to the eastward extension of the North Atlantic jet stream towards Europe
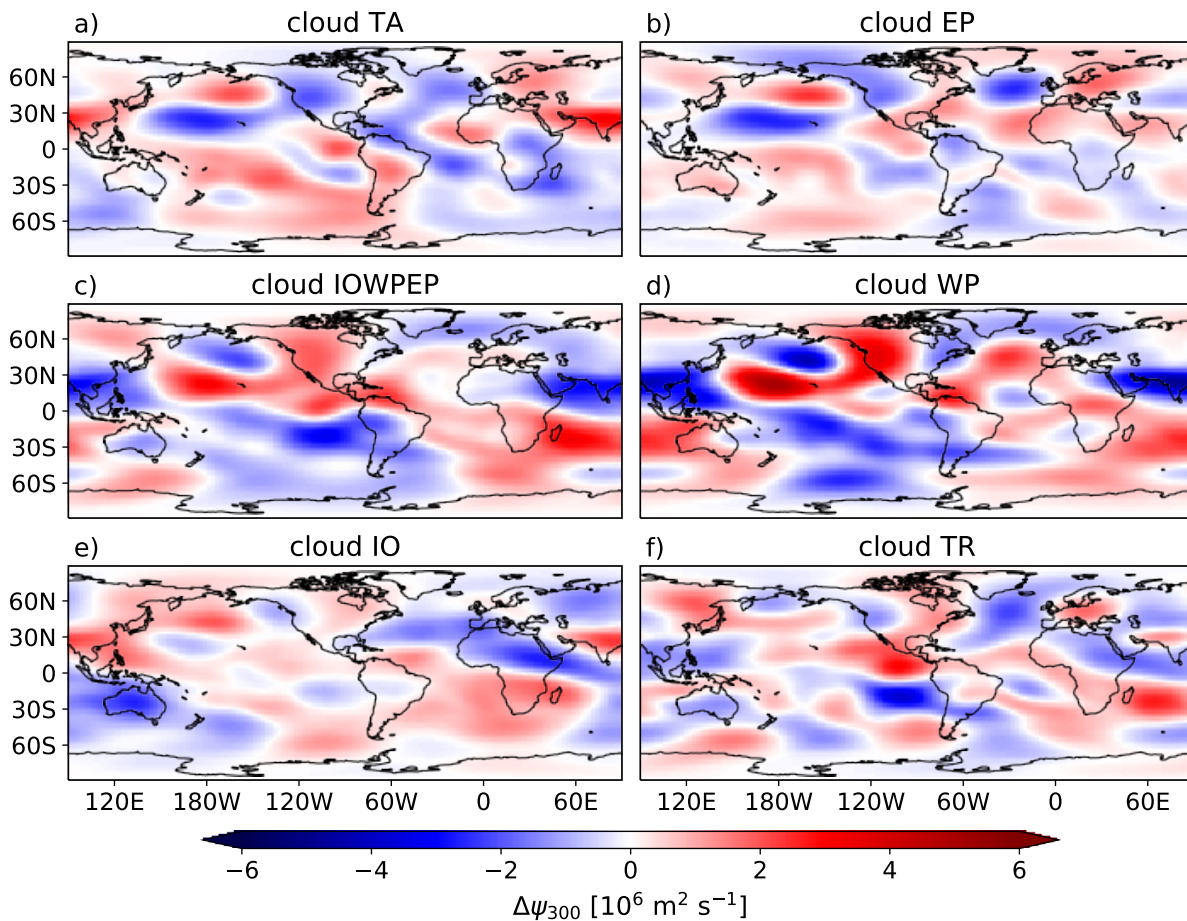
Figure 7.8.: Response of the stationary eddy stream function at 300 hPa to tropical cloud-radiative changes. Responses are shown for cloud-radiative changes over the tropical Atlantic (a), over the eastern tropical Pacific (b), over the Indian Ocean and tropical Pacific (c), over the western tropical Pacific (d), over the Indian Ocean (e), and across the whole tropics (f).

due to tropical cloud changes (Fig. 7.8f and Fig. C.5f). The same qualitative eddy stream function responses are found for the total response and the global cloud impact (Fig. C.6), and was also shown by Simpson et al. (2014) for the CMIP5 model mean response in the RCP8.5 scenario (their Fig. 13). Note that in Simpson et al. (2014), the dipole in the eddy stream function response is located further to the South compared to ICON, consistent with the further South located jet exit strengthening in the coupled CMIP5 models compared to ICON (cf. our Figs. 7.1 and 7.8 to Figs. 7 and 13 in Simpson et al., 2014, respectively).

Our results agree to a certain degree with previous studies that investigated the circulation response over the North Atlantic-European region to MJO- and ENSO-related tropical heating on shorter time scales of several days to weeks. For example, Cassou (2008) found that convection over the eastern Indian Ocean (western tropical Pacific) leads to an equatorward (poleward) shifted North Atlantic jet,

while we find a poleward jet shift in response to cloud IO and cloud WP. Palmer and Mansfield (1984) studied the circulation response to SST increases in the western and eastern tropical Pacific and found that small increases in western Pacific SST yield a poleward shifted North Atlantic jet stream while large increases in eastern Pacific SST have a rather small impact on the circulation over the North Atlantic. Ciasto et al. (2016) related the eastward extension of the North Atlantic storm track to SST changes in the western Pacific via the development of Rossby waves. However, some studies also found contradicting midlatitude circulation responses to tropical heating. For example, Goss and Feldstein (2017) showed that even though El Niño and MJO phase 1 exhibit similar patterns in tropical convection anomalies, their extratropical circulation responses differ. The same is found for the impacts of La Niña and MJO phase 5. Wild et al. (2015) studied the increased storminess over the eastern North Atlantic and British Isles during winter 2013/14 and could not find a direct connection between this response and positive SST anomalies over the western tropical Pacific. These and other studies show that the response of the North Atlantic circulation to tropical heating anomalies is still not fully understood and that further studies are needed to identify the dominating mechanisms and processes. Here, we showed that the zonal wind and jet stream responses over the North Atlantic-European region can be related to changes in tropical cloud-radiative heating and the development of Rossby waves in the Northern Hemisphere. The heating yields a dipole of equivalent barotropic anomalies in the eddy stream function over the North Atlantic or Europe, depending on the location of the heating. Yet, the Rossby waves do not develop in response to cloud-radiative changes across the whole tropics and over the Indian Ocean. This might indicate that the transient component rather than the stationary component of the response dominates for these regional cloud changes.

7.4. Conclusions

We investigate the impact of cloud-radiative changes on the global warming response over the North Atlantic-European region during boreal winter. The North Atlantic jet exit strengthening, i.e., the eastward extension of the North Atlantic jet towards Europe and the jet strengthening over Europe, are robust across coupled and atmosphere-only General Circulation Models. At the same time, the zonal wind response over the North Atlantic is not robust in any of the investigated global warming scenarios. Global cloud-radiative changes contribute robustly to the jet exit strengthening in simulations with the atmospheric components of ICON, MPI-ESM and IPSL-CM5A with prescribed SST that apply the cloud- and cloud- and water vapor-locking methods. At the same time, cloud-radiative changes contribute to the model uncertainty in the zonal wind and jet stream responses over the North Atlantic. Differences in the magnitude of the cloud-radiative impacts on the jet exit strengthening can be related to different magnitudes and patterns in the upper-tropospheric change in atmospheric cloud-radiative heating in the three models.

For ICON, we further investigate the impact of regional cloud-radiative changes on the zonal wind and jet stream responses to global warming over the North Atlantic-European region. Tropical cloud-radiative changes dominate the global cloud-radiative impact on the jet exit strengthening. Indian Ocean, western tropical Pacific and eastern tropical Pacific cloud-radiative changes all contribute about equally to the jet exit strengthening while tropical Atlantic cloud-radiative changes have a minor impact on the zonal wind response over Europe. This is consistent with the changes in atmospheric cloud-radiative heating, which are largest over the tropical Pacific and Indian Ocean. The result that none of these smaller tropical regions dominates the tropical cloud impact indicates that large-scale processes and mechanisms are important for the circulation response over the North Atlantic-European region. The North Atlantic jet response to cloud changes over the tropical Pacific and tropical Atlantic can be related to the response of the stationary eddy stream function, which is linked to the development of Rossby wave trains in the Northern Hemisphere due to cloud-radiative heating in the tropical upper troposphere. For cloud changes across the whole tropics and over the Indian Ocean, no Rossby wave evolves. This indicates that changes in the transient component rather than in the stationary component of the response might dominate the circulation response to tropical and Indian Ocean cloud changes. Further work is needed to better understand the contributions of the stationary and transient components of the circulation response to global warming, and to identify which component dominates and why.

8. Conclusions and Outlook

In this chapter, we summarize the main results of this thesis with regard to the research questions (section 8.1). Further, we discuss questions that arise from this thesis to give an outlook on possible future work (section 8.2).

8.1. Conclusions

The midlatitude jet streams and storm tracks are important components of the large-scale atmospheric circulation because they dominate the heat, momentum and moisture transport outside of the tropics. It is of special social and economic interest to reliably predict the regional jet stream and storm track responses to global warming as large parts of the world's population live in the area of influence of the jet streams and storm tracks. However, even though the responses of the jet streams and storm tracks to global warming were studied extensively during the last decades, they still remain uncertain. While the annual-mean zonal-mean response is a poleward shift in the Northern Hemisphere and a poleward shift and strengthening in the Southern Hemisphere, large regional and seasonal variations are present, especially in the Northern Hemisphere where the jet stream and storm tracks are influenced by the land-masses.

Previous studies identified several processes and mechanisms that contribute to the jet stream and storm track responses to global warming. One of them are changes in upper-tropospheric meridional temperature gradients and baroclinicity, which were found to play an important role. Changes in cloud-radiative properties strongly modify the upper-tropospheric meridional temperature gradients, mainly by upper-tropospheric cloud-radiative heating in the tropics and midlatitudes. Previous studies investigated the annual-mean zonal-mean impact of cloud-radiative changes on the jet stream response in aquaplanet and present-day simulations. They identified that cloud-radiative changes have a substantial impact on the response of the midlatitude circulation to global warming and can account for up to 50% of the annual-mean zonal-mean poleward jet shift.

In this thesis, we investigated the impact of cloud-radiative changes on the jet stream and storm track responses to global warming across seasons and regions. For this purpose, we performed global numerical simulations with the atmospheric component of the ICON model that included continents, sea ice and a seasonal cycle. We prescribed SST to isolate the impact of cloud-radiative changes via the atmospheric pathway, i.e., the impact of changes in atmospheric cloud-radiative heating in the absence of SST changes. Global warming was mimicked by a uniform 4 K or spatially-varying SST increase.

We used ICON with the physics package developed for numerical weather prediction (ICON-NWP). We showed that ICON-NWP can be used to perform long-term climate simulations by comparing the ICON simulations to reanalysis data, observations and atmosphere-only simulations of CMIP5 models.

We addressed the three research questions of this thesis in chapters 5-7. Each research question was split into more detailed sub-questions to make it more explicit. Here, we summarize the main findings of each of the three chapters with regard to the research questions.

In chapter 5, we addressed research question 1 "How large is the impact of global cloud-radiative changes on the midlatitude circulation response to global warming in a present-day simulation setup?". The main findings with regard to the more detailed sub-questions are as follows:

1.1. How important is the cloud-radiative impact for the midlatitude jet stream and storm track responses to global warming in the North Atlantic, North Pacific, and Southern Hemisphere ocean?

Changes in atmospheric cloud-radiative heating have a substantial impact on the jet stream and storm track responses to global warming. In the annual mean, cloud-radiative changes contribute one to two thirds to the poleward jet shift in all three ocean basins and support the jet strengthening in the North Atlantic and Southern Hemisphere. The cloud-radiative impact on the zonal wind response is largely zonally symmetric, consistent with a zonally symmetric change in midlatitude upper-tropospheric cloud-radiative heating. Cloud-radiative changes also impact the storm track, but the impact is more diverse across the three ocean basins.

1.2. To what extent does the cloud-radiative impact vary across seasons and ocean basins?

In the North Atlantic and North Pacific, the cloud-radiative impact on the jet response varies little from season to season in absolute terms, whereas its relative importance changes over the course of the year. In the Southern Hemisphere, cloud-radiative changes strengthen the jet in all seasons, whereas their impact on the jet shift is limited to austral summer and fall. The magnitude of the cloud-radiative impact depends on the ocean basin.

1.3. Does the cloud-radiative impact depend on the pattern of the SST increase?

The absolute value of the cloud-radiative impact is largely independent of whether global warming is mimicked by a uniform 4 K or spatially-varying sea-surface temperature increase in all three ocean basins and across seasons. Thus, the uniform 4 K SST increase provides meaningful estimates of the absolute value of the cloud-radiative impact, although it is not able to reproduce the total jet stream response of coupled climate models.

In chapter 6, we addressed research question 2 "Which regional cloud-radiative changes dominate the global cloud-radiative impact on the response of the midlatitude circulation to global warming?". To answer this question, we investigated the relative importance of tropical, midlatitude, and polar cloud-radiative changes for the annual-mean, wintertime, and summertime jet stream and storm track responses across regions. The main findings with regard to the more detailed sub-questions are as follows:

2.1. Are tropical, midlatitude or polar cloud-radiative changes more important for the global cloud impact on the zonal wind, jet stream and storm track responses to global warming? Do the results depend on the season and the ocean basin?

Tropical cloud-radiative changes dominate the global cloud-radiative impact on the zonal wind response at 850 hPa, the jet strength response, and the storm track response. This result is found for the annual mean, winter and summer, and particularly pronounced in the North Atlantic and Southern Hemisphere. For the jet shift, a more diverse picture is found. In the annual-mean and DJF, tropical and midlatitude cloud changes contribute substantially to the jet shifts in most regions. The polar cloud impact contributes to the poleward jet shifts across the Northern Hemisphere, but shifts the Southern Hemisphere jet equatorward. In JJA, the impact of regional cloud changes on the jet position is small, consistent with an overall small jet shift during this season. Thus, our results highlight the importance of tropical cloud changes.

2.2. Can we understand the circulation impact of regional cloud-radiative changes on the zonal wind and jet responses based on (established) dynamical arguments?

The temperature response to cloud-radiative heating is difficult to understand. At the same time, the zonal wind response to cloud-induced temperature changes can be understood from dry dynamics as the circulation changes are broadly consistent with the influence of cloud-radiative changes on upper-tropospheric baroclinicity. The relation between changes in upper-tropospheric meridional temperature gradients due to cloud-radiative heating and the zonal wind response is most prevalent for the tropical cloud impact and weaker for the midlatitude and polar cloud impacts. The transient component of the eddy momentum fluxes dominates the annual-mean global and tropical cloud impacts, whereas the stationary component is also important for the midlatitude and polar cloud impacts in the Northern Hemisphere.

In chapter 7, we addressed research question 3 "Do cloud-radiative changes contribute robustly to the wintertime response of the North Atlantic jet stream to global warming, and which clouds are most important?". The main findings with regard to the more detailed sub-questions are as follows:

3.1. What aspects of the global warming response over the North Atlantic-European region during boreal winter are robust across coupled and atmosphere-only climate models?

The jet exit strengthening, that is, the eastward extension of the North Atlantic jet stream towards Europe and the jet strengthening over Europe, is robust across CMIP5 coupled climate models and atmosphere-only GCMs. The zonal wind and jet stream responses over the North Atlantic, however, are not robust across these models, independent of the climate change scenario.

3.2. How much of the robust circulation response can be attributed to cloud-radiative changes, and is the cloud impact robust across models?

Cloud-radiative changes contribute robustly to the jet exit strengthening in three atmosphere-only GCMs that apply the cloud- or cloud- and water vapor-locking methods. At the same time, cloud-

radiative changes can be considered as one source of model uncertainty in the zonal wind response over the North Atlantic, where models disagree on the sign of the response. The magnitude of the cloud impact differs between the three models which can be related to differences in the magnitude and pattern of changes in upper-tropospheric atmospheric cloud-radiative heating.

3.3. Which regional cloud-radiative changes are most important for the circulation response over Europe, and how can we understand their impact?

Tropical cloud-radiative changes dominate the global cloud impact on the jet exit strengthening. Indian Ocean, western tropical Pacific and eastern tropical Pacific cloud changes all contribute about equally to the jet exit strengthening while tropical Atlantic cloud changes have a minor impact. This is consistent with the finding that the largest changes in upper-tropospheric cloud-radiative heating occur over the tropical Pacific and Indian Ocean. We relate the North Atlantic jet response to tropical Pacific and tropical Atlantic cloud changes to changes in the stationary eddy stream function, which is linked to the development of Rossby wave trains in the Northern Hemisphere due to cloud-radiative heating in the tropical upper troposphere. For cloud changes across the whole tropics and over the Indian Ocean, no Rossby wave evolves. For these two regions, the transient component of the response might be more important than the stationary component of the response.

The novelty of this thesis is that i) we used a present-day simulation setup to investigate the atmospheric pathway of the cloud-radiative impact on the jet stream and storm track responses to global warming; ii) we studied global and regional cloud impacts across regions and seasons; iii) we investigated the role of changes in SST gradients on the cloud impact; and iv) we compared the cloud-radiative impact on regional circulation responses across models. The results of this thesis provide new insights into the regional and seasonal impacts of cloud-radiative changes on the response of the midlatitude circulation to global warming. They highlight the importance of the present-day setup and the investigation of individual ocean basins for understanding the impact of cloud-radiative changes on the midlatitude circulation response to global warming. Previous studies that focused on the annual-mean zonal-mean cloud-radiative impact did not capture regional differences in the cloud-radiative impact which are linked to the presence of continents, and which we show to be important (Voigt and Shaw, 2015, 2016; Ceppi and Hartmann, 2016; Ceppi and Shepherd, 2017; Voigt et al., 2019). Further, we found that the cloud-radiative impact depends little on the pattern of SST increase and changes in SST gradients. Thus, the idealized global warming scenario of a uniform SST increase is helpful to understand the atmospheric pathway of the cloud-radiative impact as it provides meaningful estimates of the absolute value of the cloud-radiative impact. At the same time, the uniform SST increase cannot be used to determine the importance of the cloud-radiative impact relative to the total circulation response as the uniform SST increase does not reproduce the total circulation response to global warming which depends on changes in SST gradients.

Previous studies that investigated the annual-mean zonal-mean circulation response to global warming in aquaplanet simulations found that changes in meridional temperature gradients and baroclinicity dominate the cloud-induced circulation response (Voigt and Shaw, 2015, 2016; Ceppi and Hartmann, 2016). In this thesis, we showed that the cloud-induced annual-mean zonal-mean temperature response and the resulting response of the zonal wind and jet streams can be linked to changes in upper-tropospheric meridional temperature gradients and baroclinicity via dry-dynamical arguments and changes in eddy fluxes of heat and momentum. We showed that this relation is most pronounced for tropical cloud changes whose heating has the largest impact on upper-tropospheric temperature and meridional temperature gradients. This explains why tropical cloud-radiative changes dominate the global cloud-radiative impact on the midlatitude circulation response to global warming.

8.2. Outlook

For large parts of this thesis, we used one model to investigate the impact of cloud-radiative changes on the jet stream and storm track responses to global warming. However, the magnitude and pattern of the annual-mean zonal-mean change in atmospheric cloud-radiative heating and the resulting cloud-radiative impact on the circulation response differ across models and remain uncertain in both aquaplanet (Voigt and Shaw, 2015, 2016; Ceppi and Hartmann, 2016) and present-day simulations (Ceppi and Shepherd, 2017; Voigt et al., 2019). We showed that differences are also present in the regional changes in upper-tropospheric cloud-radiative heating and the cloud-radiative impact on the zonal wind response over the North Atlantic-European region across three models (cf. chapter 7). Thus, future studies should investigate the cloud-radiative impact across regions and seasons in a larger model ensemble. This would enable to quantify model differences in representing the change in cloud-radiative heating and its impact on the response of the atmospheric circulation to global warming. In particular, the impact of cloud-radiative heating over the tropical Pacific and Indian Ocean should be investigated in more depth since it dominates the circulation response in ICON and possibly in other models. These studies should also investigate the atmospheric and surface pathways of the cloud-radiative impact to identify the role of the different pathways across models. The new simulations could range from idealized dry-dynamical core Held-Suarez simulations (Held and Suarez, 1994) over aquaplanet and present-day simulations (both setups with prescribed SST and coupled to a slab ocean) to coupled climate models. Future studies should in particular focus on coupled climate models or Earth system models as the impact of cloud and other radiative changes on the atmospheric circulation response to global warming has, to date, only been diagnosed in atmosphere-only GCMs with prescribed SST or a slab ocean. Yet, it could depend on, for example, changes in sea ice, land use or time-dependent increases in greenhouse gases.

Regarding the impact of water vapor-radiative changes, future studies should contrast the impacts of cloud- and water vapor-radiative changes across regions and seasons as water vapor changes seem to counteract the poleward jet shift (Voigt and Shaw, 2015; Ceppi and Shepherd, 2017; Voigt et al., 2019,

and our chapter 7). In this thesis, we found that for the zonal wind response at 850 hPa across the North Atlantic-European region during boreal winter, the water vapor-radiative impact is more robust across three atmosphere-only GCMs than the cloud-radiative impact. This should be further investigated for other regions and across seasons as it could indicate that cloud-radiative changes contribute in some regions to the uncertainties in future climate projections while water vapor-radiative changes contribute robustly to the response.

How could the role of cloud-radiative changes and/or water vapor-radiative changes be determined in a large model ensemble? To date, the cloud-locking method is the most appropriate method to study the impact of cloud-radiative changes on the circulation response to global warming (Voigt and Albern, 2019). In Voigt and Albern (2019), we showed that the cloud-locking method reliably diagnoses the cloud-radiative impact on the circulation response to global warming. At the same time, we showed that the COOKIE method should not be used to study the cloud-induced circulation response to global warming because making clouds transparent to radiation changes the basic state of the atmospheric circulation and atmospheric water vapor. This results in misdiagnosed cloud-radiative impacts and the lack of robust circulation responses like the poleward expansion of the tropics and poleward shifts of the midlatitude jet streams (Voigt and Albern, 2019). These results suggest that a cloud-locking model intercomparison project might be needed to determine how much of the model uncertainties in response to global warming can be attributed to differences in the diagnosed cloud-radiative heating changes and the resulting cloud-radiative impact. Yet, the implementation of the cloud-locking method into general circulation models can be quite complicated, depending on how many and which variables are needed for the radiative transfer scheme. In addition, the locking method involves substantial computational costs as six simulations are needed to diagnose the global cloud-radiative impact when all other radiative properties are interactive. Investigating regional cloud-radiative impacts and locking additional cloud-radiative properties such as water vapor or surface albedo further increases the number of needed simulations.

The complexity of the cloud-locking method suggests that instead of initiating a cloud-locking model intercomparison project, it might be more feasible to develop a new method to diagnose the cloud-radiative impact, which is easier to implement in the models and which requires less computational effort. This method could be based on the COOKIE and cloud-locking approaches or it could, for example, use a machine learning approach, e.g., a neural network, to replace all or parts of the computationally expensive radiative transfer scheme. Efforts exist already to replace parts of numerical weather prediction and climate models with machine learning algorithms (e.g., `https://www.ecmwf.int/en/newsletter/163/news/ai-and-machine-learning-ecmwf`). The new method should allow to independently study the impact of different clouds, e.g., upper-tropospheric ice clouds versus lower-tropospheric cumulus clouds or tropical clouds versus midlatitude clouds, as they might have different impacts on the atmospheric circulation (e.g., Fermepin and Bony, 2014; Voigt and Shaw, 2016, and our chapters 6 and 7). In particular, the role of upper-tropospheric ice clouds should be investigated in more depth as their changes lead to the strongest cloud-radiative heating in response to global warm-

ing. Thus, they have a large potential impact on the circulation response to global warming, but their representation in climate models remains poor (e.g., Li et al., 2016; Hong et al., 2016; Zhao et al., 2018; Voigt et al., 2019). In Voigt et al. (2019), we compared the cloud-radiative heating in present-day climate from three atmosphere-only GCMs to observations from CloudSat/CALIPSO and to the ERA-Interim reanalysis. We found that the data sets disagree in particular with respect to upper-tropospheric cloud-radiative heating, and related this to differences in the representation of upper-tropospheric ice clouds (Figs. 7-8 in Voigt et al., 2019). We assumed that differences in changes in cloud-radiative heating in response to global warming in the three models are linked to the differences in present-day cloud-radiative heating.

Given the large differences in cloud ice and cloud-radiative heating between different models and between models and observations, future studies should aim to further improve the representation of clouds and their radiative effects in climate models. As clouds are parameterized in climate models, these studies should focus in more depth on cloud parameterizations like cloud microphysics, convection and radiation. For example, they could compare different types of cloud microphysics parameterizations like one- or two-moment microphysics schemes and the inclusion of additional hydrometeor classes (e.g., Zhao et al., 2018). Further, future studies could use high-resolution simulations to compare simulations that apply the convection parameterization to simulations that explicitly resolve convection and to satellite observations and data obtained from field campaigns. In ICON, for example, this would require simulations with less than 5 km horizontal grid spacing (Prill et al., 2019). This work could be based on the DYnamics of the Atmospheric general circulation Modeled On Non-hydrostatic Domains (DYAMOND, Satoh et al., 2017; Klocke et al., 2019) project that compares simulations of several climate models at storm resolving scales (1-5 km). Further, it could use data that was obtained during field campaigns such as the Small Particles in Cirrus (SPARTICUS, Muhlbauer et al., 2014), the Next-Generation Aircraft Remote Sensing for Validation Studies (NARVAL, Stevens et al., 2019), the North Atlantic Waveguide and Downstream Impact Experiment (NAWDEX, Schäfler et al., 2018) or the Elucidating the role of Cloud-Circulation Coupling in Climate (EUREC[4]A, Bony et al., 2017) campaigns, and next-generation satellite observations.

A. Appendix for Chapter 5
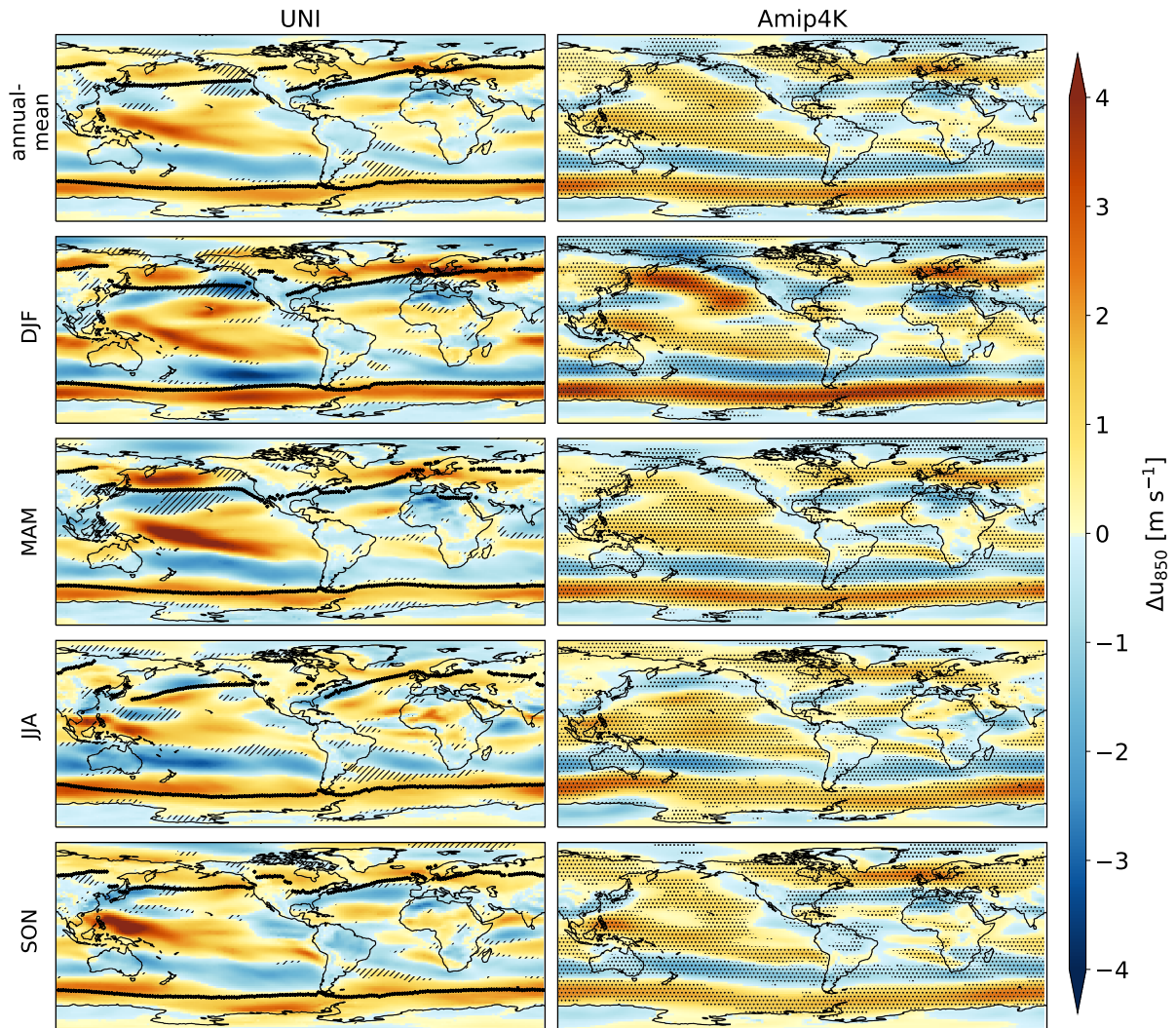
Figure A.1.: Annual-mean and seasonal-mean zonal wind response at 850 hPa in ICON with locked clouds for the UNI simulation (left) and multi-model mean response of the CMIP5 models listed in Tabs. 3.1 and 3.2 for the Amip4K simulations (right). Stippling in the right column indicates where the response is robust (sign of response agrees for 9 or more CMIP5 models). Hatching in the left column indicates where the response in ICON does not agree with the robust CMIP5 response. Reprinted from Albern et al. (2019). ©The Authors.
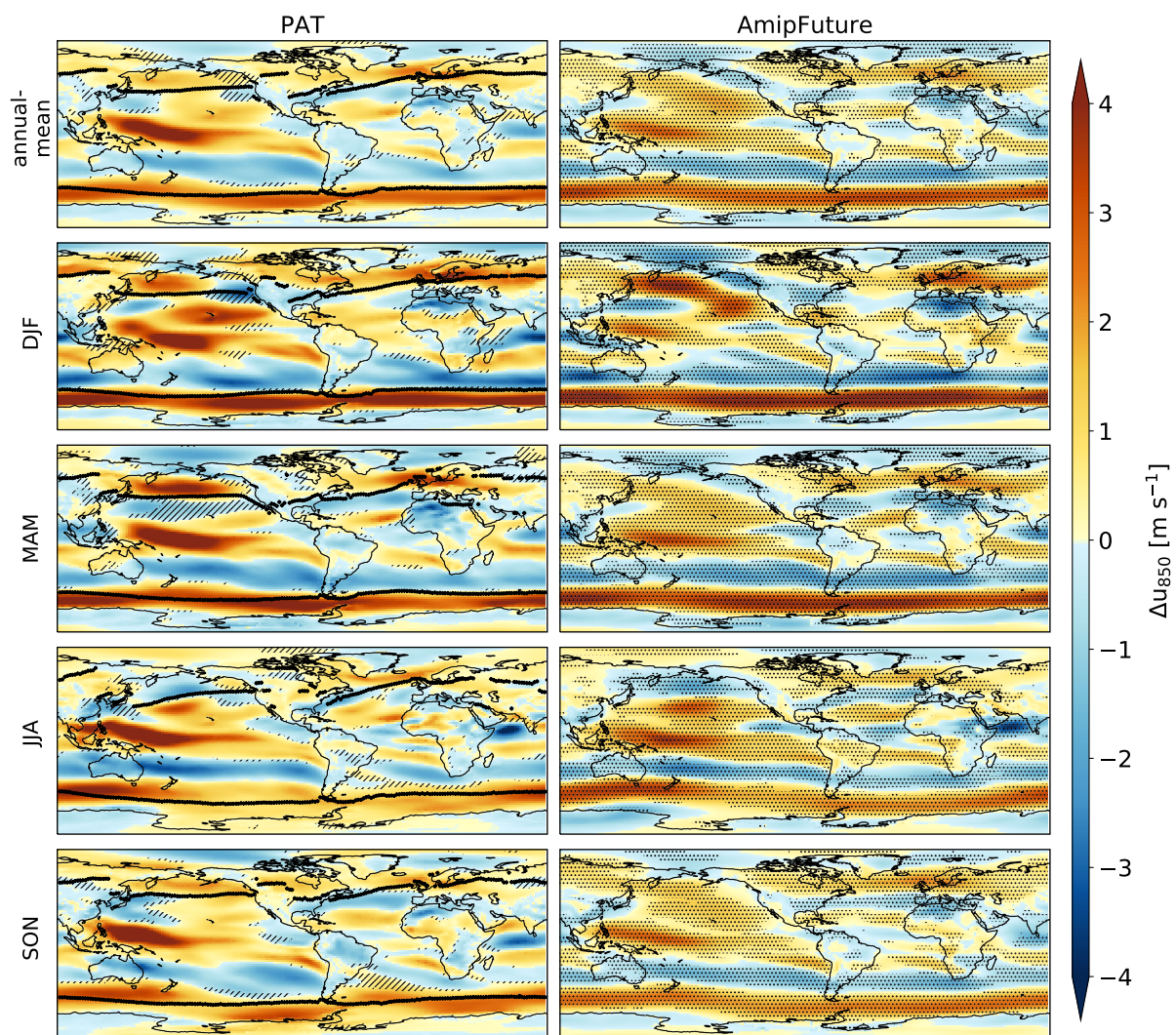
Figure A.2.: Same as Fig. A.1, but for the response in ICON with locked clouds in the PAT simulations (left) and the multi-model mean CMIP5 response in the AmipFuture simulations (right). Reprinted from Albern et al. (2019). ©The Authors.
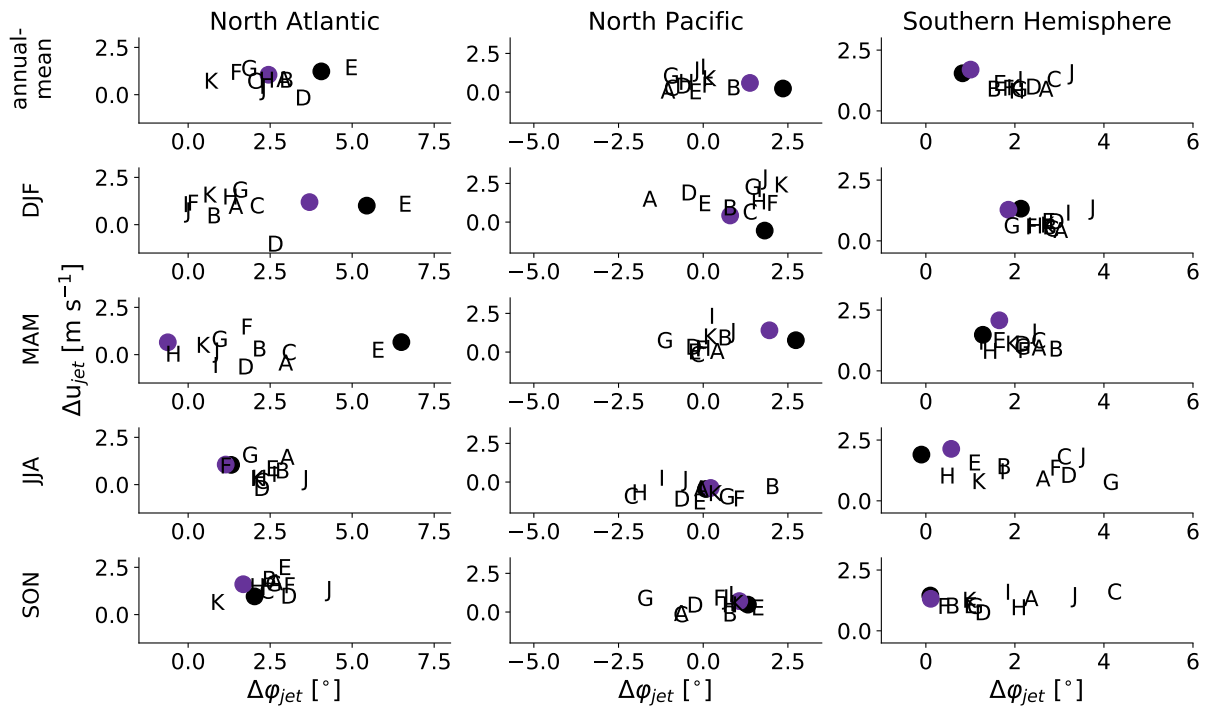
Figure A.3.: Annual-mean and seasonal-mean ocean basin mean poleward jet shift $\Delta\varphi_{jet}$ versus jet strengthening Δu_{jet} in the UNI/Amip4K simulations. The purple dot shows the total response in ICON with free clouds, the black dot shows the total response with locked clouds. The letters represent the CMIP5 models, which are listed in Tabs. 3.1 and 3.2. Reprinted from Albern et al. (2019). ©The Authors.
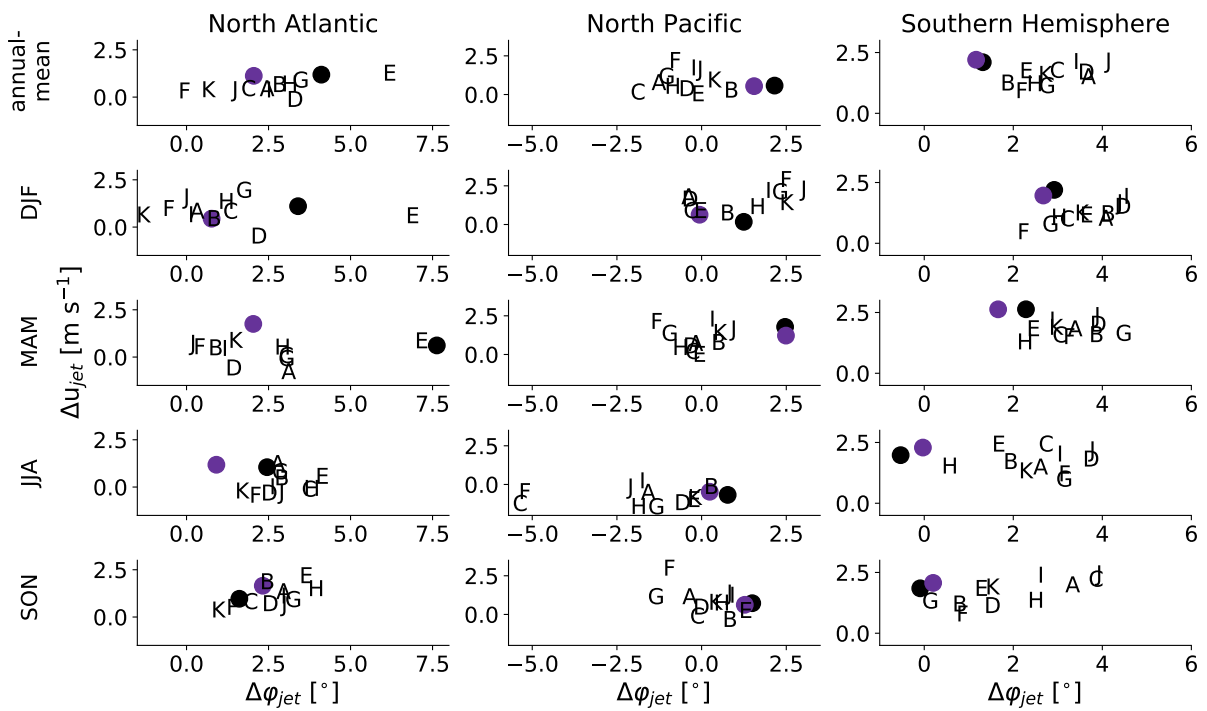
Figure A.4.: Same as in Fig. A.3 but for the PAT/AmipFuture simulations. Reprinted from Albern et al. (2019). ©The Authors.
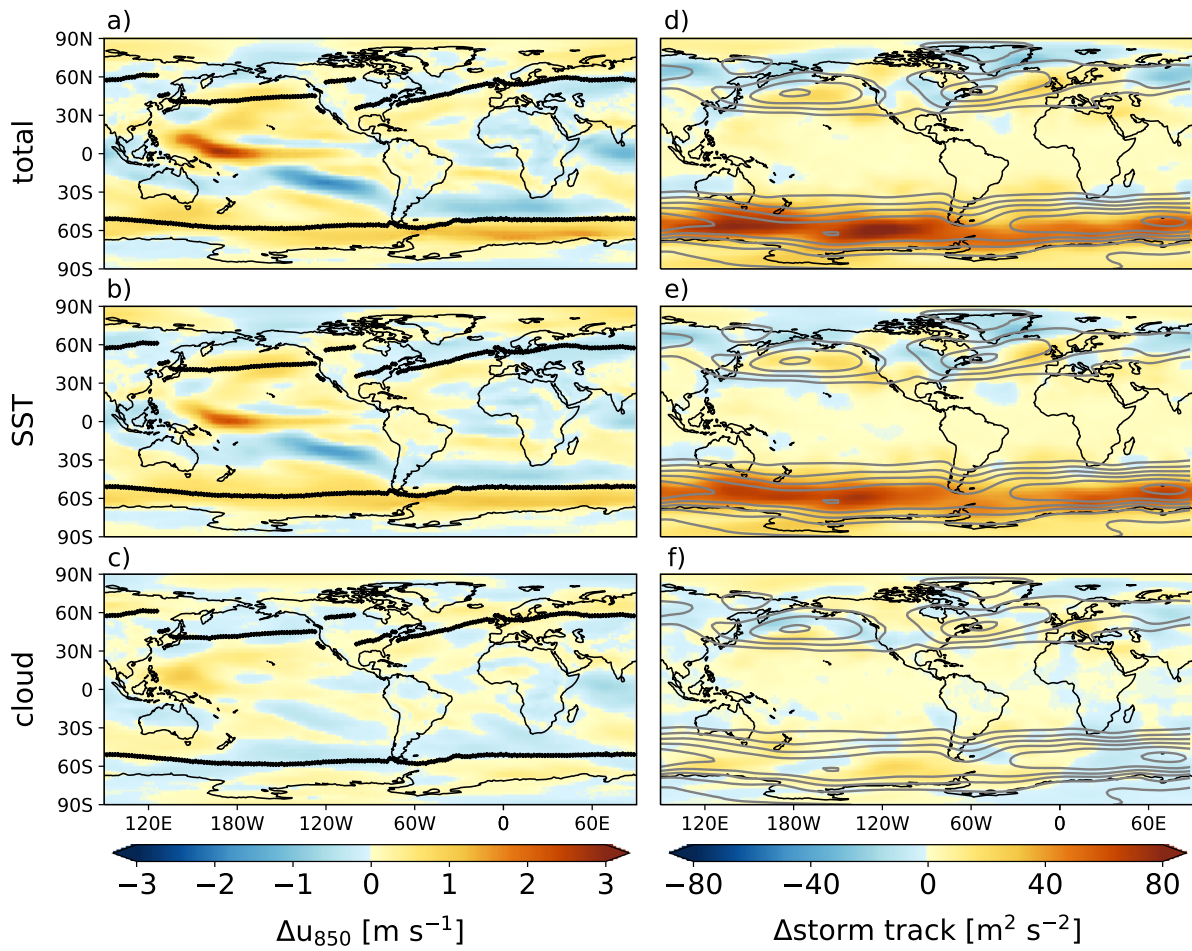
Figure A.5.: Same as Fig. 5.1 and Fig. 5.2, but for the response in the PAT simulations minus the response in the UNI simulations. Reprinted from Albern et al. (2019). ©The Authors.
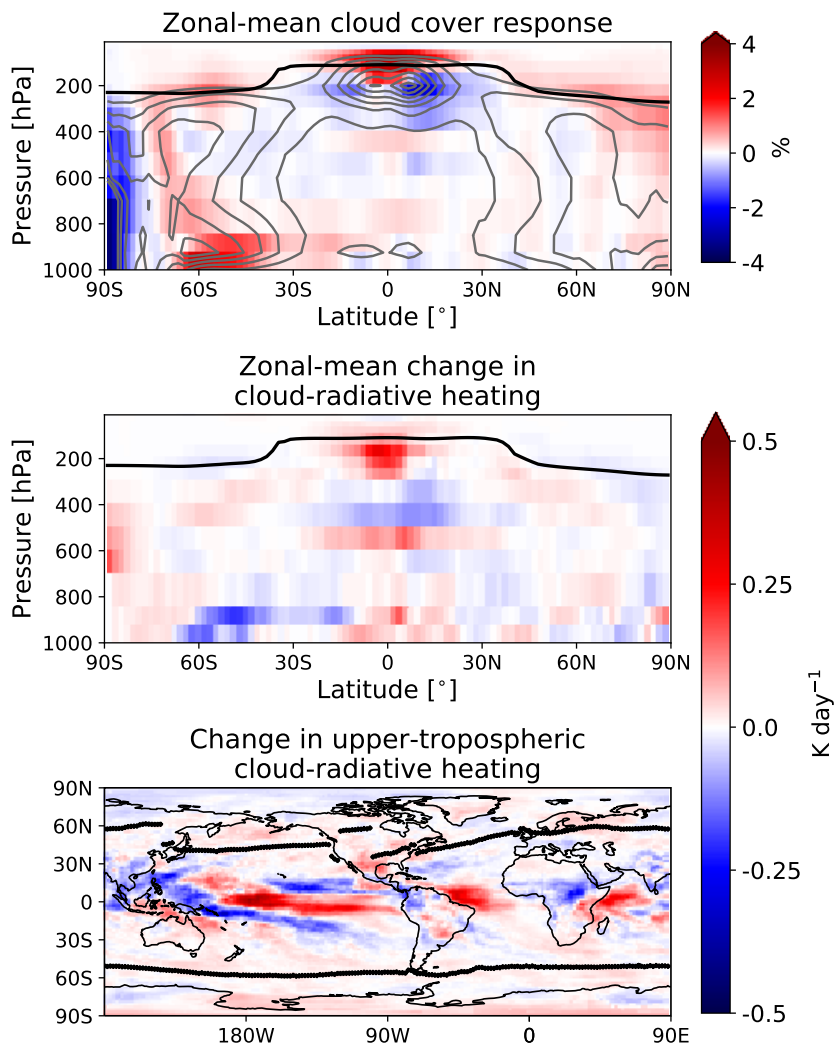
Figure A.6.: Same as Fig. 5.4, but for the response in PAT minus the response in UNI. Reprinted from Albern et al. (2019). ©The Authors.
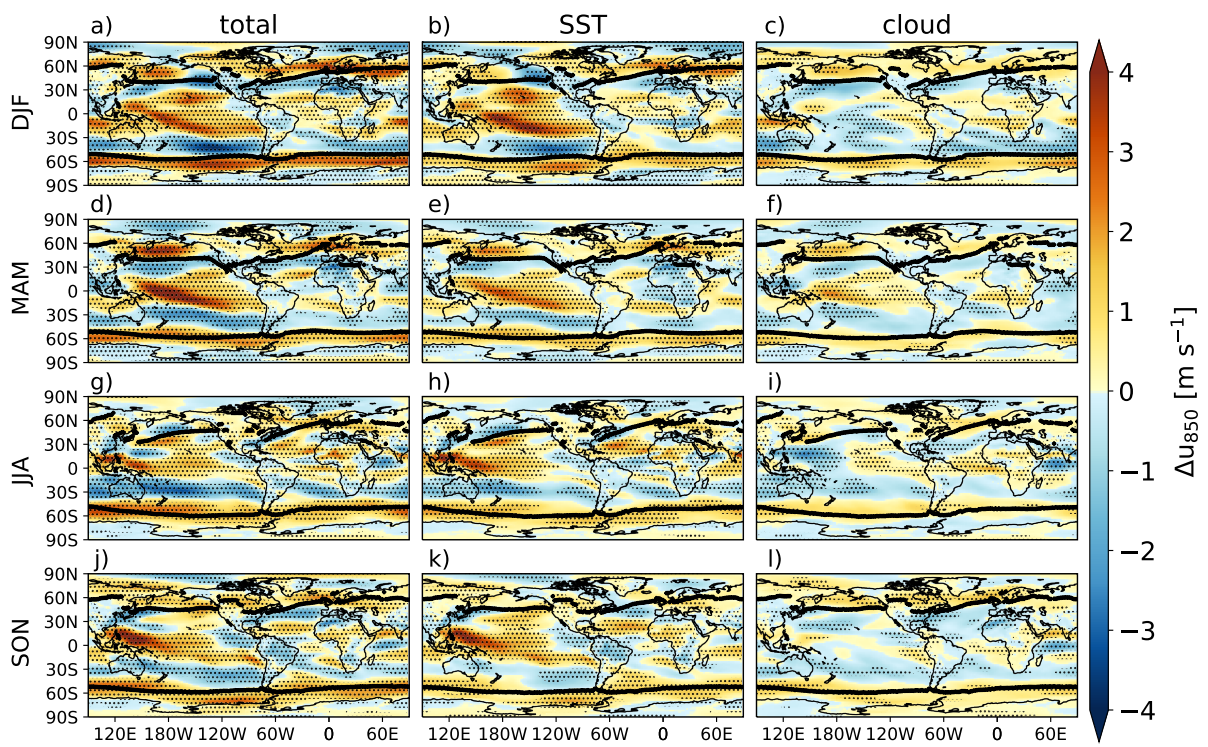
Figure A.7.: Seasonal-mean response of the zonal wind at 850 hPa in the UNI simulations. The total response (left) is decomposed into the impact of SST increase (middle) and the cloud-radiative impact (right). The black lines indicate the jet latitude in the control simulation. Dots indicate where the signal is significant at 95% level. Reprinted from Albern et al. (2019). ©The Authors.
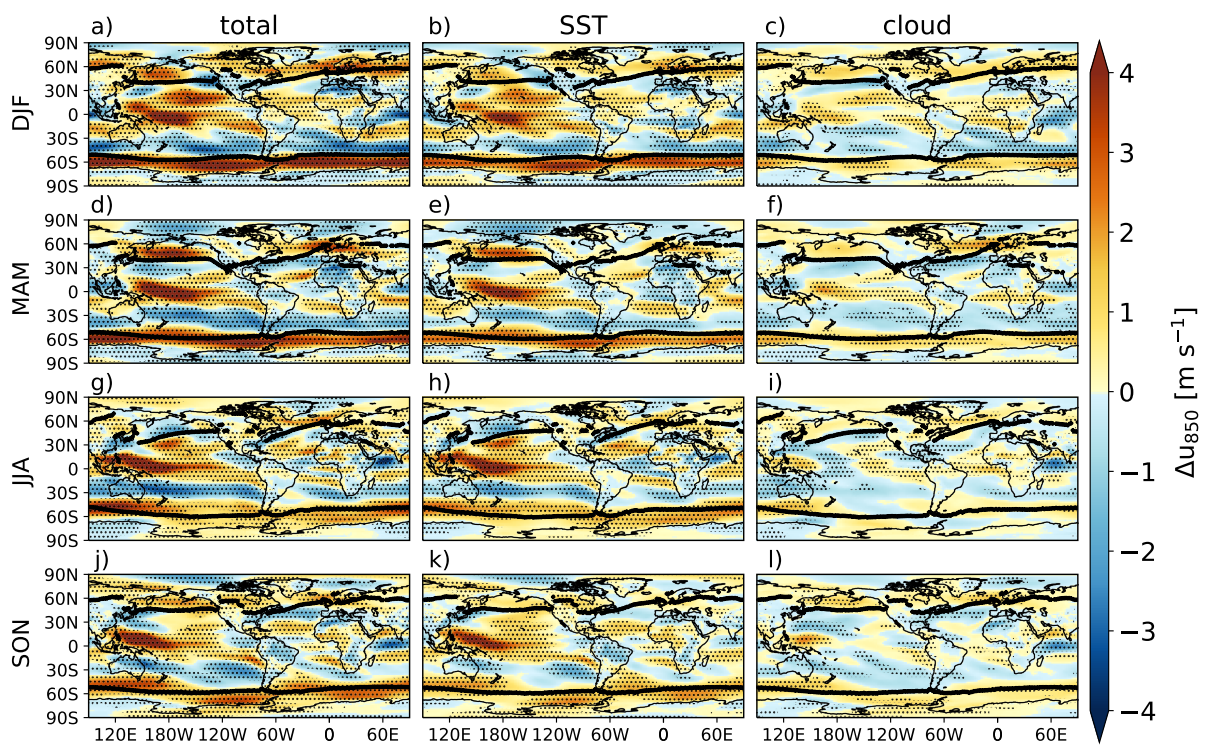
Figure A.8.: Same as Fig. A.7, but for the PAT simulations. Reprinted from Albern et al. (2019). ©The Authors.
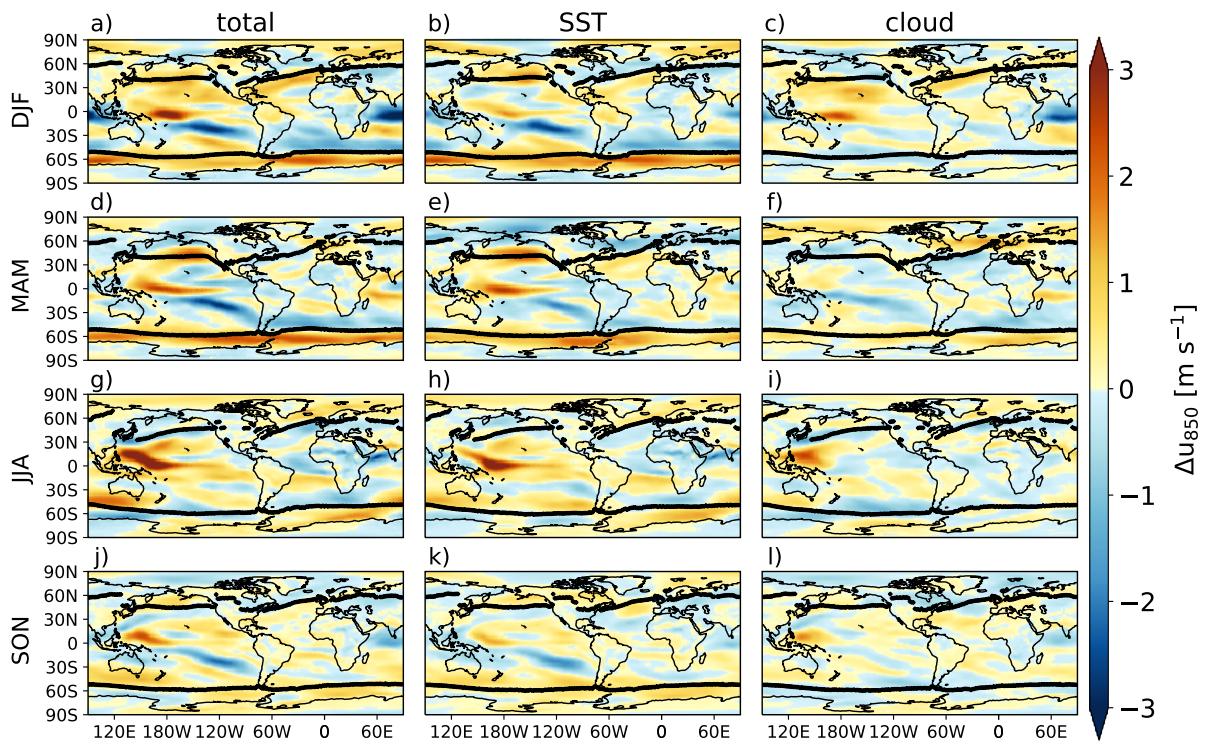
Figure A.9.: Same as Fig. A.7, but for the response in the PAT simulations minus the response in the UNI simulations. Reprinted from Albern et al. (2019). ©The Authors.
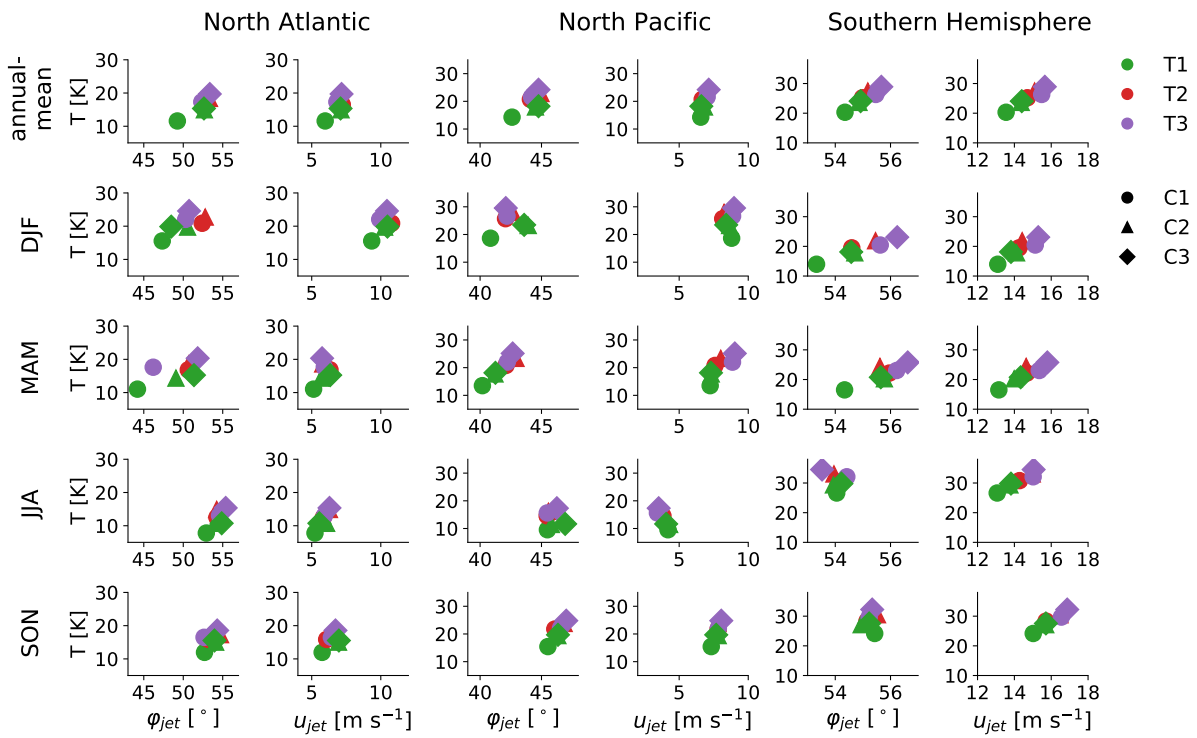
Figure A.10.: Annual-mean and seasonal-mean upper-tropospheric temperature gradient vs. jet latitude φ_{jet} and jet strength u_{jet} for the North Atlantic (left two columns), North Pacific (middle two columns) and Southern Hemisphere (right two columns). Shown are the seven simulations with locked clouds. The different colors and markers indicate whether SST (T) and cloud-radiative properties (C) are taken from CTL (1), UNI (2) or PAT (3) simulations, respectively. Reprinted from Albern et al. (2019). ©The Authors.

B. Appendix for Chapter 6
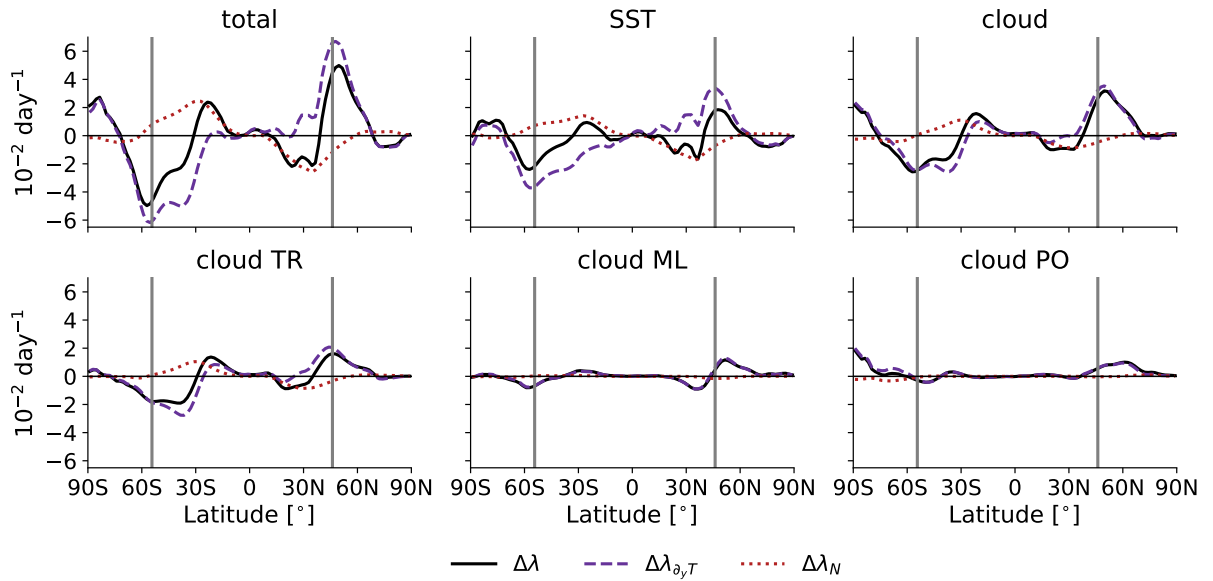
Figure B.1.: Annual-mean vertical-mean response of zonal-mean Eady growth rate $\Delta\lambda$. The response is decomposed into a contribution from changes in the meridional temperature gradient $\Delta\lambda_{\partial_y T}$ and from changes in vertical stability $\Delta\lambda_N$. The total response, SST impact, global cloud impact and tropical, midlatitude and polar cloud impacts are shown separately. The grey lines show the jet latitude in the control simulation with locked clouds. Note that we use the standard definition of the Eady growth rate (Hoskins and Valdes, 1990) and follow Eqs. 3-5 in Voigt and Shaw (2016) for the calculation of the vertical mean Eady growth rate response and its decomposition into contributions from changes in the meridional temperature gradient and from changes in vertical stability. We calculate the vertical mean between 925 hPa and 200 hPa. Reprinted from Albern et al. (2020). ©American Meteorological Society. Used with permission.

C. Appendix for Chapter 7
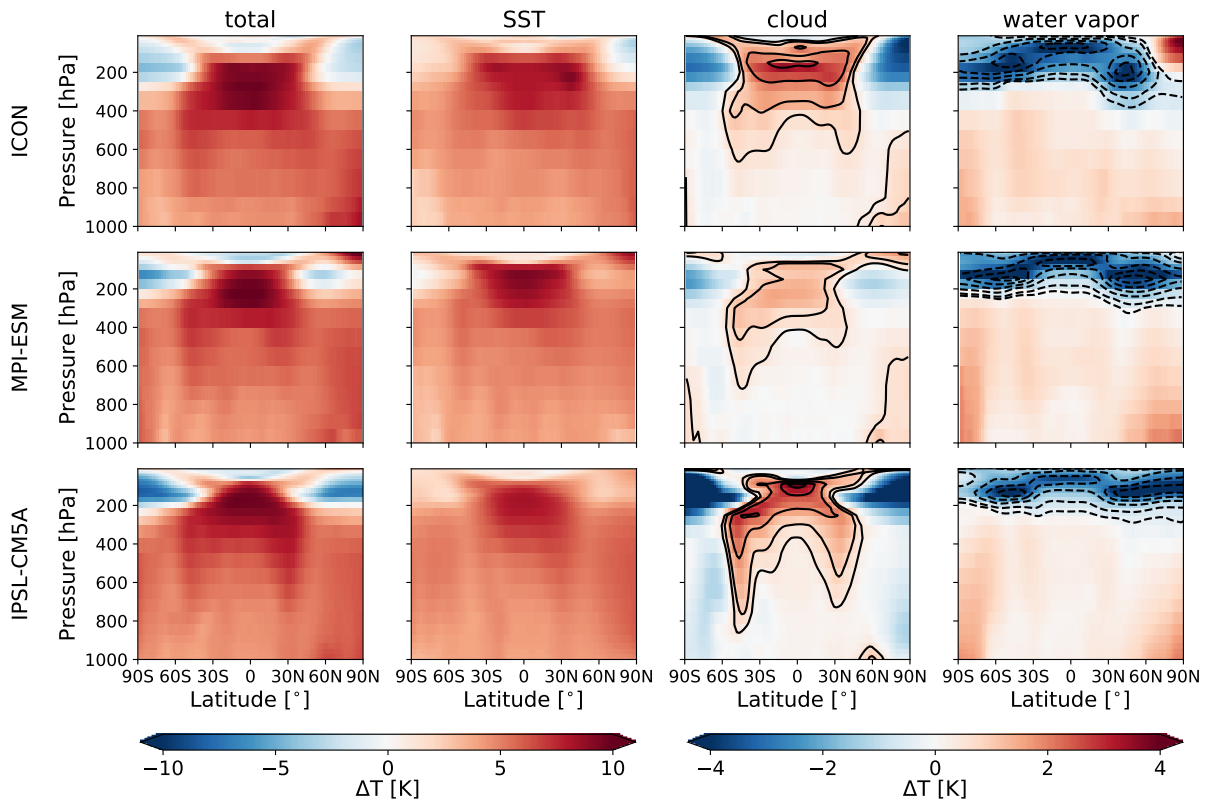
Figure C.1.: Zonal-mean atmospheric temperature response to global warming in ICON (top), MPI-ESM (center) and IPSL-CM5A (bottom). The total response (first column) is decomposed into SST impact (second column), cloud-radiative impact (third column) and water vapor-radiative impact (fourth column). To highlight the impact of cloud-induced upper-tropospheric warming and water vapor-induced upper-tropospheric cooling, we show the isotherms for plus (cloud) and minus (water vapor) 0.5, 1, 2, 3, 4, 5 K, respectively.
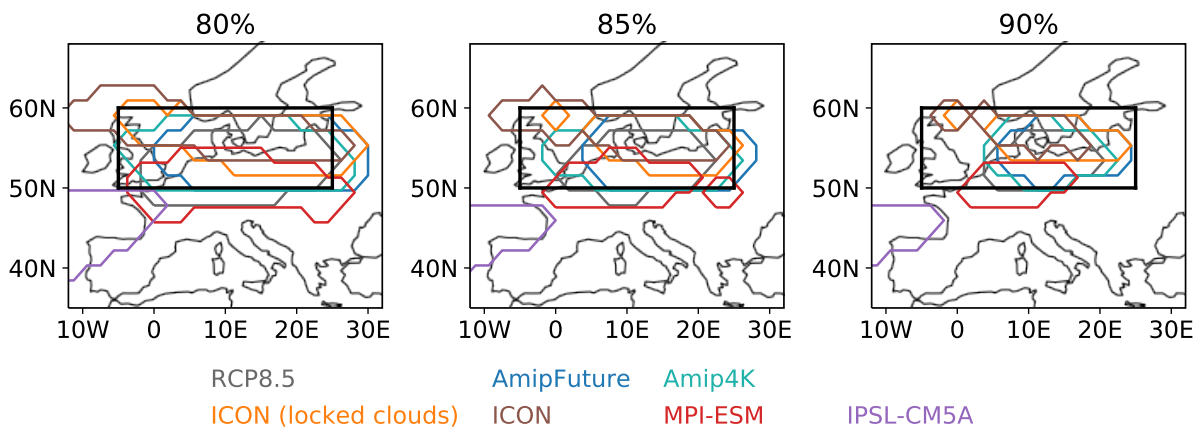
Figure C.2.: European region for which the area-mean u_{850} response is investigated (black box). The region ranges from 50°N to 60°N and from 5°W to 25°E. The contours show the isolines for which the zonal wind response exceeds 80% (left), 85% (center) and 90% (right) of the Δu_{850} maximum over Europe in the CMIP5 model mean in response to the RCP8.5, AmipFuture and Amip4K scenarios, and in ICON, MPI-ESM and IPSL-CM5A.
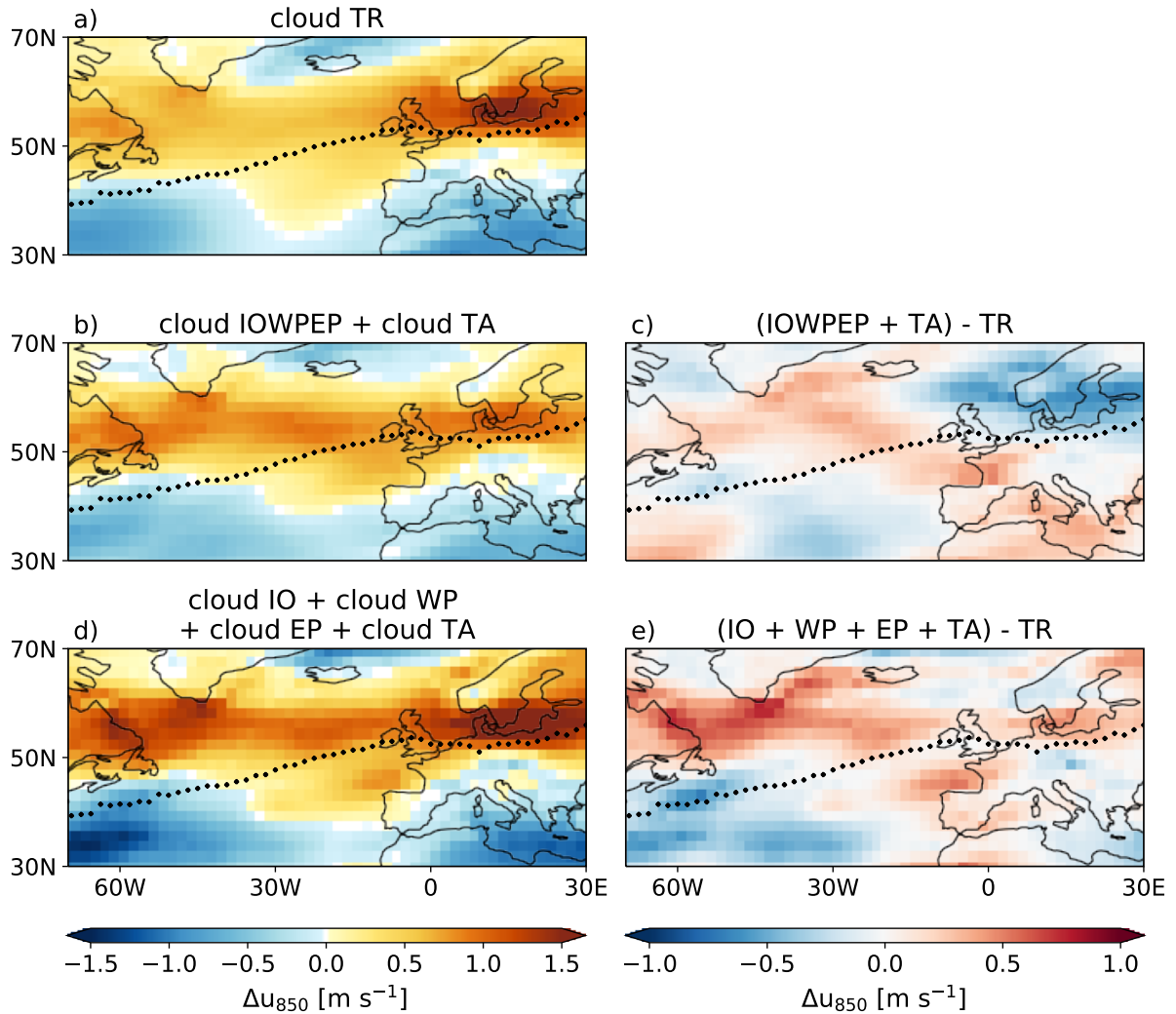
Figure C.3.: Response of zonal wind at 850 hPa to tropical cloud-radiative changes (a) and to the sum of cloud-radiative changes over the tropical Atlantic (cloud TA) and simultaneous cloud-radiative changes over the Indian Ocean, western tropical Pacific and eastern tropical Pacific (cloud IOWPEP) (b) and to the sum of individual cloud-radiative changes over the tropical Atlantic (cloud TA), the Indian Ocean (cloud IO), the western tropical Pacific (cloud WP) and the eastern tropical Pacific (cloud EP) (d). Panels (c) and (e) show the difference between the sums and the tropical cloud-radiative impact. The black dots indicate the jet latitude in the control simulation with locked clouds.
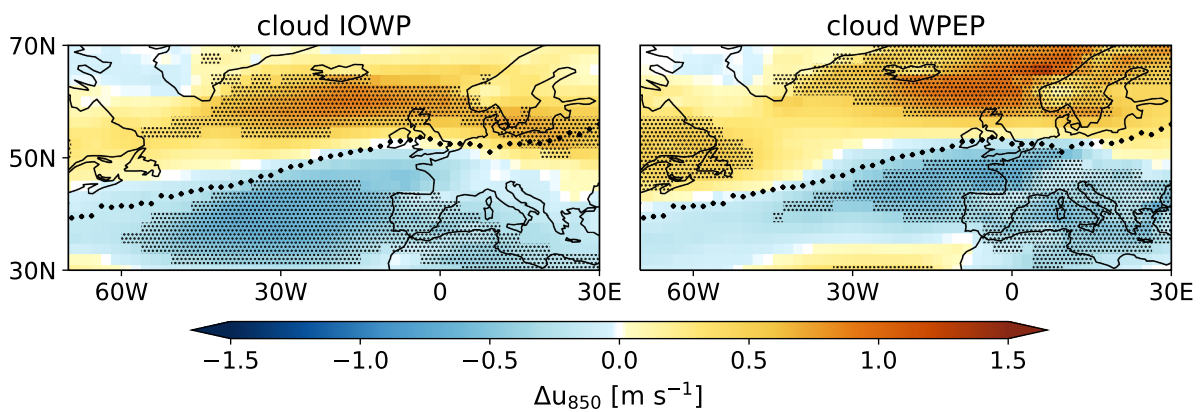
Figure C.4.: Impact of cloud-radiative changes over the Indian Ocean and western tropical Pacific (cloud IOWP, left), and over the western and eastern tropical Pacific (cloud WPEP, right) on the zonal wind response at 850 hPa, Δu_{850}. Stippling indicates where the response is statistically significant based on the 5th-95th-percentile range of the bootstrap distribution for each grid point. The thick black dots indicate the jet latitude in the control simulation with locked clouds.
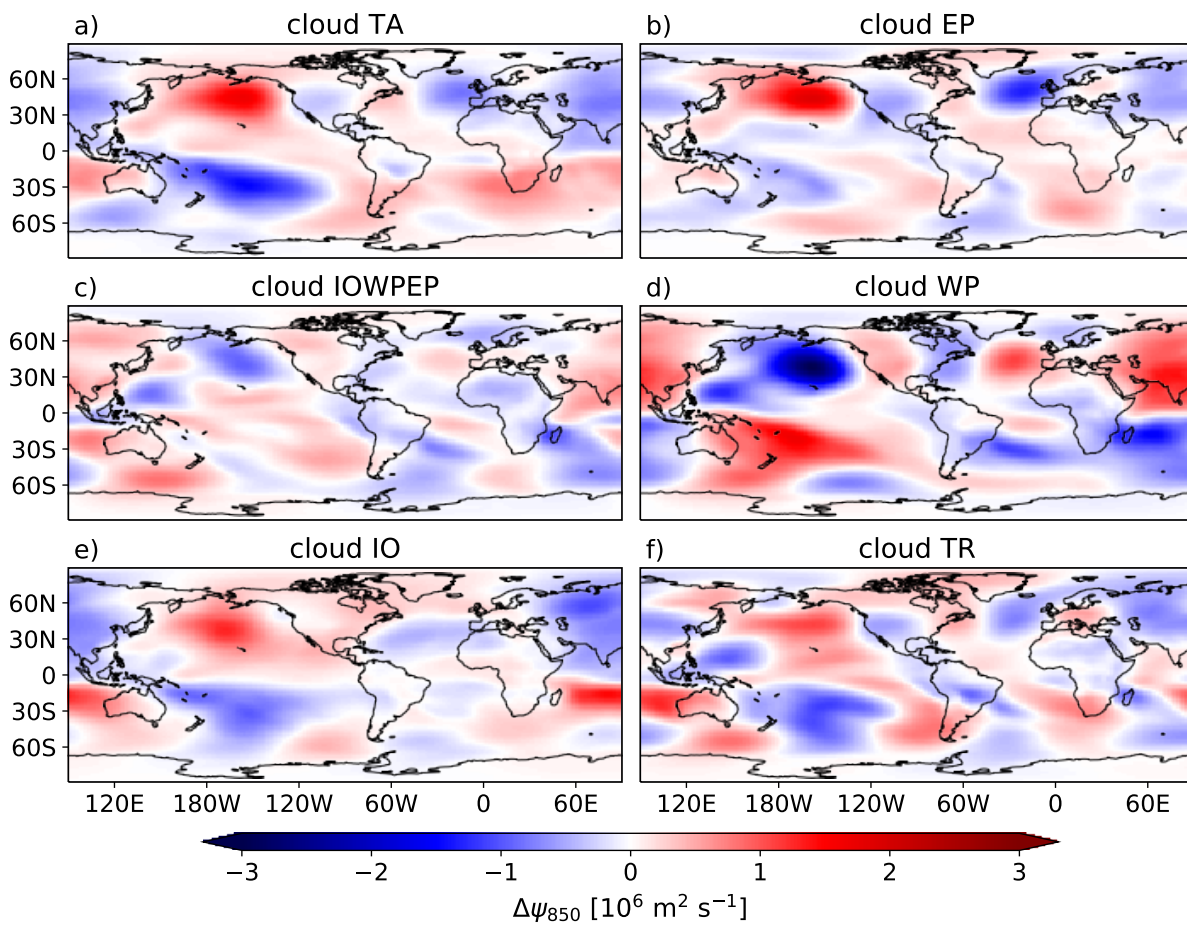
Figure C.5.: Same as Fig. 7.8, but for the response at 850 hPa.
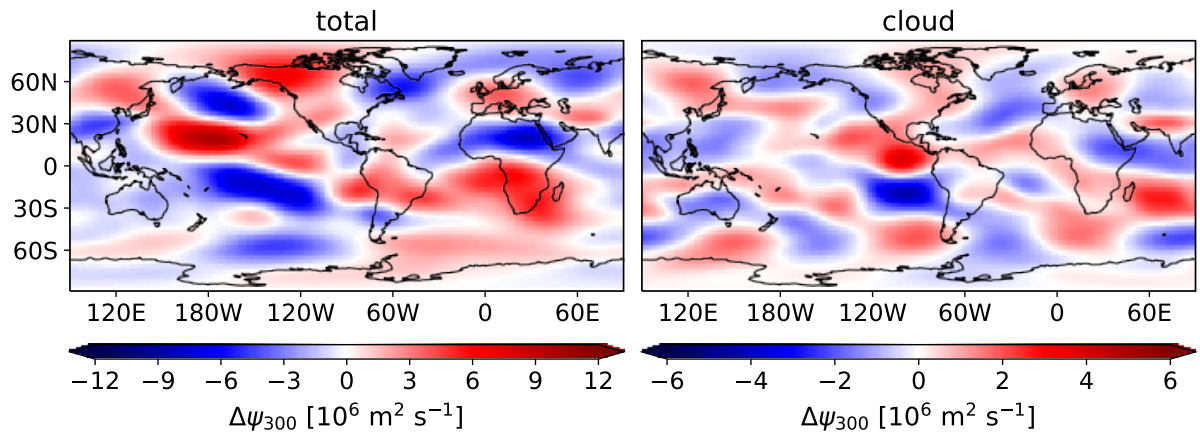
Figure C.6.: Same as Fig. 7.8, but for the total response (left) and the global cloud impact (right).

D. List of Figures

E. List of Tables

Bibliography

Albern, N., A. Voigt, S. A. Buehler, and V. Grützun, 2018: Robust and Nonrobust Impacts of Atmospheric Cloud-Radiative Interactions on the Tropical Circulation and Its Response to Surface Warming. *Geophys. Res. Lett.*, **45**, 8577–8585.

Albern, N., A. Voigt, and J. G. Pinto, 2019: Cloud-Radiative Impact on the Regional Responses of the Midlatitude Jet Streams and Storm Tracks to Global Warming. *J. Adv. Model. Earth Syst.*, **11 (7)**, 1940–1958, URL `https://doi.org/10.1029/2018MS001592`.

Albern, N., A. Voigt, D. W. J. Thompson, and J. G. Pinto, 2020: The Role of Tropical, Midlatitude, and Polar Cloud-Radiative Changes for the Midlatitude Circulation Response to Global Warming. *J. Climate*, **33 (18)**, 7927–7943, URL `https://doi.org/10.1175/JCLI-D-20-0073.1`.

Allan, R. P., 2011: Combining satellite data and models to estimate cloud radiative effect at the surface and in the atmosphere. *Met. Apps.*, **18 (3)**, 324–333.

Barnes, E. A., D. L. Hartmann, D. M. W. Frierson, and J. Kidston, 2010: Effect of latitude on the persistence of eddy-driven jets. *Geophys. Res. Lett.*, **37 (L11804)**.

Barnes, E. A. and L. M. Polvani, 2013: Response of the midlatitude jets and of their variability to increased greenhouse gases in CMIP5 models. *J. Climate*, **26**, 7117–7135.

Barnes, E. A. and D. W. J. Thompson, 2014: Comparing the Roles of Barotropic versus Baroclinic Feedbacks in the Atmosphere's Response to Mechanical Forcing. *J. Atmos. Sci.*, **71 (1)**, 177–194.

Bechtold, P., M. Köhler, T. Jung, F. Doblas-Reyes, M. Leutbecher, M. J. Rodwell, F. Vitart, and G. Balsamo, 2008: Advances in simulating atmospheric variability with the ecmwf model: From synoptic to decadal time-scales. *Q.J.R. Meteorol. Soc.*, **134 (634)**, 1337–1351.

Berrisford, P., D. Dee, P. Poli, R. Brugge, K. Fielding, M. Fuentes, P. Kållberg, S. Kobayashi, S. Uppala, and A. Simmons, 2011: The ERA-Interim archive Version 2.0. ECMWF.

Blackmon, M. L., 1976: A Climatological Spectral Study of the 500 mb Geopotential Height of the Northern Hemisphere. *J. Atmos. Sci.*, **33 (8)**, 1607–1623.

Bony, S., B. Stevens, F. Ament, S. Bigorre, P. Chazette, S. Crewell, J. Delanoë, K. Emanuel, D. Farrell, C. Flamant, S. Gross, L. Hirsch, J. Karstensen, B. Mayer, L. Nuijens, J. H. Ruppert Jr., I. Sandu,

P. Siebesma, S. Speich, F. Szczap, J. Totems, R. Vogel, M. Wendisch, and M. Wirth, 2017: EUREC[4]A: A Field Campaign to Elucidate the Couplings Between Clouds, Convection and Circulation. *Surv. Geophys.*, **38**, 1529–1568.

Bony, S., B. Stevens, D. M. W. Frierson, C. Jakob, M. Kageyama, R. Pincus, T. G. Shepherd, S. C. Sherwood, A. P. Siebesma, A. H. Sobel, M. Watanabe, and M. J. Webb, 2015: Clouds, circulation and climate sensitivity. *Nature Geosci.*, **8**, 261–268.

Bracegirdle, T. J., E. Shuckburgh, J.-B. Sallee, Z. Wang, A. J. S. Meijers, N. Bruneau, T. Phillips, and L. J. Wilcox, 2013: Assessment of surface winds over the Atlantic, Indian, and Pacific Ocean sectors of the Southern Ocean in CMIP5 models: historical bias, forcing response, and state dependence. *J. Geophys. Res. Atmos.*, **118 (2)**, 547–562.

Brayshaw, D. J., B. J. Hoskins, and M. Blackburn, 2009: The basic ingredients of the North Atlantic storm track. Part I: land-sea contrast and orography. *J. Atmos. Sci.*, **66 (9)**, 2539–2558.

Butler, A. H., D. W. Thompson, and R. Heikes, 2010: The Steady-State Atmospheric Circulation Response to Climate Change-like Thermal Forcings in a Simple General Circulation Model. *J. Climate*, **23**, 3474–3496.

Butler, A. H., D. W. J. Thompson, and T. Birner, 2011: Isentropic Slopes, Downgradient Eddy Fluxes, and the Extratropical Atmospheric Circulation Response to Tropical Tropospheric Heating. *J. Atmos. Sci.*, **68 (10)**, 2292–2305.

Cassou, C., 2008: Intraseasonal interaction between the Madden–Julian oscillation and the North Atlantic Oscillation. *Nature*, **455 (7212)**, 523–527.

Ceppi, P. and D. L. Hartmann, 2015: Connections Between Clouds, Radiation, and Midlatitude Dynamics: a Review. *Curr. Clim. Change Rep.*, **1**, 94–102.

———, 2016: Clouds and the atmospheric circulation response to warming. *J. Climate*, **29**, 783–799.

Ceppi, P., Y.-T. Hwang, D. M. W. Frierson, and D. L. Hartmann, 2012: Southern Hemisphere jet latitude biases in CMIP5 models linked to shortwave cloud forcing. *Geophys. Res. Lett.*, **39**, L19 708.

Ceppi, P., Y.-T. Hwang, X. Liu, D. M. W. Frierson, and D. L. Hartmann, 2013: The relationship between the ITCZ and the Southern Hemispheric eddy-driven jet. *J. Geophys. Res.*, **118 (11)**, 5136–5146.

Ceppi, P. and T. G. Shepherd, 2017: Contributions of Climate Feedbacks to Changes in Atmospheric Circulation. *J. Climate*, **30 (22)**, 9097–9118.

Ceppi, P., G. Zappa, T. G. Shepherd, and J. M. Gregory, 2018: Fast and Slow Components of the Extratropical Atmospheric Circulation Response to CO2 Forcing. *J. Climate*, **31 (3)**, 1091–1105.

Ceppi, P., M. D. Zelinka, and D. L. Hartmann, 2014: The Response of the Southern Hemispheric Eddy-Driven Jet to Future Changes in Shortwave Radiation in CMIP5. *Geophys. Res. Lett.*, **41**, 3244–3250.

CERES, 2020: CERES EBAF Ed4.1 - Data Quality Summary (March 3, 2020). NASA.

Chang, E. K. M., Y. Guo, and X. Xia, 2012: CMIP5 multimodel ensemble projection of storm track change under global warming. *J. Geophys. Res.*, **117 (D23118)**.

Chang, E. K. M., S. Lee, and K. L. Swanson, 2002: Storm Track Dynamics. *J. Climate*, **15 (16)**, 2163–2183.

Chen, G. and I. M. Held, 2007: Phase speed spectra and the recent poleward shift of Southern Hemisphere surface westerlies. *Geophys. Res. Lett.*, **34 (21)**.

Chen, G., J. Lu, and D. M. W. Frierson, 2008: Phase Speed Spectra and the Latitude of Surface Westerlies: Interannual Variability and Global Warming Trend. *J. Climate*, **21 (22)**, 5942–5959.

Christoph, M., U. Ulbrich, and U. Haak, 1995: Faster Determination of the Intraseasonal Variability of Storm Tracks Using Murakami's Recursive Filter. *Mon. Weather Rev.*, **123 (2)**, 578–581.

Ciasto, L. M., C. Li, J. J. Wettstein, and N. G. Kvamstø, 2016: North Atlantic Storm-Track Sensitivity to Projected Sea Surface Temperature: Local versus Remote Influences. *J. Climate*, **29 (19)**, 6973–6991.

Colman, R. A., 2003: A comparison of climate feedbacks in general circulation models. *Clim. Dyn.*, **20**, 865–873.

Colman, R. A. and B. J. McAvaney, 1997: A study of general circulation model climate feedbacks determined from perturbed sea surface temperature experiments. *J. Geophys. Res.*, **102 (D16)**, 19 383–19 402.

Dee, D. P., S. M. Uppala, A. J. Simmons, P. Berrisford, P. Poli, S. Kobayashi, U. Andrae, M. A. Balmaseda, G. Balsamo, P. Bauer, P. Bechtold, A. C. M. Beljaars, L. van de Berg, J. Bidlot, N. Bormann, C. Delsol, R. Dragani, M. Fuentes, A. J. Geer, L. Haimberger, S. B. Healy, H. Hersbach, E. V. Hólm, L. Isaksen, P. Kållberg, M. Köhler, M. Matricardi, A. P. McNally, B. M. Monge-Sanz, J.-J. Morcrette, B.-K. Park, C. Peubey, P. de Rosnay, C. Tavolato, J.-N. Thépaut, and F. Vitart, 2011: The ERA-Interim reanalysis: configuration and performance of the data assimilation system. *Q. J. R. Meteorol. Soc.*, **137 (656)**, 553–597.

Dickinson, R. E., 1969: Vertical propagation of planetary rossby waves through an atmosphere with Newtonian cooling. *J. Geophys. Res.*, **74 (4)**, 929–938.

Dipankar, A., B. Stevens, R. Heinze, C. Moseley, G. Zängl, M. Giorgetta, and S. Brdar, 2015: Large eddy simulation using the general circulation model ICON. *J. Adv. Model. Earth Syst.*, **7**, 963–986.

Doms, G. and M. Baldauf, 2018: A Description of the Nonhydrostatic Regional COSMO-Model Part I: Dynamics and Numerics. Consortium for Small-Scale Modelling, URL `http://www.cosmo-model.org`.

Doms, G., J. Förstner, E. Heise, H.-J. Herzog, D. Mironov, M. Raschendorfer, T. Reinhardt, B. Ritter, R. Schrodin, J.-P. Schulz, and G. Vogel, 2011: A Description of the Nonhydrostatic Regional COSMO-Model Part II: Physical Parameterizations. Consortium for Small-Scale Modelling, URL `http://www.cosmo-model.org`.

Dufresne, J.-L., M.-A. Foujols, S. Denvil, A. Caubel, O. Marti, O. Aumont, Y. Balkanski, S. Bekki, H. Bellenger, R. Benshila, S. Bony, L. Bopp, P. Braconnot, P. Brockmann, P. Cadule, F. Cheruy, F. Codron, A. Cozic, D. Cugnet, N. de Noblet, J.-P. Duvel, C. Ethé, L. Fairhead, T. Fichefet, S. Flavoni, P. Friedlingstein, J.-Y. Grandpeix, L. Guez, E. Guilyardi, D. Hauglustaine, F. Hourdin, A. Idelkadi, J. Ghattas, S. Joussaume, M. Kageyama, G. Krinner, S. Labetoulle, A. Lahellec, M.-P. Lefebvre, F. Lefevre, C. Levy, Z. X. Li, J. Lloyd, F. Lott, G. Madec, M. Mancip, M. Marchand, S. Masson, Y. Meurdesoif, J. Mignot, I. Musat, S. Parouty, J. Polcher, C. Rio, M. Schulz, D. Swingedouw, S. Szopa, C. Talandier, P. Terray, N. Viovy, and N. Vuichard, 2013: Climate change projections using the IPSL-CM5 Earth System Model: from CMIP3 to CMIP5. *Clim. Dyn.*, **40**, 2123–2165.

Fermepin, S. and S. Bony, 2014: Influence of low-cloud radiative effects on tropical circulation and precipitation. *J. Adv. Model. Earth Syst.*, **6 (3)**, 513–526.

Fläschner, D., T. Mauritsen, B. Stevens, and S. Bony, 2018: The Signature of Shallow Circulations, Not Cloud Radiative Effects, in the Spatial Distribution of Tropical Precipitation. *J. Climate*, **31 (23)**, 9489–9505.

Gassmann, A. and H.-J. Herzog, 2008: Towards a consistent numerical compressible non-hydrostatic model using generalized Hamiltonian tools. *Q. J. R. Meteorol. Soc.*, **134 (635)**, 1597–1613.

Gates, W. L., 1992: AMIP: The Atmospheric Model Intercomparison Project. *Bull. Amer. Meteor. Soc.*, **73 (12)**, 1962–1970.

Geoffroy, O., D. Saint-Martin, A. Voldoire, D. Salas y Mélia, and S. Sénési, 2014: Adjusted radiative forcing and global radiative feedbacks in CNRM-CM5, a closure of the partial decomposition. *Clim. Dyn.*, **42**, 1807–1818.

Gerber, E. P. and S.-W. Son, 2014: Quantifying the Summertime Response of the Austral Jet Stream and Hadley Cell to Stratospheric Ozone and Greenhouse Gases. *J. Climate*, **27**, 5538–5559.

Giorgetta, M. A., R. Brokopf, T. Crueger, M. Esch, S. Fiedler, J. Helmert, C. Hohenegger, L. Kornblueh, M. Köhler, E. Manzini, T. Mauritsen, C. Nam, T. Raddatz, S. Rast, D. Reinert, M. Sakradzija, H. Schmidt, R. Schneck, R. Schnur, L. Silvers, H. Wan, G. Zängl, and B. Stevens, 2018: ICON-A,

the Atmosphere Component of the ICON Earth System Model: I. Model Description. *J. Adv. Model. Earth Syst.*, **10 (7)**, 1613–1637.

Giorgetta, M. A., J. Jungclaus, C. H. Reick, S. Legutke, J. Bader, M. Böttinger, V. Brovkin, T. Crueger, M. Esch, K. Fieg, K. Glushak, V. Gayler, H. Haak, H.-D. Hollweg, T. Ilyina, S. Kinne, L. Kornblueh, D. Matei, T. Mauritsen, U. Mikolajewicz, W. Mueller, D. Notz, F. Pithan, T. Raddatz, S. Rast, R. Redler, E. Roeckner, H. Schmidt, R. Schnur, J. Segschneider, K. D. Six, M. Stockhause, C. Timmreck, J. Wegner, H. Widmann, K.-H. Wieners, M. Claussen, J. Marotzke, and B. Stevens, 2013: Climate and carbon cycle changes from 1850 to 2100 in MPI-ESM simulations for the Coupled Model Intercomparison Project phase 5. *J. Adv. Model. Earth Syst.*, **5 (3)**, 572–597.

Goss, M. and S. B. Feldstein, 2017: Why Do Similar Patterns of Tropical Convection Yield Extratropical Circulation Anomalies of Opposite Sign? *J. Atmos. Sci.*, **74**, 487–511.

Graff, L. S. and J. H. LaCasce, 2012: Changes in the Extratropical Storm Tracks in Response to Changes in SST in an AGCM. *J. Climate*, **25 (6)**, 1854–1870.

Grise, K. M. and B. Medeiros, 2016: Understanding the Varied Influence of Midlatitude Jet Position on Clouds and Cloud Radiative Effects in Observations and Global Climate Models. *J. Climate*, **29 (24)**, 9005–9025.

Grise, K. M. and L. M. Polvani, 2014a: Southern Hemisphere cloud-dynamics biases in CMIP5 models and their implications for climate projections. *J. Climate*, **27**, 6074–6092.

———, 2014b: The response of midlatitude jets to increased CO_2: Distinguishing the roles of sea surface temperature and direct radiative forcing. *Geophys. Res. Lett.*, **41 (19)**, 6863–6871.

Harrop, B. E. and D. L. Hartmann, 2016: The Role of Cloud Radiative Heating in Determining the Location of the ITCZ in Aquaplanet Simulations. *J. Climate*, **29**, 2741–2763.

Hartmann, D. L. and K. Larson, 2002: An important constraint on tropical cloud - climate feedback. *Geophys. Res. Lett.*, **29 (20)**, 1951.

Harvey, B., P. Cook, L. Shaffrey, and R. Schiemann, 2020: The response of the Northern Hemisphere storm tracks and jetstreams to climate change in the CMIP3, CMIP5, and CMIP6 climate models. *EGU General Assembly 2020, Online, 4–8 May 2020*, EGU2020-19711.

Harvey, B. J., L. C. Shaffrey, and T. J. Woollings, 2014: Equator-to-pole temperature differences and the extra-tropical storm track responses of the CMIP5 climate models. *Clim. Dyn.*, **43 (5)**, 1171–1182.

———, 2015: Deconstructing the climate change response of the Northern Hemisphere wintertime storm tracks. *Clim. Dyn.*, **45 (9)**, 2847–2860.

Harvey, B. J., L. C. Shaffrey, T. J. Woollings, G. Zappa, and K. I. Hodges, 2012: How large are projected 21st century storm track changes? *Geophys. Res. Lett.*, **39 (L18707)**.

Heinze, R., A. Dipankar, C. C. Henken, C. Moseley, O. Sourdeval, S. Trömel, X. Xie, P. Adamidis, F. Ament, H. Baars, C. Barthlott, A. Behrendt, U. Blahak, S. Bley, S. Brdar, M. Brueck, S. Crewell, H. Deneke, P. Di Girolamo, R. Evaristo, J. Fischer, C. Frank, P. Friederichs, T. Göcke, K. Gorges, L. Hande, M. Hanke, A. Hansen, H.-C. Hege, C. Hoose, T. Jahns, N. Kalthoff, D. Klocke, S. Kneifel, P. Knippertz, A. Kuhn, T. van Laar, A. Macke, V. Maurer, B. Mayer, C. I. Meyer, S. K. Muppa, R. A. J. Neggers, E. Orlandi, F. Pantillon, B. Pospichal, N. Röber, L. Scheck, A. Seifert, P. Seifert, F. Senf, P. Siligam, C. Simmer, S. Steinke, B. Stevens, K. Wapler, M. Weniger, V. Wulfmeyer, G. Zängl, D. Zhang, and J. Quaas, 2017: Large-eddy simulations over Germany using ICON: a comprehensive evaluation. *Q. J. R. Meteorol. Soc.*, **143 (702)**, 69–100.

Heise, E., B. Ritter, and R. Schrodin, 2006: Operational implementation of the multilayer soil model. COSMO Technical Reports No. 9, Consortium for Small-Scale Modelling, 19 pp., URL `http://www.cosmo-model.org`.

Held, I. M., 1975: Momentum Transport by Quasi-Geostrophic Eddies. *J. Atmos. Sci.*, **32 (7)**, 1494–1497.

Held, I. M. and M. J. Suarez, 1994: A Proposal for the Intercomparison of the Dynamical Cores of Atmospheric General Circulation Models. *Bull. Amer. Meteor. Soc.*, **75**, 1825–1830.

Henderson, S., E. D. Maloney, and E. Barnes, 2016: The Influence of the Madden-Julian Oscillation on Northern Hemisphere Winter Blocking. *J. Climate*, **29**, 4597–4616.

Hollingsworth, A., R. J. Engelen, C. Textor, A. Benedetti, O. Boucher, F. Chevallier, A. Dethof, H. Elbern, H. Eskes, J. Flemming, C. Granier, J. W. Kaiser, J.-J. Morcrette, P. Rayner, V.-H. Peuch, L. Rouil, M. G. Schultz, A. J. Simmons, and the GEMS Consortium, 2008: TOWARD A MONITORING AND FORECASTING SYSTEM FOR ATMOSPHERIC COMPOSITION. *Bull. Amer. Meteor. Soc.*, **89 (8)**, 1147–1164.

Holton, J. R., 2004: *An Introduction to Dynamic Meteorology*. 4th ed., International Geophysics Series, Elsevier Academic Press, Burlington, MA, 535 pp.

Hong, Y., G. Liu, and J. F. Li, 2016: Assessing the Radiative Effects of Global Ice Clouds Based on CloudSat and CALIPSO Measurements. *J. Climate*, **29**, 7651–7674.

Hoskins, B. J. and D. J. Karoly, 1981: The Steady Linear Response of a Spherical Atmosphere to Thermal and Orographic Forcing. *J. Atmos. Sci.*, **38 (6)**, 1179–1196.

Hoskins, B. J. and P. J. Valdes, 1990: On the Existence of Storm-Tracks. *J. Atmos. Sci.*, **47 (15)**, 1854–1864.

Jiménez-Esteve, B. and D. I. V. Domeisen, 2020: Nonlinearity in the tropospheric pathway of enso to the north atlantic. *Weather Clim. Dynam.*, **1**, 225–245.

Kato, S., F. G. Rose, D. A. Rutan, T. E. Thorsen, N. G. Loeb, D. R. Doelling, X. Huang, W. L. Smith, W. Su, and S.-H. Ham, 2018: Surface irradiances of Edition 4.0 Clouds and the Earth's Radiant Energy System (CERES) Energy Balanced and Filled (EBAF) data product. *J. Climate*, **31**, 4501–4527.

Kidston, J., S. M. Dean, J. A. Renwick, and G. K. Vallis, 2010: A robust increase in the eddy length scale in the simulation of future climates. *Geophys. Res. Lett.*, **37 (3)**, L03 806.

Kidston, J. and E. P. Gerber, 2010: Intermodel variability of the poleward shift of the austral jet stream in the CMIP3 integrations linked to biases in 20th century climatology. *Geophys. Res. Lett.*, **37 (9)**, L09 708.

Kidston, J., G. K. Vallis, S. M. Dean, and J. A. Renwick, 2011: Can the Increase in the Eddy Length Scale under Global Warming Cause the Poleward Shift of the Jet Streams? *J. Climate*, **24 (14)**, 3764–3780.

Klocke, D., J. Quaas, and B. Stevens, 2013: Assessment of different metrics for physical climate feedbacks. *Clim. Dyn.*, **41**, 1173–1185.

Klocke, D., T. M. Satoh, B. Stevens, F. Judt, W. Putman, M. Khairoutdinov, X. Chen, N. Wedi, and J. Biercamp, 2019: Project DYAMOND 2nd Phase – The Winter. available at `https://www.esiwace.eu/services/dyamond/dyamond-2nd-phase-the-winter-experimental-protocol`.

Kushner, P. J. and I. M. Held, 1998: A test, using atmospheric data, of a method for estimating oceanic eddy diffusivity. *Geophys. Res. Lett.*, **25 (22)**, 4213–4216.

Kushner, P. J., I. M. Held, and T. L. Delworth, 2001: Southern Hemisphere atmospheric circulation response to global warming. *J. Climate*, **14 (10)**, 2238–2249.

Langen, P. L., R. G. Graversen, and T. Mauritsen, 2012: Separation of Contributions from Radiative Feedbacks to Polar Amplification on an Aquaplanet. *J. Climate*, **25 (8)**, 3010–3024.

Li, J.-L. F., D. E. Waliser, G. Stephens, and S. Lee, 2016: Characterizing and Understanding Cloud Ice and Radiation Budget Biases in Global Climate Models and Reanalysis. *Meteor. Monogr.*, **56**, 13.1–13.20.

Li, Y. and D. W. J. Thompson, 2016: Observed Signatures of the Barotropic and Baroclinic Annular Modes in Cloud Vertical Structure and Cloud Radiative Effects. *J. Climate*, **29 (13)**, 4723–4740.

Li, Y., D. W. J. Thompson, and S. Bony, 2015: The Influence of Atmospheric Cloud Radiative Effects on the Large-Scale Atmospheric Circulation. *J. Climate*, **8**, 7263–7278.

Li, Y., D. W. J. Thompson, S. Bony, and T. M. Merlis, 2019: Thermodynamic Control on the Poleward Shift of the Extratropical Jet in Climate Change Simulations: The Role of Rising High Clouds and Their Radiative Effects. *J. Climate*, **32**, 917–934.

Li, Y., D. W. J. Thompson, G. L. Stephens, and S. Bony, 2014: A global survey of the instantaneous linkages between cloud vertical structure and large-scale climate. *J. Geophys. Res. Atmos.*, **119**, 3770–3792.

Lindzen, R. S. and B. Farrell, 1980: A Simple Approximate Result for the Maximum Growth Rate of Baroclinic Instabilities. *J. Atmos. Sci.*, **37 (7)**, 1648–1654.

Loeb, N. G., D. R. Doelling, H. Wang, W. Su, C. Nguyen, J. G. Corbett, L. Liang, C. Mitrescu, F. G. Rose, and S. Kato, 2018: Clouds and the Earth's Radiant Energy System (CERES) Energy Balanced and Filled (EBAF) Top-of-Atmosphere (TOA) Edition-4.0 Data Product. *J. Climate*, **31 (2)**, 895–918.

Lorenz, D. J. and E. T. DeWeaver, 2007: Tropopause height and zonal wind response to global warming in the ipcc scenario integrations. *J. Geophys. Res.*, **112**, D10 119.

Lott, F. and M. J. Miller, 1997: A new subgrid-scale orographic drag parametrization: Its formulation and testing. *Q. J. R. Meteorol. Soc.*, **123 (537)**, 101–127.

Lu, J., G. Chen, and D. M. W. Frierson, 2008: Response of the Zonal Mean Atmospheric Circulation to El Niño versus Global Warming. *J. Climate*, **21 (22)**, 5835–5851.

Ma, J. and S.-P. Xie, 2013: Regional Patterns of Sea Surface Temperature Change: A Source of Uncertainty in Future Projections of Precipitation and Atmospheric Circulation. *J. Climate*, **26 (8)**, 2482–2501.

Mace, G. G., Q. Zhang, M. Vaughan, R. Marchand, G. Stephens, C. Trepte, and D. Winker, 2009: A description of hydrometeor layer occurrence statistics derived from the first year of merged Cloudsat and CALIPSO data. *J. Geophys. Res. Atmos.*, **114 (D8)**.

Madden, R. A. and P. R. Julian, 1971: Detection of a 40-50 Day Oscillation in the Zonal Wind in the Tropical Pacific. *J. Atmos. Sci.*, **28**, 702–708.

———, 1972: Description of Global-Scale Circulation Cells in the Tropics with a 40-50 Day Period. *J. Atmos. Sci.*, **29**, 1109–1123.

Manabe, S. and R. T. Wetherald, 1987: Large-Scale Changes of Soil Wetness Induced by an Increase in Atmospheric Carbon Dioxide. *J. Atmos. Sci.*, **44 (8)**, 1211–1236.

Mauritsen, T., R. G. Graversen, D. Klocke, P. L. Langen, B. Stevens, and L. Tomassini, 2013: Climate feedback efficiency and synergy. *Clim. Dyn.*, **41**, 2539–2554.

McGraw, M. C. and E. A. Barnes, 2016: Seasonal Sensitivity of the Eddy-Driven Jet to Tropospheric Heating in an Idealized AGCM. *J. Climate*, **29 (14)**, 5223–5240.

Meehl, G. A., G. J. Boer, C. Covey, M. Latif, and R. J. Stouffer, 2000: The Coupled Model Intercomparison Project (CMIP). *Bull. Amer. Meteor. Soc.*, **81 (2)**, 313–318.

Meehl, G. A., C. Covey, B. McAvaney, M. Latif, and R. J. Stouffer, 2005: Overview of the Coupled Model Intercomparison Project. *Bull. Amer. Meteor. Soc.*, **86 (1)**, 89–93.

Middlemas, E. A., A. C. Clement, B. Medeiros, and B. Kirtman, 2019: Cloud Radiative Feedbacks and El Niño–Southern Oscillation. *J. Climate*, **32 (15)**, 4661–4680.

Mironov, D., E. Heise, E. Kourzeneva, B. Ritter, N. Schneider, and A. Terzhevik, 2010: Implementation of the lake parameterisation scheme FLake into the numerical weather prediction model COSMO. *Boreal Env. Res.*, **15**, 218–230.

Mironov, D., B. Ritter, J.-P. Schulz, M. Buchhold, M. Lange, and E. MacHulskaya, 2012: Parameterisation of sea and lake ice in numerical weather prediction models of the German Weather Service. *Tellus A*, **64 (1)**.

Mironov, D. V., 2008: Parameterization of lakes in numerical weather prediction. Description of a lake model. COSMO Technical Report, Consortium for Small-Scale Modelling, 41 pp. URL `http://www.cosmo-model.org`.

Mlawer, E. J., S. J. Taubman, P. D. Brown, M. J. Iacono, and S. A. Clough, 1997: Radiative transfer for inhomogeneous atmospheres: RRTM, a validated correlated-k model for the longwave. *J. Geophys. Res.*, **102 (D14)**, 16 663–16 682.

Muhlbauer, A., T. P. Ackerman, J. M. Comstock, G. S. Diskin, S. M. Evans, R. P. Lawson, and R. T. Marchand, 2014: Impact of large-scale dynamics on the microphysical properties of midlatitude cirrus. *J. Geophys. Res. Atmos.*, **119 (7)**, 3976–3996.

O'Gorman, P. A., 2010: Understanding the varied response of the extratropical storm tracks to climate change. *Proc. Natl. Acad. Sci.*, **107 (45)**, 19 176–19 180.

O'Reilly, C. H., S. Minobe, A. Kuwano-Yoshida, and T. Woollings, 2017: The Gulf Stream influence on wintertime North Atlantic jet variability. *Q. J. R. Meteorol. Soc.*, **143 (702)**, 173–183.

Orr, A., P. Bechtold, J. Scinocca, M. Ern, and M. Janiskova, 2010: Improved Middle Atmosphere Climate and Forecasts in the ECMWF Model through a Nonorographic Gravity Wave Drag Parameterization. *J. Climate*, **23 (22)**, 5905–5926.

Palmer, T. N. and D. A. Mansfield, 1984: Response of two atmospheric general circulation models to sea-surface temperature anomalies in the tropical East and West Pacific. *Nature*, **310**, 483–485.

Peixoto, J. P. and A. H. Oort, 1992: *Physics of Climate*. AIP Press.

Pfahl, S., E. Madonna, M. Boettcher, H. Joos, and H. Wernli, 2014: Warm conveyor belts in the ERA-Interim dataset (1979-2010). Part II: Moisture origin and relevance for precipitation. *J. Climate*, **27 (27-40)**.

Pinto, J. G., M. K. Karremann, K. Born, P. M. Della-Marta, and M. Klawa, 2012: Loss potentials associated with European windstorms under future climate conditions. *Clim. Res.*, **54**, 1–20.

Pinto, J. G., T. Spangehl, U. Ulbrich, and P. Speth, 2006: Assessment of winter cyclone activity in a transient ECHAM4-OPYC3 GHG experiment. *Meteorol. Z.*, **15 (3)**, 279–291.

Pinto, J. G., U. Ulbrich, G. C. Leckebusch, T. Spangehl, M. Reyers, and S. Zacharias, 2007: Changes in storm track and cyclone activity in three SRES ensemble experiments with the ECHAM5/MPI-OM1 GCM. *Clim. Dyn.*, **29 (2)**, 195–210.

Polvani, L. M., D. W. Waugh, G. J. P. Correa, and S.-W. Son, 2011: Stratospheric Ozone Depletion: The Main Driver of Twentieth-Century Atmospheric Circulation Changes in the Southern Hemisphere. *J. Climate*, **24**, 795–812.

Popp, M. and L. G. Silvers, 2017: Double and Single ITCZs with and without Clouds. *J. Climate*, **30 (22)**, 9147–9166.

Prill, F., D. Reinert, D. Rieger, G. Zängl, J. Schröter, J. Förstner, S. Werchner, M. Weimer, R. Ruhnke, and B. Vogel, 2019: *ICON Model Tutorial – Working with the ICON Model – Practical Exercises for NWP Mode and ICON-ART*. Deutscher Wetterdienst.

Rädel, G., T. Mauritsen, B. Stevens, D. Dommenget, D. Matei, K. Bellomo, and A. Clement, 2016: Amplification of El Niño by cloud longwave coupling to atmospheric circulation. *Nature Geosci.*, **9**, 106–110.

Ramanathan, V., R. D. Cess, E. F. Harrison, P. Minnis, B. R. Barkstrom, E. Ahmad, and D. Hartmann, 1989: Cloud-Radiative Forcing and Climate: Results from the Earth Radiation Budget Experiment. *Science*, **243 (4887)**, 57–63.

Raschendorfer, M., 2001: The new turbulence parameterization of LM. COSMO News Letter No. 1, Consortium for Small-Scale Modelling, 89–97, URL http://www.cosmo-model.org.

Rast, S., 2017: Using and programming ICON – a first introduction. Max Planck Institute for Meteorology.

Roberts, J. F., A. J. Champion, L. C. Dawkins, K. I. Hodges, L. C. Shaffrey, D. B. Stephenson, M. A. Stringer, H. E. Thornton, and B. D. Youngman, 2014: The XWS open access catalogue of extreme European windstorms from 1979 to 2012. *Nat. Hazards Earth Syst. Sci.*, **14 (9)**, 2487–2501.

Satoh, M., B. Stevens, C. S. Bretherton, and J. Biercamp, 2017: Project DYAMOND. available at `https://www.esiwace.eu/services/dyamond/dyamond-protocol`.

Schäfler, A., G. Craig, H. Wernli, P. Arbogast, J. D. Doyle, R. McTaggart-Cowan, J. Methven, G. Rivière, F. Ament, M. Boettcher, M. Bramberger, Q. Cazenave, R. Cotton, S. Crewell, J. Delanoë, A. Dörnbrack, A. Ehrlich, F. Ewald, A. Fix, C. M. Grams, S. L. Gray, H. Grob, S. Groß, M. Hagen, B. Harvey, L. Hirsch, M. Jacob, T. Kölling, H. Konow, C. Lemmerz, O. Lux, L. Magnusson, B. Mayer, M. Mech, R. Moore, J. Pelon, J. Quinting, S. Rahm, M. Rapp, M. Rautenhaus, O. Reitebuch, H. Reynolds, C. A. Sodemann, T. Spengler, G. Vaughan, M. Wendisch, M. Wirth, B. Witschas, K. Wolf, and T. Zinner, 2018: The North Atlantic Waveguide and Downstream Impact Experiment. *Bull. Amer. Meteor. Soc.*, **99**, 1607–1637.

Schneider, E. K., B. P. Kirtman, and R. S. Lindzen, 1999: Tropospheric Water Vapor and Climate Sensitivity. *J. Atmos. Sci.*, **56 (11)**, 1649–1658.

Schrodin, R. and E. Heise, 2001: The Multi-Layer Version of the DWD Soil Model TERRA LM. Tech. Rep. 2, Consortium for Small-Scale Modelling, 1–16 pp., URL `http://www.cosmo-model.org`.

Schwierz, C., P. Köllner-Heck, E. Zenklusen Mutter, D. N. Bresch, P.-L. Vidale, M. Wild, and C. Schär, 2010: Modelling European winter wind storm losses in current and future climate. *Clim. Change*, **101**, 485–514.

Seifert, A., 2008: A revised cloud microphysical parameterization for COSMO-LME. COSMO News Letter No. 7, Proceedings from the 8th COSMO General Meeting in Bucharest, 2006, Consortium for Small-Scale Modelling, 25–28, URL `http://www.cosmo-model.org`.

Shaw, T. A., 2019: Mechanisms of Future Predicted Changes in the Zonal Mean Mid-Latitude Circulation. *Curr. Clim. Change Rep.*, **5**, 345–357.

Shaw, T. A., M. Baldwin, E. A. Barnes, R. Caballero, C. I. Garfinkel, Y.-T. Hwang, C. Li, P. A. O'Gorman, G. Rivière, I. R. Simpson, and A. Voigt, 2016: Storm track processes and the opposing influences of climate change. *Nature Geosci.*, **9**.

Shaw, T. A. and A. Voigt, 2015: Tug of war on summertime circulation between radiative forcing and sea surface warming. *Nature Geosci.*, **8**, 560–566.

Shepherd, T. G., 2014: Atmospheric circulation as a source of uncertainty in climate change projections. *Nature Geosci.*, **7**, 703–708.

Simpson, I. R., M. Blackburn, and J. D. Haigh, 2009: The Role of Eddies in Driving the Tropospheric Response to Stratospheric Heating Perturbations. *J. Atmos. Sci.*, **66 (5)**, 1347–1365.

Simpson, I. R., T. A. Shaw, and R. Seager, 2014: A Diagnosis of the Seasonally and Longitudinally Varying Midlatitude Circulation Response to Global Warming. *J. Atmos. Sci.*, **71**, 2489–2515.

Singh, M. S. and P. A. O'Gorman, 2012: Upward Shift of the Atmospheric General Circulation under Global Warming: Theory and Simulations. *J. Climate*, **25 (23)**, 8259–8276.

Slingo, A. and J. M. Slingo, 1988: The response of a general-circulation model to cloud longwave radiative forcing. Part I: Introduction and initial experiments. *Q. J. R. Meteorol. Soc.*, **114**, 1027–1062.

Soden, B. J. and I. M. Held, 2006: An Assessment of Climate Feedbacks in Coupled Ocean–Atmosphere Models. *J. Climate*, **19 (14)**, 3354–3360.

Stephens, G. L., D. G. Vane, R. J. Boain, G. G. Mace, K. Sassen, Z. Wang, A. J. Illingworth, E. J. O'connor, W. B. Rossow, S. L. Durden, S. D. Miller, R. T. Austin, A. Benedetti, C. Mitrescu, and the CloudSat Science Team, 2002: THE CLOUDSAT MISSION AND THE A-TRAIN: A New Dimension of Space-Based Observations of Clouds and Precipitation. *Bull. Amer. Meteor. Soc.*, **83 (12)**, 1771–1790.

Stevens, B., F. Ament, S. Bony, S. Crewell, F. Ewald, S. Gross, A. Hansen, L. Hirsch, M. Jacob, T. Kölling, H. Konow, B. Mayer, M. Wendisch, M. Wirth, K. Wolf, S. Bakan, M. Bauer-Pfundstein, M. Brueck, J. Delanoë, A. Ehrlich, D. Farrell, M. Forde, F. Gödde, H. Grob, M. Hagen, E. Jäkel, F. Jansen, C. Klepp, M. Klingebiel, M. Mech, G. Peters, M. Rapp, A. A. Wing, and T. Zinner, 2019: A High-Altitude Long-Range Aircraft Configured as a Cloud Observatory: The NARVAL Expeditions. *Bull. Amer. Meteor. Soc.*, **100**, 1061–1077.

Stevens, B., S. Bony, and M. Webb, 2012: Clouds On-Off Klimate Intercomparion Experiment (COOKIE). available at `http://www.euclipse.eu/wp4/wp4.html`.

Stevens, B., M. Giorgetta, M. Esch, T. Mauritsen, T. Crueger, S. Rast, and E. Roeckner, 2013: Atmospheric component of the MPI-M Earth System Model: ECHAM6. *J. Adv. Model. Earth Syst.*, **5**, 146–172.

Taylor, K. E., R. J. Stouffer, and G. A. Meehl, 2009: A Summary of the CMIP5 Experiment Design. *PCMDI Reports*, URL `https://pcmdi.llnl.gov/mips/cmip5/experiment_design.html`.

———, 2012: An Overview of CMIP5 and the Experiment Design. *Bull. Amer. Meteor. Soc.*, **93**, 485–498.

Tegen, I., P. Hollrig, M. Chin, I. Fung, D. Jacob, and J. Penner, 1997: Contribution of different aerosol species to the global aerosol extinction optical thickness: Estimates from model results. *J. Geophys. Res.*, **102 (D20)**, 23 895–23 915.

Thompson, D. W. J., S. Bony, and Y. Li, 2017: Thermodynamic constraint on the depth of the global tropospheric circulation. *Proc. Natl. Acad. Sci.*, **114 (31)**, 8181–8186.

Tiedtke, M., 1989: A Comprehensive Mass Flux Scheme for Cumulus Parameterization in Large-Scale Models. *Mon. Wea. Rev.*, **117 (8)**, 1779–1800.

Ulbrich, U., G. C. Leckebusch, and J. G. Pinto, 2009: Extra-tropical cyclones in the present and future climate: a review. *Theor. Appl. Climatol.*, **96 (1)**, 117–131.

Ulbrich, U., J. G. Pinto, H. Kupfer, G. C. Leckebusch, T. Spangehl, and M. Reyers, 2008: Changing Northern Hemisphere Storm Tracks in an Ensemble of IPCC Climate Change Simulations. *J. Climate*, **21 (8)**, 1669–1679.

Vallis, G. K., 2017: *Atmospheric and Oceanic Fluid Dynamics: Fundamentals and Large-Scale Circulation*. 2d ed., Cambridge University Press.

Vallis, G. K., P. Zurita-Gotor, C. Cairns, and J. Kidston, 2015: Response of the large-scale structure of the atmosphere to global warming. *Q. J. R. Meteorol. Soc.*, **141**, 1479–1501.

Vavrus, S. J., 2018: The influence of arctic amplification on mid-latitude weather and climate. *Curr. Clim. Change Rep.*, **4**, 238–249.

Verlinden, K. L., D. W. J. Thompson, and G. L. Stephens, 2011: The Three-Dimensional Distribution of Clouds over the Southern Hemisphere High Latitudes. *J. Climate*, **24 (22)**, 5799–5811.

Voigt, A. and N. Albern, 2019: No Cookie for Climate Change. *Geophys. Res. Lett.*, **46 (24)**, 14 751–14 761.

Voigt, A., N. Albern, P. Ceppi, K. M. Grise, Y. Li, and B. Medeiros, 2020: Clouds, radiation and atmospheric circulation in the present-day climate and under climate change. *WIREs Clim. Change (under review)*.

Voigt, A., N. Albern, and G. Papavasileiou, 2019: The atmospheric pathway of the cloud-radiative impact on the circulation response to global warming: important and uncertain. *J. Climate*, **32 (10)**, 3051–3067.

Voigt, A. and T. A. Shaw, 2015: Circulation response to warming shaped by radiative changes of clouds and water vapor. *Nature Geosci.*, **8**, 102–106.

———, 2016: Impact of regional atmospheric cloud-radiative changes on shifts of the extratropical jet stream in response to global warming. *J. Climate*, **29 (23)**, 8399–8421.

Wetherald, R. T. and S. Manabe, 1988: Cloud Feedback Processes in a General Circulation Model. *J. Atmos. Sci.*, **45 (8)**, 1397–1416.

Wild, S., D. J. Befort, and G. C. Leckebusch, 2015: Was the Extreme Storm Season in Winter 2013/14 Over the North Atlantic and the United Kingdom Triggered by Changes in the West Pacific Warm Pool? *Bull. Amer. Meteor. Soc.*, **96**, S29–S34.

Woollings, T., 2010: Dynamical influences on European climate: an uncertain future. *Phil. Trans. R. Soc. A*, **368 (1924)**, 3733–3756.

Woollings, T. and M. Blackburn, 2012: The North Atlantic Jet Stream under Climate Change and Its Relation to the NAO and EA Patterns. *J. Climate*, **25 (3)**, 886–902.

Woollings, T., J. M. Gregory, J. G. Pinto, M. Reyers, and D. J. Brayshaw, 2012: Response of the North Atlantic storm track to climate change shaped by ocean-atmosphere coupling. *Nature Geosci.*, **5**, 313–317.

Yin, J. H., 2005: A consistent poleward shift of the storm tracks in simulations of 21st century climate. *Geophys. Res. Lett.*, **32**, L18 701.

Yuan, X., M. R. Kaplan, and M. Cane, 2018: The Interconnected Global Climate System – A Review of Tropical-Polar Teleconnections. *J. Clim.*, **31**, 5765–5792.

Yuval, J. and Y. Kaspi, 2016: Eddy Activity Sensitivity to Changes in the Vertical Structure of Baroclinicity. *J. Atmos. Sci.*, **73 (4)**, 1709–1726.

Zängl, G., D. Reinert, P. Ripodas, and M. Baldauf, 2015: The ICON (ICOsahedral Non-hydrostatic) modelling framework of DWD and MPI-M: Description of the non-hydrostatic dynamical core. *Q. J. R. Meteorol. Soc.*, **141**, 563–579.

Zappa, G., B. J. Hoskins, and T. G. Shepherd, 2015: Improving Climate Change Detection through Optimal Seasonal Averaging: The Case of the North Atlantic Jet and European Precipitation. *J. Climate*, **28 (16)**, 6381–6397.

Zappa, G., F. Pithan, and T. G. Shepherd, 2018: Multimodel evidence for an atmospheric circulation response to Arctic sea ice loss in the CMIP5 future projections. *Geophys. Res. Lett.*, **45**, 1011–1019.

Zappa, G., L. C. Shaffrey, and K. I. Hodges, 2013: The Ability of CMIP5 Models to Simulate North Atlantic Extratropical Cyclones. *J. Climate*, **26 (15)**, 5379–5396.

Zhao, W., Y. Peng, B. Wang, B. Yi, Y. Lin, and J. Li, 2018: Comparison of three ice cloud optical schemes in climate simulations with community atmospheric model version 5. *Atmos. Res.*, **204**, 37–53.

Acknowledgments